

University of Southampton Research Repository ePrints Soton

Copyright © and Moral Rights for this thesis are retained by the author and/or other copyright owners. A copy can be downloaded for personal non-commercial research or study, without prior permission or charge. This thesis cannot be reproduced or quoted extensively from without first obtaining permission in writing from the copyright holder/s. The content must not be changed in any way or sold commercially in any format or medium without the formal permission of the copyright holders.

When referring to this work, full bibliographic details including the author, title, awarding institution and date of the thesis must be given e.g.

AUTHOR (year of submission) "Full thesis title", University of Southampton, name of the University School or Department, PhD Thesis, pagination

UNIVERSITY OF SOUTHAMPTON

FACULTY OF NATURAL AND ENVIRONMENTAL SCIENCES

Electrochemistry Group

School of Chemistry

Design and characterisation of nanostructured microelectrodes for biomedical applications

by

Mohammed Abdul-Aziz Alshadokhi

Thesis for the degree of Doctor of Philosophy in chemistry

May_2014

UNIVERSITY OF SOUTHAMPTON

ABSTRACT

FACULTY OF NATURAL AND ENVIRONMENTAL SCIENCES

Electrochemistry

Thesis for the degree of Doctor of Philosophy in Chemistry

DESIGN AND CHARACTERISATION OF NANOSTRUCTURED MICROELECTRODES FOR BIOMEDICAL APPLICATIONS

Mohammed Abdul-Aziz Alshadokhi

The aim of the project is to create a nanostructured microelectrode *pH* sensor to measure the *pH* of brain fluids. This work will describe the fabrication, characterization and development of the nanostructured Pd electrodes and their assessment for use as *pH* sensors in the brain fluid. The palladium hydride $\alpha+\beta$ transition is located between the α and β phases where H/Pd atomic ratios range between 0.02 and 0.6. This region was selected to fabricate the *pH* sensor because its potential ($E_{\text{Pd-H}}$) is stable and independent of the hydrogen– palladium composition. In addition, $E_{\text{Pd-H}}$ follows a linear relationship with *pH*. A nanostructured Pd film was chosen to fabricate the *pH* sensor in order to obtain a large electroactive area because $E_{\text{Pd-H}}$ is not stable with microelectrode; a large area is needed to reach the equilibrium between palladium and hydrogen. Also, neurobiological *pH* measurements require a small sensor as a result of the limited biological sample quantities available. The nanostructured *pH* sensor H₁-e Pd was made by liquid crystal templating method (LCT). Scanning electron microscopy (SEM) and electrochemical characterisation were used to estimate the radius *a* and electroactive area of the nanostructured Pd film after the deposition process. The $\alpha+\beta$ transition was prepared by loading hydrogen electrochemically before the experiments were carried out. The nanostructured Pd hydride electrode was then used to estimate the *pH* in different solutions including artificial cerebral spinal fluid (aCSF) and real brain fluid. The results obtained demonstrate the applicability of such electrodes to function as *pH* sensors in brain fluid. The biomedical applications requires high efficiency that can be affected by the biological samples contaminations onto the electrode. Thus, attempts were made to develop the H₁-e Pd *pH* sensors performance by covering their surface with coats to stop the biological impurities.

List of Contents

ABSTRACT	i
List of Contents	1
List of Tables	v
List of Figures	vii
DECLARATION OF AUTHORSHIP	xx
Acknowledgements	xxi
List of symbols	xxii
Abbreviations	xxiv
Chapter 1. Introduction	1
1.1. <i>pH</i> measuring	2
1.2. Palladium hydride system	11
1.3. Metal nanostructured film fabrication using liquid crystal templating	21
1.4. Oxygen effect on H ₁ -e Pd electrodes	30
1.5. Summary	45
Chapter 2. Experimental	49
2.1. Generalities	49
2.2. Purified water system	49
2.3. Electrochemical cells	49
2.4. Chemicals	50
2.5. Electrodes	51
2.6. Experimental set-up	53
2.7. Instruments	53
2.8. H ₁ -e Pd film deposition processes	56
2.9. Preparation of Pd films plating mixture and plating bath	58

Chapter 3. Deposition and characterization of Pd films	61
3.1. Deposition processes	61
3.2. Pd plating cyclic voltammetry	62
3.3. Pd films chronoamperometry electrodeposition.....	65
3.4. Electrodeposition influence in geometric surface area expansion	68
3.5. Pd electrodes real surface area	74
3.6. Hydrogen sorption in H ₁ -e Pd	75
3.7. Palladium oxide reaction	76
3.8. Electroactive surface area.....	76
3.9. H ₁ -e Pd electrode erosion	80
3.10. Summary.....	83
Chapter 4. <i>pH</i> sensing in synthetic and real brain fluid with nanostructured palladium hydride electrode.....	85
4.1. Loading and stripping potentials	85
4.2. H ₁ -e Pd film potentiometric response.....	107
4.3. <i>E</i> _{Pd-H} potential with different <i>pH</i> solutions.....	110
4.4. Brain fluid analysis.....	113
4.5. Summary	124
Chapter 5. Development of coatings.....	127
5.1. Nafion.....	128
5.2. Polypyrrole (ppy)	135
5.3. Polyaniline (PANI).....	143
5.4. Diazonium salt (Boc).....	150
5.5. 1,2-diaminobenzene in H ₂ SO ₄ (OPD).....	158
5.6. Poly (phenylene oxide).....	165
5.7. Summary	172

Chapter 6. Conclusion and further work.....	176
References.....	182

List of Tables

Table 2.1: the main chemicals that were used in this project.....	50
Table 3.1: The plating mixture for H ₁ -e Pd (using Brij [®] 56 or C ₁₆ EO ₈) and plain Pd films.	61
Table 3.2: The geometrical surface area GSA^{SEM} and GSA^{CV} obtained using SEM and from $[Ru(NH_3)_6]^{3+/2+}$ voltammograms of polished Pt and Pd microdisc electrodes before and after the Pd deposition process. The theoretical limiting current i_L^{SEM} was calculated from d^{SEM} in equation 3.7.....	73
Table 3.3: The real interface area RSA^{CV} before and after H ₁ -e Pd film deposition compared to a substrate Pt electrode and a plain Pd film with equivalent deposition charge.	77
Table 3.4: Comparison between Theoretical and experimental electroactive areas for H ₁ -e Pd films deposited on different Pt discs.	79
Table 4.1: The comparison of loading charge Q_{load} and stripping charge Q_{strip} for the current waves in the potential ranges between $E_{in} = -0.15$ V and E_{fin} , where $Q_{max\ load}$ is the maximal loading charge required to complete the formation of the β phase up to the atomic ratio of H/Pd = 0.6.....	93
Table 4.2: Dependence of the loading time t_{load} , loading charge Q_{load} and hydrogen evolution charge Q_{H_2} on the loading potential E_{load} . The hydrogen was loaded into H ₁ -e Pd film ($Q_{dep} = 2500$ μ C), deposited onto a 250 μ m diameter Pt disc electrode, in a deaerated solution of 0.5 M Na ₂ SO ₄ + H ₂ SO ₄ solution (pH 1.88) at room temperature. Other conditions as stated in Figure 4.6	98
Table 4.3: Analysis of the hydrogen stripping stages from H ₁ -e Pd film ($Q_{dep} = 2500$ μ C), deposited onto a 250 μ m diameter Pt disc electrode, after potentiostatically loading hydrogen using varying loading potentials E_{load} for 1800 s, in a deaerated solution of 20 ml 0.5 M Na ₂ SO ₄ + H ₂ SO ₄ solution (pH 1.88) at room temperature; the hydrogen was	

stripped by scanning the potential from E_{load} to the stripping potential $E_{strip} = -0.15$ V vs. SMSE with a scan rate $v = 10$ mv s⁻¹. 103

Table 4.4: The estimation of pH using nanostructured Pd immediately after hydrogen was loaded under open circuit potential conditions, the working electrode was a H₁-e Pd film ($Q_{dep} = 2500$ μC) deposited onto a 250 μm diameter Pt disc electrode, in a deaerated solution of 0.5 M Na₂SO₄ + H₂SO₄ solution (pH 1.88) at 25° C. 109

Table 4.5: The mean \bar{x} , the standard deviation σ and the standard error of the mean $\sigma\bar{x}$ of E_{Pd-H} vs. SMSE / V that were obtained from ten potentiometric measurements for each test solution of commercial buffers pH 4.04, 6.98, 9.97 (Fisher Scientific), and 1 M NaOH (pH 14) carried out at 37 °C. 110

Table 4.6: The composition of the artificial cerebral spinal aCSF fluid [160]. 113

Table 4.7: The obtained E_{Pd-H} vs. SMSE / V of the potentiometric measurements for brain fluid and commercial buffers pH 4, 7, 10 (Fisher Scientific). 121

Table 5.1: The current at -0.7 V vs. SCE for CVs recorded in aerated and in Ar purged phosphate pH 7 buffer solution before and after coating of H₁-e Pd film with Nafion. 131

Table 5.2: The influence of several coatings in the $\alpha+\beta$ transition lifetime and the accuracy of the pH estimation. 172

List of Figures

Figure 1.1: The pressure-composition isotherms at various temperatures for palladium hydride solid / gas system, α , β phases and $\alpha+\beta$ transition are shown by dotted lines, reproduced from [8].	13
Figure 1.2: The palladium hydride electrode potential against atomic ratio in 1 M HClO ₄ at 25 °C, the potential was measured after hydrogen had been loaded cathodically into the PdH electrode, redrawn from [61].	15
Figure 1.3: The structures of C ₁₆ EO ₈ and Brij [®] 56 surfactants.	22
Figure 1.4: General supramolecular structures of the surfactant aggregation when dissolved in a polar solvent. The liquid crystal phases are: a) micellar I ₁ , b) hexagonal H ₁ , c) lamellar L _{α} , d) inverse hexagonal H ₂ , and e) inverse micellar L ₂ reproduced from [85].	23
Figure 1.5: The templating deposition process of the H _{1-e} Pd films, the cylinders represent the hexagonal phase of the liquid crystal in the deposition mixture redrawn from [80].	25
Figure 1.6: C ₁₆ EO ₈ (top) and Brij [®] 56 (bottom) / heptane (wt ratio 22:1) liquid crystal phase diagrams at different concentration and temperature conditions in aqueous solution of 1.40 M (NH ₄) ₂ PdCl ₄ reproduced from [80].	27
Figure 1.7: Nafion structure.	32
Figure 1.8: H ⁺ transfer in sulfonic acid groups of Nafion redrawn from [102].	33
Figure 1.9: The structure of the monomers used to make the polymeric films; a/ Pyrrole, b/ [1-(2-carboxyethyl) pyrrole], c/ Indole, d/ o-1,2-diaminobenzene, e/ Aniline, and f/ Phenol.	34
Figure 1.10: pyrrole (and derivatives) monomer polymerization redrawn from [110].	35

Figure 1.11: the repeated polymerization and overoxidation of ultrathin OPPy films redrawn from [113].	37
Figure 1.12: Indole monomers polymerization mechanism redrawn from [117].	39
Figure 1.13: o-1,2-diaminobenzene monomers polymerization mechanism redrawn from [119].	41
Figure 1.14: Aniline monomers polymerization mechanism redrawn from [121].	42
Figure 1.15: The electropolymerisation mechanism of phenol monomers redrawn from [124].	43
Figure 1.16: Mechanism for the covalent modification onto a substrate electrode taken from [127, 128].	44
Figure 1.17: The molecular structure of some covalent modification monolayer films used in this project.	44
Figure 2.1: Schematic diagram of the laboratory constructed (a) saturated calomel electrode (SCE) and saturated mercury sulphate electrode (SMSE), (b) Ag / AgCl reference electrode, (c) working electrode.	53
Figure 2.2: Schematic diagram of voltammetric and chronoamperometric electronic circuits showing a five neck pear-shaped cell.	54
Figure 2.3: Schematic diagram of the high input impedance differential amplifier electronic circuit and of the electrochemical cell.	55
Figure 2.4: A typical cyclic voltammogram for Pt microdisc ($d = 25 \mu\text{m}$) electrodes recorded in 1 M H_2SO_4 , purged with argon for 20 minutes, at room temperature, at scan rate $\nu = 200 \text{ mV s}^{-1}$.	58
Figure 2.5: Schematic diagrams of the three electrode electronic circuit for $\text{H}_{1-\text{e}}$ Pd film electrodeposition in the left diagram and the 12% wt. $(\text{NH}_4)_2\text{PdCl}_4$ plating bath in the right diagram. Typically the plating mixture consisted of 12 wt. % ammonium tetrachloropalladate (II) plus 47 wt.% of the surfactant (either Brij [®] 56 or C_{16}EO_8) with	

39 wt.% purified water and 2 wt. % of heptane. For plain Pd films the plating bath consisted of 12 wt. % ammonium tetrachloropalladate (II) plus 88 wt.% purified water.59

Figure 3.1: Cyclic voltammetry of the H₁-e Pd film mixture (which contain Brij[®] 56 as a surfactant) recorded at 10 mV s⁻¹ with a Pt microdisc electrode (*d* = 25 μm), at room temperature. Cycle sequence as indicated in the plot. The mixture used for the top voltammogram was prepared the previous day, while that used for the lower voltammogram was prepared 3 weeks before. 63

Figure 3.2: Cyclic voltammetry of the plain Pd film using a simple aqueous plating bath which contained 12 wt. % (NH₄)₂PdCl₄, recorded at 10 mV s⁻¹ with a Pt microdisc electrode (*d* = 25 μm), at room temperature. Cycle sequence as indicated in the plot. ..64

Figure 3.3: Chronoamperograms recorded during three H₁-e Pd films deposition onto a Pt microdisc electrodes (*d* = 250 μm), the potential was stepped from +0.4 V to +0.1 V vs. SCE. Deposition charge *Q*_{dep} = 2500 μC. The transients were recorded sequentially (as indicated by the time when the deposition was started) using the same mixture includes C₁₆EO₈ as a surfactant, but without reconditioning of the mixture in between each deposition. 66

Figure 3.4: Scanning electron microscopy images with scale bar = 10 μm of (a) a polished Pt substrate microdisc electrode (*d* = 25 μm), (b) a deposited H₁-e Pd film using Brij[®] 56 in the plating mixture, (c) a deposited H₁-e Pd film using C₁₆EO₈ in the plating mixture, (d) a deposited plain Pd film in plating bath. The electrochemical deposition parameters of all of them were: deposition charge *Q*_{dep} equals 25 μC, the Pd concentration was 12 wt. % of (NH₄)₂PdCl₄, deposition potential *E*_{final dep} equals +0.1 and +0.23 V vs. SCE with and without surfactant respectively. The tilt angle of the top row is 70°, and in the lower row is 0°.69

Figure 3.5: Cyclic voltammograms recorded for a range of H₁-e Pd films deposited on a Pt microdisc electrodes (*d* = 25 μm) recorded at 2 mV s⁻¹ in 5 mM Ru(NH₃)₆³⁺ + 0.5 M KCl at 25° C. The deposition charges *Q*_{dep} of H₁-e Pd are (1) 0 μC, (2) 10 μC, (3) 25 μC, and (4) 50 μC. 71

Figure 3.6: Cyclic voltammograms recorded for (1) a polished Pt microdisc electrode ($d = 25 \mu\text{m}$), (2) a polished Pd microdisc electrode ($d = 25 \mu\text{m}$), (3) a $\text{H}_1\text{-e}$ Pd film ($Q_{\text{dep}} = 25 \mu\text{C}$) onto Pt microdisc electrode ($d = 25 \mu\text{m}$) and (4) a plain Pd film ($Q_{\text{dep}} = 25 \mu\text{C}$) onto Pt microdisc electrode ($d = 25 \mu\text{m}$) recorded at 2 mV s^{-1} in $5 \text{ mM Ru}(\text{NH}_3)_6^{3+} + 0.5 \text{ M KCl}$ at 25°C 72

Figure 3.7: Cyclic voltammograms recorded at 20 mV s^{-1} in $1 \text{ M H}_2\text{SO}_4$ at room temperature for a $\text{H}_1\text{-e}$ Pd film (black line) and a plain Pd film (red line) onto polished Pt microdisc electrodes ($d = 25 \mu\text{m}$), the deposition charge Q_{dep} of both of them = $25 \mu\text{C}$ and a polished Pd microdisc electrodes ($d = 25 \mu\text{m}$) (blue line). 75

Figure 3.8: Schematic representation of a $\text{H}_1\text{-e}$ M unit cell..... 78

Figure 3.9: Scanning electron microscopy images with scale bar = $10 \mu\text{m}$ of a $\text{H}_1\text{-e}$ Pd film ($Q_{\text{dep}} = 10 \mu\text{C}$) deposited onto a polished Pt microdisc electrode ($d = 25 \mu\text{m}$) using C_{16}EO_8 as a surfactant of the mixture. The images show the same microdisc electrode. Top row shows the microdisc electrode before deposition process of $\text{H}_1\text{-e}$ Pd film, the second row shows the film directly after the deposition. The third row shows the cracking in the film following experiments. The last row shows the disappearance of the $\text{H}_1\text{-e}$ Pd film leaving the bare substrate Pt microdisc electrode. The tilt angle of the right column is 70° and 0° in the left column. 81

Figure 3.10: Theoretical domains of corrosion, immunity and passivation of palladium, at 25°C reproduced from [157]. 82

Figure 4.1: A typical cyclic voltammogram of $\text{H}_1\text{-e}$ Pd film ($Q_{\text{dep}} = 2500 \mu\text{C}$), deposited onto a $250 \mu\text{m}$ diameter Pt disc electrode. The voltammogram was recorded at scan rate $v = 20 \text{ mV s}^{-1}$ in 20 ml of $0.5 \text{ M Na}_2\text{SO}_4 + \text{H}_2\text{SO}_4$ solution ($\text{pH } 1.88$), purged with argon for 20 minutes at room temperature. The three pairs of peaks correspond to; A and B hydrogen adsorption and desorption process, C and D hydrogen absorption to form and strip the $\text{PdH } \alpha$ phase, and E and F correspond to the same process as peaks C and D but for the $\text{PdH } \beta$ phase. 86

Figure 4.2: Cyclic voltammograms of H₁-e Pd film ($Q_{\text{dep}} = 2500 \mu\text{C}$), deposited onto a 250 μm diameter Pt disc electrode. The voltammograms were recorded at scan rate $v = 20 \text{ mV s}^{-1}$ in 20 ml of 0.5 M Na₂SO₄ + H₂SO₄ solution (pH 1.88), purged with argon for 20 minutes at room temperature. The CVs recorded between -0.15 and -0.70 V (the solid red line) and between +0.65 to -0.70 V (the black dotted line)..... 88

Figure 4.3: Cyclic voltammograms of H₁-e Pd film ($Q_{\text{dep}} = 2500 \mu\text{C}$), deposited onto a 250 μm diameter Pt disc electrode. The voltammograms were recorded in 20 ml of 0.5 M Na₂SO₄ + H₂SO₄ solution (pH 1.88), purged with argon for 20 minutes, scan rate $v = 10, 20, 40, 100 \text{ mV s}^{-1}$ 89

Figure 4.4: Cyclic voltammograms of H₁-e Pd film ($Q_{\text{dep}} = 2500 \mu\text{C}$), deposited onto a 250 μm diameter Pt disc electrode. The voltammograms were recorded between the initial potential $E_{\text{in}} = -0.15 \text{ V}$ and final potential E_{fin} vs. SMSE, in 20 ml of 0.5 M Na₂SO₄ + H₂SO₄ solution (pH 1.88) at 20 mV s^{-1} , purged with argon for 20 minutes. The current peaks are: (A and B) hydrogen adsorption and desorption, (C and D) the hydrogen absorption / extraction to form and strip the α phase, E hydrogen absorption for the β phase, F hydrogen desorption of β phase, (F+D) is the overlapping between the stripping of α and β phases. (G and H) evolution / oxidation of H₂ that has evolved..... 92

Figure 4.5: Chronoamperogram for the loading and stripping of hydrogen into a H₁-e Pd film ($Q_{\text{dep}} = 2500 \mu\text{C}$), deposited onto a 250 μm diameter Pt disc electrode. Data recorded in a solution of 20 ml of 0.5 M Na₂SO₄ + H₂SO₄ solution (pH 1.88) at room temperature, purged with argon for 20 minutes; the stripping potential $E_{\text{strip}} = -0.15 \text{ V}$ and the loading potential $E_{\text{load}} = -0.75 \text{ V}$ vs. SMSE; the potential was stepped from E_{strip} to E_{load} and held for t_{load} then it was swept from E_{load} to E_{strip} at a scan rate $v = 10 \text{ mV s}^{-1}$. The insert shows the potential waveform used to load and extract hydrogen to and from the Pd nanostructure..... 95

Figure 4.6: Hydrogen loading chronoamperograms into H₁-e Pd film ($Q_{\text{dep}} = 2500 \mu\text{C}$), deposited onto a 250 μm diameter Pt disc electrode in a deaerated solution of 20 ml 0.5 M Na₂SO₄ + H₂SO₄ solution (pH 1.88) at room temperature, the potential was stepped at $t = 0 \text{ s}$ from the starting potential = -0.15 V to a range of loading potential E_{load} between

-0.65 and -0.85 V vs. SMSE. The insert shows the chronoamperogram when $E_{\text{load}} = -0.750$ V..... 97

Figure 4.7: Stripping peaks recorded after potentiostatically loading hydrogen for 1800 s into H₁-e Pd film ($Q_{\text{dep}} = 2500 \mu\text{C}$), deposited onto a 250 μm diameter Pt disc electrode in a deaerated solution of 20 ml 0.5 M Na₂SO₄ + H₂SO₄ solution (pH 1.88) at room temperature; the potential was swept from different loading potentials E_{load} to the stripping potential $E_{\text{strip}} = -0.15$ V vs. SMSE with a scan rate $v = 10$ mV s⁻¹. H _{α} , H _{β} and H_{ads} respectively indicate the stripping peaks for hydrogen from the α and β phases and from the surface. 101

Figure 4.8: Stripping peaks recorded for loading potentials more negative than those used in **Figure 4.7**. All experimental parameters are as shown in **Figure 4.7**. 102

Figure 4.9: A chronopotentiogram for the hydrogen loading at room temperature into a H₁-e Pd film ($Q_{\text{dep}} = 2500 \mu\text{C}$), deposited onto a 250 μm diameter Pt disc electrode in a deaerated solution of 20 ml commercial buffer pH 10 (Fisher Scientific / FB67162), the applied loading current $i_{\text{load}} = 10 \mu\text{A}$ 105

Figure 4.10: Potentiometric measurement of a H₁-e Pd film ($Q_{\text{dep}} = 2500 \mu\text{C}$) deposited onto a 250 μm diameter Pt disc electrode, in a deaerated solution of 0.5 M Na₂SO₄ + H₂SO₄ solution (pH 1.88) at 25° C, immediately after hydrogen was loaded into the Pd nanostructure. The potential measured $E_{\text{Pd-H}}$ is drawn in black line, while the first derivative of $E_{\text{Pd-H}}$ against the time is drawn in red. 108

Figure 4.11: Relationship of $E_{\text{Pd-H}}$ against pH obtained in deaerated commercial buffer solutions and (at pH 14 we used 1 M NaOH) at the human body temperature of 37° C. The Potentiometric measurement for each solution has been done using a H₁-e Pd film ($Q_{\text{dep}} = 2500 \mu\text{C}$) deposited onto a 250 μm diameter Pt disc electrode, immediately after hydrogen was loaded into the Pd nanostructure..... 111

Figure 4.12: The cyclic voltammograms of a H₁-e Pd film ($Q_{\text{dep}} = 2500 \mu\text{C}$) deposited onto a 250 μm diameter Pt disc electrode recorded at 20 mV s⁻¹ in 20 ml of artificial cerebral spinal fluid aCSF (pH 7) at 25° C. CVs recorded in aerated solution (black), in

Ar purged (20 min) solution (red) before the addition of 5% (w/v) bovine serum albumin, BSA, to the aCSF solution, and in aerated aCSF solution with BSA (blue). 114

Figure 4.13: Potentiometric measurements of a H₁-e Pd film ($Q_{\text{dep}} = 2500 \mu\text{C}$) deposited onto a 250 μm diameter Pt disc electrode in artificial cerebral spinal fluid aCSF pH 7 at 37° C, aerated aCSF (black), deaerated aCSF (red) and aerated aCSF with 5% (w/v) bovine serum albumin BSA, immediately after hydrogen was loaded into the Pd nanostructure..... 115

Figure 4.14: Hydrogen loading chronoamperogram into H₁-e Pd film ($Q_{\text{dep}} = 2500 \mu\text{C}$), deposited onto a 250 μm diameter Pt disc electrode in an aerated solution of 15 ml aerated buffered artificial cerebral spinal fluid, aCSF, at 37° C, the potential was stepped at $t = 0$ s from the starting potential = -0.486 V to the loading potential $E_{\text{load}} = -1.300$ V vs. SMSE..... 117

Figure 4.15: Potentiometric measurement during the titration of a H₁-e Pd film ($Q_{\text{dep}} = 2500 \mu\text{C}$) deposited onto a 250 μm diameter Pt disc electrode in aerated buffered aCSF at 37° C, immediately after hydrogen was loaded into the Pd nanostructure in same solution. To increase the pH of the aCSF aliquots of 50 μl of 3.5 M HCl were used and 50 μl of 3.5 M NaOH to decrease the pH 118

Figure 4.16: The calibration curve of $E_{\text{Pd-H}}$ vs. pH for the potentiometric titration of a H₁-e Pd film ($Q_{\text{dep}} = 2500 \mu\text{C}$) deposited onto a 250 μm diameter Pt disc electrode in aerated buffered artificial cerebral spinal fluid aCSF at 37° C, immediately after hydrogen was loaded into the Pd nanostructure in the same solution. Aliquots of 50 μl of 3.5 M HCl and 50 μl of 3.5 M NaOH were used to modify the pH of the aCSF..... 119

Figure 4.17: Potentiometric measurements with a H₁-e Pd film ($Q_{\text{dep}} = 2500 \mu\text{C}$) deposited onto a 250 μm diameter Pt disc electrode in aerated a cerebral spinal fluid CSF at 22° C and aerated commercial buffers of pH 4, 7 and 10 (Fisher Scientific), immediately after hydrogen was loaded into the Pd nanostructure. 121

Figure 4.18: The calibration curve of $E_{\text{Pd-H}}$ vs. pH for the potentiometric measurements of a H₁-e Pd film ($Q_{\text{dep}} = 2500 \mu\text{C}$) deposited onto a 250 μm diameter Pt disc electrode in

an aerated brain fluid and aerated commercial buffers of pH 4, 7 and 10 (Fisher Scientific), at 22° C. The dotted line indicates the electrode potential and corresponding pH for the sample of real brain fluid. The potentials errors ΔE_{Pd-H} for aerated solutions are: 0.005, 0.002, 0.001 and 0.002 V vs. SMSE of: buffer pH 4, brain fluid, buffer 7 and buffer 10 respectively..... 122

Figure 5.1: Scanning electron microscopy images, with different magnifications (a equals 1 mm and b equals 500 μm) of a H_1 -e Pd film ($Q_{dep} = 2500 \mu C$) deposited onto a 250 μm diameter Pt disc electrode after coating with Nafion (tilt angle 70°). 129

Figure 5.2: The cyclic voltammograms of a H_1 -e Pd film ($Q_{dep} = 2500 \mu C$) deposited onto a 250 μm diameter Pt disc electrode recorded at 20 $mV s^{-1}$ in 20 ml phosphate pH 7 buffer at 25° C. CVs recorded in aerated solution (black) and in Ar purged (20 min) solution (red), solid lines for uncoated films, dotted lines for films coated with Nafion (4 μl 5% in in water and 1-propanol). 130

Figure 5.3: The cyclic voltammograms of a H_1 -e Pd film ($Q_{dep} = 2500 \mu C$) deposited onto a 250 μm diameter Pt disc electrode recorded at 2 $mV s^{-1}$ in 20 ml of Ar purged 5 mM $Ru(NH_3)_6^{3+} + 0.5 M KCl$ at 25° C. CVs recorded before (black) and after (red) applying the Nafion coating (4 μl 5% in in water and 1-propanol). 132

Figure 5.4: Hydrogen loading chronoamperograms into H_1 -e Pd film ($Q_{dep} = 2500 \mu C$), deposited onto a 250 μm diameter Pt disc electrode, with and without Nafion coating in aerated aCSF (pH 7) at 25° C. The potential was stepped at $t = 0 s$ from the starting potential $E_{strip} = -0.486 V$ to the loading potential $E_{load} = -1.300 V$ vs. SMSE. 133

Figure 5.5: Potentiometric measurement of a H_1 -e Pd film ($Q_{dep} = 2500 \mu C$) deposited onto a 250 μm diameter Pt disc electrode, in aerated aCSF brain fluid (pH 7) at 25° C, immediately after hydrogen was loaded into the Pd nanostructure. 134

Figure 5.6: Cyclic voltammograms for the deposition of polypyrrole onto a H_1 -e Pd film ($Q_{dep} = 2500 \mu C$) itself deposited onto a 250 μm diameter Pt disc electrode, in aqueous solution of 0.05 M of pyrrole + 0.2 M K_2SO_4 at 100 $mV s^{-1}$ and room temperature. CV1, 2 and 3 are the first three cycles. 135

Figure 5.7: Cyclic voltammograms recorded to passivate the polypyrrole layer deposited on a H₁-e Pd film ($Q_{\text{dep}} = 2500 \mu\text{C}$) itself deposited onto a 250 μm diameter Pt disc electrode, in a fresh aqueous solution of 0.2 M K₂SO₄ at room temperature and 100 mV s⁻¹. CV1, CV2 and CV3 reflect the first, second and third cycles..... 136

Figure 5.8: Scanning electron microscopy images (tilt angle 70°) of a bare H₁-e Pd film (a), and H₁-e Pd film with polypyrrole layer (b and c) with different magnifications (in a and b the scale bar equals 50 μm and in c it equals 20 μm). The H₁-e Pd films were each deposited with $Q_{\text{dep}} = 2500 \mu\text{C}$ onto a 250 μm diameter Pt disc electrode..... 137

Figure 5.9: The cyclic voltammograms of a H₁-e Pd film ($Q_{\text{dep}} = 2500 \mu\text{C}$) deposited onto a 250 μm diameter Pt disc electrode recorded at 20 mV s⁻¹ in 20 ml 0.5 M KCl at 25° C. CVs recorded in aerated solution (black) and in Ar purged (20 min) solution (red), solid lines for uncoated films, dotted lines for film coated with polypyrrole. 138

Figure 5.10: Cyclic voltammograms recorded in deaerated 5 mM Ru(NH₃)₆³⁺ + 0.5 M KCl at 25° C at 2 mV s⁻¹ for a H₁-e Pd film ($Q_{\text{dep}} = 2500 \mu\text{C}$) deposited onto a 250 μm diameter Pt disc electrode. CVs recorded without (black) and with a polypyrrole layer of 315 nm thickness (red) onto H₁-e Pd film and with a bare 250 μm diameter Pt disc electrode (blue)..... 139

Figure 5.11: Hydrogen loading chronoamperograms into H₁-e Pd film ($Q_{\text{dep}} = 2500 \mu\text{C}$), deposited onto a 250 μm diameter Pt disc electrode, before (black) and after (red) polypyrrole coating in aerated aCSF (*pH* 7), the potential was stepped at $t = 0$ s from the starting potential $E_{\text{strip}} = -0.486$ V to the loading potential $E_{\text{load}} = -1.300$ V vs. SMSE. 140

Figure 5.12: Potentiometric measurement of a H₁-e Pd film ($Q_{\text{dep}} = 2500 \mu\text{C}$) deposited onto a 250 μm diameter Pt disc electrode, before (black) and after applying the polypyrrole coating (red) in an aerated solution of aCSF brain fluid (*pH* 7) at 25° C, immediately after hydrogen was loaded into the Pd nanostructure. 141

Figure 5.13: Cyclic voltammograms for the deposition of polyaniline at room temperature onto a H₁-e Pd film ($Q_{\text{dep}} = 2500 \mu\text{C}$) itself deposited onto a 250 μm diameter Pt disc electrode, in 0.2 M pure aniline + 1 M H₂SO₄ at 50 mV s⁻¹..... 143

Figure 5.14: Scanning electron microscopy images with different magnifications (a, b equals 50 μm and c equals 500 μm) at tilt angle 70° of a H₁-e Pd film ($Q_{\text{dep}} = 2500 \mu\text{C}$) deposited onto a 250 μm diameter Pt disc electrode before (left), and after the electrodeposition via 20 cycles of polyaniline (middle and right)..... 144

Figure 5.15: The cyclic voltammograms of a H₁-e Pd film ($Q_{\text{dep}} = 2500 \mu\text{C}$) deposited onto a 250 μm diameter Pt disc electrode recorded at 20 mV s^{-1} in 20 ml 0.5 M KCl at 25° C. CVs recorded in aerated solution (black) and in Ar purged (20 min) solution (red), solid lines for uncoated films, dotted lines for films coated with polyaniline. ... 145

Figure 5.16: Cyclic voltammograms recorded in 5 mM $\text{Ru}(\text{NH}_3)_6^{3+}$ + 0.5 M KCl at 25° C at 2 mV s^{-1} for a H₁-e Pd film ($Q_{\text{dep}} = 2500 \mu\text{C}$) deposited onto a 250 μm diameter Pt disc electrode. CVs recorded without (black) and with a polyaniline layer (red) onto H₁-e Pd film. 146

Figure 5.17: Hydrogen loading chronoamperograms into H₁-e Pd film ($Q_{\text{dep}} = 2500 \mu\text{C}$), deposited onto a 250 μm diameter Pt disc electrode, without (black) and with (red) polyaniline coating in aerated aCSF (pH 7). The potential was stepped at $t = 0$ s from the starting potential $E_{\text{strip}} = -0.486$ V to the loading potential $E_{\text{load}} = -1.300$ V vs. SMSE. 148

Figure 5.18: Potentiometric measurement of a H₁-e Pd film ($Q_{\text{dep}} = 2500 \mu\text{C}$) deposited onto a 250 μm diameter Pt disc electrode, without (black) and with (red) polyaniline coating in an aerated solution of aCSF brain fluid (pH 7) at 25° C, immediately after hydrogen was loaded into the Pd nanostructure..... 149

Figure 5.19: Cyclic voltammograms for the electrodeposition of diazonium salt (Boc) at room temperature onto a H₁-e Pd film ($Q_{\text{dep}} = 2500 \mu\text{C}$) deposited onto a 250 μm diameter Pt disc electrode, in 5 mM 4-(N-Boc-aminomethyl) benzene diazonium tetrafluoroborate salt in 5 mM CH_3CN containing 250 mM TBATFB at 50 mV s^{-1} . CVs reflect the cycle order..... 150

Figure 5.20: Scanning electron microscopy images (tilt angle 70°) with scale bar equals 50 μm of a H₁-e Pd film ($Q_{\text{dep}} = 2500 \mu\text{C}$) deposited onto a 250 μm diameter Pt disc

electrode before (left) and after the electrodeposition of a diazonium salt (Boc) monolayer (right). 152

Figure 5.21: The cyclic voltammograms of a H₁-e Pd film ($Q_{\text{dep}} = 2500 \mu\text{C}$) deposited onto a 250 μm diameter Pt disc electrode recorded at 20 mV s^{-1} in 20 ml 0.5 M KCl at 25° C. CVs recorded in aerated solution (black), and in Ar purged (20 min) solution (red), solid lines for uncoated films, dotted lines for film coated with the diazonium salt (Boc) coating. 153

Figure 5.22: Cyclic voltammograms recorded in 5 mM $\text{Ru}(\text{NH}_3)_6^{3+}$ + 0.5 M KCl at 25° C at 2 mV s^{-1} for a H₁-e Pd film ($Q_{\text{dep}} = 2500 \mu\text{C}$) deposited onto a 250 μm diameter Pt disc electrode. CVs recorded before (black) and after the modification with the diazonium salt (Boc) coating (red) onto H₁-e Pd film. The blue CV was recorded in the base Pt substrate electrode. 155

Figure 5.23: Hydrogen loading chronoamperograms into H₁-e Pd film ($Q_{\text{dep}} = 2500 \mu\text{C}$), deposited onto a 250 μm diameter Pt disc electrode, without (black) and with (red). The modification of diazonium salt (Boc) coating in aerated aCSF ($\text{pH } 7$), the potential was stepped at $t = 0$ s from the starting potential $E_{\text{strip}} = -0.486$ V to the loading potential $E_{\text{load}} = -1.300$ V vs. SMSE. 156

Figure 5.24: Potentiometric measurement of a H₁-e Pd film ($Q_{\text{dep}} = 2500 \mu\text{C}$) deposited onto a 250 μm diameter Pt disc electrode, without (black) and with (red) diazonium salt (Boc) coating in an aerated solution of aCSF brain fluid ($\text{pH } 7$) at 25° C, immediately after hydrogen was loaded into the Pd nanostructure. 157

Figure 5.25: Voltammograms recorded while electrodepositing 1,2-diaminobenzene onto a H₁-e Pd film ($Q_{\text{dep}} = 2500 \mu\text{C}$) deposited onto a 250 μm diameter Pt disc electrode, in 10 mM 1,2-diaminobenzene in 0.5 M H_2SO_4 , at 50 mV s^{-1} at room temperature. CV1 and CV2 reflect the first and the second cycles. 159

Figure 5.26: Scanning electron microscopy images (tilt angle 70°) with scale bar equals 50 μm of a H₁-e Pd film ($Q_{\text{dep}} = 2500 \mu\text{C}$) deposited onto a 250 μm diameter Pt disc electrode before (left), and after the electrodeposition of 1,2-diaminobenzene (right). 160

Figure 5.27: The cyclic voltammograms of a H₁-e Pd film ($Q_{\text{dep}} = 2500 \mu\text{C}$) deposited onto a 250 μm diameter Pt disc electrode recorded at 20 mV s^{-1} in 20 phosphate buffer pH 7 at 25° C in aerated solution (black), and in Ar purged (20 min) solution (red); solid lines for uncoated film, dotted lines for film covered with the 1,2-diaminobenzene coating..... 161

Figure 5.28: Cyclic voltammograms recorded in 5 mM $\text{Ru}(\text{NH}_3)_6^{3+}$ + 0.5 M KCl at 25° C at 2 mV s^{-1} for a H₁-e Pd film ($Q_{\text{dep}} = 2500 \mu\text{C}$) deposited onto a 250 μm diameter Pt disc electrode. CVs recorded without (black) and with 1,2-diaminobenzene coating (red) onto H₁-e Pd film, comparing to a 250 μm diameter Pt disc electrode (blue)..... 162

Figure 5.29: Hydrogen loading chronoamperograms into H₁-e Pd film ($Q_{\text{dep}} = 2500 \mu\text{C}$), deposited onto a 250 μm diameter Pt disc electrode, without (black) and with (red) 163

Figure 5.30: Potentiometric measurement of a H₁-e Pd film ($Q_{\text{dep}} = 2500 \mu\text{C}$) deposited onto a 250 μm diameter Pt disc electrode, without (black) and with (red) 1,2-diaminobenzene coating in an aerated solution of aCSF brain fluid (pH 7) at 25° C, immediately after hydrogen was loaded into the Pd nanostructure. 164

Figure 5.31: The electrodepositing cyclic voltammetry of poly(phenylene oxide) at room temperature onto a H₁-e Pd film ($Q_{\text{dep}} = 2500 \mu\text{C}$) deposited onto a 250 μm diameter Pt disc electrode at room temperature in 50 mM phenol, 150 mM disodium hydrogen orthophosphate pH 7 buffer, at 50 mV s^{-1} . CV1 and CV2 reflect the first and second cycles..... 166

Figure 5.32: Scanning electron microscopy images (tilt angle 70°) with scale bar equals 50 μm of a H₁-e Pd film ($Q_{\text{dep}} = 2500 \mu\text{C}$) deposited onto a 250 μm diameter Pt disc electrode before (left), and after the electrodeposition process to cover the electrode surface with poly (phenylene oxide) (right)..... 167

Figure 5.33: The cyclic voltammograms of a H₁-e Pd film ($Q_{\text{dep}} = 2500 \mu\text{C}$) deposited onto a 250 μm diameter Pt disc electrode recorded at 20 mV s^{-1} in 20 ml phosphate pH 7 buffer at 25° C. CVs recorded in aerated solution (black), and in Ar purged (20 min)

solution (red). Solid lines for uncoated films, dotted lines for film coated with poly (phenylene oxide)..... 168

Figure 5.34: Cyclic voltammograms recorded in 5 mM $\text{Ru}(\text{NH}_3)_6^{3+}$ + 0.5 M KCl at 25° C at 2 mV s⁻¹ for a H₁-e Pd film ($Q_{\text{dep}} = 2500 \mu\text{C}$) deposited onto a 250 μm diameter Pt disc electrode. CVs recorded before (black) and after the modification with the poly (phenylene oxide) (red) onto H₁-e Pd film..... 169

Figure 5.35: Hydrogen loading chronoamperograms into H₁-e Pd film ($Q_{\text{dep}} = 2500 \mu\text{C}$), deposited onto a 250 μm diameter Pt disc electrode. The uncoated H₁-e Pd film (black) and the poly (phenylene oxide) modified electrode (red) were loaded with H in aerated aCSF (*pH* 7); the potential was stepped at $t = 0$ s from the starting potential $E_{\text{strip}} = -0.486$ V to the loading potential $E_{\text{load}} = -1.300$ V vs. SMSE. 170

Figure 5.36: Potentiometric measurement of a H₁-e Pd film ($Q_{\text{dep}} = 2500 \mu\text{C}$) deposited onto a 250 μm diameter Pt disc electrode, without (black) and with (red) poly (phenylene oxide) coating in an aerated solution of aCSF brain fluid (*pH* 7) at 25° C, immediately after hydrogen was loaded into the Pd nanostructure. 171

DECLARATION OF AUTHORSHIP

I, Mohammed Abdul-Aziz Alshadokhi, declare that the thesis entitled

Design and characterisation of nanostructured microelectrodes for biomedical applications

and the work presented in the thesis are both my own, and have been generated by me as the result of my own original research. I confirm that:

- this work was done wholly or mainly while in candidature for a research degree at this University;
- where any part of this thesis has previously been submitted for a degree or any other qualification at this University or any other institution, this has been clearly stated;
- where I have consulted the published work of others, this is always clearly attributed;
- where I have quoted from the work of others, the source is always given. With the exception of such quotations, this thesis is entirely my own work;
- I have acknowledged all main sources of help;
- where the thesis is based on work done by myself jointly with others, I have made clear exactly what was done by others and what I have contributed myself;
- none of this work has been published before submission.

Siged:

Date:.....

Acknowledgements

First of all I am grateful to my God for helping me during my research. I would also like to thank the government of Saudi Arabia (Ministry of defense) for the financial scholarship support.

Many thanks to my supervisor Dr. Guy Denuault and my advisor Prof. Phil. N. Bartlett for their help, support, advice, discussions and encouragement during my research.

I thank all the past and present members of the Dr. Guy and Prof. Phil groups. My thanks to Laila, Kelly, Mara and Nawal.

Finally, I would like to thank my parents, my wife, and my children for their help and understanding.

List of symbols

Symbol	Meaning	Unit
μ_i°	standard chemical potential of species i	J mol^{-1}
A	deposition film area	cm^2
a	radius of the disc electrode	μm
a_{H^+}	hydrogen ions activity in the solution	
$a_{\text{H}^+}^{\text{in}}$	activity of hydrogen ions in the internal solution of a glassy electrode	
a_i	activity of species i	
A_{wt}	atomic weight	g mole^{-1}
c	redox ions concentration in the bulk	mole dm^3
C_{dl}	the double layer capacitance	F
C_f	conversion factor of the obtained charge from 1 cm^2 of a metal area	
d	electrode diameter	μm
D	diffusion coefficient	$\text{cm}^2 \text{ s}^{-1}$
d^{CV}	electrode diameter via cyclic voltammetry	μm
d^{SEM}	electrode diameter via SEM	μm
E	electrode potential difference between WE and the RE	V
$E_{\text{asymmetry}}$	variation in the phase boundary potential	V
E_{load}	loading potential of hydrogen into the Pd nanostructured	V
E°	Standard redox potential	V
$E_{\text{M,MO,H}^+}^{\circ}$	standard potentials of metal oxide solubility product and H_2O ionization product	V
$E_{\text{RE ex}}$	potential of the external reference electrode of a glassy electrode	V
$E_{\text{RE in}}$	potential of the internal reference electrode of a glassy electrode	V
E_{strip}	stripping potential of hydrogen out of the Pd nanostructured loading	V
F	Faraday constant = 96485	C mol^{-1}
GSA	geometric surface area	cm^2
GSA^{CV}	experimental geometrical surface area.	cm^2
GSA^{SEM}	theoretical geometric surface area	cm^2
i	current	A
i_{L}	limiting current	A
i_{L}^{CV}	experimental limiting current	A
$i_{\text{L}}^{\text{SEM}}$	theoretical limiting current	A
j	charge density	C cm^2
j_{charging}	non-Faradic current of double-layer charging	A
m	number of material amount	mole

n	number of transferred electrons	
P_{H_2}	hydrogen gas pressure of the solid – gas system at equilibrium	atm
Q_{dep}	deposition charge	μC
Q_{dep}	deposition charge of a metal	C
Q_{des-Pt}	or the hydrogen desorption charge with Pt electrodes	C
Q_{H_2}	hydrogen gas evolution charge	C
Q_{load}	loading charge for hydrogen sorption	C
Q_{ox-Pd}	Pd oxide stripping charge with Pd electrodes	C
Q_{strip}	stripping charge for hydrogen desorption	C
R	gas constant = 8.314 472	$\text{J K}^{-1} \text{mol}^{-1}$
R_f	roughness factor	
r_{pore}	H_1 -e pore radius	nm
RSA	real surface area	cm^2
RSA^{CV}	real surface area via cyclic voltammetry	cm^2
RSA^{SEM}	real surface area via SEM	cm^2
T	absolute temperature	K
t	time	s
<i>thickness</i>	deposition film thickness	μm
t_{load}	loading time	s
<i>vol.</i>	deposition film volume	cm^3
$\Delta\bar{G}$	Free energy	J mol^{-1}
ρ	material density	g cm^{-3}
v	scan rate of the potential	mVs^{-1}

Abbreviations

Symbol	Meaning
RE	reference electrode
WE	working electrode
SHE	standard hydrogen electrode
NHE	normal hydrogen electrode
SCE	standard calomel electrode
SMSE	standard mercury/mercurous sulfate electrode
SEM	scanning electron microscopy
Ag/AgCl	silver/silver chloride
P-C	pressure-composition isotherms curve in this solid/gas system
fcc	face-centered cubic
F	number of degrees of freedom at equilibrium
C	number of components
P	number of independent phases
H/Pd	hydrogen palladium ratio in palladium hydride solid / gas system
α, β	independent phases of palladium hydride solid / gas system
Brij [®] 56	$C_{16}EO_n$; $n = 4 - 12$
$C_{16}EO_8$	octaethylene glycol monohexadecyl ether
LLC	lyotropic liquid crystal
TLCT	true liquid crystal templating method
CMC	surfactant critical micelle concentration
I_1	spherical micellar surfactant of the surfactant structure
H_1	the hexagonal phase of the surfactant structure
L_α	lamellar phase of the surfactant structure
H_2	inverse hexagonal phase of the surfactant structure
L_2	inverse micellar structure of the surfactant structure
H_1 -e M	hexagonal phase of the surfactant that a metal is electrochemically deposited
H/Pd	PdH atomic ratio
Nafion	perfluorosulfonic acid- PTFEcopolymer
Py	Pyrrole
PPy	Polypyrrole
OPPy	over oxidised polypyrrole
PANI	polyaniline
Boc	tert-Butoxycarbonyl
TBATFB	tetrabutylammonium tetra-fluoroborate
aCSF	The artificial cerebral spinal fluid

Page intentionally left blank

Chapter 1. Introduction

pH is an important parameter of all chemical reactions in the aspects of life, because it plays a role in the reaction direction and compound stability. For the same reasons, *pH* is also vital to a variety of industries, such as food, wastewater treatment and medicine. Therefore, *pH* is a simple parameter to analyse the progress of chemical reaction, it allows for deep monitoring of the occurring processes. Accordingly, a reliable and sensitive *pH* sensor is required to cover all the chemical aspects of life.

pH measurements have an important place in biological applications, especially in the study of neurobiological disorders (in the brain) [1], as the *pH* of the brain fluid affects the *pH* of other body fluids including blood. The normal *pH* of brain fluids is about 7.35. But, can vary due to a number of different processes; as it decrease in lactic acid production or glucose metabolism changing the concentration of CO₂, and increase in blood flow [2]. The change in the *pH* of brain fluid can also be used in medicine to aid doctors in understanding the severity of a patient's condition, as it was shown recently that patients with a high *pH* of the brain fluid would die quicker from a long term illness than a patient exhibiting a lower *pH* [3]. *pH* measurement of brain fluids is of high significance, therefore several studies were carried out in this field over the last 20 years in several scientific journals [4-7].

Due to the limited space to measure the *pH* in the body, as well as the limited biological sample quantities available for lab work out of the body, neurobiological *pH* measurements require a small sensor. The size of a *pH* sensor is therefore of great importance.

The main aim of the project is to create an efficient *pH* sensor with the ability to measure the *pH* of the brain fluids. Furthermore, this research will investigate how their performance will be improved by covering them with a protective coat. These sensors are nanostructured palladium hydride films that will be deposited electrochemically onto platinum disc electrodes, the hydrogen will then be loaded into the nanostructure

films, allowing the amount of hydrogen loaded to be estimated by open circuit potential (potentiometric mode) [8-10].

The following section will consider the pH sensing concept, and how previous pH sensors have led to the decision to use a nanostructured sensor in this research.

1.1. pH measuring

The pH acronym means the acidity degree of the solution, the IUPAC concept of pH is defined in terms of the H^+ activity, which is formally defined by equation 1.1:

$$pH = - \log_{10} a_{H^+} = - \log_{10} \left\{ \frac{f_{H^+} [H^+]}{f^\ominus} \right\} \quad 1.1$$

where a_{H^+} is the hydrogen ions activity in the solution, f_{H^+} is the activity coefficient of H^+ at molality $[H^+]$ and f^\ominus is the standard molality that equals 1 mol Kg^{-1} .

The measuring of pH is usually done via an electrochemical cell that contains; a reference electrode (RE), a pH sensing electrode (WE) and a test solution, with a voltmeter which is used for measuring the potential difference between RE and WE. This electrochemical cell can be represented by:

Reference electrode || pH sensing electrode, test solution

The pH value which reflects H^+ activity can be estimated from the cell potential using the Nernst equation which will be discussed in the next section.

There are several pH electrodes able to measure the acidity of the test solutions vs. RE, that will be reviewed before accessing the Pd hydride electrode, which is the main pH sensor in this research.

1.1.1. Hydrogen electrodes

The two half-cell potential difference of the hydrogen working electrode and the reference electrode can be converted to a pH value using the Nernst equation.

The hydrogen electrode is composed of a platinum electrode coated with a freshly layer of Pt black immersed in the measured solution that is bubbled by pure H_2 gas. The occurring process at the surface of the hydrogen electrode is:



The Nernst equation of the hydrogen electrode can be simplified in the customary standard state, so that when the H_2 pressure is equal to 1 atm, the standard potential E° will be 0 V whatever the temperature [11-13].

$$E = \frac{RT}{F} \ln a_{H^+} = - \frac{2.303 RT}{F} pH \quad 1.3$$

where E is the electrode potential difference between the indicator electrode and the RE, R the gas constant = $8.314\,472\, \text{J K}^{-1} \text{mol}^{-1}$, T the absolute temperature and F is the Faraday constant = $96485\, \text{C mol}^{-1}$.

However, this type of pH electrode is difficult to use, because the Pt surface of the hydrogen electrode should be covered with Pt black layer, as it needs to be freshly plated before pH measurement. Therefore, the use of an alternative pH sensor to the hydrogen electrode is preferred.

1.1.2. Glass electrode

Glass electrodes have a specific ion-selective properties glassy membrane bulb, those can measure the pH through the interface between the protons in solution and the glassy membrane bulb. Usually, this bulb contains a constant pH solution (buffered chloride) and internal reference electrode RE_{in} (Ag / AgCl / sat. KCl). This bulb will be completely immersed in the test solution, whilst measuring the potential difference against an external reference electrode RE_{ex} . The thin glass membrane works as an ion-exchange material between the H^+ cations in the test solution and Na^+ cations in the glass membrane. The equation below represents the difference in potential between internal and external reference electrodes:

$$E = Constant - \frac{2.303 RT}{F} pH \quad 1.4$$

As:

$$constant = \frac{2.303 RT}{F} \log a_{H^+ in.} + E_{RE in.} - E_{RE ex.} + E_{asymmetry} \quad 1.5$$

where the $a_{H^+ in.}$ is the activity of hydrogen ions in the internal solution, $E_{RE in.}$ and $E_{RE ex.}$ are the potentials of the internal and external reference electrodes respectively, and $E_{asymmetry}$ is the asymmetry potential.

The asymmetry potential ($E_{asymmetry}$) is the variation in the phase boundary potential, even if the activity of hydrogen ions for the internal and external solutions are equal. Since $E_{asymmetry}$ tends to be approximately unchanging and small over a period of a few hours, it can be included as a constant.

Glass electrodes are widely used in biological, chemical, industrial, and environmental applications as they have a rugged structure and a rapid response. McLauchlan *et al* reported that the response of glass electrode equals 0.9 s between pH 1 and 7 at $37^\circ C$, which is very fast considering 3.4 s that is typical for other electrode materials [14].

Moreover, glass electrodes are ideal for pH measurements whatever the nature of the test solution; as they are not easily poisoned by heavy metals and can be used in aqueous or non-aqueous media [15-17]. On the other hand, glass electrodes need to be calibrated regularly, using two or three buffers (e.g. pH 2,10 and 7), to keep the theoretical response of E / pH slope within 5% of expected value that is 0.0591 V / pH at 25° C. In addition, they have a model response in specific pH range between pH 1 and 9. However, the obtained potential in very high acid media ($pH < 1$) is more than expected. So far, no explanation has been found for this error which was called acidic error. Conversely, at very high alkaline media when $pH > 9$ the obtained potential is less than expected, due to the partial substitution of H^+ by Na^+ or K^+ through the glass membrane in alkaline solution.

Also it has been suggested that cations can diffuse within the first few nanometres of the glass membrane. This error in alkaline media cannot be cancelled but it can be reduced using special glass electrode instead of sodium glass such as lithium glass to reduce the error by about half [8, 9, 18-20]. Although, glass electrodes have wide applications, in some cases glass electrode cannot be used; at high temperature or pressure, in the food industry due to the fragility of the bulb, to measure pH near surfaces or in biological systems, etc. Additionally, they are not suitable in this present application to determine brain fluid pH despite the pH of brain fluid (about 7.35) being located in the ideal performance range of glass electrodes, because this application needs as small an electrode as possible due to the limited volume of the sample and the limited space to measure the pH in the body. In the following section, more compatible pH sensors are suggested.

1.1.3. Metal /metal oxide electrodes

Metal / metal oxide electrodes have been used as pH sensors under conditions that are not favourable for glass electrodes because they have almost Nernstian pH dependent potentials described by the following equation [9, 17, 21, 22]:

$$E = E_{M,MO,H^+}^o - \frac{2.303 RT}{F} pH \quad 1.6$$

where the E_{M,MO,H^+}^o is a constant includes; the standard potentials, the metal oxide solubility product and H₂O ionization product.

There are many metals that can be used as metal/metal oxide *pH* electrodes such as Ir [23], Sb [24], Ru [25], W [26], Pd and Pt [27] Oxides. They have used to estimate *pH* values including local *pH*. They have some advantages such as easiness of their fabrication and comparatively robust structure. In contrast, they have disadvantages such as; they require calibration before and after use, their potentiometric response has poor accuracy and reproducibility and there is variance between the electrodes. Some of these metal/metal oxide electrodes will be reviewed below.

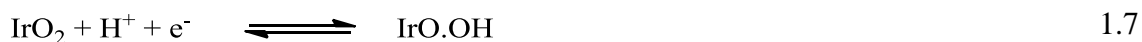
1.1.3.1. Iridium / iridium oxide

Iridium oxide electrodes are widely used to measure the acidity of solutions comprising biological samples because they have a wide *pH* range from 2 to 12, they also have low sensitivity to redox agents interference or more complexing agents [9, 28, 29] and IrOx electrodes show non-interference with cations or anions (e. g. Li⁺, K⁺, Na⁺ and F⁻, Cl⁻, Br⁻) [30].

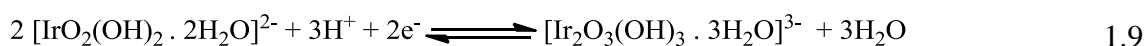
These types of electrodes can be fabricated via many methods such as; sol–gel fabrication [31], thermal oxidation [32], sputtering of IrOx [33], electrochemical oxidation [34]. The IrOx electrodes performance depends on the fabrication method, the range of *pH* sensing will be expanded when fabricated by the electrodeposition method [35].

Although most literatures for this electrode type show a consistent Nernstian *pH* response, some have reported an observed change in gradient when *pH* = 6, resulting in what appears to be two separate slopes. This can be attributed to the method of electrode preparation [30, 36].

Sputtering, sol–gel, and thermal oxidation preparation techniques of IrOx electrode tend to result in a slope of 59 mV / *pH*, and yield anhydrous iridium oxide. This corresponds to 1 electron transferred for every proton, shown by the following equations:



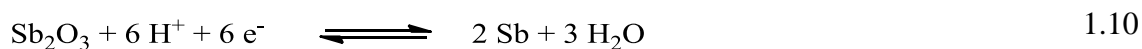
However, electrochemically oxidized iridium can produce a slope of up to 90 mV / *pH*, and yield hydrated iridium oxide. This suggests that for the electrochemically oxidized iridium, 1.5 electrons are transferred for every proton, shown in equation 1.9 :



1.1.3.2. Antimony / Antimony oxide

Like iridium oxide, the antimony oxide electrode is an important metal / metal oxide electrode *pH* sensor. Antimony oxide can work as *pH* sensor without surface pre-oxidization; it has a rapid response, a rugged construction and can be used at high temperature but with poor accuracy which enables its use in industry [9, 17, 29, 37, 38].

The antimony electrode resin contains monocrystalline antimony pieces which was then polished to expose the metal surface, or by a capillary melt method. Later, the thermal oxidation method was used to oxidise the antimony electrode, where potassium nitrate KNO_3 powder is used to cover the antimony electrode, which is then placed in an oven at 500 °C under air atmosphere for 2 hours. The redox reaction between antimony and antimony oxide can be seen in 1.10:



Equation 1.6 for the metal / metal oxide can be used to measure *pH* of a given solution because the antimony oxide electrode potential is dependent on the activity of H^+ . The *E* / *pH* response slope is linear in aqueous media between a *pH* range of 2-12, but is generally between 50 and 54 mV / *pH*, which is not the same as the theoretical value of 59 mV / *pH* [9, 24].

1.1.3.3. Ruthenium / ruthenium oxide

The Ru / RuO₂ electrode has been used as a *pH* sensor and it was found that it has Nernstian *pH* response. It can be fabricated as a screen printed active layer of RuO₂ by manually mixing it with graphite ink then laying this between a conductive silver layer and an insulating polymer layer [25, 39]. Koncki and Mascini reported that this electrode has a good linear response in acidic and neutral mediums at *pH* range 2-8 [25], with a E / pH response slope which is equal to 51 mV / *pH*. Therefore, it will show a longer response time in alkaline media compared to acidic and neutral mediums, also the electrode response will be negatively affected by the presence of reducing agents.

Mihell and Atkinson have studied the same electrode between *pH* 2-10 and they found the *pH* sensor showed a Nernstian E / pH response equal to 59 mV / *pH* [39]. They reported that the *pH* response can be affected by storage environment, as interaction between the H⁺ and OH⁻ ions on the RuO₂ surface and their surroundings will lead to change in *pH* behavior. In addition, they reported that the sensor response needs longer time in alkaline medium comparing with acidic and neutral mediums which was attributed to a chemical reaction between the solution and RuO₂ surface.

Kreider *et al* used a thin-film RuO₂ which was produced by reactive sputtering at room temperature to measure *pH* between 2 and 10 [27]. They concluded that the RuO₂ electrode is more stable than the Ir, Pd and Pt oxide electrodes, and it performed as a *pH* sensor equivalent or better than IrOx with an E / pH response equal to 54 - 59 mV / *pH*, which drops to 52-54 mV / *pH* at *pH* 10 with no hysteresis. A *pH* sensor of 30 μm thick-film ruthenium dioxide-glass composite has been prepared by McMurray *et al* [40], through sintering a mixture of ruthenium dioxide hydrate RuO₂ at 900 °C with H₂O and powdered lead borosilicate glass on Pyrex substrates.

They found the electrode can cover a *pH* range of 2 to 12 in aqueous buffer with a near-Nernstian E / pH response equal to 58 mV / *pH*, but it will be increased to be 60 mV / *pH* if the electrode has been kept in *pH* 7 buffer for 14 days. The *pH* of the test solution can be estimated by the potential of the following reaction:

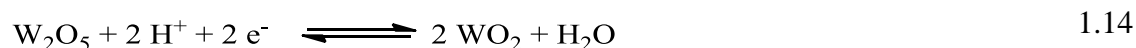


1.1.3.4. Tungsten / tungsten oxide

The tungsten oxide electrode can be used for *pH* monitoring because this electrode potential depends on the activity of H^+ . It has been fabricated by the cycling of a W wire in 2 M H_2SO_4 between +0.1 and +0.2 V vs. Ag / AgCl and then the product tungsten oxide electrode WO_3 surface was covered with a Nafion layer to protect the electrode. 1.12 shows the reaction between H^+ and WO_3 :



The WO_3 electrode has been shown to have a linear Nernstian response with a E / pH slope equal to $53.5 \pm 0.5 \text{ mV} / pH$ in the *pH* range of 2-12 [26]. The tungsten oxide electrode has been fabricated by immersing a W wire in 1 M KOH overnight with a dark colour to obtain either WO_2 using brown colour or W_2O_5 owing to the blue coloration. The obtained potential resulting from the reactions shown in equation 1.13 and equation 1.14, which can be converted to *pH* value using the Nernst equation.



These WO_x electrodes have been shown to have a linear E / pH relationship in a *pH* range of 2–11 equal to $44.8 \pm 0.5 \text{ mV} / pH$ in the steady-state mode and $42.4 \pm 0.9 \text{ mV} / pH$ in the flow injection mode [41].

1.1.3.5. Platinum and palladium oxide

Pt and Pd oxides have been studied as a *pH* sensor instead of glass electrode if conditions are tough and not suitable for the glass electrodes to be used. Pt and Pd oxides were deposited onto both silicon and alumina oxide substrates in argon-oxygen atmospheres at 420 °C for 1 hour to create about 0.5 μm thick electrodes. Palladium and platinum oxides have been found to be less stable than ruthenium oxide. Kreider *et al*

concluded that a Pt oxide electrode is not a useful pH sensor due to the differences observed in the slope depending on whether pH is increasing or decreasing [27]. The E / pH response has been found to be 50 mV / pH unit as pH is increased during the calibration curve, dropping to 24 mV / pH unit when pH is decreasing, as well as showing a large hysteresis. Furthermore, they found that the E / pH response of the Pd oxide electrode was equal to 46 mV / pH , dropping to be 40 mV / pH if the electrode was held at a pH of 10.3 for 20 hours.

PdOx can be created by other techniques such as: thermal oxidation of NaOH onto Pd wires at high temperature [29]; electrochemical anodisation in molten NaNO₃ / LiCl (98:2) [42]; and sputtering of thick film onto alumina or silicon [27]. Thermal oxidation of NaOH is the best method to produce palladium oxide as the sensitivity equals 59 ± 1.2 mV / pH , in addition it shows a long stability period in H₂O, although it can be affected by the presence of reducing agents in the reaction medium. The pH can be determined by the resulting potential of the reaction shown below [43]:



There are other pH microsensors such as optical, ISFET (ion sensitive field effect transistor) and glass microelectrodes; however, they have some disadvantages e.g.: the optical pH sensor has a limited stability due to dye leaching. ISFET sensor is sensitive to light and highly temperature dependent. The glass microelectrodes have a high impedance compared to the PdH microelectrode. To avoid the previous disadvantages the PdH electrode was chosen to use as a working electrode in this project.

1.2. Palladium hydride system

A palladium hydride electrode has a rapid, stable and reproducible response; in addition it does not need to be calibrated which makes it directly available for use. It also has a good Nernstian agreement where the gradient of the E / pH relationship equals -59 mV/ pH [10] at 298 K. Also, the compatibility in the theoretical and practical sensing behavior will be shown throughout the project. The principles of the PdH electrode will be discussed in the next sections. PdH stands for Pd hydride and does not imply a 1:1 Pd to H stoichiometry.

1.2.1. Hydrogen gas pressure P_{H_2} in solid/gas system

Palladium tends to absorb large volumes of hydrogen as discovered by Graham in 1866 [44]. This unique feature of palladium was subjected to academic study in many research papers and shows the variety of avenues in which PdH can be applied; hydrogen storage [45], hydrogen purification [46], fuel cell [47], edible oil hydrogenation [48], semi-conductors industry [49], and alternators of power station cooling [50].

A Pd electrode can be turned into a pH sensor by hydrogen sorbing (loading) using pressure to form a palladium hydride. This system was studied to observe the pressure-composition (P-C) isotherms curve in this solid/gas system [45, 51, 52]. The P-C curve shows how the equilibrium pressure depends on the hydrogen ratio in palladium hydride at constant temperature.

The sorption process of the hydrogen can be divided into two parts; adsorption when the hydrogen atoms are located on the palladium surface, and following this, absorption of the hydrogen atoms into the face-centered cubic (fcc) palladium lattice. There are three regions in the solid solution of palladium hydride system: α phase, β phase and $\alpha+\beta$ transition. The α phase occurs at low hydrogen concentration, when the hydrogen mole fraction $\leq 0.008 \pm 0.002$ at room temperature (in other literatures 0.02 [53] or 0.03

[54]) . In this phase, hydrogen atoms occupy random positions and equilibrium pressure increases with concentration. The β phase occurs at high hydrogen concentration, when the hydrogen mole fraction $\geq 0.607 \pm 0.002$ at room temperature (in other literatures 0.6 [53] or 0.57 [54]) and the hydrogen atoms are ordered in a regular basis. Finally a wide region between the previous phases has been called $\alpha+\beta$ transition, which is represented by the plateau part of the P-C curve (i.e. the $\alpha+\beta$ transition at constant pressure), the constant equilibrium pressure length depends on the temperature [45, 53, 55-57]. Equation 1.16 shows Gibbs phase rule that can be used to explain the constant equilibrium pressure of the P-C curve:

$$F = C + 2 - P \quad 1.16$$

where F is the number of degrees of freedom at equilibrium which is the number of physical variables that can be changed independently without changing the number of phases at equilibrium (temperature and pressure). C is the number of components, which equals 2 in Pd hydride system (Pd and H), P is the number of independent phases, which is 3 in PdH system; (α , β and H_2 gas). Thus, there is just 1 degree of freedom in palladium hydride system at $\alpha+\beta$ transition region, so either the temperature or pressure can be set arbitrarily. Figure 1.1 shows a plot of the pressure-composition isotherms curve at various temperatures for solid / gas systems of palladium hydride, which is considered as a solid solution.

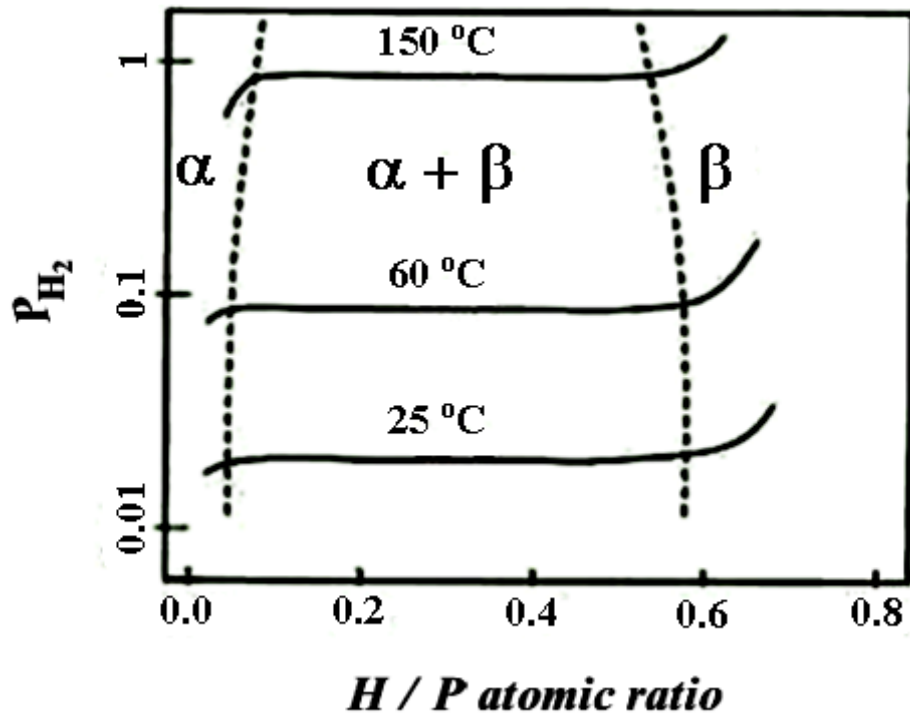


Figure 1.1: The pressure-composition isotherms at various temperatures for palladium hydride solid / gas system, α , β phases and $\alpha + \beta$ transition are shown by dotted lines, reproduced from [8].

1.2.2. Palladium hydride potential

Numerous review articles and experimental works on PdH electrodes as a function of hydrogen content have been published. The potential of palladium hydride has been studied by Hoare and Schuldiner [58], they reported that pure Pd lattice can absorb hydrogen spontaneously when placed in proton-saturated solution until H/Pd ratio equals to 0.025 and 0.36. They also stated that the potential is 0.050 V vs. SHE between a H/Pd ratio of 0.025 and 0.36.

Aben and Burgers studied the absorption of hydrogen in acid saturated with H_2 gas [59]. They found that the absorption process continues until the equilibrium concentration H/Pd is equivalent to 0.69. Flanagan and Lewis measured the potentials of a Pd hydride

electrode in acidic solutions for H/Pd atomic ratio between 0 and 0.69 [60]. Over this atomic range, they found similarities in the free energy calculated from the gas phase isotherm equation 1.17 and electrode potentials in equation 1.18:

$$\Delta \bar{G} = +RT \ln P_{H_2} \quad 1.17$$

$$\Delta \bar{G} = -nFE_{Pd-H} \quad 1.18$$

They reported that hydrogen pressure and PdH electrode potential reflect a constant free energy in $\alpha+\beta$ transition.

It is worth mentioning that hydrogen loading into a Pd lattice can be done electrochemically using either potentiostatic or galvanostatic control instead of by high pressure loading, as atmospheric pressure generally needs several hours to reach equilibrium concentration (H/Pd = 0.69), depending on the Pd layer thickness. A Pd hydride reference electrode was prepared electrochemically by Vasile and Enke [61], they studied the potential of the PdH electrode as a function of pH and H/Pd atomic ratio. At constant pH , the potential has been found to be a function of H/Pd ratio at α (H/Pd \leq 0.03) and β phases (H/Pd \geq 0.5) at 25 °C in acid solution, while it is stable and independent of electrode composition at $\alpha+\beta$ transition in $0.03 \leq$ H/Pd \leq 0.5.

So, PdH electrode can be used as a pH sensor since the potential will remain constant and reproducible during the $\alpha+\beta$ transition and depend only on the pH even though the H/Pd atomic ratio changes as shown in Figure 1.2 (redrawn from [61]).

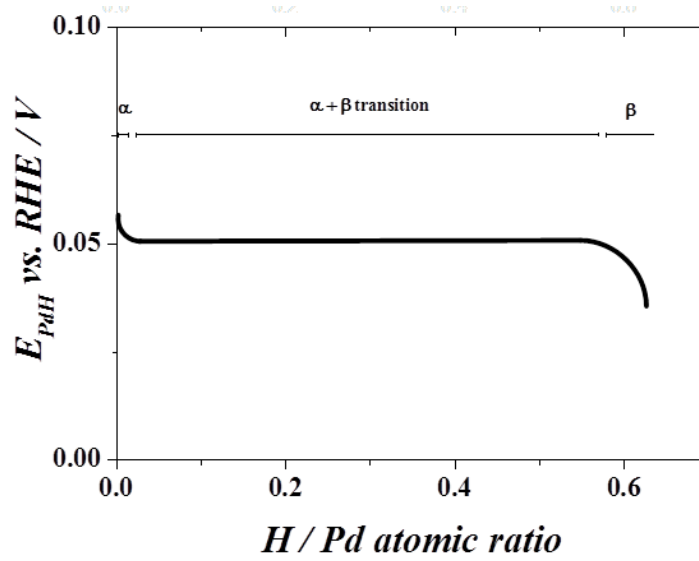
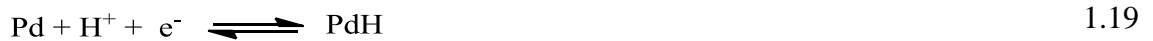


Figure 1.2: The palladium hydride electrode potential against atomic ratio in 1 M HClO₄ at 25 °C, the potential was measured after hydrogen had been loaded cathodically into the PdH electrode, redrawn from [61].

The potential determining reaction for an $\alpha+\beta$ transition palladium hydride system was suggested to be [8, 62]:



As the constant potential of the $\alpha+\beta$ transition region depends on proton activity, it can be used as a *pH* sensor. The PdH electrode potential is defined by the Nernst equation, and given by the following:

$$E_{\text{Pd-H}} = E_{\text{Pd-H}}^{\circ} + \frac{RT}{F} \ln \frac{a_{\text{H}^+}}{a_{\text{H,Pd-H}}} \quad 1.20$$

$$E_{\text{Pd-H}}^{\circ} = -\frac{1}{F} (\mu_{\text{H,Pd-H}}^{\circ} - \mu_{\text{H}^+}^{\circ} - \mu_{\text{e}^-}^{\circ}) \quad 1.21$$

where a_i and μ_i° are respectively the standard chemical potential and activity of species i .

It can be seen from equation 1.20 that at a given temperature the potential of palladium hydride electrode depends on the activity of protons in the test solution a_{H^+} and the hydrogen activity in the palladium hydride structure $a_{H,Pd-H}$. At equilibrium, between H₂ gas and Pd-H the chemical potentials for both hydrogen in the palladium hydride structure and for hydrogen gas are equal, therefore:



$$2 \mu_{H,Pd-H} = \mu_{H_2} \quad 1.23$$

Both the chemical potentials of the hydrogen into palladium hydride $\mu_{H,Pd-H}$ and hydrogen gas μ_{H_2} can be described by:

$$\mu_{H, Pd-H} = \mu_{H, Pd-H}^{\circ} + RT \ln a_{H, Pd-H} \quad 1.24$$

$$\mu_{H_2} = \mu_{H_2}^{\circ} + RT \ln P_{H_2} \quad 1.25$$

where P_{H_2} is hydrogen gas pressure of the solid – gas system at equilibrium as shown in equation 1.22. The relationship at the equilibrium between the hydrogen activity in palladium hydride $a_{H,Pd-H}$ and hydrogen gas pressure P_{H_2} in equation 1.22 can be derived by equation 1.24 and equation 1.25 into equation 1.23 to obtain $a_{H,Pd-H}$ expression as the following:

$$RT \ln a_{Pd-H} = \frac{1}{2} \mu_{H_2}^{\circ} + \mu_{Pd-H}^{\circ} + \frac{RT}{2} \ln P_{H_2} \quad 1.26$$

In equation 1.26, the solid – gas system equilibrium data have been used as a way to obtain $a_{H,Pd-H}$. The merging of equation 1.26 and equation 1.21 with equation 1.20 will produce:

$$E_{Pd-H} = -\frac{1}{F} \left(\frac{1}{2} \mu_{H_2}^{\circ} - \mu_{H^+}^{\circ} - \mu_{e^-}^{\circ} \right) - \frac{RT}{2F} \ln P_{H_2} - \frac{2.303 RT}{F} pH \quad 1.27$$

The first part of the equation can be omitted because it is equal to zero if the potential is considered with respect to SHE as a reference electrode, therefore:

$$E_{Pd-H} (vs. SHE) = - \frac{RT}{2F} \ln P_{H_2} - \frac{2.303 RT}{F} pH \quad 1.28$$

P_{H_2} in equation 1.28 is the hydrogen gas pressure at equilibrium with hydrogen in the palladium lattice as described in equation 1.22. It has been indicated that is a correlation between the hydrogen gas pressure P_{H_2} in solid/gas system (Figure 1.1) and electrode potential E_{Pd-H} in acid solutions (Figure 1.2) at certain temperatures [61, 63]. Thus the palladium hydride phases can be described as follows:

α - phase: the equilibrium hydrogen gas pressure P_{H_2} increases at $H/Pd \leq 0.025$ as shown in Figure 1.1, so the electrode potential E_{Pd-H} shifts to more negative value as predicted by equation 1.28.

- 1- $\alpha+\beta$ transition: the equilibrium hydrogen gas pressure P_{H_2} is constant and independent of the hydrogen content at $0.025 \leq H/Pd \leq 0.5$ as mentioned previously. Equation 1.28 will obtain a stable electrode potential E_{Pd-H} . The value of the hydrogen gas pressure P_{H_2} in this region can be found using the average of absorption and desorption isotherms hysteresis, and it was reported in the literature that ($\log P_{H_2}$ at $0^\circ C < T < 180^\circ C = 4.44698 - 1835.4/T$) to be 0.0194 atm at $T = 25^\circ C$ [63, 64]. The relationship between pH and the potential of the palladium hydride electrode could be written as:

$$E_{Pd-H}(vs. SHE, at T = 25^\circ C) = 0.05 - 0.0592 pH \quad 1.29$$

Therefore, the electrode potential will be 0.05 V vs. RHE at pH 0, which is in a good agreement with the plateau potential at $\alpha+\beta$ transition in Figure 1.2.

- 2- β – phase: when the equilibrium hydrogen gas pressure P_{H_2} increases again at atomic ratio $H/Pd \geq 0.5$ as shown in Figure 1.1, which will lead electrode potential to shift to negative values, as can be expected from equation 1.28.

1.2.3. Sorption reactions of palladium hydride electrodes

The potential of the $\alpha+\beta$ transition Pd hydride electrode has been used extensively as a pH sensor [61, 63, 65, 66], because it is dependent on the H^+ activity of the solution as mentioned in equation 1.28, and shows a reproducible theoretical pH response with a slope = $-0.059 \text{ V} / pH$ (at $T= 25 \text{ }^\circ\text{C}$). It has been chosen instead of other electrode materials (like glass), because PdH is suitable in harsh conditions, such as high temperatures and pressures.

The Palladium hydride can be prepared by loading palladium electrodes with hydrogen, either by bubbling hydrogen through the solution or electrochemically - where the surface activity of the electrode surface is raised by cyclic voltammetry or Pd black layer electroplating. The palladium electrodes can come in many forms, such as; wires, rods, foils, plates, disc and urchin-like nanostructures [45], etc.

The hydrogen evolution/sorption mechanism on Pd follows a multistep reaction known as the Volmer-Heyrovski-Tafel route [9, 67-71]. The Volmer reaction is the first step of this mechanism where the hydrogen atoms locate onto adsorption sites on the Pd surface to form H_{ads} as shown in equation 1.30.



As soon as the adsorption is overachieved, H_2 gas can be generated electrochemically via the Heyrovsky reaction (shown in equation 1.31), or by chemical recombination via the Tafel reaction (shown in equation 1.32):

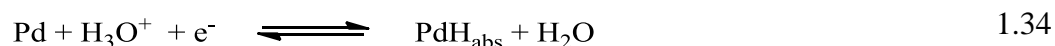


Graham discovered in 1866 that Pd has the ability to absorb large volumes of hydrogen into its lattice in solid state reservoirs [44]. Therefore, the adsorption of hydrogen atoms can be followed by an absorption step, where hydrogen inserts into bulk Pd (equation 1.33) instead of evolution via either the Heyrovsky reaction or Tafel reaction.



It is not currently known how hydrogen atoms insert into the bulk Pd, however three theories have been suggested:

1. “Direct hydrogen absorption reaction” - Direct hydrogen insertion into bulk Pd without passing through an adsorption step, (shown in equation 1.34).

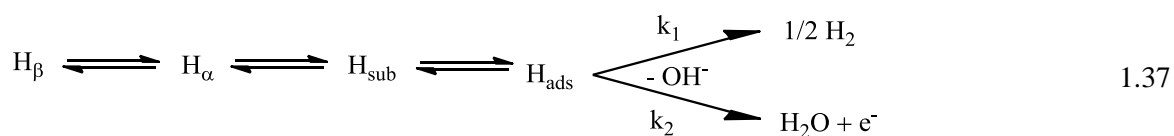
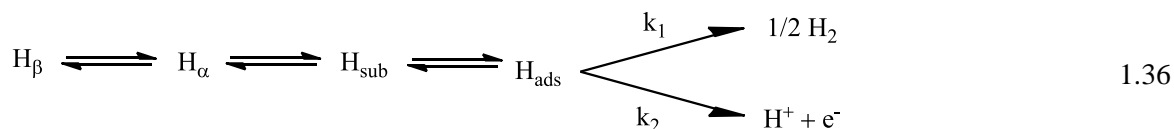


2. “Diffusion controlled indirect hydrogen absorption reaction” - Initial adsorption of hydrogen atoms onto the electrode surface as stated in the Volmer reaction (1.30), then diffusion into bulk Pd. This reaction will be in competition with the Heyrovsky reaction (equation 1.31) or Tafel reaction (equation 1.32).



3. “Subsurface hydrogen” - Hydrogen atoms dissolve to form a layer directly under the Pd surface (20-50 nm) [72-76]. The hydrogen absorption process into bulk Pd is then divided into four steps:
 - i. H^+ then H_{ads} coupled chemisorption.
 - ii. H_{ads} transfer from the surface to subsurface to form H_{sub} .
 - iii. Diffusion of H_{sub} into bulk Pd along H chemical potential gradient.
 - iv. Parallel processes of surface H_{ads} desorption as H_2 through Heyrovsky reaction (equation 1.31) or Tafel reaction (equation 1.32).

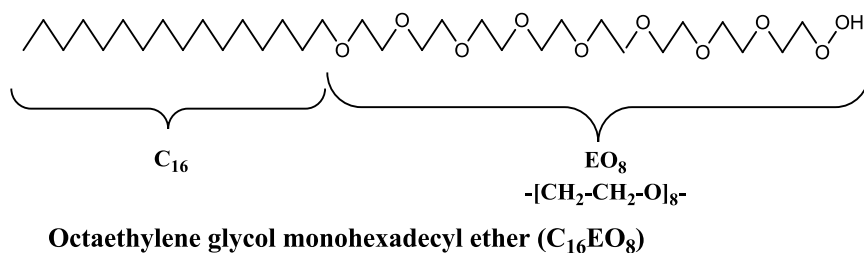
The subsurface hydrogen theory agrees with research done by Czerwinski *et al.* [73, 77, 78], they found that experimental observation supports the hypotheses of H absorption into bulk Pd as a subsurface layer H_{sub} . Moreover, they suggested H_{sub} exist during both the hydrogen absorption and desorption processes. Equation 1.36 and equation 1.37 show the overall scheme for H desorption in the acidic and alkaline media respectively.



Both equation 1.36 and equation 1.37 have the same H_{sub} subsurface layer formation as the primary step of adsorption onto the Pd surface, followed either by electrochemical desorption via the Heyrovsky reaction (equation 1.31) or by chemical recombination via the Tafel reaction (equation 1.32). The redox reactions of palladium electrodes will be discussed with more details in the result sections.

1.3. Metal nanostructured film fabrication using liquid crystal templating

Lyotropic LC can be defined as the materials that arranged in appropriate solvent in specific order under suitable conditions of concentration and temperature. Hence, the lyotropic liquid crystal is a material which has both liquid and solid crystal characteristics when it adds to a solvent, such as the surfactant. The lyotropic liquid crystal surfactants present amphiphilic features. In other words, the surfactant shows affinity to both aqueous and oil solvents, because there are hydrophilic and hydrophobic parts in the same molecule. The surfactant head contains a simple polar group (as -OH, -NH₂), or complex polar group like carboxylic acid, while the surfactant tail can include n-alkyl chains, or alkylbenzenes [79]. Both the non-ionic surfactant Brij[®] 56 and octaethylene glycol monohexadecyl ether (C₁₆EO₈) were used as lyotropic liquid crystal (LLC) surfactants in the manufacture of the nanostructured film in this study. C₁₆EO₈ is highly purified as it has the same EO₈ headgroup (-[CH₂O]₈-) , resulting in the surfactant being a monodisperse material. In contrast, Brij[®] 56 is a polydisperse material because it has a mixture of headgroups, from C₁₆EO₁₂ to C₁₆EO₄, with C₁₆EO₈ as the majority headgroup [80]. The structures of C₁₆EO₈ and Brij[®] 56 are shown in Figure 1.3.



Hydrophobic tail **Hydrophilic head**

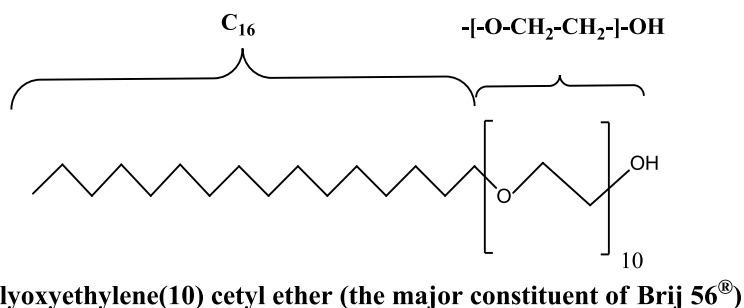


Figure 1.3: The structures of C₁₆EO₈ and Brij[®] 56 surfactants.

The surfactants have specific behavior in aqueous media, where the particular aggregation depends on the concentration and temperature. Figure 1.4 shows the aggregation of surfactants with increasing concentration. The surfactant molecules coalesce together in different formations as the concentration in aqueous solution changes. When the surfactant concentration equals 1 wt%, the distribution of surfactant molecule is random. However, at the critical micelle concentration (CMC), the surfactant molecules establish the supramolecular structure. First, the supramolecular structure is spherical micellar (I₁), where the surfactant molecule heads emerge on the surface of the spherical structure (Figure 1.4 a). If the surfactant concentration rises, the second phase of the liquid crystal appears, the hexagonal phase (H₁) - where the hydrophobic tails point inside a cylinder shape (Figure 1.4 b). At higher surfactant concentration, the lamellar phase (L_α) starts forming (Figure 1.4 c), where two layers connect together by the hydrophobic tails with the hydrophilic heads emerging outside

the lamellar structure. At very high concentrations, the inverse hexagonal phase (H_2) is seen (Figure 1.4 d), where the hydrophobic tails emerge outside the cylinder shape. The inverse micellar structure (L_2) (Figure 1.4 e) forms in higher surfactant concentrations, where a spherical shape forms as the hydrophobic tails come out of the structure [81, 82]. This specific phenomenon of the surfactant aggregation has been applied to fabrication of the nanostructured electrode by the true liquid crystal templating (TLCT) method, which was developed by Attard *et al* to fabricate an ordered mesoporous nanostructured material [83, 84].

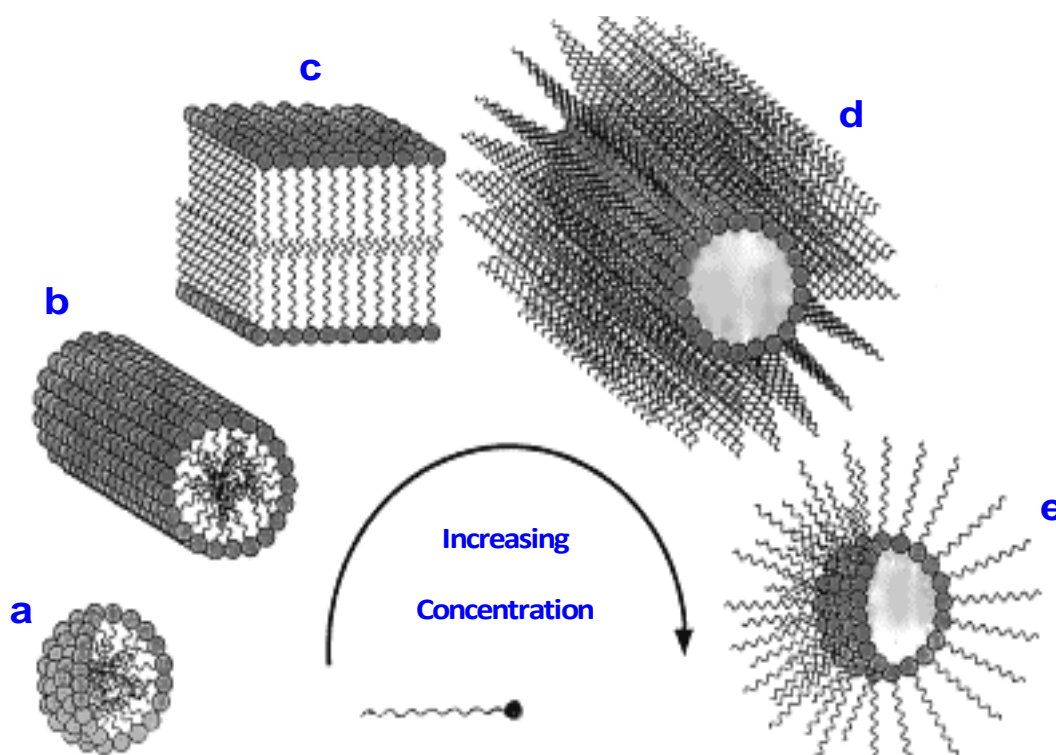


Figure 1.4: General supramolecular structures of the surfactant aggregation when dissolved in a polar solvent. The liquid crystal phases are: a) micellar I_1 , b) hexagonal H_1 , c) lamellar L_a , d) inverse hexagonal H_2 , and e) inverse micellar L_2 reproduced from [85].

1.3.1. H₁-e M nanostructured film formation via liquid crystal template

The H₁-e M acronym comes from the hexagonal phase (H₁) of the surfactant in which the metal (M) is electrochemically (-e) deposited. Although metal nanostructured electrodes can be formed from all surfactant phases, the hexagonal phase is used in many published articles to create the nanostructured electrode, and it has been shown to give good results [10, 62, 80, 86]. Accordingly, this liquid crystalline phase will be used in the deposition of the metal in the present study. The metal salt will be solvated in the surfactant solution at the required concentration and temperature to form the H₁ phase. Brij[®] 56 or C₁₆EO₈ will be added to the metal plating mixture to obtain a homogeneous paste of liquid crystalline template. The nanostructured film will then be formed using an electrochemical method to deposit metal ions Mⁿ⁺ as a film onto the substrate microdisc electrode. The electrochemical technique of chronoamperometry used in the deposition process, which requires determination of potentiostat setting-up to identify the initial and the final potentials. This includes the initial potential $E_{\text{initial dep}}$ - where the current is close to zero and hence no deposition occurs, and the final potential $E_{\text{final dep}}$ (deposition potential) - where the metal electrodeposition occurs [87]. Cyclic voltammetry of the metal homogeneous liquid crystalline template will be implemented to identify the $E_{\text{initial dep}}$ and $E_{\text{final dep}}$. The thickness of the H₁-e M film has been controlled by setting the value of the deposition charge, which will be discussed in more detail in the experimental section. The ions of the metal Mⁿ⁺ will be deposited as atoms M⁰ in the aqueous region in the interstitial spaces between the surfactant cylinders of the H₁ hexagonal phase. Later, the surfactant can be easily removed by washing with water to leave the deposited metal film with nanostructured pore. The wall thickness and size of the pores in the film can be modified by adding heptane, which has been used as a co-solvent to swell the diameter of the hexagonal rods in the lyotropic liquid crystal [80].

Figure 1.5 shows and explains the three steps of the true liquid crystal templating (TLCT) method; dissolution of metal salt, metal electrodeposition and surfactant removal.

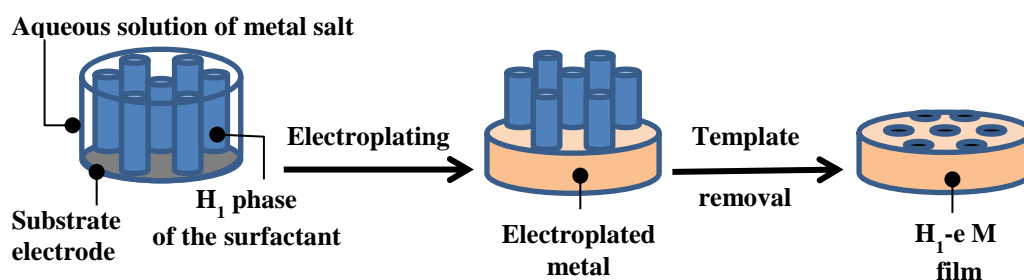


Figure 1.5: The templating deposition process of the H_1 -e Pd films, the cylinders represent the hexagonal phase of the liquid crystal in the deposition mixture redrawn from [80].

1.3.2. Electrodes of H_1 -e Pd films

Since Attard *et al.* first produced a platinum thin film by true liquid crystal templating TLCT technique [84], many other H_1 -e nanostructured films have been fabricated using the same method with other metals such as; Co [88-90], Ni [91], Rh [92], Bi [93], Pd [80, 94] films. Moreover some studies have been done using TLCT to deposit two nanostructured metal layers, for example; an H_1 -e Pd film onto an H_1 -e Rh layer over the substrate electrode [86]. Furthermore, true liquid crystal templating has been used to obtain the deposition of H_1 -e metal compounds, for instance H_1 -e PbS [93], H_1 -e Ni(OH)₂ [95], and H_1 -e TiO₂ [96] films. H_1 -e M films have high surface areas as a result of the contribution from internal area due to the large numbers of nanostructured pores e.g.; the surface areas for H_1 -e Rh [92] and H_1 -e Pt are 32 and 60 m²g⁻¹ respectively. This H_1 -e feature has been exploited to improve the efficiency of the surface characteristics for the palladium hydride electrode, building on the rapid, stable and reproducible response and good Nernstian behaviour mentioned in section 1.2.

Bartlett *et al.* used the TLCT method to successfully produce an H₁-e Pd film onto an Au substrate electrode ($d = 1$ mm) [80]. They used deposition paste contained a non-ionic surfactants (Brij[®] 56 or C₁₆EO₈) and an aqueous solution of 1.40 M (NH₄)₂PdCl₄, to study that surfactants phases transformation in the templating mixture within 20-100 of wt.% at temperature range between 20-80 °C.

Figure 1.6 shows the obtained phase schemes for C₁₆EO₈ and Brij[®] 56 in the mentioned template mixture. These diagrams show the required conditions to obtain the H₁ phase. It is shown to appear at room temperature in the percentage concentration range of about 40-80 wt.%. As the temperature rises, the range in which the H₁ phase appears to shrink, so that at 55° C the phase is only forms at around 55 wt.%. Furthermore, Bartlett *et al.* have shown that the Pd nanostructure film has regular cylindrical pores ($d \approx 3$ nm), that are separated by Pd walls (wall thickness ≈ 2.8 nm) [80]. Bartlett *et al.* characterised the electroactive surface area of the palladium nanostructured film electrochemically by cycling in 1 M sulphuric acid solution, and estimated the electroactive surface area to be 91 m² g⁻¹ from the H₁-e Pd oxide stripping peak. They also found that H₁-e Pd film hydrogen reactions are very fast, and the formation of adsorbed/absorbed hydrogen has clear resolved peaks - attributed to the higher electroactive surface area of the H₁-e Pd film in comparison to the plain Pd electrode. Additionally the H₁-e Pd film is stable on cycling to cathodic potentials in acid solution.

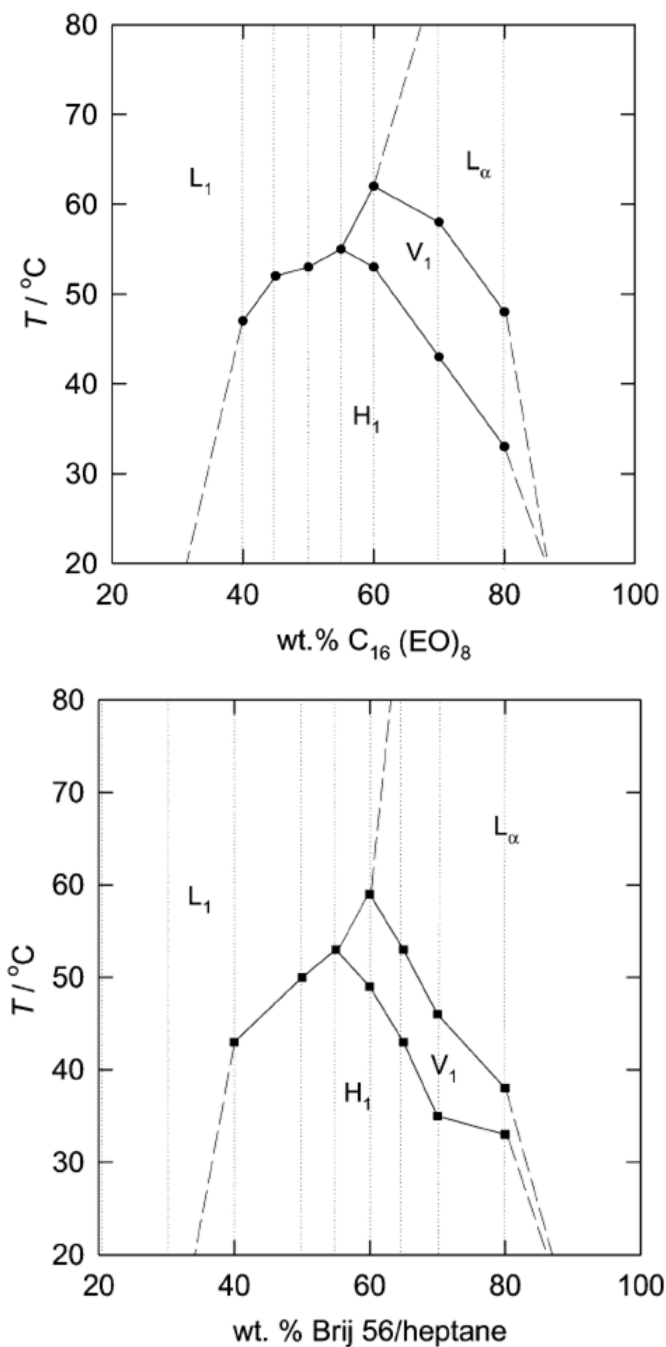


Figure 1.6: C₁₆EO₈ (top) and Brij[®] 56 (bottom) / heptane (wt ratio 22:1) liquid crystal phase diagrams at different concentration and temperature conditions in aqueous solution of 1.40 M (NH₄)₂PdCl₄ reproduced from [80].

Bartlett and Marwan investigated the hydrogen region of the H₁-e Pd film with cyclic voltammetry in 1 M H₂SO₄ [62]. They observed the influence of crystal violet on the H₁-e Pd film surface, and found that the hydrogen formation is blocked.

Denuault *et al.* started to use H₁-e Pd as a *pH* sensor by converting $\alpha+\beta$ transition potential to *pH* value in the potentiometric mode [10]. They fabricated a H₁-e Pd film onto a Pt microdisc electrode using TLCT technique to multiply the electroactive area of the PdH *pH* probe up to 900 times larger than the substrate electrode; while maintaining the geometric area of the Pt substrate microelectrode. Thus the imperfections of the conventional Pd hydride microdisc *pH* sensor can be avoided e.g.: a poor potentiometric response in comparing to other microdisc electrodes, slow hydrogen loading, and an unstable potential as a result of hydrogen continually diffusing into the Pd wire. They characterized the H₁-e Pd film with cyclic voltammetry in 1 M H₂SO₄ and found that the peaks currents of the H₁-e Pd are greater than the substrate electrode. This has been attributed to the magnitude of electroactive surface area of H₁-e Pd. They observed that the H₁-e Pd film made with C₁₆EO₈ has double the electroactive surface area of the film made with Brij[®] 56. Although if they have equal thickness, with both the surfactants the relationship between electro active area and the deposition charge is almost linear. The H₁-e Pd film *pH* sensor was electrochemically loaded with hydrogen to form the PdH $\alpha+\beta$ transition, where the optimum hydrogen loading conditions were presented to obtain excellent potentiometric response. They reported that the shape of the potential transient are similar for the H₁-e Pd and bulk Pd. The Pd hydride has been formed by stepping the potential from the double layer region of acid voltammogram to hydrogen region, then held until the loading is complete. They applied the potentiometric mode to the H₁-e Pd film after hydrogen loading, the potentiometric response of the Pd nanostructured electrodes is comparable to that of the Pd black. The loading amount of the hydrogen depends on the size of Pd nanostructured, as it works as H reservoir. Titrations and calibrations was carried out at 25 °C using buffered media, that have been used to potentiometrically investigate the *pH* sensing of H₁-e Pd electrode. Hydrogen loading was done immediately before every single experiment at -0.75 V vs. SMSE in a 0.5 M Na₂SO₄ + H₂SO₄ solution (*pH* 1.88). Then

open circuit potential mode was used to observe the $\alpha+\beta$ transition potential, that when stable, will be used to monitor the solution pH . The pH of the solution was adjusted by diluted NaOH or H₂SO₄ addition. The test solution was deaerated and stirred constantly throughout the titration with Ar gas. The responses of the $\alpha+\beta$ transition and the glass pH electrode were monitored concurrently, with adjustments in pH by the addition of diluted NaOH or H₂SO₄. Output potential shows a rapid and stable response against change in pH . A calibration curve was produced using the results from the titration experiment, it shows E / pH slope is equal to $-0.0587 \text{ V}/pH$, which is very close to theoretical value ($-2.303RT/F = -0.0592 \text{ V}/pH$ at $25 \text{ }^\circ\text{C}$). The intercept is shown to be -0.0587 V vs. SMSE, which is very close to the conventional plateau potential of the $\alpha+\beta$ transition in $pH 0$ at $25 \text{ }^\circ\text{C}$.

Denuault *et al.* reported that the Pd pH sensor is in some respects, better than all the other potentiometric pH microsensors [8]. For instance; it shows an ideal Nernstian response between $pH 2$ and 12 , a great reproducibility between H₁-e Pd pH electrodes, it does not need to be calibrated before and after measurements, it has a stable slope ($-59 \text{ mV}/pH$ at $25 \text{ }^\circ\text{C}$) and a constant intercept (-50.9 mV vs. SHE) regardless of the pH regions, and the amperometric response is without hysteresis. They improved the Pd pH sensor efficiency by using a Pd nanostructure electrode, which needs shorter times for hydrogen loading because of high surface area, and as a result is quicker and more stable at monitoring changes in pH . The H₁-e Pd pH sensor has a linear $\alpha+\beta$ transition potential relationship which shows excellent long term stability ($\pm 1.2 \text{ mV}$ over 2 h). The charge passed when reloading hydrogen into the nanostructure has been found to be the same, which indicates that the H₁-e Pd film is not destroyed by expansion of about 3% as a result of hydrogen insertion into the film Pd nanostructure film [80].

1.4. Oxygen effect on H₁-e Pd electrodes

The H₁-e Pd electrode can work as a *pH* sensor by the $\alpha+\beta$ transition potential converted to a *pH* value as mentioned previously in equation 1.29. The palladium hydride $\alpha+\beta$ has been formed by electrochemical hydrogen loading into the Pd nanostructure, with hydrogen first adsorbing onto the palladium surface (equation 1.30) then absorbing into the lattice (equation 1.33). When the potentiometric mode is switched on, the obtained potential will remain constant and depend only on the *pH* as long as the H/Pd atomic ratio is between 0.02 and 0.6 [8, 53, 61]. The amount of hydrogen in the PdH will decrease gradually but the potential will remain stable until the H/Pd atomic ratio equals 0.02 at the beginning of the α phase. The sensor performance period (i.e. the lifetime of the $\alpha+\beta$ transition) before hydrogen reloading depends on the hydrogen reservoir volume. This applies simply in deaerated solutions. Equation 1.19 shows that at equilibrium only the hydrogen oxidation process consumes the hydrogen from the PdH, so the hydrogen oxidation rate almost equals the rate of H⁺ reduction.

However, oxygen presence in the test solution has been found to increase the rate of PdH hydrogen consumption, which impacts on the performance duration of H₁-e Pd *pH* sensor [10]. This has been attributed to hydroxyl groups formation (equation 1.38), which then reacts with PdH to form Pd and water (equation 1.39) [97, 98].



This makes the overall of these reactions as following:



Equation 1.40 shows that O₂ will participate in the hydrogen consuming of the PdH of H₁-e Pd *pH* sensor, which will lead to an accelerated hydrogen oxidation process, thus decreasing the lifetime of the $\alpha+\beta$ transition. Therefore, at equilibrium in aerated

solutions the rate of PdH hydrogen oxidation equals the rate of H^+ reduction (equation 1.19) in addition to the rate of O_2 reduction (equation 1.40).

O_2 presence can be eliminated by degassing with Ar gas before carrying out the experiment as done by Denuault *et al.* [10].

1.4.1. H_1 -e Pd electrodes coating

In this project, H_1 -e Pd electrode will be used to estimate the pH of brain fluid, which initially contains O_2 (157 ± 23 mmol / 100 g) [99]. Degassing with Ar is impractical in viscous solutions such as brain fluid, because it will create severe foaming and diminish an already limited available volume.

Covering with a selective coat is an alternative method which can protect the H_1 -e Pd pH sensor from the O_2 effect. Many coats can be used, but they must achieve certain requirements, such as; allow hydrogen infiltration through the coat, stop or at least slow O_2 diffusion to the H_1 -e Pd surface, and be stable with long term usage. Controlling the thickness and quality of the coat is also a requirement, which is greatly dependent on the coat formation technique. Hence, a coating will be considered successful if all these requirements are achieved. An investigation in H_1 -e Pd electrode efficiency will be done before and after the application of the coatings to compare between them.

1.4.2. Nafion

Nafion was developed in the 1960s by DuPont [100-104], and since has been researched as one of the most permselective coats. Nafion has been shown to decrease the diffusion coefficient of O_2 [105]. It has been characterized as a selective membrane, as it allows the permeation of H^+ whilst blocking any other species. It occupies an important position in the development of fuel cells research which is based on the hydrogen and oxygen electrochemical reaction. The structure of Nafion makes it exceptionally

chemically stable, as it has a perfluorinated backbone attached with a side chain with H⁺ exchange sites. Figure 1.7 shows the structure of Nafion.

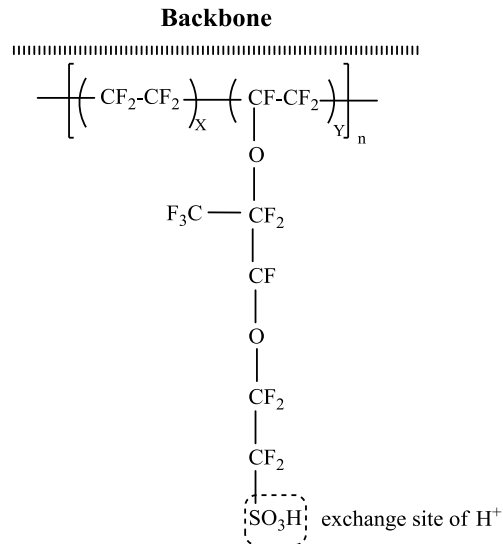


Figure 1.7: Nafion structure.

The backbone is highly hydrophobic, whilst sulfonic acid groups are hydrophilic therefore allowing proton conductivity. A conductive hydrophilic field is formed in the presence of H₂O, as sulfonic H⁺ dissociates from their opposite anionic ion SO₃⁻ and solvates in water. The permselectivity of Nafion arises from all species but H⁺ ions being repelled by the SO₃⁻ anion sites provides a mechanism for the H⁺ ions to pass through the film, as shown in Figure 1.8 [102].

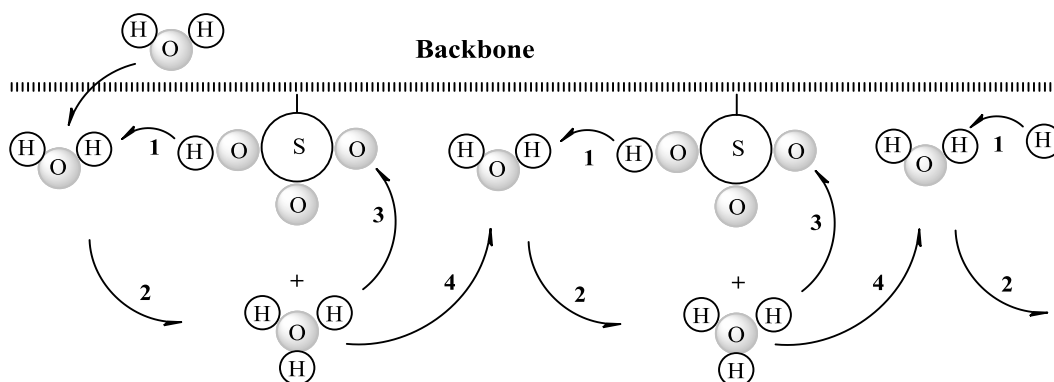


Figure 1.8: H^+ transfer in sulfonic acid groups of Nafion redrawn from [102].

Kinlen *et al.* have studied the response of the Nafion coated Iridium oxide pH sensor (IrOx). They found that there is no interference between sensitivity and the pH response, moreover they found that the Nafion coating lead to improved Iridium oxide pH sensing, because it corrects the non-linear pH response [100].

Cyclic voltammetry in 0.5 M $Na_2SO_4 + H_2SO_4$ solution (pH 7) has been done to compare the H_1 -e Pd pH electrode voltammograms before and after the Nafion coating [9]. It has been found that the Nafion coating will decrease the surface activity meaning there is a reduction in the electroactive area of the H_1 -e Pd surface, suggesting that the reaction of O_2 in the solution with adsorbed hydrogen has been decreased without reducing the amount of hydrogen absorbed into the palladium nanostructured. This infers that the rate of hydrogen desorption from inside the palladium is slower after the application of Nafion, thus increasing the H_1 -e Pd pH sensor performance.

On the other hand, Nafion has some disadvantages, such as slow response times as a result of the low diffusion coefficients of analytes in the film. Brain fluid has a high cation content such as Na^+ , K^+ , Ca^{2+} and Mg^{2+} . This leads to the saturation of anionic sites that may create difficulties in the pH sensing process. The H^+ conductivity of the Nafion coat depends on the hydration level, so it is expected that the performance of H_1 -e Pd pH sensor would be improved by the high water content of brain fluid. The Nafion layer can be applied by two methods; the annealing procedure at high temperature

which requires 2 hours and results in a stable long lived Nafion coat [100], or the ‘dip and dry’ technique at room temperature which requires a matter of minutes but leads to a less stable Nafion coat [9]. Both previous techniques produce non-uniform coats, and thus it is difficult to control the thickness of the Nafion layer, as opposed to coatings controlled by the charge passed using electrochemical methods.

This disadvantage of Nafion has led to the interest of other coatings, which might not show the same proton selectivity, but are easier deposited and still block interfering species.

1.4.3. Polymeric films

The polymer modified electrodes have been used to improve electrochemical behavior including sensors sensitivity and selectivity [106], which will be exploited to develop the performance of the H₁-e Pd *pH* sensor. There are numerous organic monomers which can be used to coat the H₁-e Pd surface. The electropolymerisation and overoxidation coating technique can be applied to these organic monomers to yield a coating which can improve the properties of the H₁-e Pd electrode. **Figure 1.9** shows some examples of organic monomers.

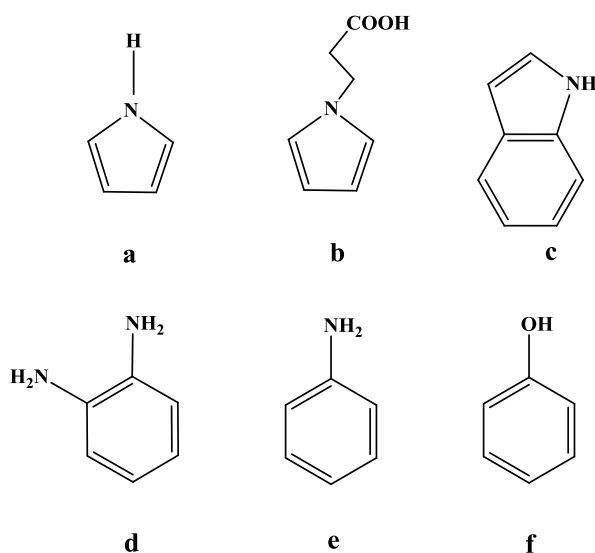


Figure 1.9: The structure of the monomers used to make the polymeric films; a/ Pyrrole, b/ [1-(2-carboxyethyl) pyrrole], c/ Indole, d/ o-1,2-diaminobenzene, e/ Aniline, and f/ Phenol.

Polypyrrole (PPy) was prepared in 1979 by Diaz *et al.* [107], it was produced electrochemically from n-substituted pyrroles (Py) using physically trapped catalysts or by choosing counter-ions, both methods utilizing the π -electrons on pyrrole [108, 109]. **Figure 1.10** shows the monomer polymerization process of pyrrole and its derivatives [110, 111].

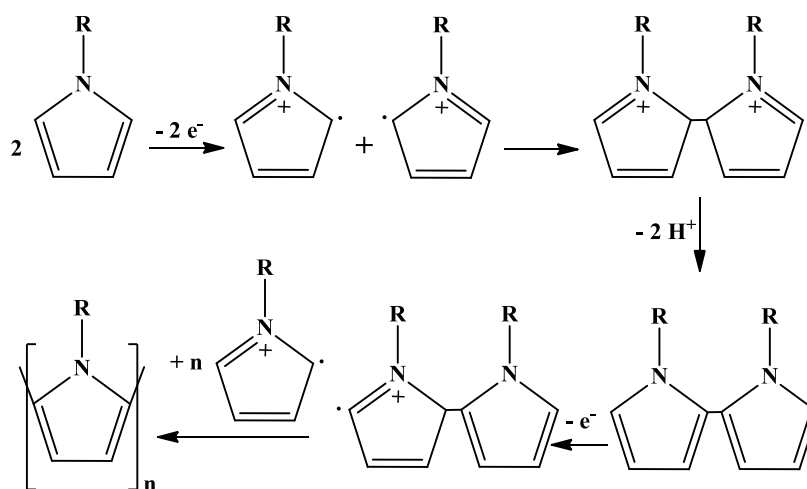


Figure 1.10: pyrrole (and derivatives) monomer polymerization redrawn from [110].

Freund *et al.* described a modification in the deposition technique of polypyrrole films [112], which is called over oxidised polypyrrole (OPPy). The modification technique involves the complete irreversible oxidation of polypyrrole leading to a change in the film's characteristics. The electrochemical oxidation process will be achieved over +1.0 V vs. SCE, as the highly positive voltage encourages a nucleophilic attack by anions/water on the cationic pyrrole nuclei in polypyrrole., which produces a neutral carbonyl group on the polymer backbone. This impedes anion diffusion, reduces its degree of conjugation and thus decreases the conductivity of the film. Therefore, covering the electrode with OPpy has the potential to selectively suppress redox reactions depending on the charge of the redox couple. Cyclic voltammetry responses show that neutral or cationic couples are allowed to diffuse through the film down to the

electrode surface, while OPPy film prevents anions from reaching the electrode. In comparison with the Nafion coat, the OPPy film is less H⁺ selective, as it does not prevent other cations or neutral species, but uniform thickness coat of the OPPy film can be obtained electrochemically. A rapid response with increased sensitivity is expected with a thinner ion-selective film. ultrathin OPPy films have been produced by a new technique of Hsueh *et al.* [113].

Equation 1.41 reflects the permeability of the OPPy film:

$$P_m = \frac{\alpha D_m}{\text{Film thickness}} = \frac{D_{app}}{\text{Film thickness}} \quad 1.41$$

where P_m is the permeability of the film, α is the membrane partition coefficient, D_m is the diffusion coefficient into the film and D_{app} is the apparent diffusion coefficient in the film.

The previous equation clarifies that a thin film provides higher sensitivity as film thickness decreases. However, decreasing film thickness leads to defects such as pinholes which allow anionic species to diffuse through the thin film and reach the electrode surface thus leading to a loss of permselectivity.

Polymer films can be deposited onto the substrate electrode by the “continual electroprecipitation” method as follows; oligomeric chains formed from monomers in solution precipitate onto the substrate forming the first polymer layer. Which will contain a number of pinholes and defects; any subsequent polymer layers can be formed by either addition of monomers onto the end of polymer chains, or by precipitation of other oligomeric chains onto the substrate surface in the pinholes of the first layer; as the precipitation onto the substrate is favored, the pin holes become filled leaving an ultra-thin layer of polymeric film. Thus, the disadvantage of the expected increase in defects with decreasing film thickness can be avoided by repeating monomer

polymerization then overoxidation steps [113, 114]. Figure 1.11 shows the repeated polymerization and overoxidation of ultrathin OPPy films.

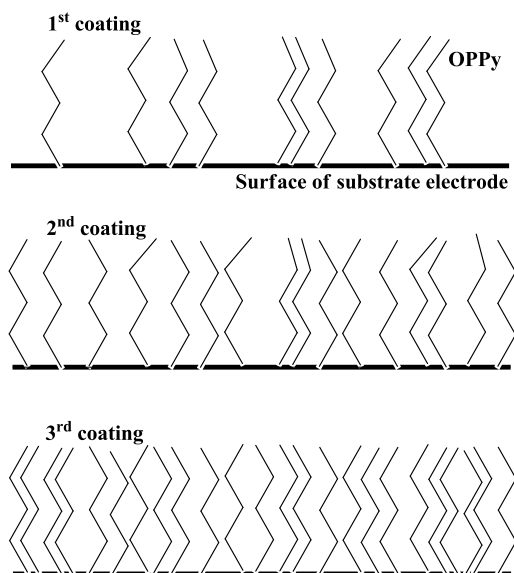


Figure 1.11: the repeated polymerization and overoxidation of ultrathin OPPy films redrawn from [113].

In general, the OPPy formation method is based on two steps; PPy film electrosynthesis then overoxidation, to yield OPPy films thickness of about 0.1-1 μ m.

A new technique, developed by Debiemme-Chouvy *et al.* is based on a single electrochemical step to obtain a pinhole free and very thin OPPy coat, with a thickness of about 10 nm [114]. A weak-acidic anion of HPO_4^{2-} ions was used for PPy electrogeneration, which allows a rapid and direct single step to a very thin OPPy film. A positively charged redox couple $\text{Ru}(\text{NH}_3)^{3+/2+}$ and negatively charged redox couple $\text{Fe}(\text{CN})_6^{3-/4-}$ were used to confirm the cation permselectivity of OPPy films. The limiting current of the $\text{Ru}(\text{NH}_3)^{3+/2+}$ cyclic voltammetry was slightly decreased after the fourth coating, while $\text{Fe}(\text{CN})_6^{3-/4-}$ showed that the OPPy film has a high degree of efficiency

for the anion rejection, complete suppression of the $\text{Fe}(\text{CN})_6^{3-/4-}$ limiting current was noted after the fourth coating [113].

Poly[1-(2-carboxyethyl)pyrrole] or PolyCEP was studied by Arrigan *et al.* [115]; it is characterized as containing an additional acidic functional group. The overoxidation process for PolyCEP films was carried out in alkaline, neutral and acid media namely: 0.1 M NaOH, phosphate buffer *pH* 7.0 and 1 M HClO_4 respectively. It was observed that overoxidised PolyCEP films in phosphate buffer *pH* 7.0 are brittle and flaky membrane films, which easily leave the surface of the substrate electrode during hydrodynamic experiments. Films overoxidised in NaOH were immediately dislodged from the substrate electrode surface during the overoxidation. In contrast, the most physically stable film was obtained when PolyCEP was overoxidised in 1 M HClO_4 . This could be due to the degree of polymer cross-linking when carried out in solutions capable of deprotonating the carboxylic acid group, and as a result allowing a nucleophilic attack on the oxidized pyrrole rings. This does not occur in the HClO_4 case, because the carboxylic acid is not deprotonated, therefore it is less nucleophilic and the attacking nucleophile is expected to be perchlorate or H_2O . To sum up, PolyCEP films overoxidised in natural or alkaline media are less efficient and stable than OPPy films, as the OPPy overoxidation process can be done in multiple *pH* solutions without losing the physical stability of the film. However PolyCEP films overoxidised in acidic media improved the electrode properties more than OPPy film, because the anionic character imparted to the film making it more cation selective.

An indole monomer (see **Figure 1.9**) has also been used to form a polymeric coat onto the substrate electrode surface, using the same electropolymerisation and overoxidation technique seen previously, to yield an overoxidised polyindole membrane OPIn. Similar to PolyCEP films, the OPIn heterocyclic ring will be destroyed by nucleophilic attack, therefore losing aromaticity and hence conductivity. However, in the indole case, electropolymerisation cannot be carried out in aqueous media because this will result in H_2O nucleophilic attack on the radical species generated by indole electrochemical oxidation, preventing dimerization, oligomerisation and polyindole growth. Therefore,

Polyindole electropolymerisation has been implemented in non-aqueous medium by Ghita *et al.*[116]. They obtained an excellent cation permselective film, observed by comparing the cyclic voltammetry of $\text{Ru}(\text{NH}_3)_6^{3+/2+}$ and $\text{Fe}(\text{CN})_6^{3-/4-}$. **Figure 1.12** shows the indole polymerization process [117].

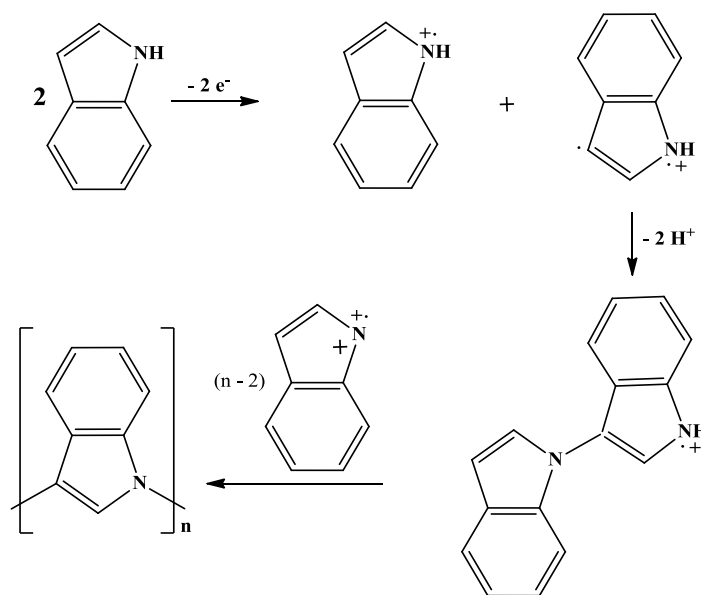


Figure 1.12: Indole monomers polymerization mechanism redrawn from [117].

Similarly, o-1,2-phenylenediamine OPD (i.e. o-1,2-diaminobenzene see **Figure 1.9**) is further coating derived from electropolymerisation of a monomer. Poly(o-1,2-diaminobenzene) was produced using the overoxidation technique mentioned previously in combination with true liquid crystal templating (TLCT), which lead to the creation of very thin films [106]. The porosity of the coat can be controlled by modifying the surfactant concentration, producing various types of OPD films such as the e OPD film (obtained from a conventional aqueous solution, 0% w/w C_{16}EO_8 , the L_1 -e OPD film (obtained from a liquid crystalline micellar solution, 20% w/w C_{16}EO_8 mixture), and the H_1 -e OPD film (obtained from a liquid crystalline hexagonal phase solution, 50% w/w C_{16}EO_8 mixture). Bartlett *et al.* reported that e OPD and L_1 -e OPD are not permselective and blocked both negatively and positively charged ions [106]. However the H_1 -e OPD film is reported to be ion selective, preventing negatively charged ions from crossing the

film to react at the electrode surface, whilst allowing positively charged ions, such as the $\text{Ru}(\text{NH}_3)^{3+/2+}$ redox couple, to react at the electrode surface. The unique behavior of $\text{H}_1\text{-e}$ OPD cannot be attributed to film permeability, since the $\text{H}_1\text{-e}$ OPD film is thicker than the e OPD film, as a result of the 16 potential cycles in the deposition of the $\text{H}_1\text{-e}$ OPD film, compared to the 2 potential cycles for the e OPD film. Also, the unique behavior of $\text{H}_1\text{-e}$ OPD cannot be attributed to the addition of liquid crystal templating as the $\text{L}_1\text{-e}$ OPD film is not cation selective. Furthermore, although the $\text{H}_1\text{-e}$ OPD film has a mesoporous structure (unlike the $\text{L}_1\text{-e}$ OPD film), cation selectivity cannot be attributed to the size of the pores, as both the positive and negative redox couples occur in the same size range (5 to 8 Å). Therefore cation selectivity is attributable to differences in charge. Even though the $\text{H}_1\text{-e}$ OPD film charge is neutral, the aromatic rings and nitrogen lone pairs provide a high electron density environment, which is responsible for anion repulsion [106]. This phenomenon is known as Donnan exclusion behaviour, when some charged particles can pass through the film while others cannot because of the charge of the barrier [118]. Donnan exclusion behaviour has been used to verify the source of permselectivity in the $\text{H}_1\text{-e}$ OPD film by Bartlett *et al.* They investigated how $\text{H}_1\text{-e}$ OPD permselectivity is controlled by charge selectivity using Gouy-Chapman theory, which describes the change of double-layer thickness with background electrolyte concentration. According to the theory, at low electrolyte concentrations anions will be excluded as a result of negative charges held in the $\text{H}_1\text{-e}$ OPD film pores. But at high electrolyte concentrations the negative charge on the pores walls of $\text{H}_1\text{-e}$ OPD film will be balanced, so both cations and anions can enter. It has been found that the electrochemical behavior of the $\text{H}_1\text{-e}$ OPD film is affected by the background electrolyte concentration, hence proving that the unique electrochemical behavior of $\text{H}_1\text{-e}$ OPD can be attributed to the Donnan exclusion effect [106]. **Figure 1.13** shows o-1,2-diaminobenzene monomers polymerization mechanism [119].

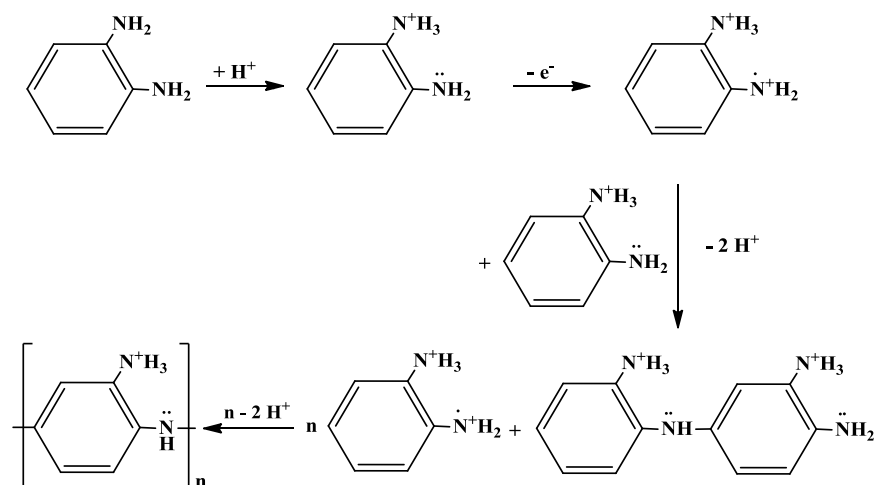


Figure 1.13: o-1,2-diaminobenzene monomers polymerization mechanism redrawn from [119].

The polyaniline (PANI) coat has been prepared electrochemically by Birss *et al.* [120], who used the potential multicycling method to form PANI film onto Au, Pt and glassy carbon GC electrodes. They succeeded in producing two types of PANI membranes depending on the upper limits in the multicycling formation process; the conducting PANI (type I) film – created by cycling in 0.1 M aniline + 1 M H_2SO_4 solution between 0 and 1 V vs. RHE, and the insulating PANI (type II) film - created by cycling in 0.02 M aniline + 1 M H_2SO_4 solution at 0 and 1.7 V vs. RHE. They found the PANI film is only conducting over a narrow potential range (between +0.95 to +1.1 V vs. RHE), however it is insulating if the upper limits are over 1.1 V vs. RHE. The GC surface electrode lacks a barrier oxide layer that presents onto Au and Pt surface. It has been shown that the porosity of PANI (type I) does not depend on the film thickness but on the material of the substrate electrode. Porosity equals 45-50% when PANI (type 1) is formed onto Pt or Au, but increases to 77% when formed onto GC electrodes this is attributed to the varying growth rates between the materials. In addition, the main oxidation potential ($E_{p,A1}$) during the cyclic voltammetry of the PANI (type II) film growth has been shown to be dependent on the material of the substrate electrode. The anodic and cathodic peak potentials shift with film thickness if Au is the substrate

electrode, but for GC there is only an anodic shift and for Pt the $E_{p,A1}$ position is stable with changing thickness [120]. **Figure 1.14** shows polyaniline formation mechanism [121].

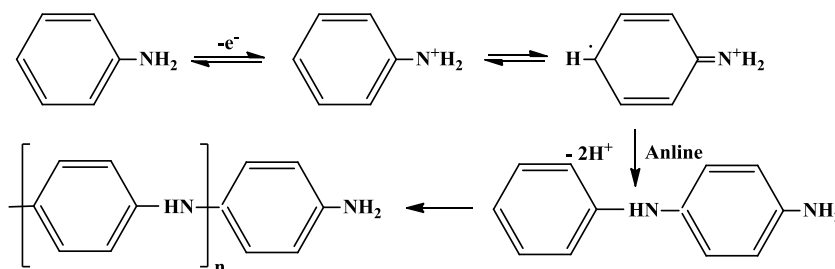


Figure 1.14: Aniline monomers polymerization mechanism redrawn from [121].

Poly(phenylene oxide) thin films have been electrochemically prepared from phenol and its derivatives by Bartlett *et al.* [122, 123]. It was found that phenol is the most promising monomer in comparison to its derivatives, as it is very selective and stable for more than 40 days. The poly(phenylene oxide) film was deposited electrochemically and has been characterized as an ion selective film because of its ability to block anions such as $Fe(CN)_6^{4-/3-}$. The film also shows an ability to stop the interference of biological substances such as L-ascorbic acid, acetoamidophenol and uric acid. **Figure 1.15** shows the electropolymerisation mechanism of phenol monomers [124, 125].

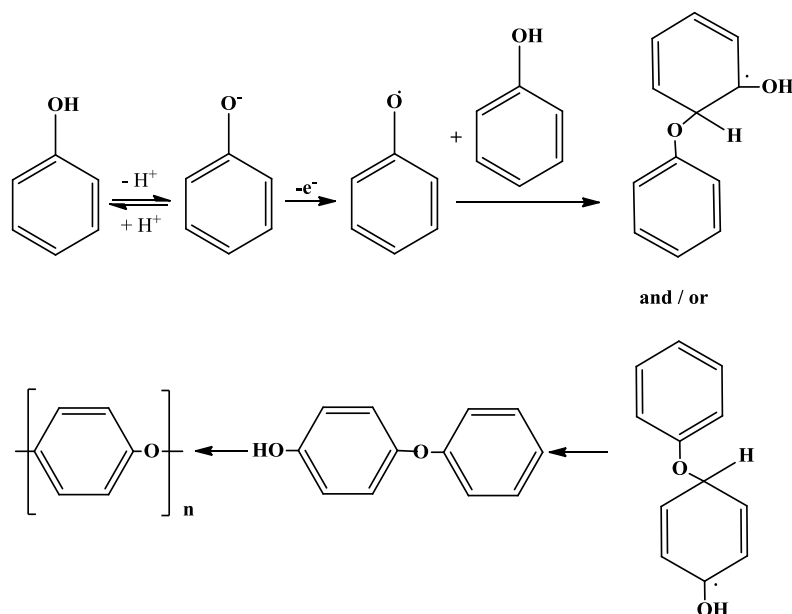


Figure 1.15: The electropolymerisation mechanism of phenol monomers redrawn from [124].

1.4.4. Covalent modification

The H_1 -e Pd *pH* sensor can be coated directly by creating a covalent bond between a monolayer of molecules and the substrate electrode surface. Subsequently the chemical composition of the attached molecules can be adjusted to modify their properties by chemical reaction. This technique has been developed to provide diverse and adjustable coatings by Pinson *et al.* [126]. The membranes synthesis involves the electrochemical reduction of aryl diazonium salts, which form a covalent bond between the organic molecules and the electrode surface. **Figure 1.16** shows the mechanism for the covalent modification of an electrode surface [127]. The substrate electrode can be modified with various methods based on the configuration of the attached organic molecules. The resulting coating is stable and reproducible; moreover the formation of polymer chains and bridges can be avoided, producing a thin monolayer film. The attached group structure will control the length and configuration of the linker arm. Furthermore, covalent modification is simple because it can be carried out electrochemically.

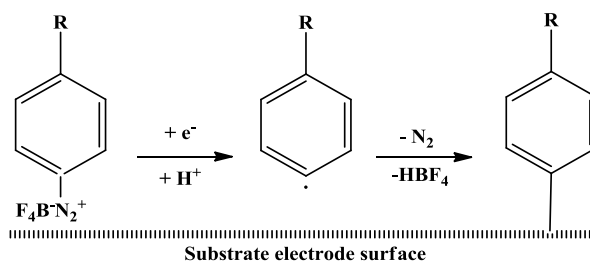


Figure 1.16: Mechanism for the covalent modification onto a substrate electrode taken from [127, 128].

It should be noted that most of the research involving covalent modification of electrodes has been done using carbon electrode types, so when using a H₁-e Pd electrode, the strength of the covalent bond required may not be sufficient to install the membrane onto the electrode surface. However, if this technique works with H₁-e Pd electrodes, it can be expanded to apply other H⁺ selective monolayer coats, such as various mono-Boc-protected diamines that using by Ghanem *et al.* [129, 130].

Figure 1.17 shows two of the covalent monolayer films that have been selected for H₁-e Pd electrodes coating in this project [128, 131].

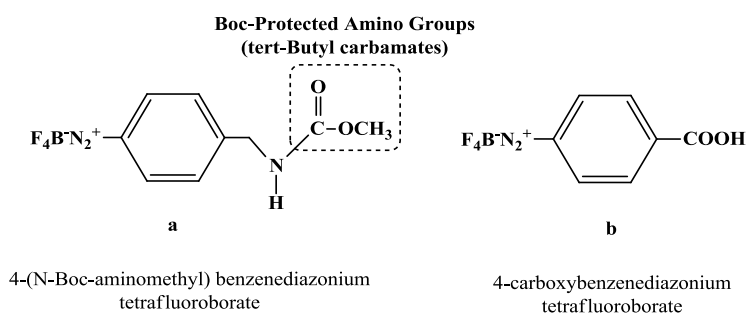


Figure 1.17: The molecular structure of some covalent modification monolayer films used in this project.

1.5. Summary

The degree of acidity in a solution is important for the chemical reactions of biological solutions such as brain fluid, because it affects reaction direction. It symbolized by pH which a variety of sensors can measure by converting an obtained potential value.

One of the most famous pH sensors is the hydrogen electrode which can cover the entire pH range. However, there are some practical difficulties when using this electrode: the Pt electrode surface has to be freshly plated and H_2 gas has to be vented before the pH measurement.

The glass electrode is commonly used to measure the pH in many applications such as; biological, chemical, industrial, and environmental fields. It has a rugged structure, a rapid response, can be used in oxidation or reduction reactions, is not easily poisoned by heavy metals and it can be used in aqueous or non-aqueous media. On the other hand, it can suffer from poor reproducibility when miniaturised, and thus needs to be calibrated regularly, and does not cover the whole pH range but just between $1 < pH < 12$. Some experimental conditions can make it difficult to use glass electrodes for example: limited sample volume, high temperature or pressure and samples, e.g. foodstuff, where the fragility of the glass bulb prevents its use. Moreover, PdH has a very low impedance compared to the glass electrode.

The many different types of metal/metal oxide electrodes (e.g Ir, Sb, Ru, Pd, and Pt oxides) can be used to measure pH , but also local pH . They are easy to fabricate and have a robust structure in comparison to other electrode materials. However, they need to be calibrated before and after use, show a potentiometric response with poor reproducibility, present variance between the same metal oxide electrodes and operate in a limited pH range. The above mentioned disadvantages have led to the requirement for a new type of pH sensing material.

A palladium hydride electrode can overcome the limitations of other electrode materials with a rapid, stable and reproducible response and no need to calibrate the electrode before and after each experiment.

This is because the obtained potential is independent of composition within the $\alpha+\beta$ transition range between a Pd/H atomic ratio of 0.02 and 0.6. The PdH electrode shows a good Nernstian agreement with a linear potential- pH calibration curve equal to -59 mV/ pH at 25 °C, and the practical potentiometric response is in a good agreement with theoretical response. Nevertheless, the limited surface area of the Pd microdisc electrode makes hydrogen loading slow and the potential becomes unstable as hydrogen continues to diffuse into the Pd wire. A deposited thin Pd film onto another metallic microwire will accelerate the hydrogen loading process but will result in a short lifetime for the PdH sensor.

The PdH electrode electroactive surface area can be increased whilst maintaining the geometric surface area by using the true liquid crystal templating technique. This technique produces a nanostructured Pd film, with a high surface area as a result of the large number of nanostructured pores. The surfactant hexagonal phase H_1 can be used to fabricate the H_1 -e Pd nanostructure film, with regular cylindrical pores ($d \approx 3$ nm), that are separated by Pd walls (wall thickness ≈ 2.8 nm). These pores have been shown to greatly increase the rate of hydrogen loading circa 50 times that observed with bulk Pd.

The hydrogen reloading charge has been found to be stable, which indicates that the H_1 -e Pd film is not destroyed by expansion as a result of hydrogen insertion into the nanostructured. H_1 -e Pd was used to estimate pH potentiometrically, and it was found that the potential was the same as that of the plain Pd film, but with a longer $\alpha+\beta$ transition lifetime. The E / pH slope was equal to -58.7 mV/ pH , which is very close to the theoretical value ($-2.303RT/F = -59.2$ mV/ pH at 25 °C), while the intercept is -50.9 mV vs. SHE, close to the conventional plateau potential of the $\alpha+\beta$ transition in pH 0 at 25 °C. The H_1 -e Pd pH sensor shows an ideal Nernstian response between pH 2 and 12

which is greatly reproducible between H₁-e Pd electrodes. It also does not need to be calibrated before and after measurements, and has a stable slope and constant intercept.

The H₁-e Pd *pH* sensor lifetime is decreased by O₂ presence in the test solution; this has been attributed to the reaction of oxygen with PdH forming a hydroxyl group and subsequently H₂O. This reaction accelerates the hydrogen consumption process and decreases the lifetime of the $\alpha+\beta$ transition. In aerated solutions, the effect of O₂ can be avoided by degassing with Ar gas before carrying out the experiment, but this cannot be done in low volume viscous solutions like brain fluid.

Coating with a selective layer is another method to limit the effect of O₂. There are many coatings which can be used to achieve this, as long as they allow hydrogen diffusion through, are stable with long term usage and stop or at least slow O₂ diffusion to the H₁-e Pd surface. The preparation technique plays a key role in the coating performance as it will control the film thickness and quality. So, three types of coating will be used in this study; direct application, polymeric films and covalent modification. In this project, several of these types of coatings will be applied to the H₁-e Pd *pH* sensor in order to clarify which film shows the best selectivity towards protons, increases the $\alpha+\beta$ transition lifetime and improves the *pH* sensor performance.

The rest of the thesis is organized as follows: Chapter 2 shows all the chemicals, the electrodes, the instruments and the experimental set-up that were used in this project. Chapter 3 presents the deposition procedures of Pd electrodes and their characterization. Chapter 4 demonstrates how to use the H₁-e Pd electrode as a *pH* sensor in different solutions including buffers and artificial then real brain fluid. Chapter 5 reports the attempts that were done in this research to improve the H₁-e Pd electrode *pH* probe performance.

Page intentionally left blank

Chapter 2. Experimental

2.1. Generalities

This chapter contains all experiments details that were followed in lab work unless otherwise stated, A water bath GD120 – Grant instruments (Cambridge) LTD was used to stabilise test solution temperature in the cells.

2.2. Purified water system

All aqueous solutions were prepared with purified water from a PURITE Select system (Purite Ltd., Thame, England). Water purification was performed in the following steps:

1. A pre-filter of carbon remove 95% of the 5 μm particulates and dechlorinate the water till < 0.5 ppm, to protect the purified water system reverse osmosis membrane from chlorine degradation.
2. The pre-filtered water then passes through the reverse osmosis membrane to remove 85% - 95% of the salts.
3. A cartridge of activated carbon and mixed ion-exchange resin and a high purity resin is used to deionise the water.
4. Finally, the water is further purified with ultra violet light to remove organics and deactivate any living bacteria.

Overall, its conductivity is about $18 \text{ M } \Omega \text{ cm}$.

2.3. Electrochemical cells

All the cells are five neck pear- shaped cells, they were made by the glass workshop of the School of Chemistry, at the University of Southampton. They have a water jacket to control the temperature if necessary. The volume of each cell is 15 ml. Test solutions were degassed by Ar gas for 20 min before starting the measurements if required, unless otherwise stated. All glassware including the cells were soaked overnight in a 5% Decon 90 solution (BDH) and then rinsed with purified water before use.

2.4. Chemicals

All the chemicals were used as received without any extra purification. **Table 2.1** shows details of the main chemicals used.

Table 2.1: the main chemicals that were used in this project.

Chemical name	formula	Purity	Supplier
H₁-e Pd film mixture			
Brij [®] 56 (C ₁₆ EO _n); n = 4 - 12)	C ₁₆ H ₃₃ (OCH ₂ CH ₂) _n OH	-	Aldrich
Octaethylene glycol monohexadecyle ether (C ₁₆ EO ₈)	C ₁₆ H ₃₃ (OCH ₂ CH ₂) ₈ OH	≥ 98.00%	Fluka
Ammonium tetrachloropalladate (II)	[(NH ₄) ₂ Pd]Cl ₄	97.00%	Aldrich
n-heptane	CH ₃ (CH ₂) ₅ CH ₃	99.00%	BDH
<u>Electrochemical measurements test materials</u>			
Argon gas	Ar	99.99%	BOC
Sulfuric acid	H ₂ SO ₄	ARISTAR	BDH
Sodium hydroxide	NaOH	AnalaR	BDH
Potassium chloride	KCl	AnalaR	Fisher
Hexaammineruthenium(III) chloride	[Ru(NH ₃) ₆]Cl ₃	98.00%	Aldrich
Sodium sulphate	Na ₂ SO ₄	AnalaR	BDH
Hydrochloric acid	HCl	ARISTAR	BDH
<u>Artificial cerebral spinal fluid (aCSF)</u>			
Sodium chloride	NaCl	AnalaR	Fisher
Potassium chloride	KCl	AnalaR	Fisher
Calcium chloride 2-hydrate	CaCl ₂ .2H ₂ O	≥ 99.00%	Sigma
Magnesium chloride 6-hydrate	MgCl ₂ .6H ₂ O	AnalaR	Fisher
Sodium dihydrogen orthophosphate 2-hydrate	NaH ₂ PO ₄ .2H ₂ O	AnalaR	Fisher
Di-sodium hydrogen orthophosphate 12-hydrate	Na ₂ HPO ₄ .12H ₂ O	AnalaR	BDH
Bovine serum albumin BSA		≥96%	Sigma
<u>H₁-e Pd film Coats</u>			
Nafion perfluorosulfonic acid- PTFEcopolymer	C ₇ HF ₁₃ O ₅ S.C ₂ F ₄	5% w/w	Alfa Aesar
Pyrrrole	C ₄ H ₅ N	98.00%	Aldrich
Phenol	C ₆ H ₆ O	99.00%	Alfa Aesar
Carboxylic tetrafluoroborate diazonium salt	BF ₄ ⁻ N ₂ ⁺ C ₆ H ₄ COOH	95.00%	Lab-made
BOC tetrafluoroborate diazonium salt	BF ₄ ⁻	95.00%	Lab-made
Aniline	C ₆ H ₅ NH ₂	99.50%	Sigma
O-phenylenediamine (1,2-Diaminobenzene)	C ₆ H ₈ N ₂	95.00%	Sigma

2.5. Electrodes

2.5.1. Reference electrodes

2.5.1.1. Saturated mercury / mercury salt electrodes SMSE and SCE

The reference electrodes used were homemade reference electrodes; they were saturated mercury / mercurous sulphate electrode (SMSE) and saturated calomel electrode (SCE). The SMSE reference electrode was used in the lab work more than SCE to avoid the Cl^- contamination. The SCE were used in some experiments when the test solution contained Cl^- . The preparation procedure of Bartlett was followed to fabricate the SMSE and SCE reference electrodes [132]. The reference electrode has two glass parts that can screw together; the lower one of them has an outer tube closed with a porous frit and the upper part has an inner pipette containing a Pt wire. The Pt wire was coated with mercury drops to form a mercury layer onto it, which connects with a paste of same ratio of Hg_2SO_4 and K_2SO_4 and saturated K_2SO_4 solution in SMSE electrode, or connects with a paste of Hg_2Cl_2 and KCl with saturated KCl solution in SCE electrode. The mercury layer was then covered by the paste to fill the internal pipette, a glass wool was then placed at the lower side of the internal pipette to prevent the paste and the mercury from falling. The pipette was then screwed with the outer tube, which was filled with internal saturated solution of K_2SO_4 in SMSE case, or with KCl in SCE situation. They were stored at least 24 hours when the electrode was new in the same internal solutions to reach equilibrium and rinsed with purified water before carrying out any electrochemical processes. They were then tested against a standard, e.g. a commercial reference electrode of the same type. The homemade reference electrode is appropriate to use if there is just ± 1 mV or less with respect to the standard [8]. **Figure 2.1** shows the typical construction of SMSE and SCE reference electrodes.

2.5.1.2. Ag/AgCl electrode

The Ag/AgCl quasi-reference electrode was used as a reference electrode in the cases that needed non-aqueous solution. It was made electrochemically by the formation of AgCl onto polished silver wire. The Ag wire was dipped in saturated KCl solution then 1 V vs. Pt wire was applied for 60 min. at room temperature. The AgCl layer onto Ag wire can be observed by the conversion of the wire colour from shiny silver to dark grey. It was stored in saturated KCl solution and rinsed with purified water then dried gently with Ar gas before carrying out any electrochemical processes. The Ag/AgCl wire could be used as a conventional reference electrode by use it with same outer tube of the SCE electrode, which was filled with internal saturated solution of KCl. **Figure 2.1** shows this type of reference electrodes [133].

2.5.2. Working electrode

The working electrodes were used are 25, 50 and 250 μm diameter Pt electrodes (99.99% Goodfellow Company) and 25 μm diameter Pd (99.99% Goodfellow Company), they were sealed inside soda glass pipette by glass workshop of the School of Chemistry, at the University of Southampton. An electrical connection was made by silver loaded epoxy (RS), to connect the wire with a copper wire (RS). Finally, the open end of the electrode pipette was closed with epoxy resin to protect the connection from the cutting. **Figure 2.1** shows a schematic representation of reference electrodes and working electrodes in this research work.

2.5.3. Counter electrode

A Pt mesh was used as counter electrode during palladium deposition and when depositing a film on the Pt electrode. A Pt wire was used as a quasi reference electrode during some of the potentiometric measurements. Before each experiment, they were rinsed with purified water after being flamed till glowing and dried by Ar gas.

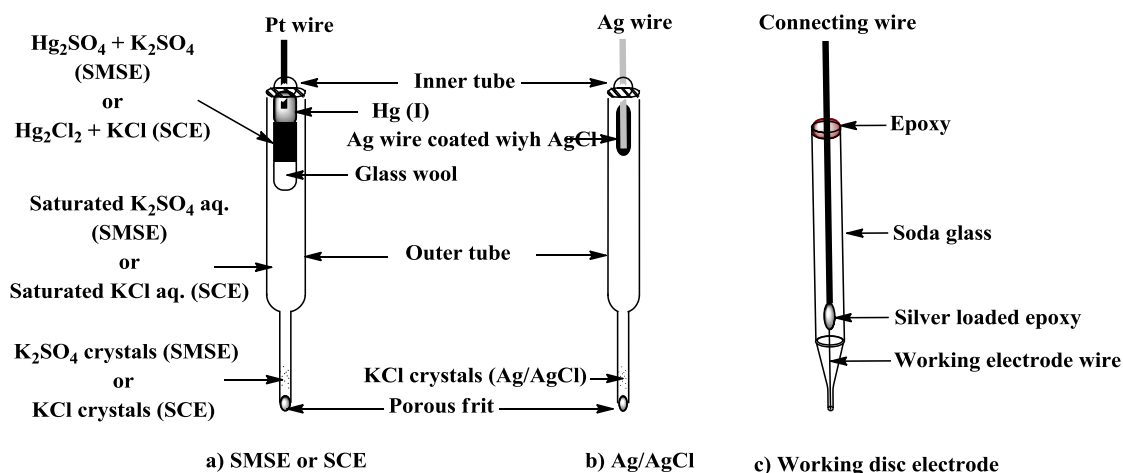


Figure 2.1: Schematic diagram of the laboratory constructed (a) saturated calomel electrode (SCE) and saturated mercury sulphate electrode (SMSE), (b) Ag / AgCl reference electrode, (c) working electrode.

2.6. Experimental set-up

All the experiments were carried out in an aluminum Faraday cage that was connected to the earth to reduce the electrical noise. Shielding cables were used for electric connection which were made as short as possible. The equipment for voltammetric, chronoamperometric and potentiometric measurements was connected to a PC via an Analog to Digital interface and the signals were acquired using labVIEWTM (version 5.1). The experimental data were treated using Origin 8 (OriginLab Corporation).

2.7. Instruments

2.7.1. Voltammetric and chronoamperometric measurements

The voltammetric measurements in this project are characterized as two-electrode system, as the reference electrode additionally works as a counter electrode. A two-electrode configuration could be used owing to the low amount of resulting current on electrodes. The potential applied to the working electrode was controlled using a PPR1 waveform generator - Hi-Tek instruments, while Keithley 486 picoammeter current

follower was used to observe the current. **Figure 2.2** shows the configuration for voltammetric and chronoamperometric measurements. Although, the previous studies showed that the hydrogen loading galvanostatically is preferred than potentiostatic loading [9], the available instrument was potentiostatic device, thus hydrogen was loaded potentiostatically.

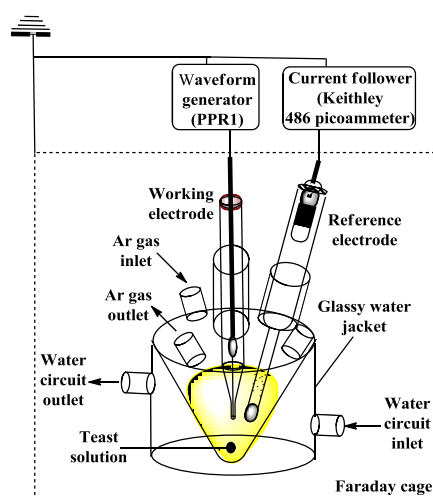


Figure 2.2: Schematic diagram of voltammetric and chronoamperometric electronic circuits showing a five neck pear-shaped cell.

2.7.2. Potentiometric experiments

The nanostructured palladium works as a solid state reservoir of hydrogen. This phenomenon was used to load or strip hydrogen into and out of the H_1-e Pd film. The potentiostatic technique was used to load and strip H_1-e Pd film with hydrogen respectively. The potentiometric measurements were carried out after the hydrogen was fully loaded into the nanostructured film potentiostatically using the PPR1 waveform generator. Then, potentiometric experiments were carried out with a homemade battery operated high input impedance differential amplifier; it was employed to ensure that the input bias current was small. The reducing of the leakage current was very important since the working electrode is a microelectrode; any flow of current will produce a voltage error or will lead to chemical change at the sensor surface.

The high impedance differential amplifier is a three-electrode system which connects to a reference, working and counter electrodes (inert large Pt wire). The working and counter electrodes potential difference is compared to the reference and counter electrodes potential difference. The counter electrode was connected to the electronic circuit earth. The high impedance box inputs were buffered with voltage followers. A precision unity-gain differential amplifier (AMP03GP from Analogue Devices) was used to compare the potential differences. **Figure 2.3** shows a schematic diagram of the high input impedance differential amplifier and of the electrochemical cell.

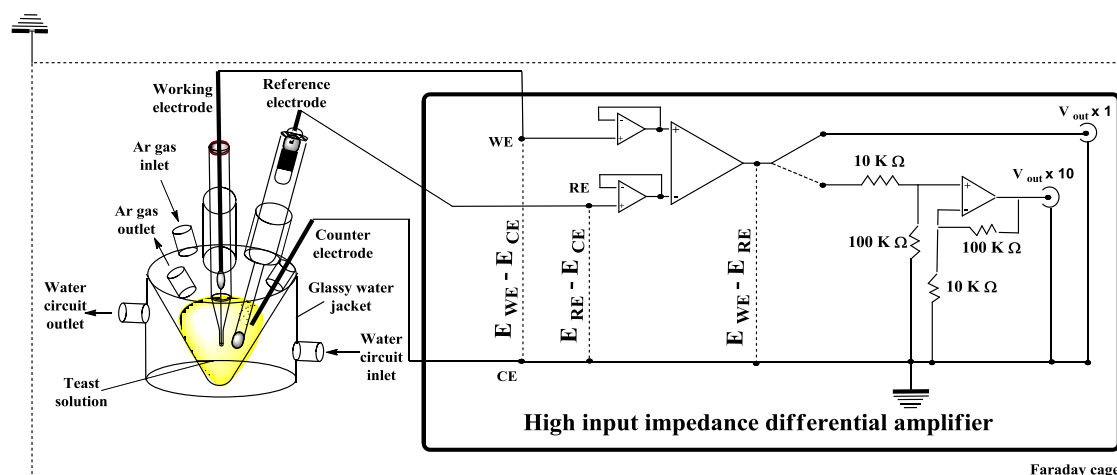


Figure 2.3: Schematic diagram of the high input impedance differential amplifier electronic circuit and of the electrochemical cell.

2.7.3. Electrodeposition processes

The electrodeposition of the palladium nanostructured and plain Pd film were performed at room temperature using a computer – controlled μ - Autolab III (Eco – chemie, Utrecht, Netherlands) using GPES (version 4.9[©]) Copyright 2007 EcoChemie. All the electrochemical deposition processes were carried out at room temperature using the same instrument.

2.7.4. Scanning Electron Microscopy (SEM)

The surface of the electrode was studied by scanning electron microscopy SEM (XL30 ESEM, Philips). The beam gun sends primary electrons PE whilst the detector collects the secondary electrons SE to produce the image. SEM was used to observe the morphology of the electrode surface to compare before and after the deposition process of H₁-e Pd film then after the nanostructured film coating process. The imaging was performed with the wet mode of the microscope, which allows between 0.1 and 20 Torr of water vapour gas inside the SEM sample chamber. The detector used in the wet mode is the gaseous secondary electron detector (GSED), which has a positive bias to sense the nanostructured surface by accelerating SE towards the detector [134]. The accelerated electrons ionise molecules of water vapor gas to produce positive ions and further SE to amplify the signal. Even though the beam charges the electrode surface, the wet atmosphere prevents the build-up of charges on the sample by positive ions of gas ionization which keeps the surface charge neutral. In the high vacuum mode, the non-conductive specimens need to cover with Au or C to eliminate the charge. So, the wet mode was chosen to avoid samples covering, as the electrode cover layer will change the electrode surface, hence it cannot be anymore treated the electrode as a Pd nanostructured electrode.

2.8. H₁-e Pd film deposition processes

2.8.1. Polishing and cleaning processes

At first, the working electrode surfaces were polished by silicon carbide papers SIC (Norton), with sizes P320 for 1 min, then P600 for 2 min, and P1200 for 4 min, followed by an Alumina aqueous slurry (Al₂O₃ Micropolish; Buehler), that was positioned on a polishing cloth (Buehler) and manually polished using circular or figure of eight motion, using grades 5 μm for 15 min and 1.0 μm for 20 min.

Then the electrode was washed with purified water and wiped smoothly with a dry polishing cloth (Microcloth PSA, Buehler) to remove any residual alumina on the electrode surface. Lastly, cyclic voltammetry was performed in 1 M H₂SO₄ voltammogram was obtained.

2.8.2. Substrate disc electrode

The H₁-e Pd film was deposited onto the substrate Pt disc electrode ($d = 25, 50$ and $250 \mu\text{m}$). Each electrode was polished and cleaned as previously reported immediately before the deposition process; this was done to ensure uniform and reproducible nanostructure morphology. The cyclic voltammetry in 1 M sulphuric acid was used to characterize the substrate Pt disc electrode and enable comparison of the surface characteristics before and after the H₁-e Pd film deposition. The cyclic voltammetry was carried out until the voltammogram stabilized. Figure 2.4 shows an example of a typical voltammogram. When the voltammogram features were not as expected (large current, peaks distorted shape etc.) the electrode was repolished. The substrate Pt disc electrode was then washed with purified water to remove any residue of the acid, and used for the H₁-e Pd electrochemical deposition.

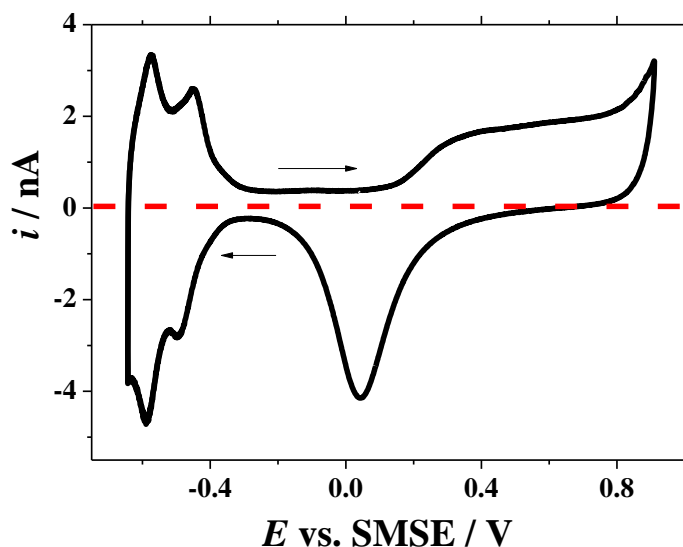


Figure 2.4: A typical cyclic voltammogram for Pt microdisc ($d = 25 \mu\text{m}$) electrodes recorded in $1 \text{ M H}_2\text{SO}_4$, purged with argon for 20 minutes, at room temperature, at scan rate $\nu = 200 \text{ mV s}^{-1}$.

2.9. Preparation of Pd films plating mixture and plating bath

The H_1 -e Pd deposition mixture was prepared following the procedure described by Bartlett *et al.* [62, 80, 86] and consisted of: 12 wt. % ammonium tetrachloropalladate (II) plus 47 wt.% of the surfactant (either Brij[®] 56 or C_{16}EO_8) and 39 wt.% purified water. Next, 2 wt. % of heptane was added to the mixture. Weight percentages of the components were determined to form the hexagonal H_1 phase of the surfactant. The container was stirred and placed in an oven (LEEC) at 40°C for 30 min. The materials were then cooled, mixed and returned to the oven at 40°C for a further 30 min. lastly, the mixture was allowed to cool before use. The heating, cooling then stirring processes were carried out to ensure the homogeneity of the mixture and to keep the surfactant in the hexagonal phase (H_1), as the plating mixture is very viscous at room temperature. The hexagonal H_1 liquid crystalline phase of the mixture was observed under the

polarising optical microscope as a charcoal-like texture, which indicates the presence of the required phase before H_1 -e Pd film deposition [81].

The plain Pd films without nanostructure were produced to clarify the extent of improvement in electroactive area characteristics with H_1 -e Pd film; it was carried out at room temperature using the same instrument with 12 wt. % ammonium tetrachloropalladate (II) aqueous solution. SCE was used as reference electrode. A Pt gauze (2 cm^2) was used as counter electrode and a polished substrate Pt disc electrodes ($d = 25\ \mu\text{m}$) were used as working electrodes. Figure 2.5 shows the Schematic diagrams of the three electrodes electronic circuit electrodeposition system for the plain Pd and H_1 -e Pd films.

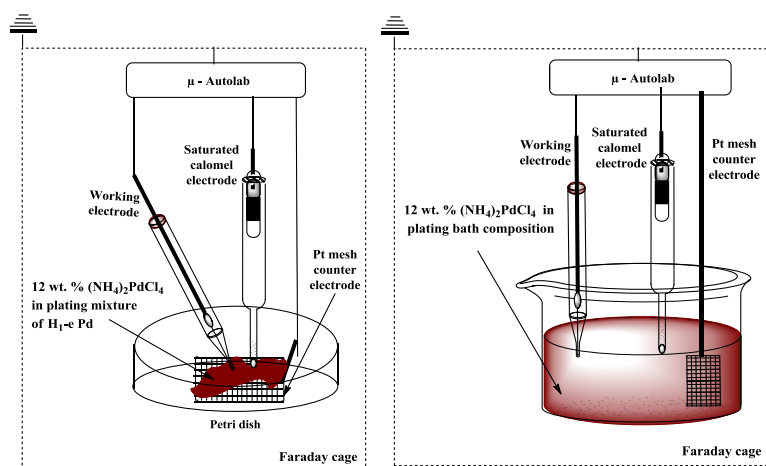


Figure 2.5: Schematic diagrams of the three electrode electronic circuit for H_1 -e Pd film electrodeposition in the left diagram and the 12% wt. $(\text{NH}_4)_2\text{PdCl}_4$ plating bath in the right diagram. Typically the plating mixture consisted of 12 wt. % ammonium tetrachloropalladate (II) plus 47 wt.% of the surfactant (either Brij[®] 56 or C_{16}EO_8) with 39 wt.% purified water and 2 wt. % of heptane. For plain Pd films the plating bath consisted of 12 wt. % ammonium tetrachloropalladate (II) plus 88 wt.% purified water.

The next chapter will investigate the electrodeposition of the H_1 -e Pd films and their characterization via cyclic voltammetry and SEM.

Page intentionally left blank

Chapter 3. Deposition and characterization of Pd films

3.1. Deposition processes

In this present study H₁-e Pd films were formed utilizing Brij[®] 56 or C₁₆EO₈ surfactants, which were added to the Pd deposition mixture. Plain Pd films without nanostructure were produced without any addition of the surfactants to the plating mixture, in order to demonstrate the improvement in electroactive area characteristics of the H₁-e Pd film. Pt electrodes ($d = 25, 50$ and $250 \mu\text{m}$) were used as the substrate for the H₁-e Pd and plain Pd films, The substrate Pt disc electrodes were chosen to be different from Pd to prevent Hydrogen diffusing from the H₁-ePd to the substrate below. In addition, that Pt was chosen because its voltammetry in acid is very characteristic and a good indicator of the cleanliness of the electrode before the deposition process. SCE was used as the reference electrode in the electrochemical deposition processes. The palladium salt (NH₄)₂PdCl₄ was used to fabricate H₁-e Pd or plain Pd films in all plating processes. The expected Pd deposition reaction is shown in equation 3.1, while **Table 3.1** sums up the composition of the deposition plating mixture for the H₁-e Pd and plain Pd films.



Table 3.1: The plating mixture for H₁-e Pd (using Brij[®] 56 or C₁₆EO₈) and plain Pd films.

Pd film	(NH ₄) ₂ PdCl ₄	Surfactant (Brij [®] 56 or C ₁₆ EO ₈)	n-heptane	H ₂ O
H ₁ -e Pd	12 wt%	47 wt%	2 wt%	39 wt%
Plain Pd	12 wt%	0 wt%	0 wt%	88 wt%

3.2. Pd plating cyclic voltammetry

The Pd films were deposited using the chronoamperometry technique. Therefore, cyclic voltammetry was carried out to identify the initial $E_{\text{initial dep}}$ and the final $E_{\text{final dep}}$ potentials. The deposition of plain and H₁-e Pd films was carried out in a bath containing the plating mixture. The sweep rate of cyclic voltammetry was 10 mVs⁻¹. SCE was used as the reference electrode, Pt mesh (2 cm²) the counter electrode, and a Pt microdisc ($d = 25 \mu\text{m}$) as the working electrode.

Figure 3.1 shows the cyclic voltammograms of a fresh (prepared the previous day) and old (prepared 3 weeks before) Pd plating mixture, both with the mixture containing 47 wt% Brij[®] 56 as a surfactant. The first cycle of the H₁-e Pd mixture voltammogram illustrates that the Pd reduction current is observed from about +0.2 V vs. SCE on the cathodic (forward) sweep. On the anodic (reverse) sweep, the deposition current continues to almost +0.25 V vs. SCE. In the second and third cycles the current was observed from about +0.25 V vs. SCE on the forward sweep. This occurs because the nucleation process of the first cycle requires a higher over potential in comparison to the growth process of the subsequent cycles. This phenomenon has also been detected in other substrate electrodes like Au and Pt [8, 85]. In all of the cycles the current was also seen to be lower in the cathodic than in the anodic sweep. Furthermore, the current can be seen to increase with each repetition of the cyclic voltammetry; this is attributed to the increasing electrode geometric surface area (GSA) as palladium is deposited.

Figure 3.1 indicates that when E equals +0.4 V vs. SCE, the current was virtually equal to zero in all three sweeps. As a result, that potential was used in the deposition chronoamperometry process as $E_{\text{initial dep}}$. $E_{\text{final dep}}$ was chosen at +0.1 V vs. SCE for H₁-e Pd chronoamperometry electrodeposition, which corresponds to the potential used by Bartlett *et al.* when performing the same deposition process [62, 80, 86]. Cyclic voltammograms show the deposition current is controlled not with mass transport but by the kinetics process.

Imokawa reported that the voltammetry of the plating mixture that contains Brij[®] 56 has a similar shape with less current than that containing C₁₆EO₈; this was attributed to the low diffusion coefficient of the [PdCl₄]⁻ [8]. The role of viscosity can be indicated using old and fresh mixtures, **Figure 3.1** shows a Pd salt reduction current, as a result of drying out in the old mixture.

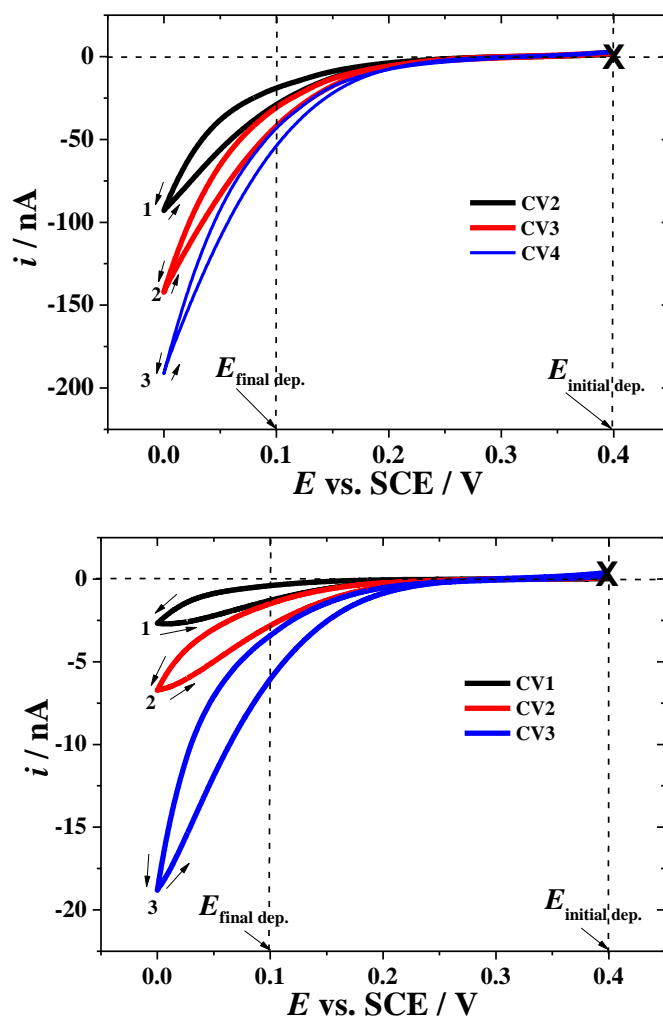


Figure 3.1: Cyclic voltammetry of the H₁-e Pd film mixture (which contain Brij[®] 56 as a surfactant) recorded at 10 mV s⁻¹ with a Pt microdisc electrode ($d = 25 \mu\text{m}$), at room temperature. Cycle sequence as indicated in the plot. The mixture used for the top voltammogram was prepared the previous day, while that used for the lower voltammogram was prepared 3 weeks before.

Likewise, the plain Pd film chronoamperometry potentiostat parameters were identified by cyclic voltammetry, which was carried out in the same conditions as for the H₁-e deposition mentioned previously, except that the cyclic voltammetry was done in a simple aqueous plating bath containing 12 wt. % (NH₄)₂PdCl₄.

Figure 3.2 shows the features of the cyclic voltammetry performed in the plating bath. The voltammetry shows that the current increases with each following sweep as a result of the increase of the geometric surface area of the working electrode, which can be confirmed by scanning electron micrographs and cyclic voltammetry (in sections 3.4.1 and 3.4.2). Similarly, to the H₁-e voltammetry, a higher overpotential is required in the first sweep as the Pd nucleates. The cyclic voltammogram also shows that the deposition current was almost equal to zero in all three sweeps when E equals +0.4 V vs. SCE ; this potential was used as $E_{\text{initial dep}}$. The deposition of plain Pd film using $E_{\text{final dep}}$ at +0.1 V vs. SCE produces a disfigured plain Pd film. Therefore, the Pd deposition will be done in a more positive potential at $E_{\text{final dep}} = +0.23$ V vs. SCE to obtain a smooth plain Pd film. This corresponds to what was reported by Imokawa [8].

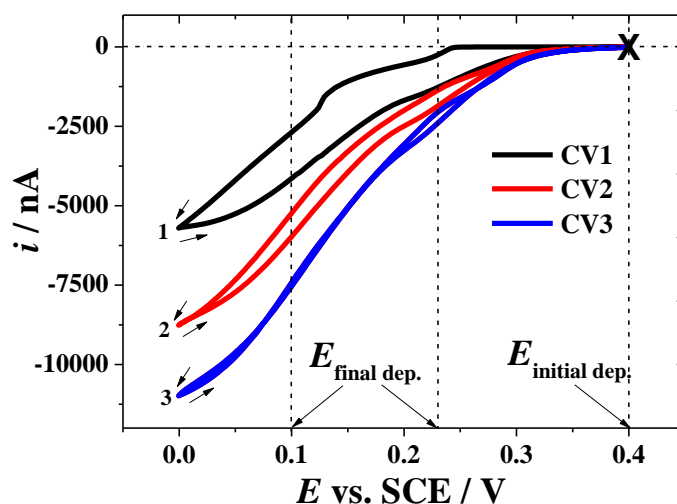


Figure 3.2: Cyclic voltammetry of the plain Pd film using a simple aqueous plating bath which contained 12 wt. % (NH₄)₂PdCl₄, recorded at 10 mV s⁻¹ with a Pt microdisc electrode ($d = 25$ μm), at room temperature. Cycle sequence as indicated in the plot.

3.3. Pd films chronoamperometry electrodeposition

All the plating mixtures and plating baths of Pd films were prepared as mentioned in Table 3.1. The chronoamperometry processes was carried out by stepping the potential from $E_{\text{initial dep}} = +0.4$ V vs. SCE at $t = 0$ s to $E_{\text{final dep}} = +0.1$ or $+0.23$ V vs. SCE to obtain a H₁-e Pd or plain Pd film respectively. The deposition charges Q_{dep} used were 25, 100 and 2500 μC ; they were respectively applied to the polished substrate working Pt disc electrodes ($d = 25, 50$ and 250 μm), to maintain a uniform deposition charge density j of 5.09 C cm^{-2} for all electrodes. The H₁-e Pd film plating mixture was prepared following the procedure described by Bartlett *et al.* [62, 80, 86]. SCE was used as the reference electrode, with the tip being covered by a small amount of plating mixture. This was also done with the tip of the working electrode to make sure that the electrical circuit was closed. As soon as the H₁-e Pd plating mixture was ready to be used, it was spread on the Pt gauze counter electrode (2 cm^2). After the required Q_{dep} was passed, the electrode was then rinsed with purified water, and then kept in a purified water beaker with gentle stirring for 24 hours, in order to wash the surfactant from the nanostructured film.

The plain Pd films were produced to explain the magnitude of the improvement in electroactive area with the nanostructured H₁-e Pd film. The deposition was carried out at room temperature using the same instruments and settings as with the H₁-e Pd deposition, with a simple aqueous solution of 12 wt. % $(\text{NH}_4)_2\text{PdCl}_4$.

Figure 3.3 shows resulting three amperometric diagrams performed on the same day using same deposition plating mixture, their current are stopped when the required deposition charge Q_{dep} (2500 μC) was reached. The currents are consistent as they large initially, and then drop but after a minimum the current gently rises again. This steady raising in the current suggesting that the GSA increases by the deposition of the Pd nanostructured. On the one hand, The currents are dissimilar as the current vs. time curve shows a drop in the current maximum from 4.3 to 2.5 then 1.8 μA , while the deposition times were increased from 725 to 1148 then 1918 s respectively. This can be

attributed once again to the viscosities rising because the mixture is losing its humidity during the duration of the deposition in open air.

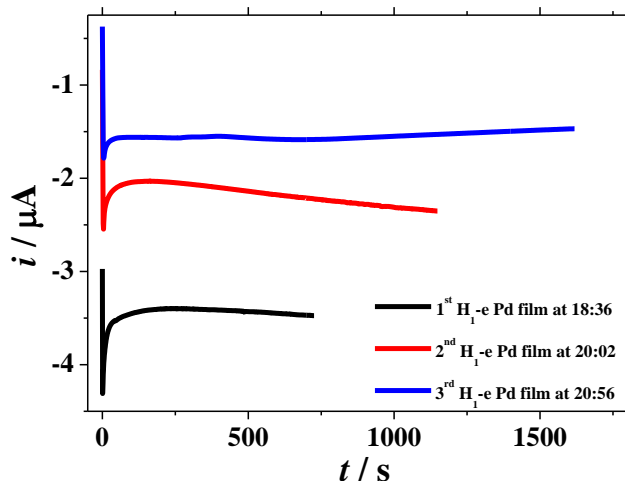


Figure 3.3: Chronoamperograms recorded during three H₁-e Pd films deposition onto a Pt microdisc electrodes ($d = 250 \mu\text{m}$), the potential was stepped from +0.4 V to +0.1 V vs. SCE. Deposition charge $Q_{\text{dep}} = 2500 \mu\text{C}$. The transients were recorded sequentially (as indicated by the time when the deposition was started) using the same mixture includes C₁₆EO₈ as a surfactant, but without reconditioning of the mixture in between each deposition.

The Pd films thickness can be controlled by varying the deposition charge Q_{dep} and can be obtained by equation 3.4 derived as follows [135]:

$$Q_{\text{dep.}} = \int_0^t i dt \tag{3.2}$$

$$Q_{\text{dep.}} = mnF \tag{3.3}$$

As:

$$m = \frac{\text{mass}}{Awt} \quad , \quad \rho = \frac{\text{mass}}{\text{vol.}} \quad , \quad \text{and} \quad \text{vol.} = A \cdot \text{thickness}$$

So:

$$\text{thickness} = \frac{Q_{\text{dep.}} \cdot Awt}{nF\rho A} \tag{3.4}$$

where Q_{dep} is the palladium deposition charge, i is the applied current, t is the deposition time, m is the number of deposited material moles, Awt is the atomic weight, n is the number of transferred electrons, F is the Faraday's constant ($F = 96485 \text{ C mol}^{-1}$), ρ is the density, $vol.$ is the film volume, A is the film area and $thickness$ is the film thickness. Assuming 100% current efficiency, the deposition charge density j of 5.09 C cm^{-2} should yield a uniform thickness of $2.3 \text{ }\mu\text{m}$ for a plain Pd film. However, these conditions will produce H₁-e Pd film with thinner thickness between 2.2 and $2.3 \text{ }\mu\text{m}$, as its current efficiency between 95 and 99% [80].

3.4. Electrodeposition influence in geometric surface area expansion

The geometric surface area (*GSA*) is a useful value to characterize Pd films. The *GSA* gives an indication of the change in geometric surface area before and after the Pd film deposition, and can be calculated using equation 3.5 [9]:

$$GSA = \frac{\pi d^2}{4} \quad 3.5$$

where *d* is the diameter determined by SEM or by cyclic voltammogram.

3.4.1. Pd films *GSA* by SEM

The working electrode was studied by scanning electron microscopy SEM. This was used for the accurate estimation of the change in geometric surface area before and after the electrochemical deposition of Pd films.

The theoretical geometric surface area value GSA^{SEM} can be estimated using the electrode diameter d^{SEM} that is obtained by SEM. **Figure 3.4** shows the images of four microdisc electrodes ($d = 25 \mu\text{m}$) before and after the Pd deposition process. The d^{SEM} of each Pt microdisc electrode was $25.8 \mu\text{m}$ before the deposition giving a GSA^{SEM} value equal to $5.23 \times 10^{-6} \text{ cm}^2$. Applying a deposition charge $Q_{dep} = 25 \mu\text{C}$ ($j = 5.09 \text{ C cm}^{-2}$), GSA^{SEM} increased by 41.4% to $7.40 \times 10^{-6} \text{ cm}^2$ after the H₁-e Pd deposition using Brij[®] 56 as the surfactant. Similar results were seen when C₁₆EO₈ was used as the surfactant, with the GSA^{SEM} increasing by 41.6% to $7.41 \times 10^{-6} \text{ cm}^2$. Furthermore, SEM images show that the H₁-e Pd film deposited using Brij[®] 56 is much rougher than the H₁-e Pd film formed using C₁₆EO₈.

SEM images show that the GSA^{SEM} of plain Pd films is larger than that of H₁-e Pd films, with an expansion of 25.6% to $9.96 \times 10^{-6} \text{ cm}^2$. Which could be attributed to the edge effects in absence of surfactant and Pd²⁺ ion diffusion is faster in a plain Pd plating mixture, as the H₁-e mixture contains a higher level of surfactant (47 wt%), causing lower viscosity.

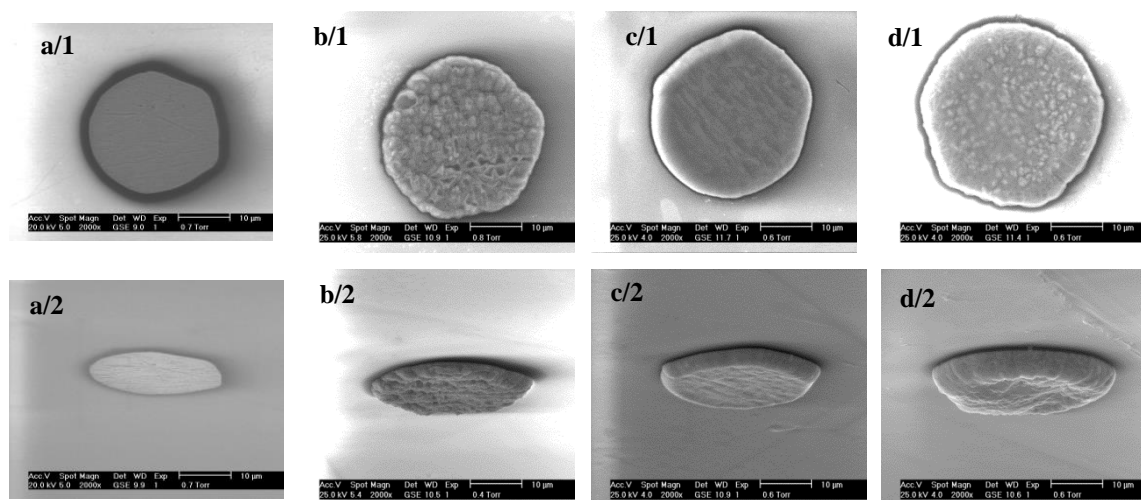


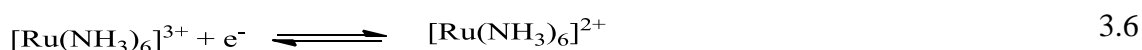
Figure 3.4: Scanning electron microscopy images with scale bar = 10 μm of (a) a polished Pt substrate microdisc electrode ($d = 25 \mu\text{m}$), (b) a deposited H₁-e Pd film using Brij[®] 56 in the plating mixture, (c) a deposited H₁-e Pd film using C₁₆EO₈ in the plating mixture, (d) a deposited plain Pd film in plating bath. The electrochemical deposition parameters of all of them were: deposition charge Q_{dep} equals 25 μC , the Pd concentration was 12 wt. % of (NH₄)₂PdCl₄, deposition potential $E_{\text{final dep}}$ equals +0.1 and +0.23 V vs. SCE with and without surfactant respectively. The tilt angle of the top row is 70°, and in the lower row is 0°.

3.4.2. Pd films GSA by Cyclic voltammetry

The working electrode GSA can be found experimentally before and after the Pd film deposition process from the limiting current i_L of a diffusion controlled voltammogram for a fast redox couple. Cyclic voltammetry was used to obtain the experimental limiting current i_L^{CV} , which was used to determine the experimental geometrical surface area GSA^{CV} . The redox reaction of 5 mM [Ru(NH₃)₆]^{3+/2+} was used because it is a clean model system where the molecules do not form an adsorbed layer onto the electrode surface, and the reaction is a fast one-electron redox process.

0.5 M KCl was used as a supporting electrolyte to avoid a migration current, as it increases the ionic strength of the solution, therefore the electric field will be homogeneous and near-zero, and hence unperturbed by the analyte oxidation or reduction [136].

The redox reaction of $[\text{Ru}(\text{NH}_3)_6]^{3+/2+}$ is shown by the following equation:



The i_L^{CV} is given by equation 3.7 [137-139]:

$$i_L^{\text{CV}} = 4nFDac \quad 3.7$$

where n is the number of transferred electrons, F is the Faraday's constant ($F = 96485 \text{ C mol}^{-1}$), D is the diffusion coefficient, c is the redox ions concentration in the bulk and a is radius of the microdisc electrode [140, 141].

The selected sweep rate was 2 mV s^{-1} , chosen to minimise the non-Faradic current of double-layer charging j_{charging} seen with the enlarged $\text{H}_1\text{-e Pd}$ surface area. As shown in equation 3.8 [135]:

$$j_{\text{charging}} = v C_{dl} \quad 3.8$$

where v is the potential scan rate, C_{dl} the double layer capacitance.

Figure 3.5 shows that under the chosen conditions, the redox reaction of $[\text{Ru}(\text{NH}_3)_6]^{3+/2+}$ is a purely diffusion controlled system. Therefore, it follows a steady state voltammogram, which has a sigmoidal shape with a small hysteresis, typical of what is observed with microdisc electrodes.

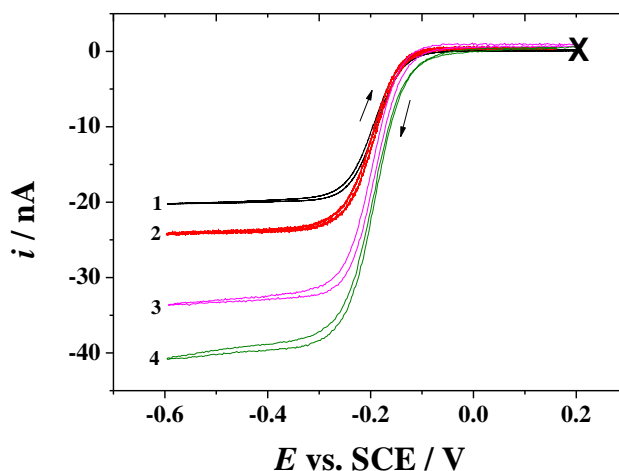


Figure 3.5: Cyclic voltammograms recorded for a range of H_{1-e} Pd films deposited on a Pt microdisc electrodes ($d = 25 \mu\text{m}$) recorded at 2 mV s^{-1} in $5 \text{ mM Ru(NH}_3)_6^{3+} + 0.5 \text{ M KCl}$ at 25°C . The deposition charges Q_{dep} of H_{1-e} Pd are (1) $0 \mu\text{C}$, (2) $10 \mu\text{C}$, (3) $25 \mu\text{C}$, and (4) $50 \mu\text{C}$.

Furthermore, equation 3.7 was used to estimate the diffusion coefficient D . The limiting current is determined from the voltammetry and the equation can be applied using polished Pt microdisc electrodes ($d = 10, 25$ and $50 \mu\text{m}$): D is calculated to be $8.3 \times 10^{-6} \text{ cm}^2 \text{ s}^{-1}$, which is approximately consistent with the reported value found in the literatures between 8.5×10^{-6} and $9.1 \times 10^{-6} \text{ cm}^2 \text{ s}^{-1}$ [136, 139, 142, 143].

The GSA^{CV} values can be found using the experimental electrode diameter d^{CV} calculated from the i_L^{CV} of $[\text{Ru(NH}_3)_6]^{3+/2+}$ redox in equation 3.7.

The steady state voltammetry was performed to study the effect of the H_{1-e} Pd film deposition process on the GSA^{CV} , which was found to increase as a result of the edge effect following the deposition process. **Figure 3.5** shows typical cyclic voltammograms for a range of deposition charges Q_{dep} of H_{1-e} Pd films in $5 \text{ mM Ru(NH}_3)_6^{3+} + 0.5 \text{ M KCl}$ at 25°C . The i_L^{CV} increases due to the expansion of the H_{1-e} Pd film area commensurate with equation 3.7, since i_L^{CV} is proportional to the working electrode radius that will be used to obtain GSA^{CV} .

Figure 3.6 shows a comparison of steady state voltammograms for different microdisc electrodes, in the same conditions as **Figure 3.5**. The used electrodes were; a polished Pt ($d = 25 \mu\text{m}$), a polished Pd ($d = 25 \mu\text{m}$), a H₁-e Pd film ($Q_{\text{dep}} = 25 \mu\text{C}$) onto a Pt microdisc electrodes ($d = 25 \mu\text{m}$) and a plain Pd film ($Q_{\text{dep}} = 25 \mu\text{C}$) onto a Pt microdisc electrodes ($d = 25 \mu\text{m}$). The GSA^{CV} of both polished Pt and Pd microdisc electrodes are in good agreement with GSA^{SEM} .

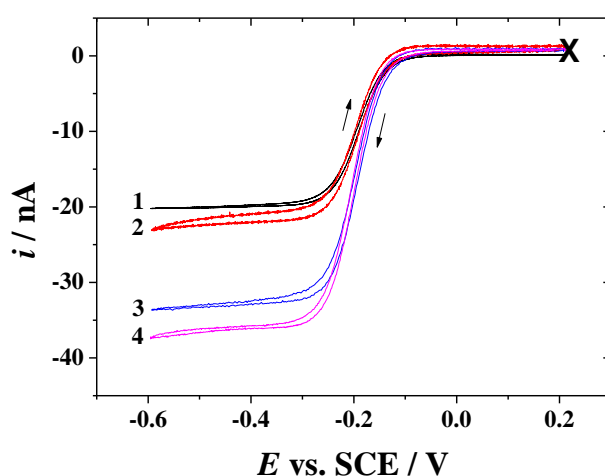


Figure 3.6: Cyclic voltammograms recorded for (1) a polished Pt microdisc electrode ($d = 25 \mu\text{m}$), (2) a polished Pd microdisc electrode ($d = 25 \mu\text{m}$), (3) a H₁-e Pd film ($Q_{\text{dep}} = 25 \mu\text{C}$) onto Pt microdisc electrode ($d = 25 \mu\text{m}$) and (4) a plain Pd film ($Q_{\text{dep}} = 25 \mu\text{C}$) onto Pt microdisc electrode ($d = 25 \mu\text{m}$) recorded at 2 mV s^{-1} in $5 \text{ mM Ru}(\text{NH}_3)_6^{3+} + 0.5 \text{ M KCl}$ at 25°C .

It can be seen from Figure 3.5 and **Figure 3.6** that i_L^{CV} increases with the expansion of the electrode diameter as described by equation 3.7. This agreement holds true for $Q_{\text{dep}} \leq 10 \mu\text{C}$, but for $Q_{\text{dep}} > 10 \mu\text{C}$, the i_L^{CV} becomes higher than expected. This is because the increasing GSA is not only explained by the increasing diameter, but also by the wall height of the deposition film due to the increasing of the film thickness, which gives the electrode extra area that contribute to the increase of the GSA^{CV} , that makes GSA^{CV} larger than GSA^{SEM} when Q_{dep} increases above $10 \mu\text{C}$.

Since the GSA^{CV} is an apparent GSA determined from a diffusion controlled experiment while the GSA^{SEM} is directly observed on the SEM image. Likewise, this can also be observed with a thicker plain Pd film even though it has the same deposition charge of H₁-e Pd film, which has a higher diameter and thickness than H₁-e Pd film. The difference between the GSA^{CV} of deposited nanostructure using either Brij[®] 56 or C₁₆EO₈ surfactants with same Q_{dep} is negligible considering to i_L^{CV} difference is very small. **Table 3.2** shows the GSA values obtained from SEM images and [Ru(NH₃)₆]^{3+/2+} voltammograms in **Figure 3.5** and **Figure 3.6**.

Table 3.2: The geometrical surface area GSA^{SEM} and GSA^{CV} obtained using SEM and from [Ru(NH₃)₆]^{3+/2+} voltammograms of polished Pt and Pd microdisc electrodes before and after the Pd deposition process. The theoretical limiting current i_L^{SEM} was calculated from d^{SEM} in equation 3.7.

Microdisc electrode	d^{SEM} (μm)	GSA^{SEM} (cm^2)	i_L^{SEM} (nA)	i_L^{CV} (nA)	d^{CV} (μm)	GSA^{CV} (cm^2)
Polished Pt ($d= 25 \mu\text{m}$)	25.8	5.23×10^{-6}	20.66	20.14	25.1	5.0×10^{-6}
Polished Pd ($d= 25 \mu\text{m}$)	26.28	5.43×10^{-6}	21.55	22.37	27.9	6.1×10^{-6}
Plain Pd film ($Q_{dep} = 25 \mu\text{C}$)	35.6	9.96×10^{-6}	29.20	36.70	45.8	1.7×10^{-5}
H ₁ -e Pd film ($Q_{dep} = 10 \mu\text{C}$) Brij [®] 56	29.3	6.75×10^{-6}	24.03	24.02	30.0	7.1×10^{-6}
H ₁ -e Pd film ($Q_{dep} = 25 \mu\text{C}$) Brij [®] 56	30.68	7.40×10^{-6}	25.16	32.98	41.2	1.3×10^{-5}
H ₁ -e Pd film ($Q_{dep} = 25 \mu\text{C}$) C ₁₆ EO ₈	30.7	7.41×10^{-6}	25.18	33.29	41.6	1.4×10^{-5}
H ₁ -e Pd film ($Q_{dep} = 50 \mu\text{C}$) Brij [®] 56	34.5	9.35×10^{-6}	28.29	40.25	50.3	2.0×10^{-5}

3.5. Pd electrodes real surface area

The electrochemical behavior of Pd electrodes was studied by cyclic voltammetry in an acid test solution to identify the surface reactions and the experimental real surface area RSA^{CV} of the electrode (i.e. electroactive surface area or real interface area). The RSA^{CV} was estimated before and after the deposition of H₁-e Pd and plain Pd and compared to a polished Pd electrode to clarify the benefits of the H₁-e nanostructure. In addition, theoretical and experimental real surface areas were calculated to estimate the roughness factor.

Figure 3.7 shows cyclic voltammograms in 1 M H₂SO₄ for a H₁-e Pd film, a plain Pd film, and a polished Pd electrode ($d = 25 \mu\text{m}$). The two Pd film electrodes were deposited with a Q_{dep} of 25 μC onto a Pt microdisc electrode ($d = 25 \mu\text{m}$). The H₁-e Pd cyclic voltammetry gives the well-known fingerprint of Pd surface redox processes [10, 80, 86, 144-146], showing three distinct regions: the hydride region, and the oxide region, separated by the double layer region which is located approximately between -0.1 and -0.35 V vs. SMSE. In contrast, the plain Pd film and polished Pd electrode voltammograms show remarkable dissimilarity compared to the H₁-e Pd film. They have similar surface oxide formation / stripping potentials but with much lower currents. In addition, the plain Pd voltammogram is unresolved and broad, and the polished Pd electrode is less resolved compared to the plain Pd film in the cathodic potential range, with just a single wave of cathodic current and one peak for anodic current being observed. The very clear characteristics of resolved peaks in the H₁-e Pd voltammogram have been attributed to the higher electroactive area of the H₁-e Pd film in comparison to the plain Pd film and Pd electrode. This will be discussed in more details in the following chapter.

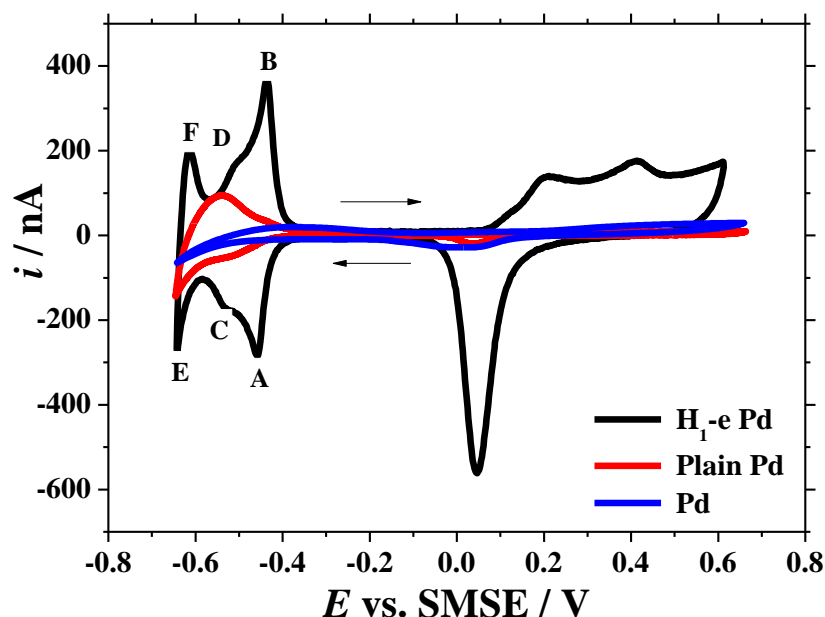


Figure 3.7: Cyclic voltammograms recorded at 20 mV s^{-1} in $1 \text{ M H}_2\text{SO}_4$ at room temperature for a $\text{H}_1\text{-e Pd}$ film (black line) and a plain Pd film (red line) onto polished Pt microdisc electrodes ($d = 25 \text{ }\mu\text{m}$), the deposition charge Q_{dep} of both of them = $25 \text{ }\mu\text{C}$ and a polished Pd microdisc electrodes ($d = 25 \text{ }\mu\text{m}$) (blue line). The peaks labelled with letters A to F are described in the section below.

3.6. Hydrogen sorption in $\text{H}_1\text{-e Pd}$

The property of the Pd to load with hydrogen was reviewed in section 1.2. This can be illustrated using cyclic voltammetry in $1 \text{ M H}_2\text{SO}_4$. **Figure 3.7** shows cyclic voltammograms of a polished Pd microdisc electrode, a plain Pd film and $\text{H}_1\text{-e Pd}$ film. The voltammogram in acid of plain Pd is unresolved and broad in the hydride region, and the polished Pd electrode is less resolved compared to the plain Pd film. While the $\text{H}_1\text{-e Pd}$ film voltammogram shows clear and non-overlapping peaks in the hydride region, it has three pairs of peaks of hydrogen sorption then stripping below -0.4 V vs. SMSE; the very sharp pair of peaks (A and B) around -0.45 V reflect the hydrogen adsorption / desorption process onto the surface of $\text{H}_1\text{-e Pd}$ film, then smaller broader peaks (C and D) at -0.52 V correspond to the hydrogen absorption to form and strip the

PdH α phase, the last pair of peaks (E and F) about -0.625 V correspond to the onset of the hydrogen absorption to form and then strip the PdH β phase [80, 147].

3.7. Palladium oxide reaction

The Pd surface oxide formation can be seen from about +0.1 V vs. SMSE in the H₁-e Pd film voltammogram in Figure 3.7. On the cathodic sweep there is a sharp peak at about +0.01 V vs. SMSE related to the stripping of Pd surface oxide. This peak height can be used to compare between the bare Pt electrode and the H₁-e Pd film microdisc electrode to confirm Pd deposition. The reaction of palladium oxide formation/stripping is [144-146, 148]:



Pd is dissolved in acidic media in the potential range of oxide formation, this is one of the reasons the monolayer oxide stripping peak is often used to estimate the real interface area of the Pd electrodes [80, 149]. The the real interface area of the H₁-e Pd films can be estimated by integrating the charge passed in the surface oxide stripping reaction recorded in 1 M H₂SO₄ [62].

3.8. Electroactive surface area

The real surface area (*RSA*) is the real interface area of the plain Pd film, H₁-e Pd film, polished Pd, and substrate Pt electrodes. Experimental real surface area RSA^{CV} was calculated by cyclic voltammetry in 1 M H₂SO₄. RSA^{CV} can be measured indirectly using either the Pd oxide stripping charge Q_{ox-Pd} with Pd electrodes or the hydrogen desorption charge Q_{des-Pt} with Pt electrodes, both Q_{ox-Pd} and Q_{des-Pt} were calculated by dividing the area of the Pd oxide stripping or Pt hydrogen desorption peaks by the scan rate ν . They are symbolised by Q_{des-Pt} or Q_{ox-Pd} in equation 3.10 which shows the RSA^{CV} calculation:

$$RSA^{CV} = \frac{Q_{des-Pt \text{ or } ox-Pd}}{Cf} \quad 3.10$$

where C_f , the conversion factor means the obtained charge from 1 cm^2 , which for Pt hydrogen desorption is equal to $208 \mu\text{C cm}^{-2}$ and for Pd oxide stripping is equal to $424 \mu\text{C cm}^{-2}$ [101, 150].

Subsequently, RSA^{CV} will be compared with GSA^{CV} to clarify the improvement in the H_1 -e Pd film surface characteristics against a plain Pd film (with equivalent Q_{dep}), a polished Pd electrode and the substrate Pt electrode. The comparative analysis between the electrodes gave the roughness factor R_f that is shown in equation 3.11 [151, 152]:

$$R_f = \frac{RSA^{CV}}{GSA^{CV}} \quad 3.11$$

Table 3.3 shows the R_f of the H_1 -e Pd film ($Q_{\text{dep}} = 25 \mu\text{C}$) is 354, which is much higher than the 5 seen with polished Pt ($d = 25 \mu\text{m}$), 49 with polished Pd ($d = 25 \mu\text{m}$), and 17 with plain Pd ($Q_{\text{dep}} = 25 \mu\text{C}$). This clearly displays the surface improvement that can be achieved using the nanostructured film.

Table 3.3: The real interface area RSA^{CV} before and after H_1 -e Pd film deposition compared to a substrate Pt electrode and a plain Pd film with equivalent deposition charge.

Microdisc electrode	$Q_{\text{des-Pt}}$ or $Q_{\text{ox-Pd}} / \text{C}$	RSA^{CV} / cm^2	GSA^{CV} / cm^2	R_f
Polished Pt ($d = 25 \mu\text{m}$)	4.9×10^{-9}	2.3×10^{-5}	4.7×10^{-6}	5
Polished Pd ($d = 25 \mu\text{m}$)	1.2×10^{-7}	2.8×10^{-4}	5.8×10^{-6}	49
Plain Pd film ($Q_{\text{dep}} = 25 \mu\text{C}$)	9.1×10^{-8}	2.1×10^{-4}	1.3×10^{-5}	17
H_1 -e Pd film ($Q_{\text{dep}} = 25 \mu\text{C}$)	2.4×10^{-6}	5.7×10^{-3}	1.6×10^{-5}	354

The surface improvement of the nanostructure can be illustrated by the theoretical real surface area RSA^{Theor} which is based on TEM images of the H_1 -e Pd film. This technique is used to estimate the diameter of the pores that were revealed when the cylindrical rods of the hexagonal phase of the surfactant were washed away. The H_1 -e pore radius r_{pore} has been assessed to be 1.5 nm with about 3 nm of wall thickness between them for several metals such as Pd, Pt, Co and Rh [10, 80, 84, 86, 153]. The

H₁-e film thickness depends on the Q_{dep} as was mentioned in equation 3.4. Hence, the unit cell can be determined using these dimensions, which is the area located in the middle of four pores, as can be seen in Figure 3.8.

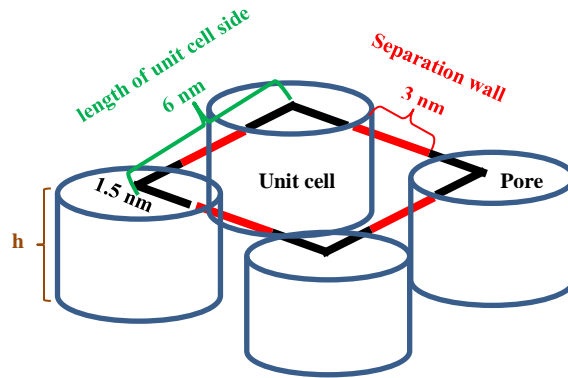


Figure 3.8: Schematic representation of a H₁-e M unit cell.

The RSA^{Theor} can be derived in 3.12:

$$RSA^{Theor} = [unit\ cell\ area - pore\ mouth\ area + wall\ pore\ area] \times No.\ of\ pores \quad 3.12$$

As:

$$unit\ cell\ area = \frac{\sqrt{3}}{2} \cdot (length\ of\ unit\ cell\ side)^2 \quad , \quad Pore\ mouth\ area = \pi \cdot r_{pore}^2$$

$$Internal\ pore\ wall\ area = 2 \cdot \pi \cdot r_{pore} \cdot film\ thickness \quad , \quad No.\ of\ pores = \frac{GSA}{unit\ cell\ area}$$

TEM dimensions of length of the unit cell side and separation wall yield a unit cell area equal to $2.17 \times 10^{-13} \text{ cm}^2$, and the pore mouth area equal to $7.07 \times 10^{-14} \text{ cm}^2$. The pore number depends on GSA^{SEM} of the H₁-e Pd film, thus different diameters of substrate Pt disc electrodes ($d = 25, 50$ and $250 \mu\text{m}$) were used to investigate the effect of the pore number on the RSA^{Theor} . The internal pore wall area depends on the H₁-e Pd film thickness, which was mentioned in equation 3.4, hence a uniform deposition charge density j of 5.09 C cm^{-2} was applied on the substrate electrodes to maintain the H₁-e Pd film thickness. **Table 3.4** shows the RSA^{Theor} and RSA^{CV} with different GSA for H₁-e Pd films onto Pt disc electrodes ($d = 25, 50$ and $250 \mu\text{m}$), which evidence that there is a relatively good agreement observed between RSA^{Theor} and RSA^{CV} . In addition, the

expansion of GSA leads to increase the unit cells number of the Pd nanostructured and then improves the H_1 -e Pd electrode surface features.

Table 3.4: Comparison between Theoretical and experimental electroactive areas for H_1 -e Pd films deposited on different Pt discs.

H_1 -e Pd film ($C_{16}EO_8$)	GSA^{SEM} (cm^2)	No. of the pores	RSA^{Theor} (cm^2)	GSA^{CV} (cm^2)	RSA^{CV} (cm^2)
$Q_{dep} = 25 \mu C$ onto Pt ($d = 25 \mu m$)	1.36×10^{-5}	4.36×10^7	6.2×10^{-3}	1.6×10^{-5}	5.4×10^{-3}
$Q_{dep} = 100 \mu C$ onto Pt ($d = 50 \mu m$)	2.09×10^{-5}	6.69×10^7	9.5×10^{-3}	2.94×10^{-5}	8.9×10^{-3}
$Q_{dep} = 2500 \mu C$ onto Pt ($d = 250 \mu m$)	5.13×10^{-4}	1.64×10^9	2.3×10^{-1}	5.92×10^{-4}	6.2×10^{-2}

3.9. H₁-e Pd electrode erosion

Although the Pd nanostructure film improves the working electrode performance by increasing the interface area, this increase also promotes the rate of corrosion of the electrode surface. One of the interesting issues in the H₁-e Pd film deposition processes is the disappearance of the film after use; this was observed in both palladium structured films prepared whether by C₁₆EO₈ or Brij[®] 56. **Figure 3.9** shows the SEM images of one of the H₁-e Pd film microdisc electrodes before and immediately after the deposition process, and how subsequent experiments, such as hydrogen loading and characterization via cyclic voltammetry in acid, result in the cracking and then disappearance of the film.

This phenomenon has been attributed to physical and electrochemical processes during the initial characterization of the H₁-e Pd film. The physical process occurs during the hydrogen absorption/desorption into the H₁-e Pd film to form palladium hydride, where periodic expansion and contraction of the thin nanostructure palladium film volume lead to stress on the film and cause protrusions and cracks, equivalent to the Nowakowski *et al.* observation [154]. The electrochemical corrosion starts at 0.1 V vs. SMSE; sweeping beyond this potential leads to the dissolution of the Pd nanostructure [80, 145, 155, 156]. Juodkazis *et al.* estimated 1.0 – 1.5 μg/cm² of a plain Pd will be dissolved electrochemically during a single anodic/cathodic cycle [148]. In this project, the working electrodes are mesoporous nanostructured electrodes, therefore more sensitive to the corrosion as they have a massive interface area in comparison to plain Pd electrodes.

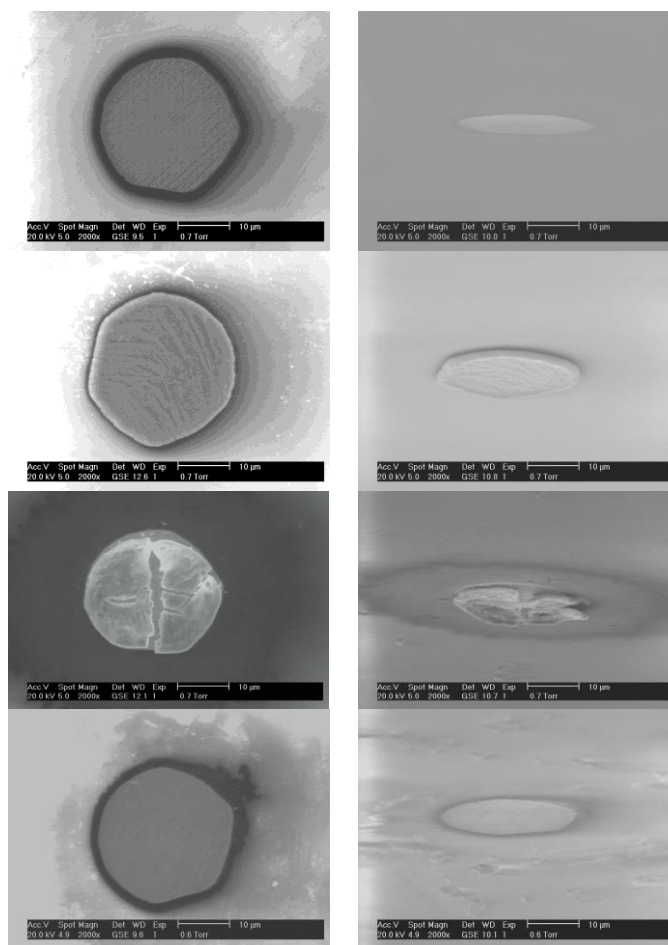


Figure 3.9: Scanning electron microscopy images with scale bar = 10 μm of a $\text{H}_1\text{-e Pd}$ film ($Q_{\text{dep}} = 10 \mu\text{C}$) deposited onto a polished Pt microdisc electrode ($d = 25 \mu\text{m}$) using C_{16}EO_8 as a surfactant of the mixture. The images show the same microdisc electrode. Top row shows the microdisc electrode before deposition process of $\text{H}_1\text{-e Pd}$ film, the second row shows the film directly after the deposition. The third row shows the cracking in the film following experiments. The last row shows the disappearance of the $\text{H}_1\text{-e Pd}$ film leaving the bare substrate Pt microdisc electrode. The tilt angle of the right column is 70° and 0° in the left column.

Figure 3.10 shows the palladium Pourbaix diagram for a wide range of potentials vs. SHE and *pH* [157]. The diagram shows the conditions in which a combination of potential and *pH* will result in the corrosion of the palladium film. Pourbaix diagram of Pd is in good agreement with previous observations as the study of the H₁-e Pd film by cyclic voltammetry between -0.65 and +0.65 V vs. SMSE in 1 M sulphuric acid at room temperature, showed corrosion in the same region as seen in the Figure between +1.4 and +0.8 V vs. SHE at *pH*.

The electrochemical dissolution effect can be decreased by using the minimum number of cycles (2 or 3 anodic-cathodic cycles) to study the electrode properties, and avoiding repeatedly cycling the H₁-e p film into the oxide formation region [80].

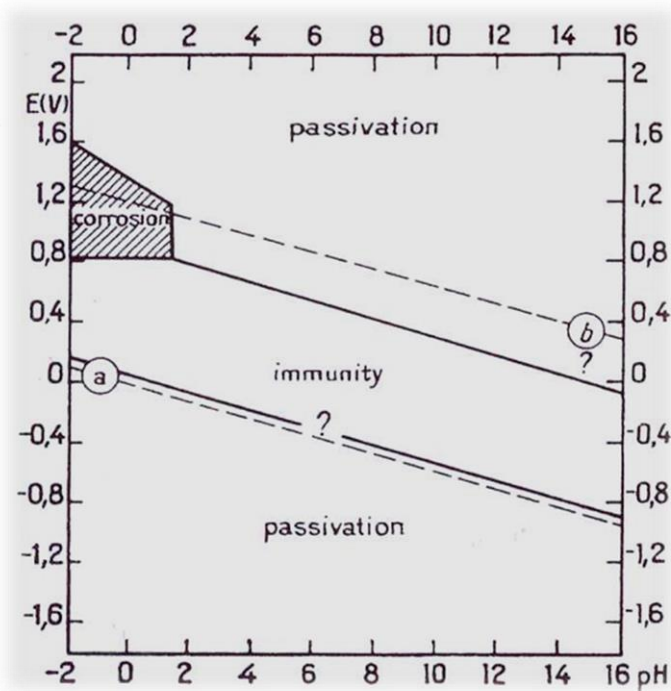


Figure 3.10: Theoretical domains of corrosion, immunity and passivation of palladium, at 25° C reproduced from [157].

3.10. Summary

In this chapter, the preparation and characterization a range of H₁-e Pd films have been done including the chronoamperometry of the deposition process, and the controlling of the H₁-e Pd film thickness by the deposition charge.

The surface features of the H₁-e Pd film were compared against of a similar diameter of: a plain Pd film, a polished Pt and a polished Pd electrodes. These comparisons have been done using SEM images and by cyclic voltammetry to observe the differences in the geometric areas of the electrodes. Then the real interface areas of these electrodes were compared via acid cyclic voltammetry; this clearly displays the surface improvement that can be achieved using the nanostructured film, even though other electrodes have similar or larger geometric area.

The corrosion conditions of H₁-e Pd films have been stated to avoid the possible erosion of the Pd nanostructure during the lab work.

The next chapter will be show the sensing of *pH* with the H₁-e Pd films including hydrogen loading. The Pd nanostructure will be used to probe the *pH* of different solutions such as buffers, artificial brain fluid and real brain fluid.

Page intentionally left blank

Chapter 4. *pH* sensing in synthetic and real brain fluid with nanostructured palladium hydride electrode

For the H₁-e Pd hydride electrode to be used as a *pH* sensor of brain fluid, the Pd nanostructure needs to be loaded with hydrogen. Once loaded, the H₁-e Pd film works as a solid state reservoir of hydrogen, as the hydrogen is free to move in and out of the palladium lattice [8-10, 158]. In this chapter, PdH created both potentiostatically and galvanostatically will be shown. Hydrogen loading into the H₁-e Pd film will be studied in a well-known solution of 0.5 M Na₂SO₄ + H₂SO₄ (*pH* 1.88) before proceeding to biological solutions. This is done to observe the electrochemical behaviour of the H₁-e Pd film during the hydrogen loading and *pH* sensing.

The potentials and currents that will be used to insert hydrogen into the H₁-e Pd film will be determined. This will be followed with a chronopotentiometric measurement to estimate the *pH* of the solution from the measured potential via conversion with the Nernst (equation 1.29).

4.1. Loading and stripping potentials

The potential will be applied as a driving force onto the H₁-e Pd film to insert hydrogen into the palladium nanostructure, while the hydrogen stripped from the palladium nanostructure after the loading process will enable the measurement of the amount of hydrogen inserted into the H₁-e Pd film. Cyclic voltammetry in a test solution will be employed to identify the loading and stripping potentials.

4.1.1. The electrochemical behavior of H₁-e Pd film in cyclic voltammetry

The loading potential E_{load} can be identified initially by the cyclic voltammogram of the H₁-e Pd film in 0.5 M Na₂SO₄ + H₂SO₄ solution (pH 1.88) as a test solution of hydrogen loading [8]. This solution was used to avoid the corrosion of the H₁-e Pd film that occurs when cyclic voltammetry is carried out in acid ($pH = 0$), as mentioned in **Figure 3.10**. **Figure 4.1** shows the cyclic voltammetry of H₁-e Pd film in the stated solution.

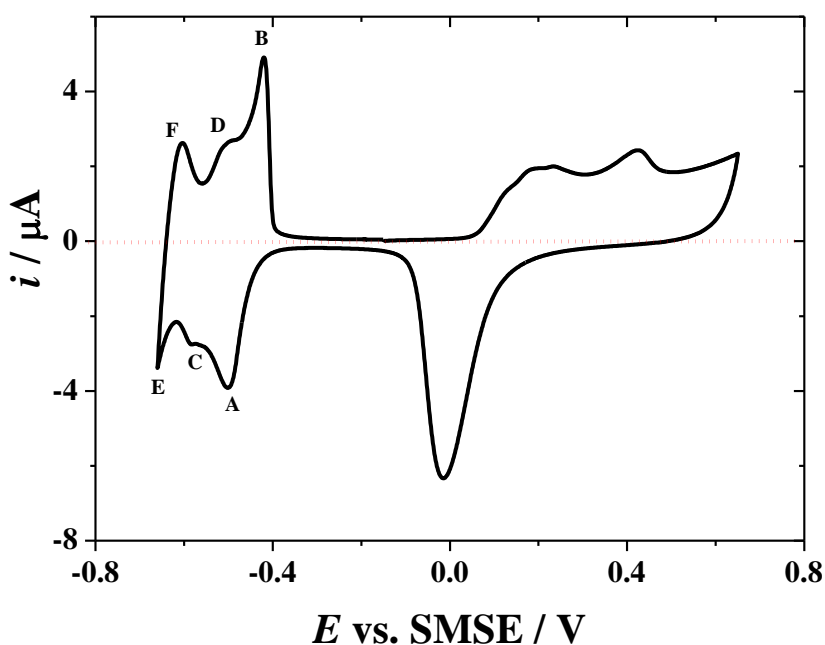


Figure 4.1: A typical cyclic voltammogram of H₁-e Pd film ($Q_{dep} = 2500 \mu C$), deposited onto a 250 μm diameter Pt disc electrode. The voltammogram was recorded at scan rate $v = 20 \text{ mV s}^{-1}$ in 20 ml of 0.5 M Na₂SO₄ + H₂SO₄ solution (pH 1.88), purged with argon for 20 minutes at room temperature. The three pairs of peaks correspond to; A and B hydrogen adsorption and desorption process, C and D hydrogen absorption to form and strip the PdH α phase, and E and F correspond to the same process as peaks C and D but for the PdH β phase.

The cyclic voltammetry was carried out using a wide potential region in 0.5 M Na₂SO₄ + H₂SO₄ solution (*pH* 1.88), in order to illustrate the processes of surface oxidation, hydrogen surface adsorption and absorption into the palladium nanostructure.

It can be observed that the shape of the voltammogram shown in **Figure 4.1** corresponds to that of **Figure 3.7** which was carried out in 1 M H₂SO₄ (*pH* = 0). However, the peaks have been shifted negative compared to the voltammetry in acid because of the variation in *pH* between the measured solutions.

The voltammogram peaks of the electrochemical processes can be identified according to the discussion of cyclic voltammetry in acid in section 3.6. The formation of Pd surface oxide can be seen from about +0.03 V vs. SMSE in the forward (cathodic) sweep, and the oxide stripping process appears as a sharp peak in the reverse sweep between +0.25 and -0.15 V vs. SMSE.

Moreover, the voltammogram shows a long double layer region between about -0.35 and +0.03 V in the reverse sweep, and between about -0.35 and -0.15 V vs. SMSE in the forward scan.

Additionally, the hydrogen adsorption and absorption region appears in the potential range after about -0.35 V vs. SMSE in the reverse scan. **Figure 4.1** shows three pairs of peaks; A and B (shown between -0.50 and -0.42 V) reflect hydrogen adsorption and desorption process, C and D (shown between -0.59 and -0.50 V) correspond to hydrogen absorption to form and strip the PdH α phase, and E and F (shown between -0.66 and -0.61 V) correspond to the same process as peaks C and D but for the PdH β phase.

The clarity of the current wave with non-overlapping peaks helps decide the loading potential. Hydrogen region peaks (e.g. A) have been shown to be sharper in the acid voltammogram than in 0.5 M Na₂SO₄ + H₂SO₄ solution (*pH* 1.88) voltammetry. Therefore **Figure 4.2** shows the cyclic voltammetry that has been done in the hydrogen region between -0.15 to -0.70 V vs. SMSE to avoid any effects from other electrochemical processes.

Figure 4.2 shows how a shorter potential range results in more defined peaks of the voltammogram. Peak A is shown to be broader in the large potential range of the

complete voltammogram between +0.65 to -0.70 V, than when just the hydrogen region is scanned between -0.15 to -0.70 V. This means that the scanning of the potential through the surface oxide region affects the current peaks (including peak A). This is consistent with the results of Imokawa, who suggested that there is potentially an interference with the adsorption of impurities and the hydrogen adsorption [8].

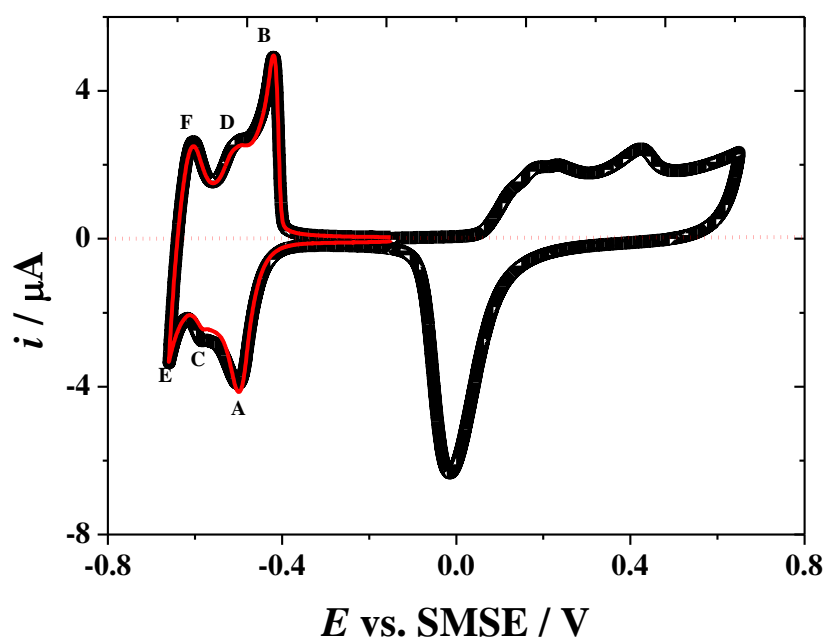


Figure 4.2: Cyclic voltammograms of H_{1-e} Pd film ($Q_{\text{dep}} = 2500 \mu\text{C}$), deposited onto a 250 μm diameter Pt disc electrode. The voltammograms were recorded at scan rate $\nu = 20 \text{ mV s}^{-1}$ in 20 ml of 0.5 M $\text{Na}_2\text{SO}_4 + \text{H}_2\text{SO}_4$ solution ($\text{pH } 1.88$), purged with argon for 20 minutes at room temperature. The CVs recorded between -0.15 and -0.70 V (the red line) and between +0.65 to -0.70 V (the black line).

The scan rate is another factor that can broaden the current peaks. **Figure 4.3** shows four voltammograms with various scan rates; 10, 20, 40, 100 mV s^{-1} . It can be seen from the voltammograms that the effect of increasing the scan rate is to further broaden the peaks as they overlap. As expected for the voltammetry of adsorbed species the peak currents are proportional to the scan rate.

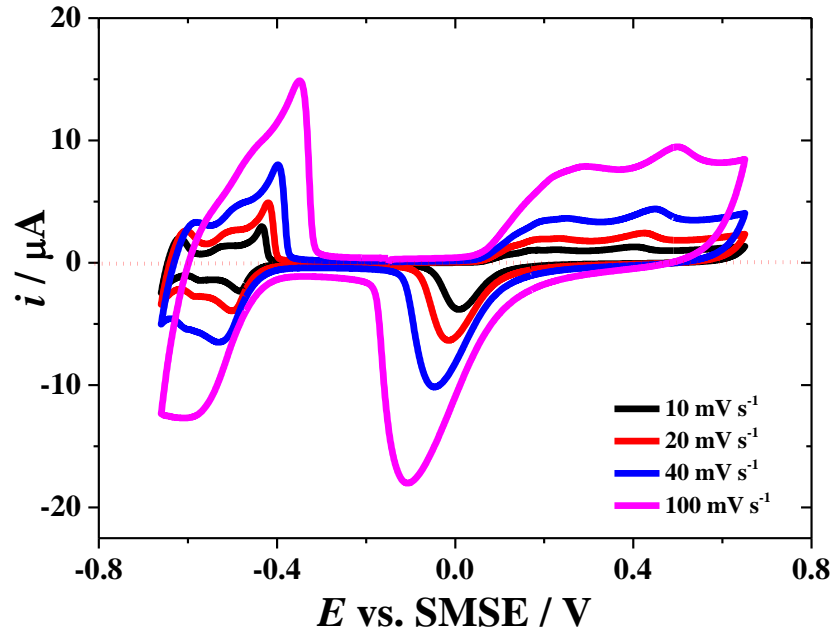


Figure 4.3: Cyclic voltammograms of H₁-e Pd film ($Q_{\text{dep}} = 2500 \mu\text{C}$), deposited onto a 250 μm diameter Pt disc electrode. The voltammograms were recorded in 20 ml of 0.5 M Na₂SO₄ + H₂SO₄ solution (pH 1.88), purged with argon for 20 minutes, scan rate $\nu = 10, 20, 40, 100 \text{ mV s}^{-1}$.

Moreover, the increasing scan rate causes the peaks to shift to more positive values for the forward sweep and to more negative values for the reverse sweep. This has been attributed to the pH contrast inside the H₁-e Pd pores [8], because H⁺ consumption via the cathodic reaction will lead to a local increase in pH , and the formation of Pd-H. This is shown in the following equations:



$$E_{\text{H}^+, \text{Pd-H}} = E^o + \frac{RT}{F} \ln \frac{a_{\text{H}^+}}{a_{\text{Pd-H}}} \quad 4.2$$

$$E_{\text{H}^+, \text{Pd-H}} = E^o - 0.059 \text{pH} - 0.059 \log a_{\text{Pd-H}} \quad 4.3$$

Likewise, palladium oxide reduction affects the local pH as follows:



$$E_{\text{PdO,Pd}} = E^{\circ} + \frac{RT}{F} \ln a_{\text{H}^+} \quad 4.5$$

$$E_{\text{PdO,Pd}} = E^{\circ} - 0.059 \text{ pH} \quad 4.6$$

Equation 4.3 and equation 4.6 show clearly how pH changes within $\text{H}_1\text{-e Pd}$ pores affect the equilibrium potential. As a result, at higher scan rate (e.g. 100 mV s^{-1}) the peaks for hydrogen adsorption and α phase absorption overlap, and the peak for the surface oxide stripping becomes broader and shifts negatively toward the hydrogen region. Similarly, the anodic peaks incur a positive shift, because of the decrease in pH due to H^+ generated during palladium hydride dissociation and surface oxide formation, as mentioned in equation 4.1 and equation 4.4.

Therefore in the following cyclic voltammetric studies, the hydrogen region will be scanned at 20 mV s^{-1} to avoid the complications discussed above.

The hydrogen absorption into $\text{H}_1\text{-e Pd}$ film was studied in the hydrogen region using various potential ranges. The initial potential E_{in} was chosen from the double layer region where faradic current = 0 A (-0.15 V vs. SMSE), while the final potential E_{fin} was negatively increased from -0.65 V to -1.00 V vs. SMSE in -0.050 V increments.

The working electrode was a fresh $\text{H}_1\text{-e Pd}$ film ($Q_{\text{dep}} = 2500 \mu\text{C}$), deposited onto a $250 \mu\text{m}$ diameter Pt disc electrode; all the voltammograms were done at 20 mV s^{-1} and recorded in a deaerated $0.5 \text{ M Na}_2\text{SO}_4 + \text{H}_2\text{SO}_4$ solution ($pH 1.88$) at room temperature.

Figure 4.4 shows eight voltammograms with the lower vertex potential in the hydrogen region so as to include hydrogen adsorption, hydrogen absorption to form the α and β phases and hydrogen evolution.

The hydrogen adsorption peak is marked by A at -0.50 V, whilst the peak of the α PdH phase has been marked by C. A large reduction current peak E has appeared at -0.90 V which reflects the hydrogen PdH β phase absorption. This is followed by the beginning of hydrogen gas evolution from about -0.95 V.

On the reverse (anodic) scan, an anodic shoulder has been marked by H corresponds to the oxidation of H_2 that has evolved. F and D peaks are the peaks of β and α phases hydrogen stripping respectively. These two peaks then overlap and are united as a single large oxidation peak (F + D peak). This overlapping of F and D oxidation peaks can be attributed to the massive current for the stripping of the β phase, which dominates the oxidation peaks as E_{fin} becomes more negative.

The β phase stripping peak becomes more positive as the charge increases; this may reflect the rise in proton concentration leading to a drop in pH within the pores of the nanostructured Pd. Finally, the peak for hydrogen desorption from the H_{1-e} Pd surface is marked by B.

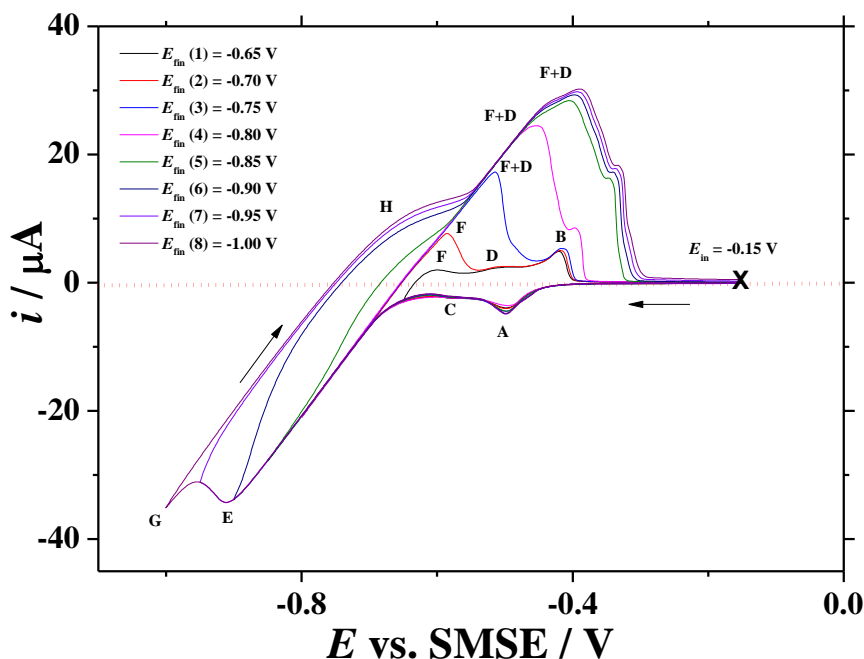


Figure 4.4: Cyclic voltammograms of H_{1-e} Pd film ($Q_{\text{dep}} = 2500 \mu\text{C}$), deposited onto a 250 μm diameter Pt disc electrode. The voltammograms were recorded between the initial potential $E_{\text{in}} = -0.15 \text{ V}$ and final potential E_{fin} vs. SMSE, in 20 ml of 0.5 M $\text{Na}_2\text{SO}_4 + \text{H}_2\text{SO}_4$ solution ($\text{pH} 1.88$) at 20 mV s^{-1} , purged with argon for 20 minutes. The current peaks are: (A and B) hydrogen adsorption and desorption, (C and D) the hydrogen absorption / extraction to form and strip the α phase, E hydrogen absorption for the β phase, F hydrogen desorption from the β phase, (F+D) is the overlapping between the stripping of α and β phases. (G and H) evolution / oxidation of H_2 that has evolved.

Table 4.1 shows the resulting loading charge Q_{load} and stripping charge Q_{strip} for hydrogen adsorption and α phase formation measured for the different voltammograms shown in **Figure 4.4** up to $E_{\text{fin}} = -0.90 \text{ V}$ vs. SMSE, the stripping charge is, within experimental error, equal to the loading charge. This indicates that up to this potential all the charge is used to absorb hydrogen and form the Pd hydride. When $E_{\text{fin}} < -0.90 \text{ V}$ vs. SMSE the stripping charge becomes smaller than the loading charge. This suggests that the remaining part of Q_{load} corresponds to H_2 evolution.

Table 4.1: The comparison of loading charge Q_{load} and stripping charge Q_{strip} for the current waves in the potential ranges between $E_{\text{in}} = -0.15$ V and E_{fin} , where $Q_{\text{max load}}$ is the maximal loading charge required to complete the formation of the β phase up to the atomic ratio of H/Pd = 0.6.

E_{fin} vs. SMSE / V	$Q_{\text{load}} / \text{C}$	$Q_{\text{load}} / Q_{\text{max load}}$	$Q_{\text{strip}} / \text{C}$	$ Q_{\text{load}} / Q_{\text{strip}} $
-0.65	-30.1×10^{-6}	0.06	27.7×10^{-6}	1.09
-0.70	-48.2×10^{-6}	0.10	45.4×10^{-6}	1.06
-0.75	-99.5×10^{-6}	0.21	96.6×10^{-6}	1.03
-0.80	-185×10^{-6}	0.40	181×10^{-6}	1.02
-0.85	-288×10^{-6}	0.62	284×10^{-6}	1.01
-0.90	-359×10^{-6}	0.77	332×10^{-6}	1.08
-0.95	-468×10^{-6}	1.00	353×10^{-6}	1.32
-1.00	-618×10^{-6}	1.32	371×10^{-6}	1.67

The amount of hydrogen (hydrogen moles) inside the nanostructured palladium can be estimated mathematically using the following equation:

$$Q = mnF \quad 4.7$$

where Q is the hydrogen loading or stripping charge and m is the hydrogen amount in moles, inserted into or extracted from the $\text{H}_{1\text{-e}}$ Pd film.

The largest quantity of hydrogen in the $\text{H}_{1\text{-e}}$ Pd film can be found from the maximal charge $Q_{\text{max load}}$ in equation 4.7. $Q_{\text{max load}}$ can be calculated using the loading charge before the start of hydrogen gas evolution to avoid any interference with hydrogen evolution charge (at potential range between -0.15 and -0.95 V vs. SMSE). $Q_{\text{max load}}$ has been found to be $-467.8 \mu\text{C}$ for Pd nanostructure film ($Q_{\text{dep}} = 2500 \mu\text{C}$) deposited onto a $250 \mu\text{m}$ diameter Pt disc electrode.

4.1.2. The potentiostatic loading of hydrogen

The potentiostatic loading of hydrogen via potential step, will be used to insert hydrogen into a fresh H₁-e Pd film ($Q_{\text{dep}} = 2500 \mu\text{C}$), deposited onto a 250 μm diameter Pt disc electrode in 0.5 M Na₂SO₄ + H₂SO₄ solution (pH 1.88). Initially, the potential was held in the double layer region to ensure the system was at equilibrium; typically the potential was stepped from the starting (or stripping) potential E_{strip} (-0.15 V where faradic current = 0 A) to the loading potentials E_{load} for loading time t_{load} until the hydrogen reached a H/Pd ratio of 0.6 into the nanostructured. The current was measured during t_{load} whilst loading the hydrogen.

The resulting chronoamperogram can be analysed in terms of the progress of the H/Pd through the different PdH phases [8, 9]:

- (i) $0 < \text{H/Pd} < 0.02$: A rapid decline in the current corresponds to hydrogen adsorption followed by hydrogen absorption to form the α phase ($\text{H/Pd} = 0.02$).
- (ii) $0.02 < \text{H/Pd} < 0.6$: A long plateau of stable current corresponds to the insertion of hydrogen in convert the α phase into the β phase. The $\alpha+\beta$ transition lasts until the hydrogen loading is completed at the end of t_{load} , when the β phase is reached ($\text{H/Pd} = 0.6$).
- (iii) $\text{H/Pd} > 0.6$: The current increases gradually when the β phase is complete and then it stabilises to create another plateau where the current $\neq 0$ A; this is a reflection of hydrogen gas evolution.

To analyse the amount of hydrogen inserted, a linear sweep is used to strip the hydrogen from the nanostructure. It is worth mentioning that the hydrogen stripping sweep is not performed when measuring the pH , but is used just to know the amount of hydrogen inserted into the H₁-e Pd film without hydrogen evolution charge. The hydrogen stripping is carried out by sweeping from E_{load} to E_{strip} with scan rate $v = 10 \text{ mV s}^{-1}$. This produces a current peak which once integrated yields Q_{strip} . The amount of hydrogen extracted can be estimated from the charge for hydrogen extraction Q_{strip} and equation 4.7. The stripping peak includes the extraction of hydrogen from the α and β

phases and from the desorption of hydrogen from the surface. **Figure 4.5** shows the combination of loading and stripping chronoamperograms.

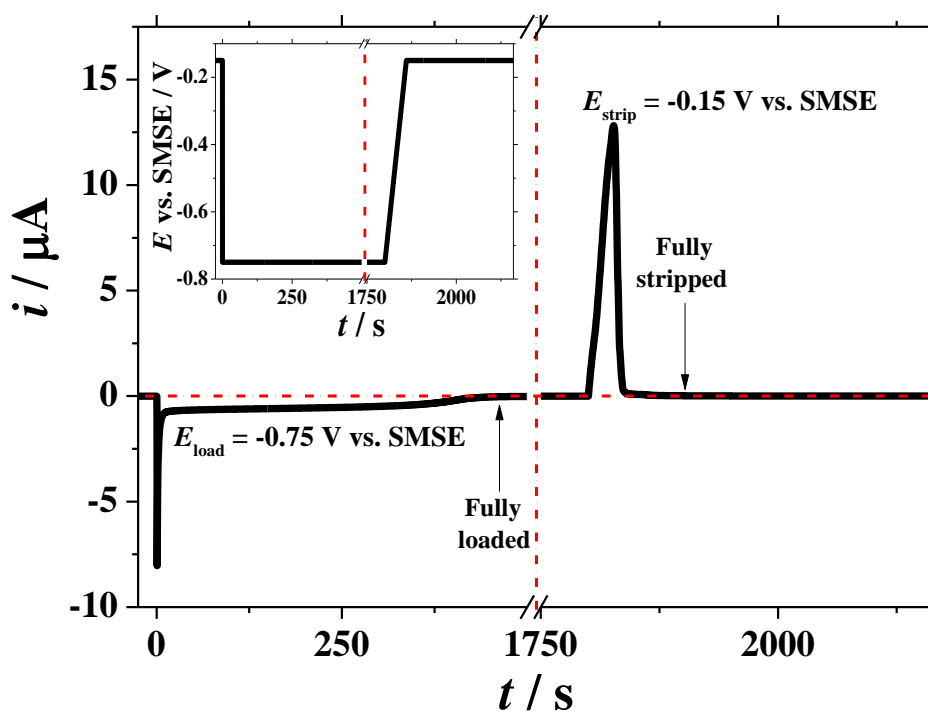


Figure 4.5: Chronoamperogram for the loading and stripping of hydrogen into a H_{1-e} Pd film ($Q_{\text{dep}} = 2500 \mu\text{C}$), deposited onto a $250 \mu\text{m}$ diameter Pt disc electrode. Data recorded in a solution of 20 ml of 0.5 M $\text{Na}_2\text{SO}_4 + \text{H}_2\text{SO}_4$ solution (pH 1.88) at room temperature, purged with argon for 20 minutes; the stripping potential $E_{\text{strip}} = -0.15 \text{ V}$ and the loading potential $E_{\text{load}} = -0.75 \text{ V}$ vs. SMSE; the potential was stepped from E_{strip} to E_{load} and held for t_{load} then it was swept from E_{load} to E_{strip} at a scan rate $v = 10 \text{ mV s}^{-1}$. The insert shows the potential waveform used to load and extract hydrogen to and from the Pd nanostructure.

Chronoamperometric comparison was done using various loading potentials to study their effect on the potentiostatic hydrogen loading process, and to help to choose a typical E_{load} : a potential too positive will make the hydrogen loading period t_{load} too long to reach the required PdH atomic ratio at $\text{H/Pd} = 0.6$. On the other hand, an extreme

negative E_{load} will generate immoderate evolution of H_2 gas on the electrode surface, which could potentially damage the $\text{H}_1\text{-e Pd}$ film.

Figure 4.6 shows a comparison between nine loading potentials E_{load} between -0.65 V and -0.85 V vs. SMSE with -0.025 V increments. For the comparison between the loading potentials, E_{load} was stepped for $t_{\text{load}} = 1800$ s in all the chronoamperograms. The current transient curves have similar shapes in the hydrogen adsorption and α phase absorption regions. However, the loading time t_{load} which is the time required to complete β phase loading decreases as E_{load} drops below -0.725 V, with t_{load} that taking more than 1800 s if $E_{\text{load}} \geq -0.725$ V. This is because the negative potential of the electrode is the driving force for the insertion of H^+ from the solution into $\text{H}_1\text{-e Pd}$ film. Moreover, it can be noted that the second current plateau shows greater current reflecting a higher rate of H_2 gas evolution as E_{load} becomes more negative.

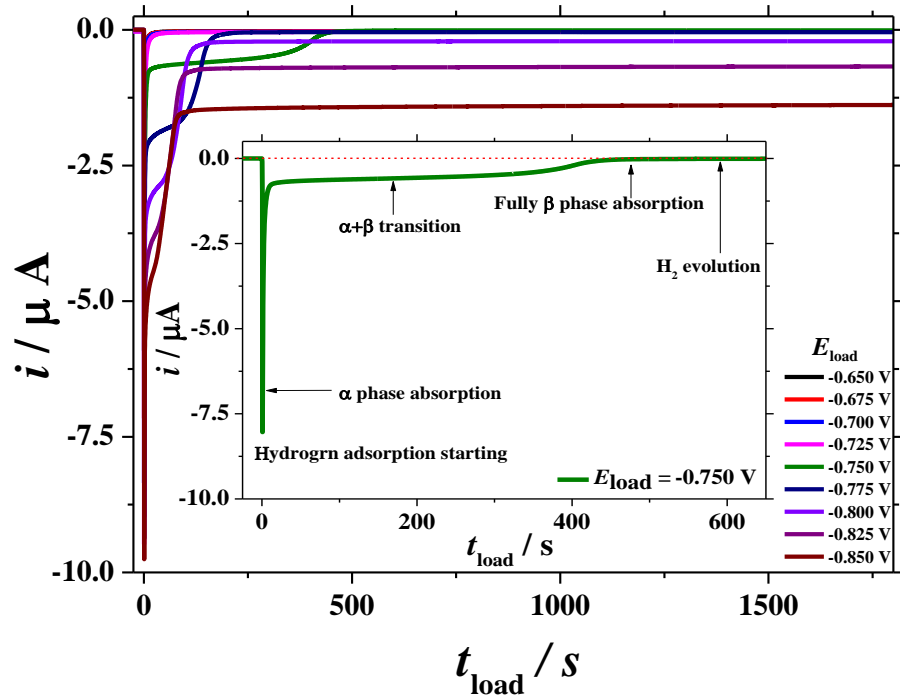


Figure 4.6: Hydrogen loading chronoamperograms into H₁-e Pd film ($Q_{\text{dep}} = 2500 \mu\text{C}$), deposited onto a 250 μm diameter Pt disc electrode in a deaerated solution of 20 ml 0.5 M $\text{Na}_2\text{SO}_4 + \text{H}_2\text{SO}_4$ solution (pH 1.88) at room temperature, the potential was stepped at $t = 0 \text{ s}$ from the starting potential = -0.15 V to a range of loading potential E_{load} between -0.65 and -0.85 V vs. SMSE. The insert shows the chronoamperogram when $E_{\text{load}} = -0.750 \text{ V}$.

The duration of t_{load} tends to be too long and more than 1800 s when $E_{\text{load}} \geq -0.725 \text{ V}$ vs. SMSE. However, it decreases as the E_{load} shifts more negative. Moreover, as E_{load} shifts below -0.725 V the combined adsorption and absorption charge Q_{load} tends to increase. Q_{load} appears to go through a maximum $-2.40 \times 10^{-4} \text{ C}$ at $E_{\text{load}} = -0.775 \text{ V}$. Furthermore, the charge for hydrogen gas evolution Q_{H_2} which was estimated by integrating the current for the second plateau is also influenced by E_{load} , as E_{load} becomes more negative.

The ideal E_{load} is that providing a high rate of hydrogen loading into the H₁-e Pd film to reach H/Pd=0.6. This requires a very negative E_{load} but a very negative E_{load} will induce the unwanted hydrogen gas evolution, which can destroy the H₁-e Pd film [9]. Therefore, an E_{load} of -0.750 V vs. SMSE was chosen from **Table 4.2** to load the hydrogen into the nanostructure; this will provide the lowest possible Q_{H_2} (1.39×10^{-5} C) to avoid the damage of the H₁-e Pd film within a reasonable t_{load} (475 s).

Table 4.2 shows the effect of varying the loading potentials E_{load} on: the loading time t_{load} , the loading charge Q_{load} , and the charge for hydrogen gas evolution Q_{H_2} . The maximum loading time was used $t_{\text{load}} = 1800$ s to compare between the varying loading potentials, when the potential was stepped from the starting potential $E_{\text{strip}} = -0.15$ V at $t = 0$ s to a range of loading potential E_{load} between -0.65 and -0.85 V vs. SMSE as stated in **Figure 4.6**.

Table 4.2: Dependence of the loading time t_{load} , loading charge Q_{load} and hydrogen evolution charge Q_{H_2} on the loading potential E_{load} . The hydrogen was loaded into H₁-e Pd film ($Q_{\text{dep}} = 2500 \mu\text{C}$), deposited onto a 250 μm diameter Pt disc electrode, in a deaerated solution of 0.5 M Na₂SO₄ + H₂SO₄ solution (pH 1.88) at room temperature. Other conditions as stated in **Figure 4.6**.

E_{load} vs. SMSE / V	t_{load} / s	Q_{load} / C	Q_{H_2} / C
-0.650	> 1800	-9.96×10^{-6}	4.74×10^{-5}
-0.675	> 1800	-1.16×10^{-5}	4.22×10^{-5}
-0.700	> 1800	-1.33×10^{-5}	6.22×10^{-5}
-0.725	> 1800	-2.36×10^{-5}	5.81×10^{-5}
-0.750	475	-2.29×10^{-4}	1.39×10^{-5}
-0.775	200	-2.40×10^{-4}	6.93×10^{-5}
-0.800	160	-2.34×10^{-4}	3.74×10^{-4}
-0.825	100	-2.24×10^{-4}	1.23×10^{-3}
-0.850	85	-2.20×10^{-4}	2.48×10^{-3}

Figure 4.5 shows the hydrogen stripping peak at $t = 1800$ s recorded by ramping up the potential from $E_{\text{load}} = -0.750$ V to the $E_{\text{strip}} = -0.15$ V vs. SMSE after loading hydrogen

into the H₁-e Pd film. The stripping peak is a combination of three overlapping peaks: extraction of H from the PdH β (H_β) and α (H_α) phases and stripping of hydrogen adsorbed (H_{ads}) on the surface of the H₁-e Pd film. These stripping peaks can be studied by reducing the loading charge Q_{load} by varying E_{load} while keeping t_{load} constant.

The loading potentials were determined from the cyclic voltammograms in **Figure 4.4**. Loading was compared using E_{load} between -0.500 V and -0.525 V for hydrogen adsorption H_{ads}, -0.600 V and -0.625 V for PdH α phase hydrogen absorption H_α, and -0.700 and -0.725 V for PdH β phase hydrogen absorption H_β.

Figure 4.7 shows the resulting stripping peaks after potentiostatically loading hydrogen for 1800 s into H₁-e Pd film ($Q_{dep} = 2500 \mu\text{C}$), deposited onto a 250 μm diameter Pt disc electrode in a deaerated solution of 20 ml 0.5 M Na₂SO₄ + H₂SO₄ solution (*pH* 1.88) at room temperature. The hydrogen was stripped from the palladium nanostructure by sweeping from the loading potentials E_{load} to the stripping potential $E_{strip} = -0.15 \text{ V}$ vs. SMSE with a scan rate $\nu = 10 \text{ mV s}^{-1}$.

Figure 4.7 shows a single stripping peak when using $E_{load} = -0.500 \text{ V}$ and -0.525 V from the hydrogen adsorption region. As they are before what is required to start the hydrogen absorption, the peak reflects the stripping of hydrogen adsorbed on the surface H_{ads}. The stripping peak continues to grow with further negative potential from -0.500 to -0.525 V presumably because the adsorption driving force increases and also because more time is spent in the adsorption region while sweeping.

The second chosen pair of loading potentials was -0.600 V and -0.625 V; these are located in the PdH α phase hydrogen absorption region. **Figure 4.7** shows that the stripping wave starts dividing into double peaks. The first peak around -0.55 V (i.e. 6.25 s) increases as E_{load} is made more negative, this confirms that the growing peak reflects the hydrogen extraction of α phase H_α. While the second peak around -0.16 V (i.e. 47.25 s) is stable with a constant stripping charge ($Q_{strip} = 2.11 \times 10^{-6} \text{ C}$) and attributed to the desorption of H_{ads}.

When E_{load} is located in the PdH β phase hydrogen absorption region (at -0.700 V) three stripping peaks appear: one for the extraction of hydrogen from the β phase H_β, circa -0.68 V, another for the extraction of hydrogen from the α phase H_α, circa -0.53 V, and

the last one for the desorption of hydrogen from the surface H_{ads} , -0.15 V. Taking E_{load} to values below -0.725 V increases the driving force for β palladium hydride formation and increases the H_{β} extraction peak making it easier to identify. This confirms that the first peak reflects H_{β} as the nanostructure only becomes saturated with hydrogen when H/Pd approaches = 0.6. While the second and third peaks are stable with their stripping charges Q_{strip} equal to 2.11×10^{-6} C and 1.24×10^{-5} C respectively; this occurs when the H_1 -Pd film surface has a full coverage of H atoms and then when the PdH α phase has reached $H/Pd = 0.02$.

Overall the stripping peaks of the chronoamperograms reflect the amount of hydrogen loaded in the palladium and their sequence reflects the extraction of H_{β} and H_{α} from the PdH, and finally the desorption of H_{ads} from the electrode surface.

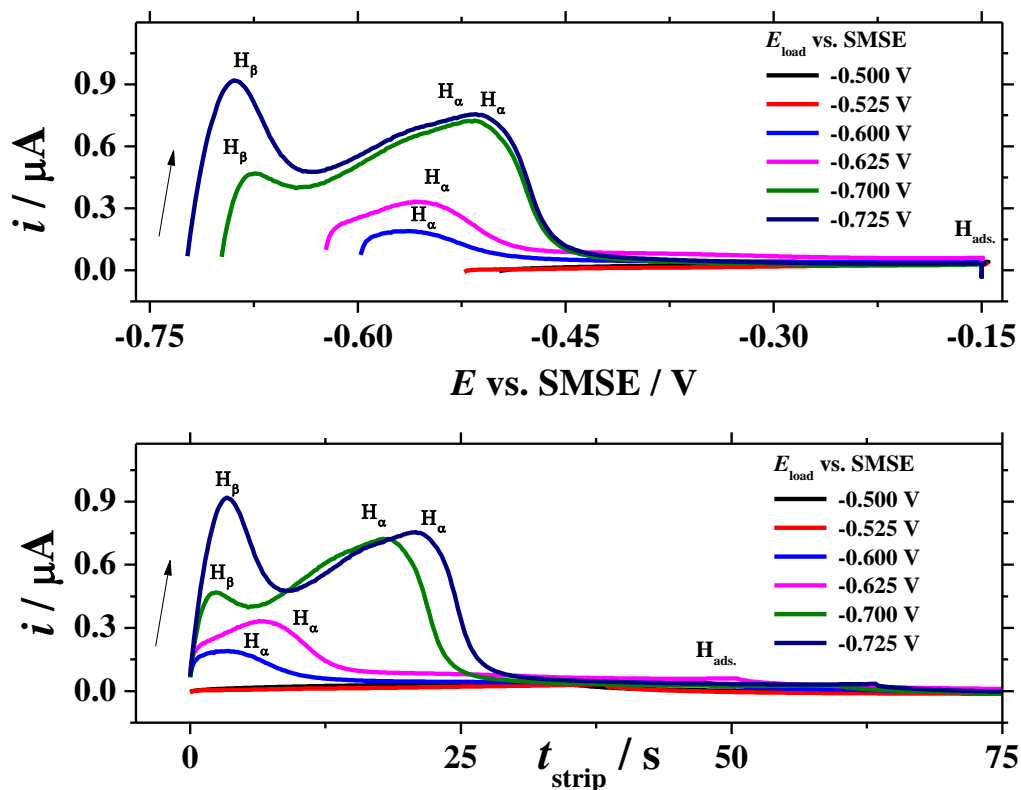


Figure 4.7: Stripping peaks recorded after potentiostatically loading hydrogen for 1800 s into H_{1-e} Pd film ($Q_{\text{dep}} = 2500 \mu\text{C}$), deposited onto a 250 μm diameter Pt disc electrode in a deaerated solution of 20 ml 0.5 M Na₂SO₄ + H₂SO₄ solution (pH 1.88) at room temperature; the potential was swept from different loading potentials E_{load} to the stripping potential $E_{\text{strip}} = -0.15 \text{ V}$ vs. SMSE with a scan rate $v = 10 \text{ mV s}^{-1}$. H_{α} , H_{β} and H_{ads} respectively indicate the stripping peaks for hydrogen from the α and β phases and from the surface.

Figure 4.8 shows that the H_{α} and H_{ads} stripping peaks suddenly overlap with the massive H_{β} stripping peak when $E_{\text{load}} \leq -0.725 \text{ V}$. This single peak keeps growing until a maximum stripping charge $Q_{\text{max strip}}$ is reached circa $2.65 \times 10^{-4} \text{ C}$, when the loading potential $E_{\text{load}} \geq -0.825 \text{ V}$. This is in stark contrast with **Figure 4.7** where the three stripping events were clearly distinct.

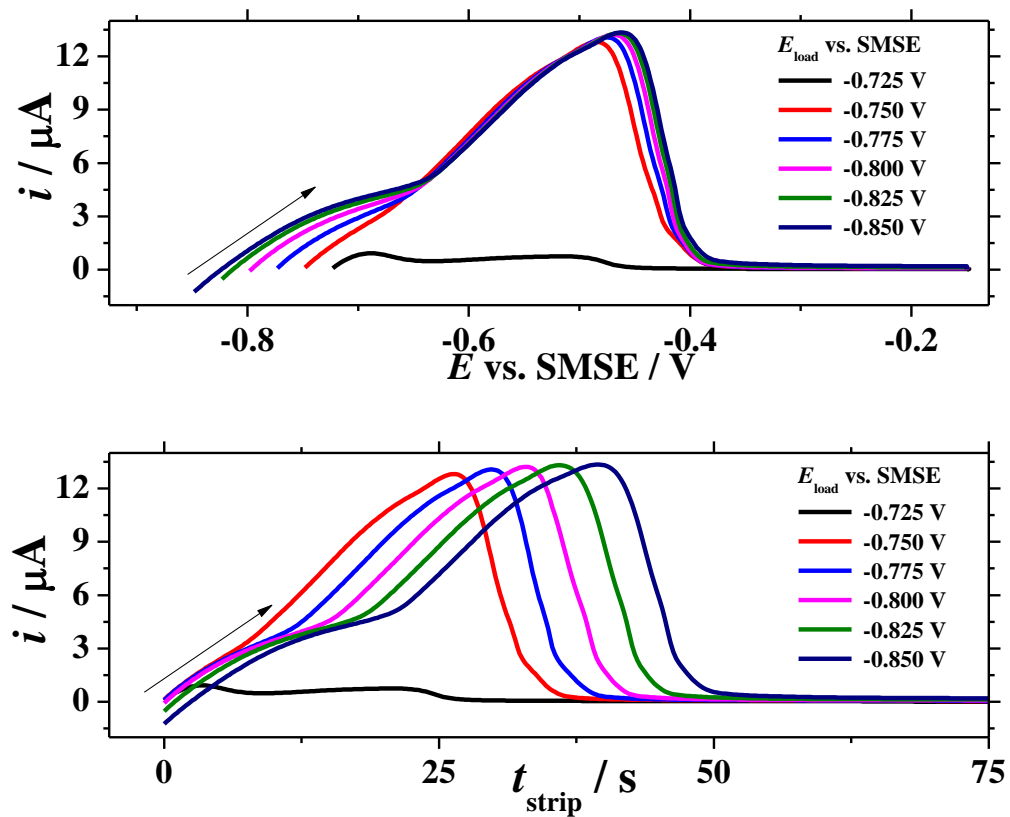


Figure 4.8: Stripping peaks recorded for loading potentials more negative than those used in **Figure 4.7**. All experimental parameters are as shown in **Figure 4.7**.

Table 4.3 summarises the three stripping peaks for the results presented in **Figure 4.7** and **Figure 4.8**.

Table 4.3: Analysis of the hydrogen stripping stages from H₁-e Pd film ($Q_{\text{dep}} = 2500 \mu\text{C}$), deposited onto a 250 μm diameter Pt disc electrode, after potentiostatically loading hydrogen using varying loading potentials E_{load} for 1800 s, in a deaerated solution of 20 ml 0.5 M Na₂SO₄ + H₂SO₄ solution (pH 1.88) at room temperature; the hydrogen was stripped by scanning the potential from E_{load} to the stripping potential $E_{\text{strip}} = -0.15$ V vs. SMSE with a scan rate $v = 10$ mv s⁻¹.

E_{load} vs. SMSE V	$t_{\text{strip}} / \text{s}$			$Q_{\text{strip}} / \text{C}$		
	β PdH	α PdH	H _{ads}	β PdH	α PdH	H _{ads}
-0.500	N/A	N/A	36	N/A	N/A	1.77×10^{-6}
-0.525	N/A	N/A	38	N/A	N/A	2.11×10^{-6}
-0.600	N/A	4	45	N/A	2.30×10^{-6}	2.11×10^{-6}
-0.625	N/A	7	48	N/A	4.91×10^{-6}	2.11×10^{-6}
-0.700	3	18	55	2.12×10^{-6}	1.24×10^{-5}	2.11×10^{-6}
-0.725	4	21	58	6.01×10^{-6}	1.24×10^{-5}	2.11×10^{-6}
-0.750	27	N/A	N/A	2.20×10^{-4}	N/A	N/A
-0.775	30	N/A	N/A	2.39×10^{-4}	N/A	N/A
-0.800	33	N/A	N/A	2.52×10^{-4}	N/A	N/A
-0.825	36	N/A	N/A	2.65×10^{-4}	N/A	N/A
-0.850	39	N/A	N/A	2.65×10^{-4}	N/A	N/A

4.1.3. The galvanostatically loading of hydrogen

The galvanostatic process of hydrogen loading into the H_{1-e} Pd film was carried out successfully by K.-J. Williams [9], who used a constant current as the driving force instead of the potentiostatic loading method. This technique can be implemented by applying the controlled current through the H_{1-e} Pd film while measuring the potential difference between the nanostructured Pd and the reference electrode. The galvanostatic method provides a higher level of control of the $\alpha + \beta$ transition than the potentiostatic method, as the amount of hydrogen loaded into the H_{1-e} Pd film can be directly controlled via the duration of the loading. With the potentiostatic approach it is difficult to control the amount of hydrogen loaded in the $\alpha + \beta$ transition region because the potential is constant during the $\alpha + \beta$ transition for H/Pd ratios between 0.02 and 0.6, and only depends on the activity of H⁺ of the measured solution. With the galvanostatic approach the amount of hydrogen loaded into the H_{1-e} Pd film can be set via the charge passed, i.e. by controlling of the applied current and the duration of the loading. The significance of the degree of loading comes from the reservoir nature of the H_{1-e} Pd film. When fully saturated at H/Pd ratio = 0.6 the lifetime of the *pH* sensor will be at maximum, since the $\alpha + \beta$ transition is located between H/Pd = 0.02 and 0.6.

Figure 4.9 shows an example of galvanostatic hydrogen loading into a H_{1-e} Pd film. Firstly, the nanostructured film was held at open circuit potential where there is no current flowing through the film. Then the loading current i_{load} was applied at loading time $t_{load} = 0$ s to allow the hydrogen to absorb into the H_{1-e} Pd film. i_{load} was applied during t_{load} .

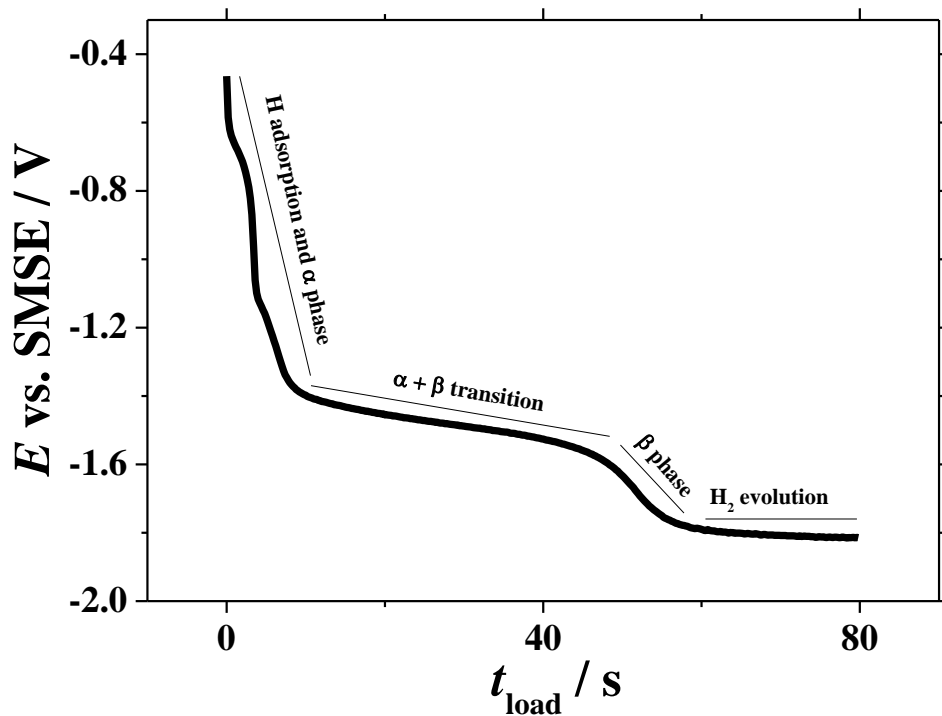


Figure 4.9: A chronopotentiogram for the hydrogen loading at room temperature into a H_1 -e Pd film ($Q_{\text{dep}} = 2500 \mu\text{C}$), deposited onto a $250 \mu\text{m}$ diameter Pt disc electrode in a deaerated solution of 20 ml commercial buffer pH 10 (Fisher Scientific / FB67162), the applied loading current $i_{\text{load}} = 10 \mu\text{A}$.

There is a similarity between the potentiostatic and galvanostatic hydrogen loading processes, thus according to K.-J. Williams, the chronopotentiogram can be divided into four distinct regions depending on the phases and phase transitions of H/Pd ratio [9]:

- (i) t_{load} between 0 and 8.8s: A rapid decline in the potential includes hydrogen adsorption followed by α phase absorption.
- (ii) t_{load} between 8.8 and 46.2 s: The first semi-plateau reflects the $\alpha+\beta$ phase transition region
- (iii) t_{load} between 46.2 and 59.4 s: The potential again decreases until the hydrogen loading is complete and the β phase is reached.
- (iv) $t_{\text{load}} > 59.4$ s: Following the completion of the β phase, the region of hydrogen gas evolution begins.

Hydrogen loading can be done either by the potentiostatic or by the galvanostatic processes, but the galvanostatic hydrogen loading is preferred because the quantity of hydrogen loaded into the H₁-e Pd film can be directly obtained from the loading charge Q_{load} (the loading current i_{load} multiplied by the loading time t_{load}). Moreover, by suitably choosing the loading current galvanostatic hydrogen loading can be done in a shorter period than potentiostatic approach. For example, to load hydrogen into a H₁-e Pd film ($Q_{\text{dep}} = 2500 \mu\text{C}$) deposited onto a 250 μm diameter Pt disc electrode, the galvanostatic process takes 59.4 s with $i_{\text{load}} = 10 \mu\text{A}$, which is 12.5% of the 475 s which the potentiostatic process takes.

4.2. H₁-e Pd film potentiometric response

Section 1.2.2 indicates that the potentiometric measurement of a palladium hydride electrode shows a stable and reproducible potential $E_{\text{Pd-H}}$ during the $\alpha+\beta$ transition ($0.02 \leq \text{H/Pd} \leq 0.6$), since the $E_{\text{Pd-H}}$ is independent of electrode composition during the $\alpha+\beta$ transition and only dependent on the pH . The theoretical $E_{\text{Pd-H}}$ potential can be obtained as stated in equation 1.29:

$$E_{\text{Pd-H}} \text{ V vs. SHE, at } 25^\circ\text{C} = 0.05 - 0.0592 \text{ pH} \quad 1.29$$

where the $E_{\text{Pd-H}} \text{ V vs. SMSE} = E_{\text{Pd-H}} \text{ V vs. SHE} - 0.64 \text{ V}$, thus a H₁-e Pd film can be used as a pH sensor using the obtained potentiometric measurement $E_{\text{Pd-H}} \text{ vs. SMSE}$, to estimate the pH of the solution as follows:

$$pH = \frac{E_{\text{Pd-H}} \text{ vs. SMSE, at } 25^\circ\text{C} + 0.59}{-0.0592} \quad 4.8$$

Figure 4.10 shows $E_{\text{Pd-H}}$ (black line) in a test solution of 0.5 M Na₂SO₄ + H₂SO₄ solution (pH 1.88) at 25° C. The resulting potential $E_{\text{Pd-H}}$ has been monitored between the working electrode and the SMSE reference electrode as stated in section 2.7.2. The working electrode was a fresh H₁-e Pd film ($Q_{\text{dep}} = 2500 \mu\text{C}$) deposited onto a 250 μm diameter Pt disc electrode, which had been loaded with hydrogen until fully saturated. Figure 4.10 can be divided into three parts, due to the dependency of the $E_{\text{Pd-H}}$ on the H/Pd ratio, since the H/ Pd ratio of a saturated H₁-e Pd film (i.e. H/Pd = 0.6) decreases after the $E_{\text{Pd-H}}$ reaches the α phase conditions (H/Pd = 0.02) under the open circuit conditions [8]. This indicates that the hydrogen is extracted during the potentiometric measurement.

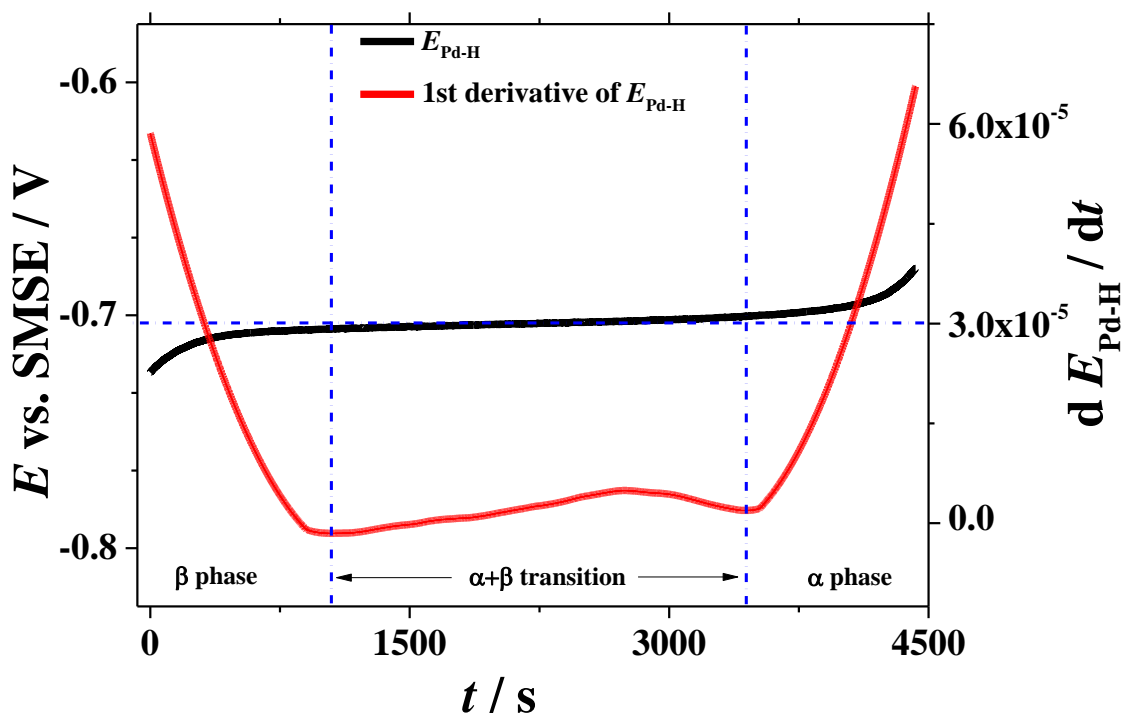


Figure 4.10: Potentiometric measurement of a H_{1-e} Pd film ($Q_{dep} = 2500 \mu C$) deposited onto a $250 \mu m$ diameter Pt disc electrode, in a deaerated solution of $0.5 M Na_2SO_4 + H_2SO_4$ solution (pH 1.88) at $25^\circ C$, immediately after hydrogen was loaded into the Pd nanostructure. The potential measured E_{Pd-H} is drawn in black line, while the first derivative of E_{Pd-H} against the time is drawn in red.

One complex question is to determine the limits of the $\alpha+\beta$ transition period, The first derivative of E_{Pd-H} against time (i.e. dE_{Pd-H} / dt) was used as a systematic method to determinate the start and end of the $\alpha+\beta$ transition period. **Figure 4.10** shows the first derivative of E_{Pd-H} (the red line), the base level points were selected to be the $\alpha+\beta$ transition period limits of the potentiometric measurement.

In **Figure 4.10**, the $\alpha+\beta$ transition is located between 1045 s and 3440 s. This period is important because it reflects the lifetime of the H_{1-e} Pd pH sensor before the need to load hydrogen into the pH sensor once again.

Thus, the average potential of the $\alpha+\beta$ transition period was calculated to assess variation and errors in the potentials as follows:

$$E_{\text{Pd-H}} = \frac{E_{\text{Pd-H of } \alpha+\beta \text{ start}} + E_{\text{Pd-H of } \alpha+\beta \text{ end}}}{2} \quad 4.9$$

$$\Delta E_{\text{Pd-H}} = \left| \frac{E_{\text{Pd-H of } \alpha+\beta \text{ start}} - E_{\text{Pd-H of } \alpha+\beta \text{ end}}}{2} \right| \quad 4.10$$

The $E_{\text{Pd-H}}$ of the $\alpha+\beta$ transition region in **Figure 4.10** equals -0.703 ± 0.003 V between 1045 and 3440 s, giving a lifetime of 2395 s, and $pH = 1.91 \pm 0.05$. The $E_{\text{Pd-H}}$ errors can be minimized by narrowing the $\alpha+\beta$ transition lifetime limits, but that will decrease the usage period of the $\text{H}_1\text{-e Pd}$ pH sensor as can be noted in **Table 4.4**.

Table 4.4: The estimation of pH using nanostructured Pd immediately after hydrogen was loaded under open circuit potential conditions, the working electrode was a $\text{H}_1\text{-e Pd}$ film ($Q_{\text{dep}} = 2500 \mu\text{C}$) deposited onto a 250 μm diameter Pt disc electrode, in a deaerated solution of 0.5 M $\text{Na}_2\text{SO}_4 + \text{H}_2\text{SO}_4$ solution (pH 1.88) at 25° C.

t / s			$E_{\text{Pd-H}} / \text{V vs. SMSE}$				pH	
$t_{\alpha+\beta}$ start	$t_{\alpha+\beta}$ end	$\alpha+\beta$ transition life time	$E_{\alpha+\beta}$ start	$E_{\alpha+\beta}$ end	Av. $E_{\text{Pd-H}}$	$\Delta E_{\text{Pd-H}}$	Av. pH	ΔpH
1045	3440	2395	-0.7059	-0.7005	-0.703	0.003	1.91	0.05
1095	3390	2295	-0.7057	-0.7007	-0.703	0.003	1.91	0.04
1145	3340	2195	-0.7057	-0.7009	-0.703	0.002	1.91	0.04
1195	3290	2095	-0.7056	-0.7010	-0.703	0.002	1.91	0.04
1245	3240	1995	-0.7055	-0.7012	-0.703	0.002	1.92	0.04
1295	3190	1895	-0.7053	-0.7014	-0.703	0.002	1.92	0.03
1345	3140	1795	-0.7052	-0.7015	-0.703	0.002	1.92	0.03
1395	3090	1695	-0.7051	-0.7017	-0.703	0.002	1.91	0.03
1445	3040	1595	-0.7049	-0.7018	-0.703	0.002	1.92	0.03
1495	2990	1495	-0.7048	-0.7020	-0.703	0.001	1.91	0.02

4.3. E_{Pd-H} potential with different pH solutions

The main aim of the project is to develop a nanostructured palladium hydride pH sensor of the brain fluid using the the $\alpha+\beta$ transition potentials E_{Pd-H} , converted to pH . This pH probe will be located in the patient’s body or with other sensors in a catheter carrying the brain fluid away from the patient. If the probe is inserted in the patient the measurement will be carried out at body temperature. However, with the catheter the measurement will be done near room temperature. The E_{Pd-H} can be affected by the temperature, as can be seen in equation 4.11.

$$E_{Pd-H} (vs. SMSE) = -0.64 - \frac{RT}{2F} \ln P_{H_2} - \frac{2.303 RT}{F} pH \tag{4.11}$$

which justifies the need for a calibration curve at the human body temperature of 37° C to mimic the real conditions [159]. The potentiometric response of the H₁-e Pd pH sensor can be studied with various pH test solutions to plot the calibration curve at 37° C to determine the slope and the intercept. The used test solutions were commercial buffers pH 4.04, 6.98, 9.97 (Fisher Scientific), and 1 M NaOH (pH 14). **Table 4.5** shows the potentiometric measurements that were taken ten times for each solution to obtain E_{Pd-H} vs. SMSE / V; then, the following calculations were made:

The mean $\bar{x} = \frac{1}{10} \sum E_{Pd-H}$, the standard deviation $\sigma = \sqrt{\frac{1}{10} \sum (E_{Pd-H} - \bar{x})^2}$, and the standard error of the mean $\sigma_{\bar{x}} = \frac{\sigma}{\sqrt{10}} \cdot \bar{x}$

Table 4.5: The mean \bar{x} , the standard deviation σ and the standard error of the mean $\sigma_{\bar{x}}$ of E_{Pd-H} vs. SMSE / V that were obtained from ten potentiometric measurements for each test solution of commercial buffers pH 4.04, 6.98, 9.97 (Fisher Scientific), and 1 M NaOH (pH 14) carried out at 37 °C.

pH	$\bar{x} E_{Pd-H} / V$	$\sigma E_{Pd-H} / V$	$\sigma_{\bar{x}} E_{Pd-H} / V$
4.04	-0.7791	0.0016	0.0005
6.98	-0.9674	0.0021	0.0007
9.97	-1.1621	0.0022	0.0007
14	-1.3787	0.0010	0.0003

Figure 4.11 shows the obtained calibration curve of the mean E_{Pd-H} vs. pH using the values in **Table 4.5**.

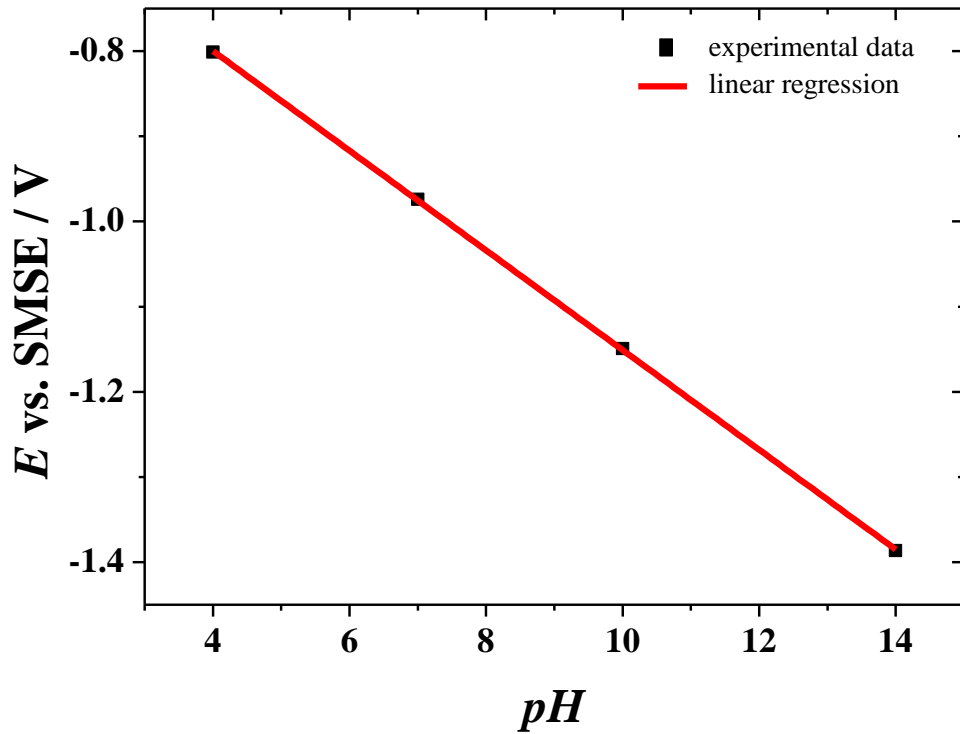


Figure 4.11: Relationship of E_{Pd-H} against pH obtained in deaerated commercial buffer solutions and (at pH 14 we used 1 M NaOH) at the human body temperature of $37^\circ C$. The Potentiometric measurement for each solution has been done using a H_1 -e Pd film ($Q_{dep} = 2500 \mu C$) deposited onto a $250 \mu m$ diameter Pt disc electrode, immediately after hydrogen was loaded into the Pd nanostructure.

The calibration curve of E_{Pd-H} shows a linear relationship with pH . Equation 4.12 shows the relationship between the potential of the palladium hydride electrode pH and at the human body temperature of $37^\circ C$.

$$E_{Pd-H} \text{ V vs. SMSE, at } 37^\circ C = -0.5621 - 0.0584 pH \quad 4.12$$

$$r^2 = 0.998$$

Equation 4.12 shows that the experimental slope equals $-0.0584 \text{ V} / pH$, which is in good agreement with the theoretical slope, $-0.0615 \text{ V} / pH$, in equation 4.11. The experimental intercept equals -0.5621 V vs. SMSE, while the theoretical intercept equals -0.5947 V vs. SMSE.

The electrochemical behaviour of the H_1 -e Pd pH probe in the brain fluid at human body temperature will be discussed in section 4.4.

4.4. Brain fluid analysis

The main aim of this research is the analysis of biological samples. In this stage of the project, the role of the nanostructured biosensor will be clarified to improve the analysis of the brain fluid. The artificial cerebral spinal fluid aCSF was used instead of real brain fluid, as it is difficult to obtain a large enough real brain fluid sample for lab work. **Table 4.6** shows the composition of aCSF [160], which was buffered by a phosphate buffer to keep the *pH* stability of the solution to be *pH* 7.

Table 4.6: The composition of the artificial cerebral spinal aCSF fluid [160].

The chemicals	Concentration / mM
NaCl	128.0
KCl	3.0
CaCl ₂	1.3
MgCl ₂	1.0
Na ₂ HPO ₄	21.0
NaH ₂ PO ₄	1.3

The salts are dissolved in distilled water with stirring until a colourless solution is formed. The stock solution of aCSF was prepared every two weeks and kept in the refrigerator under $T = 8^{\circ} \text{C}$ to avoid bacteria proliferation; this typically occurs when aCSF is kept for a long period of time. Otherwise, the stock solution of aCSF would need an added biocide.

The serum proteins in the real biological samples can adsorb onto the biosensor surfaces, resulting in a nonspecific response, which impedes the quantification of the biological samples biomarkers [161, 162]. Bovine serum albumin, BSA, can be used to obtain a realistic protein content for interference studies by adding 5% (w/v) BSA to the measured aCSF solution [163]. **Figure 4.12** shows the cyclic voltammetry of the aCSF.

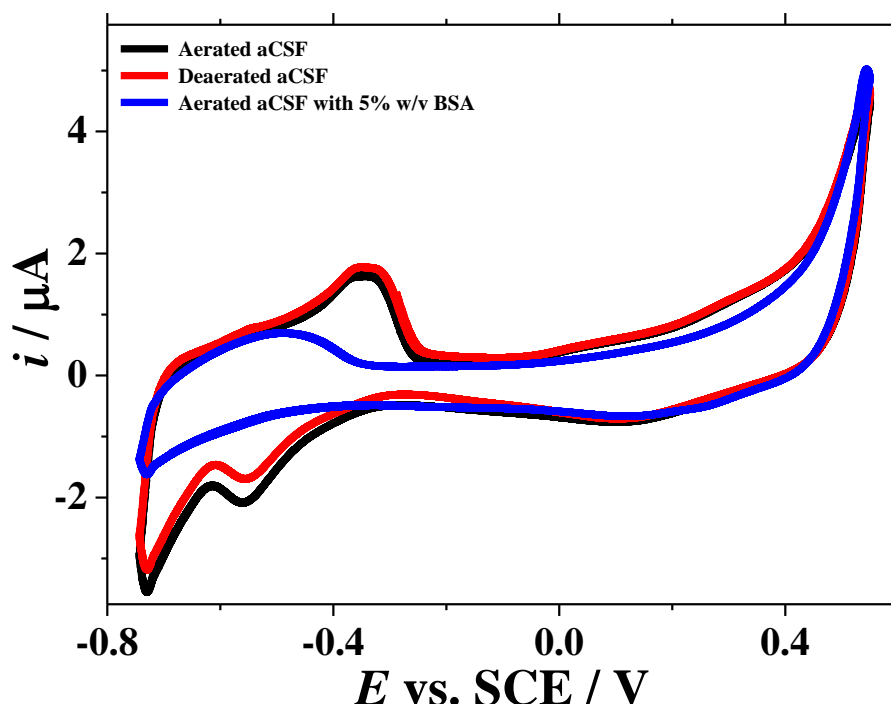


Figure 4.12: The cyclic voltammograms of a H₁-e Pd film ($Q_{\text{dep}} = 2500 \mu\text{C}$) deposited onto a 250 μm diameter Pt disc electrode recorded at 20 mV s^{-1} in 20 ml of artificial cerebral spinal fluid aCSF ($pH 7$) at 25°C . CVs recorded in aerated solution (black), in Ar purged (20 min) solution (red) before the addition of 5% (w/v) bovine serum albumin, BSA, to the aCSF solution, and in aerated aCSF solution with BSA (blue).

The H₁-e Pd film voltammetry in aCSF ($pH 7$) seems to be in line with the cyclic voltammetry in **Figure 3.7** and **Figure 4.1**, which were carried out in 1 M H₂SO₄ ($pH 0$) and 0.5 M Na₂SO₄ + H₂SO₄ ($pH 1.88$). However, the peaks have shifted negatively because of the variation in pH between the measured solutions. Hydrogen adsorption peaks are not seen but the peaks for hydrogen absorption and desorption are clear.

The voltammograms of aerated and deaerated aCSF before the BSA addition show consistency especially in the oxide and the double layer regions, while there is a shifting down in the peaks of the hydrogen region in aerated aCSF, which can be attributed to the overlapping of the hydrogen region peaks with the oxygen reduction reaction. On the other hand, addition of BSA to the aerated aCSF solution significantly decreases the

current for the O_2 reduction and the hydrogen adsorption peaks. This indicates that BSA slows down the rate of oxygen reduction and hydrogen adsorption, presumably by adsorbing on the H_{1-e} Pd pH sensor surface. BSA may well block the pores of the Pd nanostructure, as the BSA molecule ($d = 22 \pm 5$ nm) is wider than the pore diameter ($d = 3.5$ nm). The protein may also denature and unravel sufficiently to penetrate the nanostructure and adsorb on the pore walls. It is also possible that impurities from the BSA stock solution adsorb on the Pd surface. The H_{1-e} Pd film was used to measure the pH of aCSF. **Figure 4.13** shows the potentiometric measurements of aCSF at a human body temperature of 37° C to mimic the real conditions.

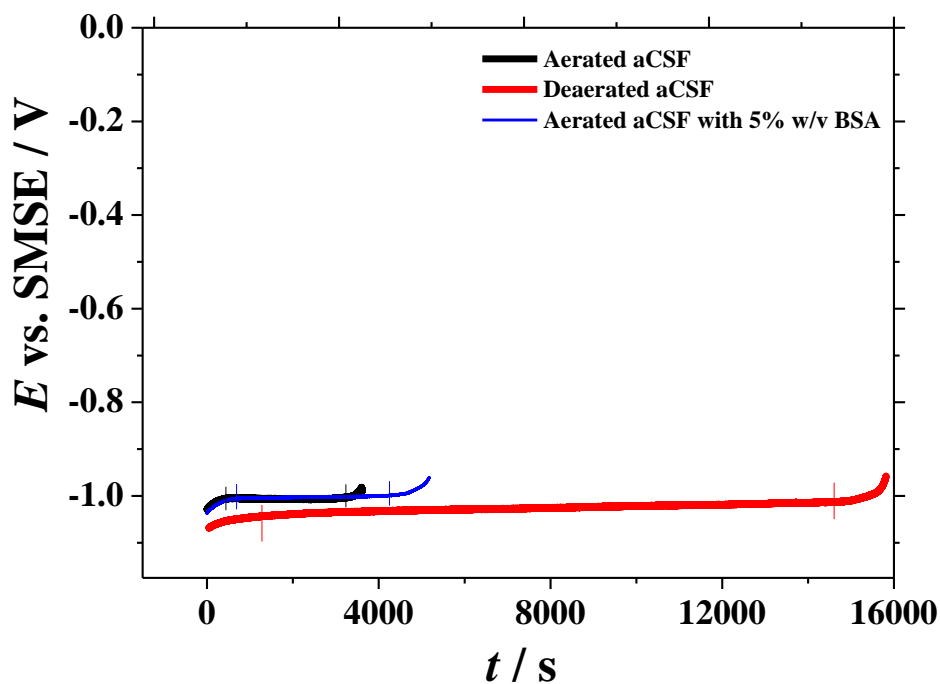


Figure 4.13: Potentiometric measurements of a H_{1-e} Pd film ($Q_{dep} = 2500 \mu C$) deposited onto a $250 \mu m$ diameter Pt disc electrode in artificial cerebral spinal fluid aCSF pH 7 at 37° C, aerated aCSF (black), deaerated aCSF (red) and aerated aCSF with 5% (w/v) bovine serum albumin BSA, immediately after hydrogen was loaded into the Pd nanostructure.

The effect of the BSA on the H₁-e Pd *pH* sensor can be studied using the potentiometric comparison of aerated aCSF (*pH* 7) with and without the 5% w/v BSA addition. There is agreement between the $\alpha+\beta$ transition potentials $E_{\text{Pd-H}}$ of the aerated aCSF with and without BSA; -1.004 ± 0.001 and -1.002 ± 0.003 V vs. SMSE respectively correspond to $pH = 6.99 \pm 0.02$ and 6.97 ± 0.05 for the aerated aCSF before and after the BSA addition. It was also found that there is an increase in the $\alpha+\beta$ transition lifetime after the BSA addition to aerated aCSF from 2790 s to 3650 s, while the lifetime of the $\alpha+\beta$ transition equals 13350 s in the deaerated aCSF without BSA. The increase for the $\alpha+\beta$ transition lifetime in aerated aCSF after the BSA addition is thought to arise from the lower rate of oxygen reduction resulting from the adsorption of BSA or impurities onto the H₁-e Pd surface. However compared to the lifetime observed in deaerated aCSF, it is clear that oxygen is still affecting the sensor. The rise in potential of the blue curve in **Figure 4.13** clearly indicates that the nanostructure was loaded with hydrogen sufficiently to form the β phase. However, the cyclic voltammetry in **Figure 4.12** shows that the hydrogen absorption/extraction currents are much lower in presence of BSA and this may reflect that a smaller volume of Pd is available for hydrogen insertion in presence of BSA.

The bottom line is that the nanostructured Pd can improve the efficiency of the biosensor to analyze the biological samples by diminishing the impact of protein adsorption on the biosensor surface. Because, assuming it does not denature, the protein will be adsorbed onto the external surface but not onto the electroactive surface of the electrode, as the protein molecule is wider than the pore diameter.

4.4.1. Calibration curves of aCSF at body temperature

Titration can be used to study the potentiometric response of the H₁-e Pd sensor against the *pH* variation of aCSF. The experiment was carried out in the presence of oxygen to mimic the conditions of the aerated real sample. The BSA was not added to the sample to avoid the degradation of BSA at low *pH* during the titration [164].

The H₁-e Pd film was loaded with hydrogen in the measuring solution potentiostatically by stepping the potential at $t = 0$ s from the starting potential = -0.486 V to the loading potential $E_{\text{load}} = -1.300$ V vs. SMSE. **Figure 4.14** shows the chronoamperogram for the loading of hydrogen into the H₁-e Pd film immediately before the titration.

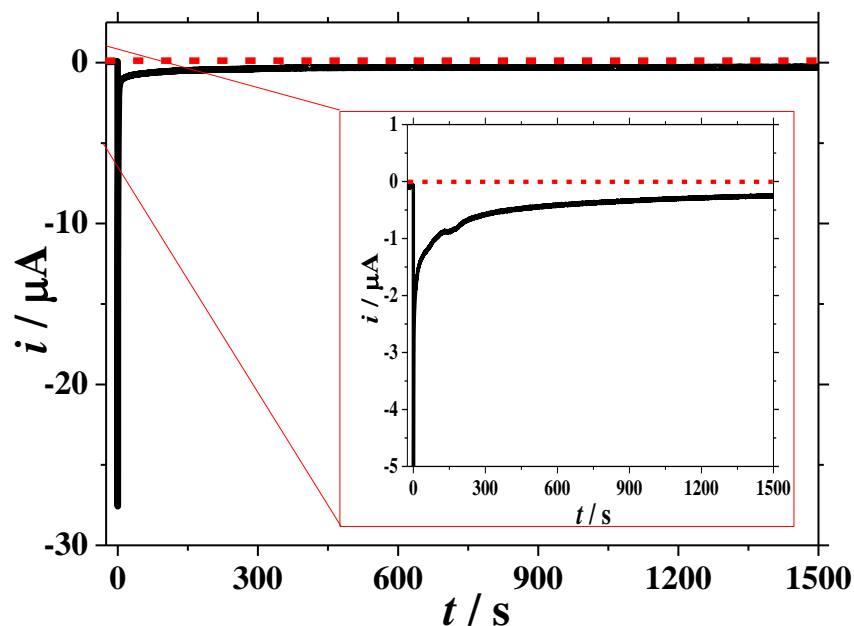


Figure 4.14: Hydrogen loading chronoamperogram into H₁-e Pd film ($Q_{\text{dep}} = 2500 \mu\text{C}$), deposited onto a 250 μm diameter Pt disc electrode in an aerated solution of 15 ml aerated buffered artificial cerebral spinal fluid, aCSF, at 37° C, the potential was stepped at $t = 0$ s from the starting potential = -0.486 V to the loading potential $E_{\text{load}} = -1.300$ V vs. SMSE.

The potentiometric measurement was done directly after the loading process finished in the same solution once the electrode potential $E_{\text{Pd-H}}$ was stable. Ten aliquots of 50 μl HCl were added to the measuring solution followed by nine aliquots of 50 μl NaOH to first reduce then raise the pH of aCSF during the titration. The concentrations of the acid and the base were 3.5 M to be able to modify the pH of the buffered aCSF. The $\alpha+\beta$ transition potential was monitored, while a companion glass pH meter electrode was used to record pH values of aCSF during titration. **Figure 4.15** shows the resulting output of the titration.

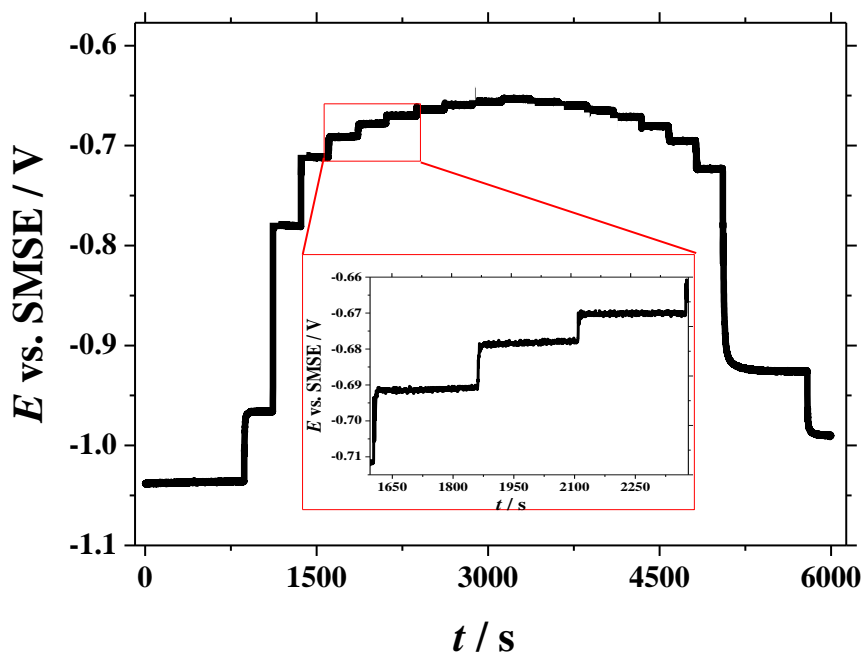


Figure 4.15: Potentiometric measurement recorded with a H_{1-e} Pd film ($Q_{dep} = 2500 \mu C$) deposited onto a $250 \mu m$ diameter Pt disc electrode in aerated buffered aCSF at $37^\circ C$, immediately after hydrogen was loaded into the Pd nanostructure in same solution. To increase the pH of the aCSF aliquots of $50 \mu l$ of $3.5 M$ HCl were used and $50 \mu l$ of $3.5 M$ NaOH to decrease the pH .

The open circuit potential recorded during the brain fluid titration shows the shift of E_{Pd-H} as the pH changed after each addition of acid or base; in each case E_{Pd-H} is found to be stable with a variation circa $0.6 mV$. Moreover, the potentiometric measurement shows a response time within $5 s$, which can be defined as the period that is required for the probe output to change from the previous value to the next stable values after the addition during the titration. The response time of H_{1-e} Pd probe is faster than $10 sec$ response reported for pH sensor made of fiber optic coated with polymer multilayers nano-coatings [165].

Figure 4.16 shows the calibration curve of E_{Pd-H} vs. pH , which was obtained using each plateau of $\alpha+\beta$ transition potential recorded during the acid-base titration.

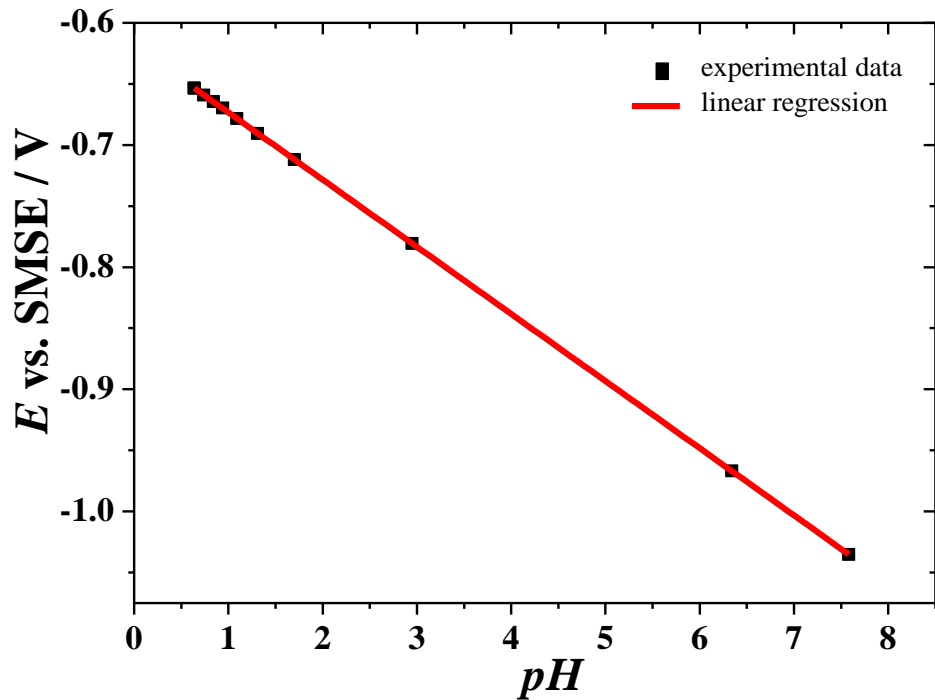


Figure 4.16: The calibration curve of E_{Pd-H} vs. pH for the potentiometric titration of a H_1 -e Pd film ($Q_{dep} = 2500 \mu C$) deposited onto a $250 \mu m$ diameter Pt disc electrode in aerated buffered artificial cerebral spinal fluid aCSF at $37^\circ C$, immediately after hydrogen was loaded into the Pd nanostructure in the same solution. Aliquots of $50 \mu l$ of $3.5 M$ HCl and $50 \mu l$ of $3.5 M$ NaOH were used to modify the pH of the aCSF.

The calibration curve of the E_{Pd-H} shows a linear relationship with pH using aCSF. **Figure 4.16** shows the relationship between the potential of the palladium hydride electrode and pH measured by the pH meter during the titration, which could be adapted to equation 4.14 to estimate the brain fluid at a human body temperature of $37^\circ C$.

$$E_{Pd-H} V \text{ vs. SMSE, at } 37^\circ C = -0.6184 - 0.055 pH \quad 4.13$$

$$pH = \frac{E_{Pd-H} V \text{ vs. SMSE, at } 37^\circ C + 0.6184}{-0.055} \quad 4.14$$

4.4.2. *pH* sensing in real brain fluid with a H₁-e Pd electrode

The *pH* sensing of the brain fluid was done in vitro after the cerebral spinal fluid was obtained from a microdialysis probe. However, it is difficult to obtain enough brain fluid samples for lab work from the patient, as the flow rate through the microdialysis probe is 2 $\mu\text{l min}^{-1}$ [166], with the result that there are only 840 μl from each patient after 7 hours. So, until now the artificial brain fluid has been used as a model to study the *pH* of the cerebral spinal fluid. The potentiometric measurement cannot be carried out at a human body temperature of 37° C, because at this temperature the limited quantity of the sample would evaporate during measurement leading to change in the concentrations of analytes. What is required, then, is to decrease the temperature of the measurements to a room temperature of 22° C.

Equation 4.11 indicates that variance in temperature will affect the $E_{\text{Pd-H}}$. For this reason, potentiometric measurements of the brain fluid with commercial buffers of *pH* 4, 7 and 10 were carried out at 22° C to obtain the calibration curve of the $E_{\text{Pd-H}}$ against *pH*.

Figure 4.17 shows the potentiometric measurements of the real brain fluid sample with commercial buffers of *pH* 4, 7 and 10 (Fisher Scientific).

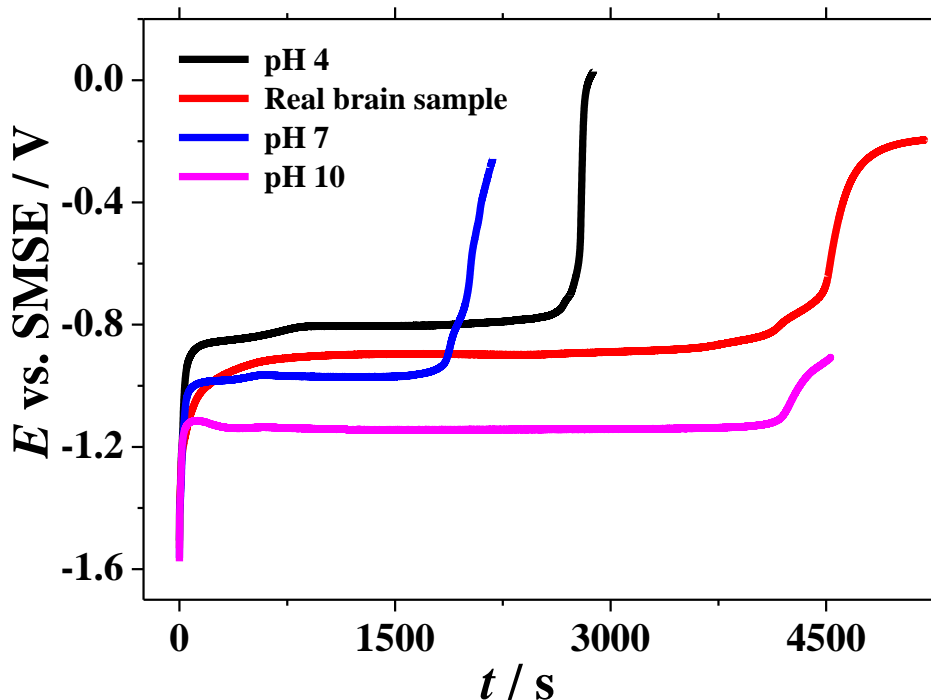


Figure 4.17: Potentiometric measurements with a H_1 -e Pd film ($Q_{dep} = 2500 \mu C$) deposited onto a $250 \mu m$ diameter Pt disc electrode in aerated a cerebral spinal fluid CSF at $22^\circ C$ and aerated commercial buffers of pH 4, 7 and 10 (Fisher Scientific), immediately after hydrogen was loaded into the Pd nanostructure.

Table 4.7 summarizes the data obtained from the potentiometric measurements done in Figure 4.17, which were used to obtain the calibration curve of E_{Pd-H} vs. pH at $22^\circ C$.

Table 4.7: The obtained E_{Pd-H} vs. SMSE / V of the potentiometric measurements for brain fluid and commercial buffers pH 4, 7, 10 (Fisher Scientific).

pH	E_{Pd-H} / V	$\Delta E_{Pd-H} / V$
4	-0.804	0.005
CSF	-0.897	0.002
7	-0.968	0.001
10	-1.140	0.002

Figure 4.18 shows the calibration curve of E_{Pd-H} vs. pH at $22^\circ C$ drawn from **Table 4.7**. The brain fluid pH was derived from the calibration curve by its output E_{Pd-H} .

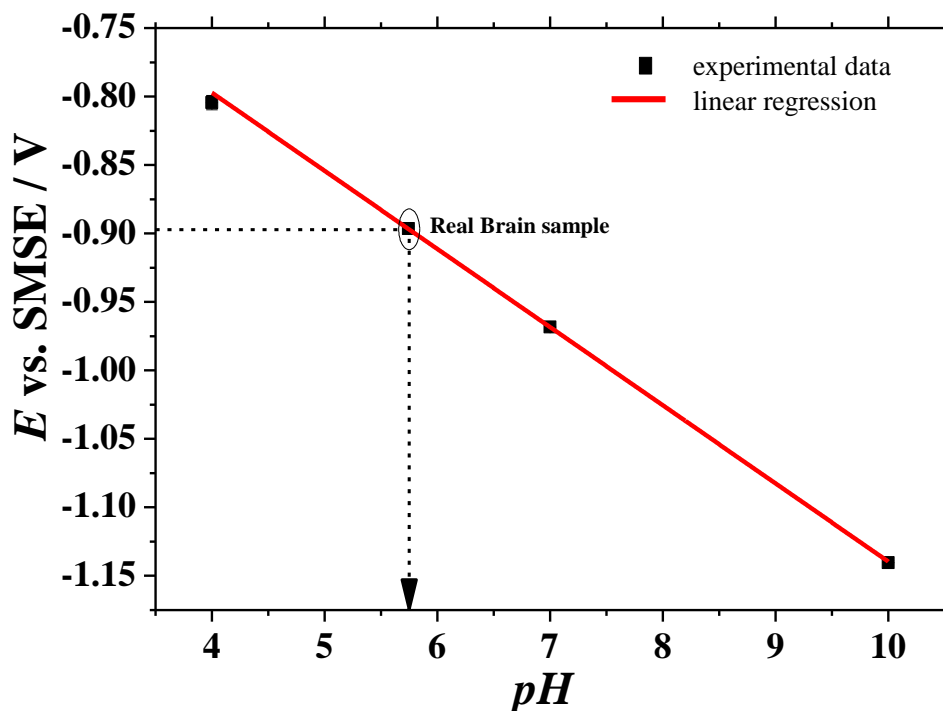


Figure 4.18: The calibration curve of E_{Pd-H} vs. pH for the potentiometric measurements of a H_1-e Pd film ($Q_{dep} = 2500 \mu C$) deposited onto a $250 \mu m$ diameter Pt disc electrode in an aerated brain fluid and aerated commercial buffers of pH 4, 7 and 10 (Fisher Scientific), at $22^\circ C$. The dotted line indicates the electrode potential and corresponding pH for the sample of real brain fluid. The potentials errors ΔE_{Pd-H} for aerated solutions are: 0.005, 0.002, 0.001 and 0.002 V vs. SMSE of: buffer pH 4, brain fluid, buffer 7 and buffer 10 respectively.

The calibration curve of E_{Pd-H} has a linear relationship with pH . Equation 4.15 shows the relationship between pH and the potential of the H_1-e Pd pH probe at $22^\circ C$:

$$E_{Pd-H} \text{ V vs. SMSE, at } 22^\circ C = -0.5689 - 0.0571 \text{ pH} \tag{4.15}$$

$$r^2 = 0.9998$$

The pH of the measuring solutions at 22° C was obtained directly by conversion of equation 4.15 to equation 4.16:

$$pH = \frac{E_{Pd-H} \text{ V vs. SMSE, at } 37^{\circ}C + 0.5689}{-0.0571} \quad 4.16$$

The pH of the brain fluid sample was found to be 5.74 ± 0.03 corresponding to

$$E_{Pd-H} = -0.8965 \pm 0.0017 \text{ V vs. SMSE.}$$

Equation 4.11 was used to calculate the theoretical slope and the intercept at 22° C. It was found that both the theoretical slope = $-0.0585 \text{ V} / pH$ and the theoretical intercept = -0.5969 V agree with the experimental slope and intercept shown in equation 4.15.

4.5. Summary

In this chapter, the hydrogen loading into Pd nanostructure was reviewed, considering that the loading can be done either by the potentiostatic or by the galvanostatic techniques. Both the potentials in the potentiostatic loading and the currents of galvanostatic method to insert hydrogen into the H_{1-e} Pd film were determined. The loading step was followed by chronopotentiometric measurement to estimate the *pH* of the solution via conversion the measured potential using the Nernst equation.

The potentiostatic loading potential E_{load} of the hydrogen into the H_{1-e} Pd film was first identified using cyclic voltammetry, and then by chronoamperometry in from the hydrogen absorption region until the maximal loading charge Q_{load} was obtained since this reflects the loading hydrogen quantity in the H_{1-e} Pd film (i.e. the atomic ratio H/Pd). Chronoamperometric comparison was done with various loading potentials to choose the most appropriate E_{load} : an extreme positive potential would make the hydrogen loading period t_{load} too long to reach full hydrogen loading at H/Pd = 0.6, and an extreme negative E_{load} would cause H₂ gas to evolve immoderately on the electrode surface potentially damaging the H_{1-e} Pd film. The order of hydrogen extraction from the H_{1-e} Pd film was studied, and it was shown that the extraction of hydrogen began by the hydrogen from the β phase H _{β} , continued by hydrogen from the α phase H _{α} , and finished with hydrogen being desorbed from the surface of the Pd nanostructure H_{ads}.

For the hydrogen loading, the galvanostatic method is preferred than the potentiostatic technique, because the loading charge Q_{load} (the loading current i_{load} multiplied by the loading time t_{load}) can obtained directly. Moreover, galvanostatic hydrogen loading can be done in a shorter period than potentiostatic hydrogen loading.

The $E_{\text{Pd-H}}$ potential was estimated theoretically by the Nernst equation at 25° C, then the $E_{\text{Pd-H}}$ during the $\alpha+\beta$ transition period was obtained by potentiometric measurements and the error in its potential ($\pm E_{\text{Pd-H}}$) equals ± 0.0014 V vs. SMSE, which would makes the sensitivity of the H_{1-e} Pd *pH* sensor ($\pm pH$) equals ± 0.024 .

The calibration curve of $E_{\text{Pd-H}}$ vs. pH was drawn at the human body temperature of 37°C through various pH solutions; it was found that $E_{\text{Pd-H}}$ has a linear relationship with pH . The composition of the artificial cerebral spinal fluid (aCSF) was shown. The impact of the serum proteins adsorption on the surface of the $\text{H}_1\text{-e Pd}$ pH sensor was studied, before potentiometric measurements were made in aerated and deaerated aCSF. The calibration curve of aCSF at human body temperature was determined by titration, and it was found that the $E_{\text{Pd-H}}$ was quite stable in the $\alpha+\beta$ transition potential, with a reasonable response time (within 5 s), and that the calibration curve of $E_{\text{Pd-H}}$ had a linear relationship with pH in the aCSF solution.

The sensing of the real brain fluid pH was done in vitro at room temperature, because at human body temperature the limited quantity of the sample would evaporate during the measurement, thus changing the concentrations of analytes. Therefore, another calibration curve was done at 22°C , since variance in temperature would change the $E_{\text{Pd-H}}$ leading to the need to adjust the calibration curve's slope and intercept. It was then found that the slope and the intercept of the calibration curve agreed with those of the theoretical calculations at 22°C .

The next chapter will present the attempts that were made to improve the performance of the $\text{H}_1\text{-e Pd}$ pH sensor by covering the surface of the Pd nanostructure with different protective coatings.

Page intentionally left blank

Chapter 5. Development of coatings

The main aim of this study was to fabricate nanostructured H₁-e Pd electrodes for *pH* sensing in biomedical applications. In this chapter the aim is to protect them from the biological samples contaminations. Their lifetime can be decreased as a result of oxygen presence in the biological sample; this will affect the *pH* sensors efficiency as mentioned in section 1.4. Thus, the main aim of this section of work was to cover the H₁-e Pd films with coatings. To avoid confusion with the Pd film, this chapter uses the word “coating” to describe the layer used to protect the H₁-e Pd film. This should stop the contamination and extend the $\alpha+\beta$ transition lifetime of the electrode under open circuit potential conditions. This approach is preferred to the alternative requiring pre-treatment of the measuring solution. These coatings were fabricated with a variety of modifications then characterized and compared to assess which coating provided the most efficient protection of the electrode without affecting the hydrogen loading and ability of the nanostructured PdH to work as a *pH* sensor. Comparison was done between bare and coated H₁-e Pd electrodes using cyclic voltammetry during the coating process. The H₁-e Pd films were evaluated after the coating process via SEM images to study the effect on the Pd nanostructure. Voltammetry was used to estimate the coatings thicknesses and to confirm the ability of the coatings to prevent interfering species from reaching the H₁-e Pd surface and decreasing the $\alpha+\beta$ transition lifetime. Voltammetry was also used to estimate the ability of the coatings to block O₂ from reacting with the H₁-e Pd surface. The hydrogen loading process was compared between uncoated and modified H₁-e Pd films to study the effect of the coating on the hydrogen absorption into the H₁-e Pd film through the coating. Finally, open circuit potentials were recorded to verify the ability of the coated Pd nanostructures to act as a *pH* sensor. Three types of coatings were used in this study:

- Direct application of Nafion Ionomers: no possibility to electrodeposit or control the thickness of the coating.

- Polymeric films with multilayers: can be electrodeposited and offer same degree of thickness control .e.g. polypyrrole, polyaniline, poly (phenylene oxide).
- Covalent modification using monolayer coatings which can be electrodeposited such as diazonium salt (Boc).

5.1. Nafion

This coating was used to cover the *pH* sensor with a permselective layer, since it is very successful to slow down oxygen transport while allowing H^+ to diffuse through the Nafion coating and reach the *pH* sensor underneath [100-102]. So, Nafion is expected to increase the lifetime of the $\alpha+\beta$ transition. This coating was made by covering the H_1 -e Pd film with 4 μ l of Nafion (5% w/w Perfluorosulfonic acid- PTFE copolymer in water and 1-propanol / 42117 Alfa Aesar), then drying overnight. This approach does not offer great control on the coating thickness.

5.1.1. Nafion: SEM imaging

Nafion is not deposited electrochemically which means the Pd nanostructure is unlikely to be lost during the coating process. SEM images, **Figure 5.1**, show that the H_1 -e Pd film is covered with an approximately 30 μ m thick layer of Nafion, compared with 2.2 μ m of the H_1 -e Pd film thickness.

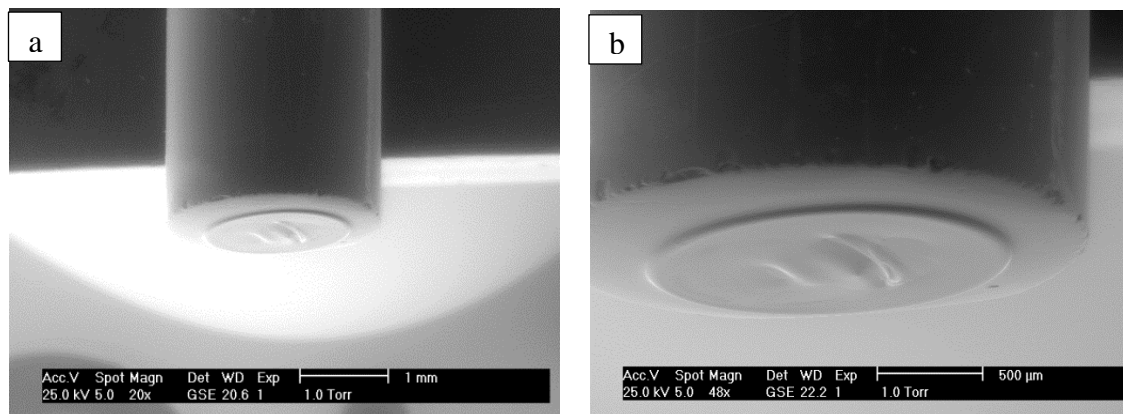


Figure 5.1: Scanning electron microscopy images, with different magnifications (a equals 1 mm and b equals 500 μm) of a H₁-e Pd film ($Q_{\text{dep}} = 2500 \mu\text{C}$) deposited onto a 250 μm diameter Pt disc electrode after coating with Nafion (tilt angle 70°).

5.1.2. Nafion: oxygen blocking

The ability of the Nafion coating to act as a barrier to O₂ was studied by cyclic voltammetry with and without oxygen using bare and coated H₁-e Pd films. **Figure 5.2** shows the cyclic voltammograms in aerated and deaerated solution of phosphate *pH* 7 buffer before and after the Nafion coating was applied onto the H₁-e Pd *pH* sensor.

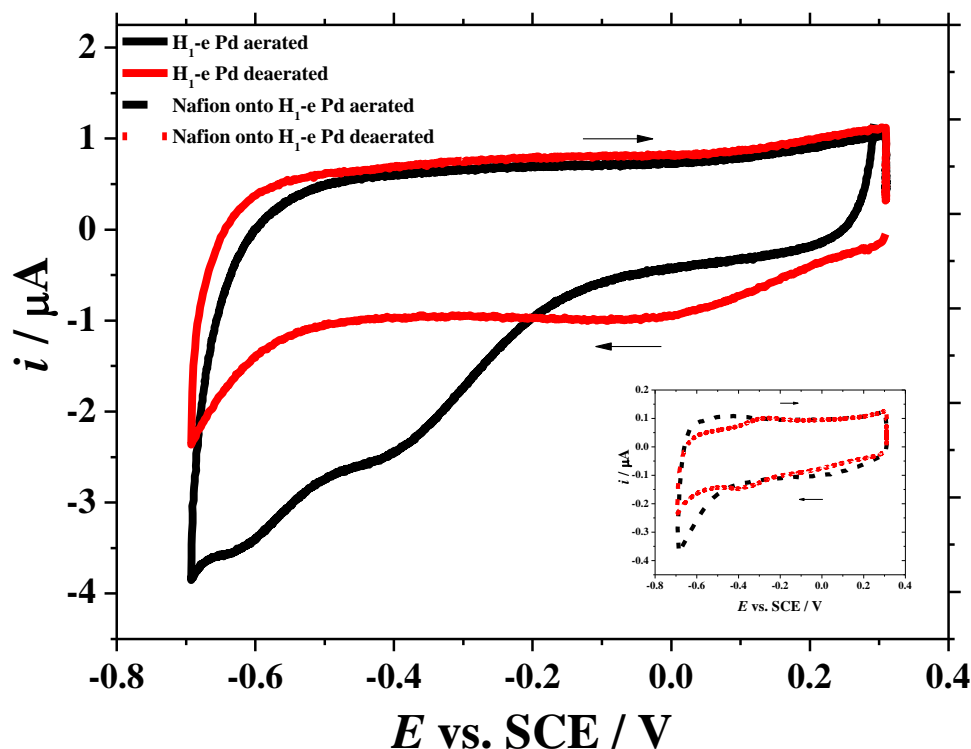


Figure 5.2: The cyclic voltammograms of a H_{1-e} Pd film ($Q_{\text{dep}} = 2500 \mu\text{C}$) deposited onto a 250 μm diameter Pt disc electrode recorded at 20 mV s^{-1} in 20 ml phosphate pH 7 buffer at 25°C . CVs recorded in aerated solution (black) and in Ar purged (20 min) solution (red), solid lines for uncoated films, dotted lines for films coated with Nafion (4 μl 5% in in water and 1-propanol).

The cyclic voltammetry was done in presence and absence of O_2 before and after applying the coating. The current was monitored between +0.3 V to -0.7 V vs. SCE, i.e. in the potential range between the double layer region and the required potential for PdH formation. **Table 5.1** shows the current at -0.7 V vs. SCE for CVs recorded in aerated and in Ar purged phosphate pH 7 buffer solutions for uncoated and Nafion coated H_{1-e} Pd films.

Table 5.1: The current at -0.7 V vs. SCE for CVs recorded in aerated and in Ar purged phosphate *pH* 7 buffer solution before and after coating of H₁-e Pd film with Nafion.

	Bare H ₁ -e Pd film	Nafion coated H ₁ -e Pd film
aerated phosphate <i>pH</i> 7 buffer	-3.933 μ A	-0.375 μ A
deaerated phosphate <i>pH</i> 7 buffer	-2.478 μ A	-0.240 μ A

The Nafion coating leads to a significant drop in the oxygen reduction current therefore indicating a massive ability of Nafion to block oxygen from reaching the H₁-e Pd *pH* sensor surface.

5.1.3. Nafion: blocking of other interfering species

The blocking of interfering species from reaching the H₁-e Pd film surface by the coating was investigated with the cyclic voltammetry of electroactive species such as Ru(NH₃)₆³⁺, as shown in **Figure 5.3**. The apparent limiting current i_L was estimated to be 326 nA at $E = -0.45$ V vs. SCE for the bare H₁-e Pd. This reduced to 92 nA after coating with Nafion. It can be seen that the Nafion reduces the apparent i_L , presumably by decreasing the diffusion coefficient of electroactive species involved, as stated in equation 3.7. The drop in limiting current suggests that the flux of Ru(NH₃)₆^{3+/2+} ions to the electrode has more than two thirds in presence of Nafion. The CVs recorded before and after applying Nafion shown similar degree of double layer charging current therefore suggesting that the electroactive area of the nanostructured has not been affected.

The confirmation that the Nafion coating will decrease the diffusion of interfering species with a similar size (or bigger) to Ru(NH₃)₆^{3+/2+} bodes well for the use of the coating for the medical application in which it is intended – as biological molecules present in brain fluid are bigger than the 0.55 nm diameter of the ruthenium hexamine ion [167].

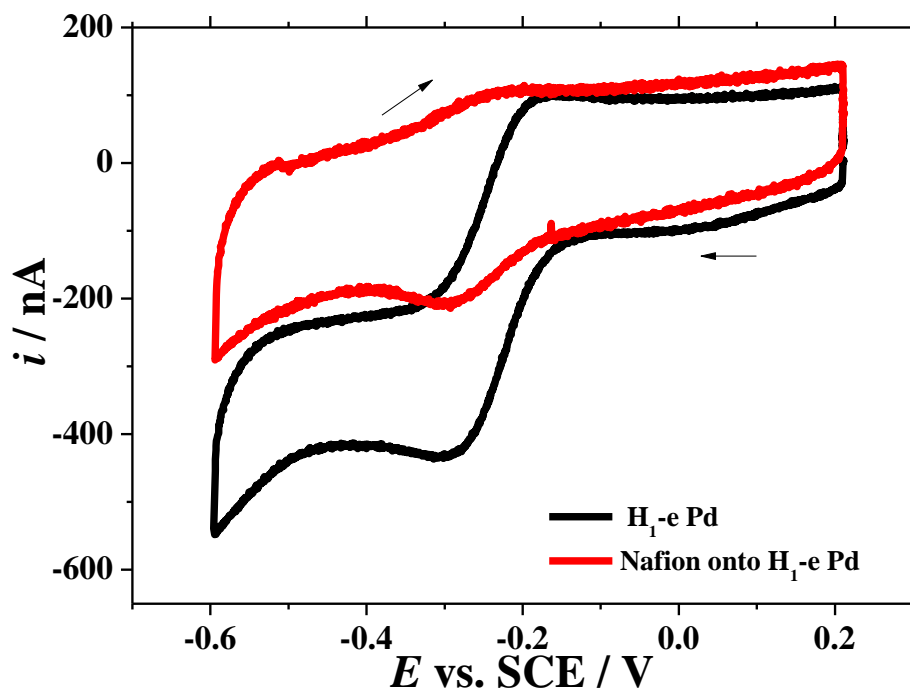


Figure 5.3: The cyclic voltammograms of a H₁-e Pd film ($Q_{\text{dep}} = 2500 \mu\text{C}$) deposited onto a 250 μm diameter Pt disc electrode recorded at 2 mV s^{-1} in 20 ml of Ar purged 5 mM $\text{Ru}(\text{NH}_3)_6^{3+}$ + 0.5 M KCl at 25° C. CVs recorded before (black) and after (red) applying the Nafion coating (4 μl 5% in in water and 1-propanol).

5.1.4. Nafion: effect on hydrogen loading and *pH* sensing

The hydrogen was loaded into H₁-e Pd film ($Q_{\text{dep}} = 2500 \mu\text{C}$), deposited onto a 250 μm diameter Pt disc electrode before and after the Nafion coating to observe the effect the modification had had. **Figure 5.4** shows the chronoamperograms for hydrogen loading into a H₁-e Pd film before and after the modification in aerated aCSF (*pH* 7).

The bare H₁-e Pd film needs 475 s to completely load hydrogen to a loading charge $Q_{\text{load}} = -777.09 \mu\text{C}$, equivalent to 8.05×10^{-9} mole of loaded hydrogen using equation 4.7. The Nafion coated H₁-e Pd film does not reach the full hydrogen loading even though the loading time was extended to $t_{\text{load}} = 4000$ s. This corresponds to a loading charge $Q_{\text{load}} = -309.36 \mu\text{C}$, equivalent to 3.21×10^{-9} mole of hydrogen. This is expected because the thick Nafion layer (about 30 μm) slows hydrogen diffusion to the H₁-e Pd film, therefore extending the t_{load} .

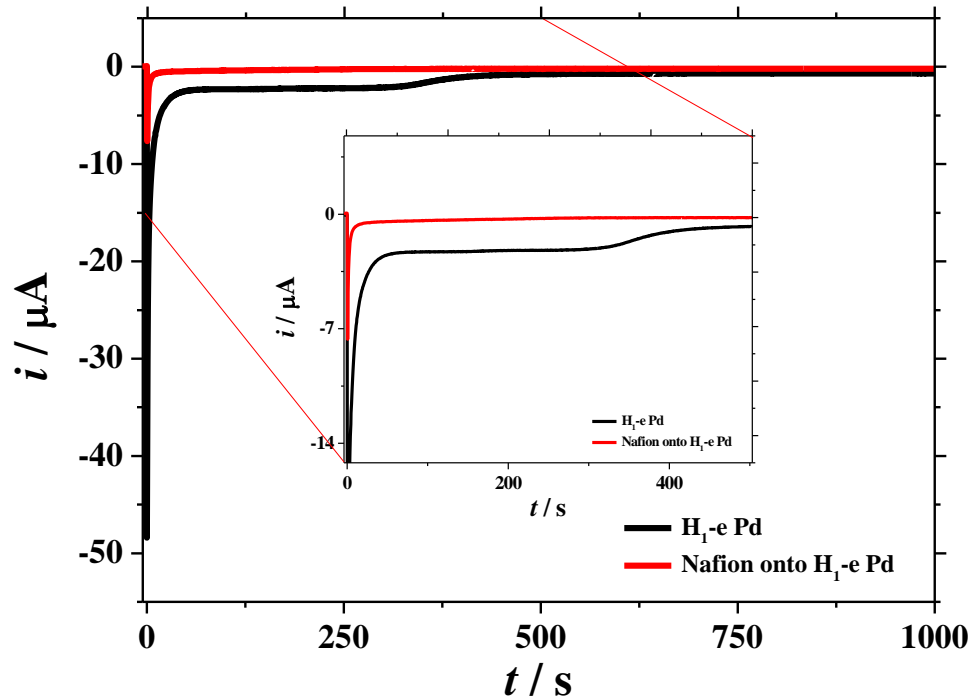


Figure 5.4: Hydrogen loading chronoamperograms into H_1 -e Pd film ($Q_{\text{dep}} = 2500 \mu\text{C}$), deposited onto a $250 \mu\text{m}$ diameter Pt disc electrode, with and without Nafion coating in aerated aCSF ($pH 7$) at 25°C . The potential was stepped at $t = 0 \text{ s}$ from the starting potential $E_{\text{strip}} = -0.486 \text{ V}$ to the loading potential $E_{\text{load}} = -1.300 \text{ V}$ vs. SMSE.

The open circuit potential of the H_1 -e Pd microdisc was recorded in aerated aCSF ($pH 7$ as measured with a glass electrode) before and after applying the Nafion coating. **Figure 5.5** clearly shows the lifetime extension of H_1 -e Pd $\alpha+\beta$ transition, increasing from 2450 s for a bare H_1 -e Pd electrode to 17000 s after the modification.

This can be attributed to a reduction in the rate of hydrogen (PdH) consumption by oxygen as stated in section 1.4, since the Nafion reduces the flux of O_2 to the nanostructured Pd surface. The deceleration of hydrogen diffusion through the Nafion coating can also play a role.

On the other hand, the $\alpha+\beta$ transition of the bare H_1 -e Pd shows a plateau with minimal error, as the average potentials $E_{\text{Pd-H}}$ equals $-1.004 \pm 0.001 \text{ V}$ vs. SMSE, which

corresponds to $pH\ 6.99 \pm 0.02$. Conversely, the $\alpha+\beta$ transition of the Nafion coated H_1 -e Pd electrode does not show a plateau, but a slope - which gives a large error. The E_{Pd-H} at the $\alpha+\beta$ transition period has been calculated to be $-1.074 \pm 0.04\ V$ vs. SMSE, which corresponds to $pH\ 8.18 \pm 0.62$.

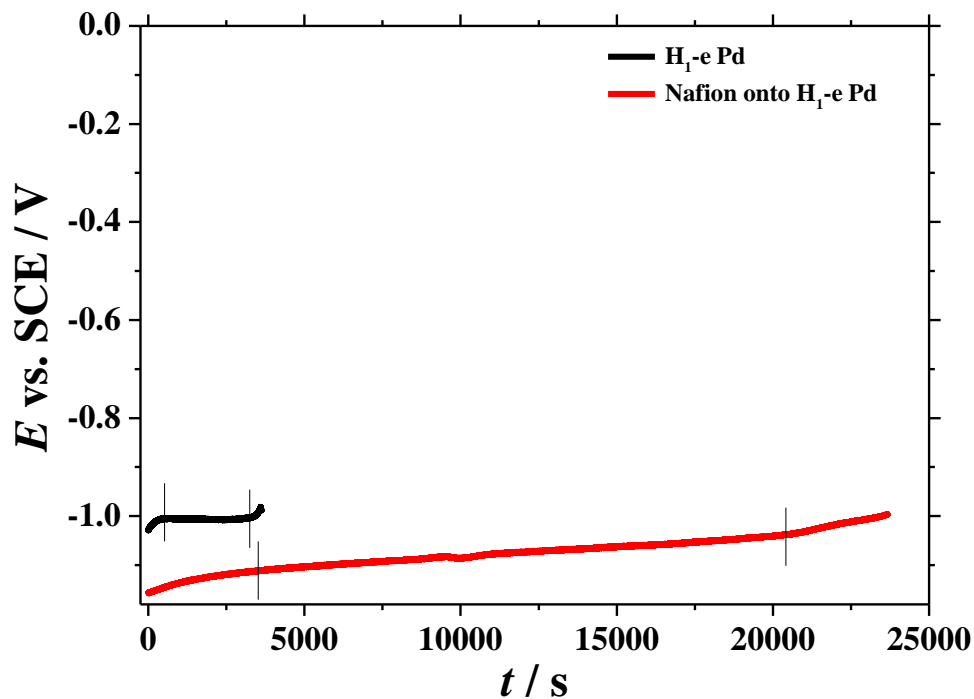


Figure 5.5: Potentiometric measurement of a H_1 -e Pd film ($Q_{dep} = 2500\ \mu C$) deposited onto a $250\ \mu m$ diameter Pt disc electrode, in aerated aCSF brain fluid ($pH\ 7$) at $25^\circ C$, immediately after hydrogen was loaded into the Pd nanostructure.

5.2. Polypyrrole (ppy)

5.2.1. Polypyrrole electrodeposition

The H₁-e Pd film was coated with polypyrrole using a three electrode system: a H₁-e Pd film ($Q_{\text{dep}} = 2500 \mu\text{C}$) deposited onto a 250 μm diameter Pt disc electrode as the working electrode, SCE as the reference electrode and a Pt mesh as the counter electrode. The coating process was carried out electrochemically using cyclic voltammetry for three scans between 0.0 and 1.2 V vs. SCE in aqueous solution of 0.05 M of pyrrole + 0.2 M K₂SO₄ at room temperature and 100 mV s⁻¹. Then the coated electrode was washed with deionised H₂O [108]. Figure 5.6 shows the current dropping during the second and third cycles of the voltammetry indicating the successful deposition of polypyrrole, with most surface sites on the H₁-e Pd surface blocked in the first cycle.

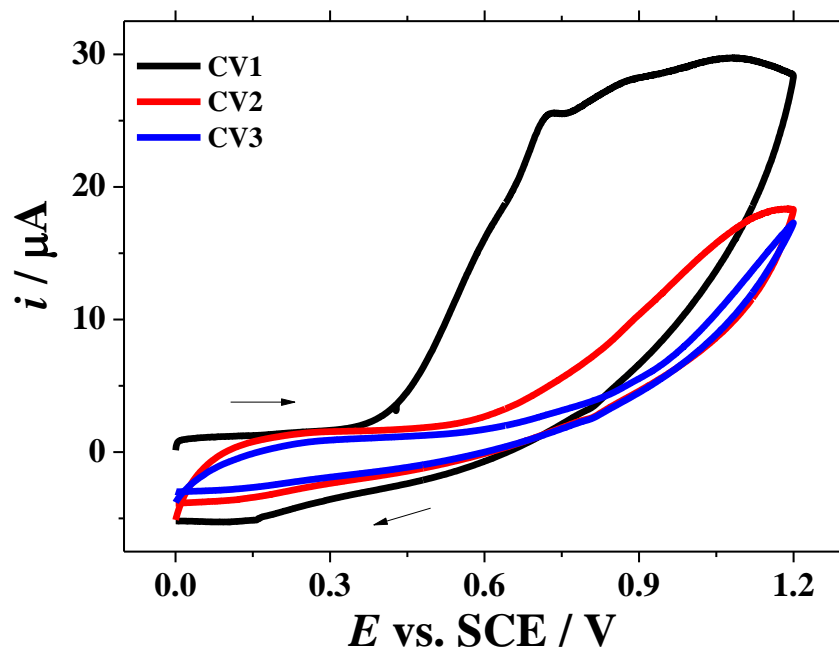


Figure 5.6: Cyclic voltammograms for the deposition of polypyrrole onto a H₁-e Pd film ($Q_{\text{dep}} = 2500 \mu\text{C}$) itself deposited onto a 250 μm diameter Pt disc electrode, in aqueous solution of 0.05 M of pyrrole + 0.2 M K₂SO₄ at 100 mV s⁻¹ and room temperature. CV1, 2 and 3 reflect the first, second and third cycles..

The polypyrrole coating was then passivated, as described by Tietje-Girault *et al.* [108], using cyclic voltammetry between 0.0 and -1.2 V vs. SCE in a fresh background electrolyte 0.2 M K₂SO₄ at room temperature and 100 mV s⁻¹ as shown in **Figure 5.7**. This passivation process was executed to keep the metal in its reduced form. Equation 3.4 will be used to calculate the thickness of the polypyrrole coating.

$$thickness = \frac{Q_{dep} \cdot Mwt}{nF\rho A} \tag{3.4}$$

where Q_{dep} is the charge passed during the polypyrrole electrodeposition, which can be obtained by integrating the curve of the current-potential electrodeposition then dividing by the scan rate. Assuming all of the charge represents the formation of polypyrrole, the obtained thickness of the polypyrrole layer onto the H₁-e Pd film is 315 nm.

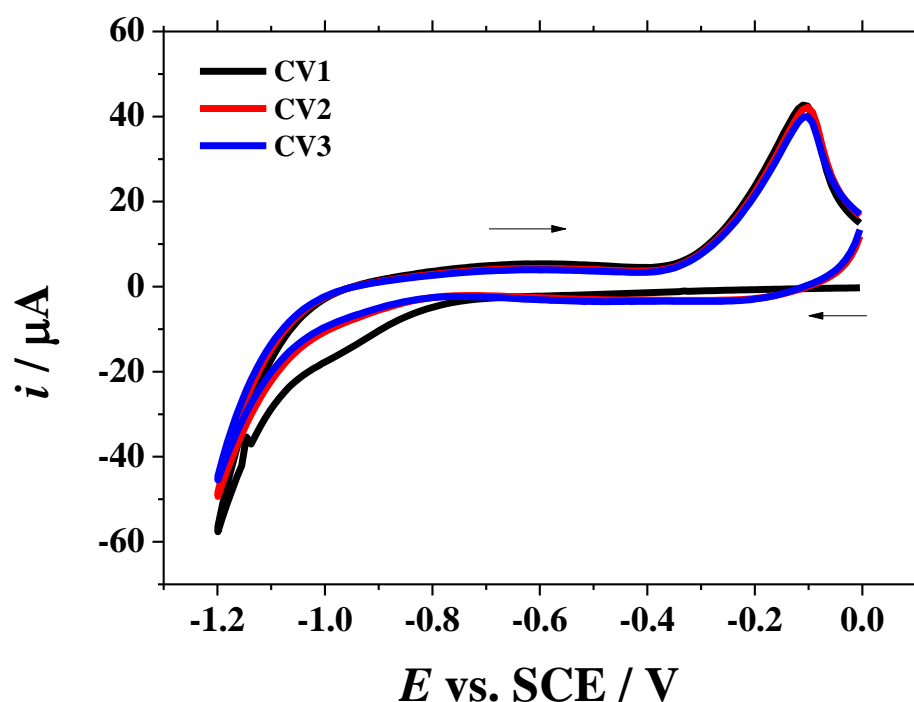


Figure 5.7: Cyclic voltammograms recorded to passivate the polypyrrole layer deposited on a H₁-e Pd film ($Q_{dep} = 2500 \mu\text{C}$) itself deposited onto a 250 μm diameter Pt disc electrode, in a fresh aqueous solution of 0.2 M K₂SO₄ at room temperature and 100 mV s⁻¹. CV1, CV2 and CV3 reflect the first, second and third cycles.

5.2.2. Polypyrrole: SEM imaging

The nanostructured Pd was compared with and without the polypyrrole coat using SEM images. In **Figure 5.8**, it can be seen that the scanning electron microscopy images confirm that the H₁-e Pd film is not damaged by the polypyrrole electrodeposition process. Comparing the SEM images of the coated and bare electrode shows the formation of the polymer film over the electrode. The dimples (**Figure 5.8** b and c) were only observed after deposition of polypyrrole but they unexpectedly also appeared on the glass.

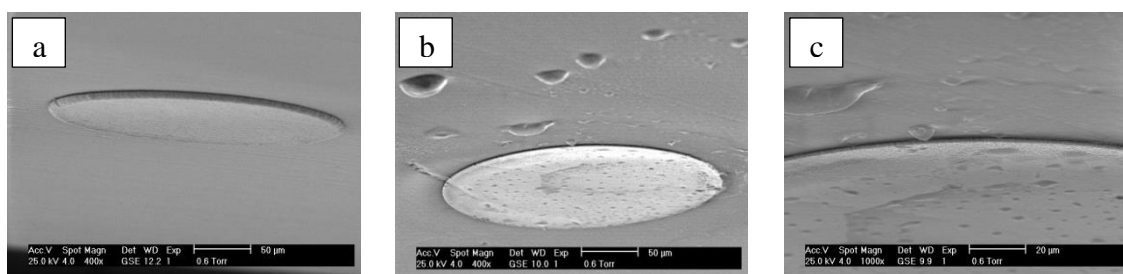


Figure 5.8: Scanning electron microscopy images (tilt angle 70°) of a bare H₁-e Pd film (a), and H₁-e Pd film with polypyrrole layer (b and c) with different magnifications (in a and b the scale bar equals 50 μm and in c it equals 20 μm). The H₁-e Pd films were each deposited with $Q_{\text{dep}} = 2500 \mu\text{C}$ onto a 250 μm diameter Pt disc electrode.

5.2.3. Polypyrrole: oxygen blocking

Cyclic voltammetry was used to investigate the viability of the polypyrrole coating in obstructing oxygen to reach the H₁-e Pd *pH* sensor surface. **Figure 5.9** shows the cyclic voltammograms in aerated and deaerated solutions of 0.5 M KCl before and after depositing the polypyrrole coating onto the H₁-e Pd *pH* sensor.

The cyclic voltammetry was done in presence and absence of O₂ before and after applying the polypyrrole coating. The potential range was chosen from the double layer region to the required potential of HPd formation between +0.3 V to -0.7 V vs. SCE. Irrespective of the presence or absence of oxygen, the polypyrrole film decreased the voltammetric response of the nanostructured Pd electrode by a factor of circa 20.

The polypyrrole coat appears to significantly hinder the access of oxygen to the surface of the H₁-e Pd film as the current for oxygen reduction (measured at -0.7 V in aerated 0.5 M KCl solution) dropped from -2.066 μ A without polypyrrole to -0.153 μ A in presence of polypyrrole. This should limit the sensitivity of the sensor to oxygen. This indicates the massive ability of polypyrrole coat to block oxygen from reaching the H₁-e Pd pH sensor surface. However, the polypyrrole coating significantly reduced the double layer charging current and this suggests that the nanostructured is no longer accessible to the solution.

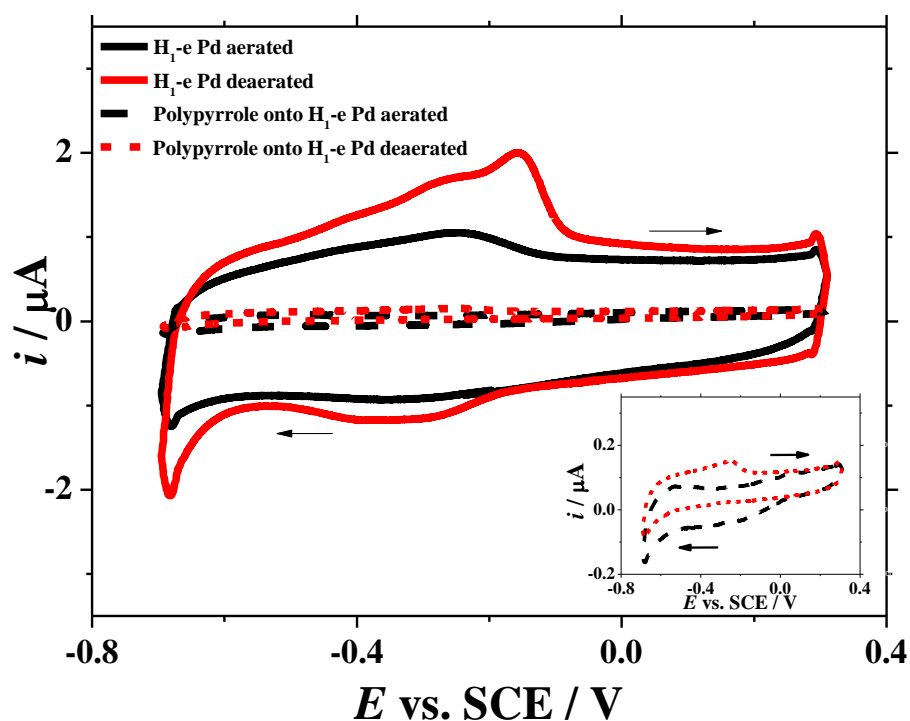


Figure 5.9: The cyclic voltammograms of a H₁-e Pd film ($Q_{\text{dep}} = 2500 \mu\text{C}$) deposited onto a 250 μm diameter Pt disc electrode recorded at 20 mV s^{-1} in 20 ml 0.5 M KCl at 25° C. CVs recorded in aerated solution (black) and in Ar purged (20 min) solution (red), solid lines for uncoated films, dotted lines for film coated with polypyrrole.

5.2.4. Polypyrrole: prevention vs. interfering species

The blocking of interfering species by the polypyrrole coating onto H₁-e Pd film was studied to verify if polypyrrole provides a barrier to potentially contaminating species. **Figure 5.10** shows the cyclic voltammograms for Ru(NH₃)₆³⁺. The cyclic voltammetry shows that the capacitance of the coated H₁-e Pd electrode decreased at -0.25 V from 116 nA to 35 nA after applying the polypyrrole coating, to be very similar to that of the substrate Pt electrode. The coating process significantly influence in the electrochemical active surface area of the modified H₁-e Pd electrode, indicating that the polypyrrole has blocked the H₁-e Pd pores. That may lead to a shortage in the H loading charge Q_{load} , and to a decreased lifetime of the $\alpha+\beta$ transition. This will be discussed in the next section.

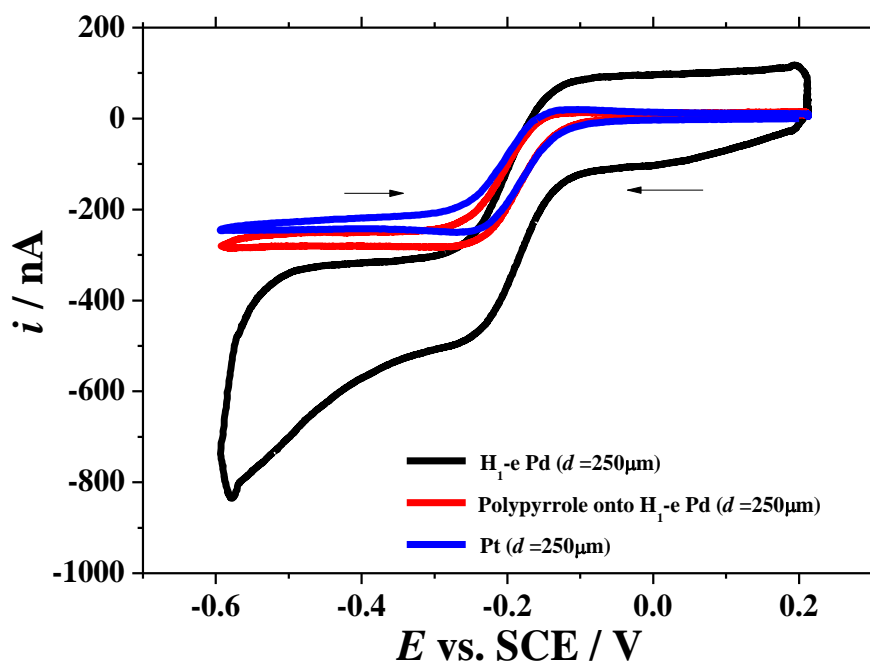


Figure 5.10: Cyclic voltammograms recorded in deaerated 5 mM Ru(NH₃)₆³⁺ + 0.5 M KCl at 25° C at 2 mV s⁻¹ for a H₁-e Pd film ($Q_{\text{dep}} = 2500 \mu\text{C}$) deposited onto a 250 μm diameter Pt disc electrode. CVs recorded without (black) and with a polypyrrole layer of 315 nm thickness (red) onto H₁-e Pd film and with a bare 250 μm diameter Pt disc electrode (blue).

5.2.5. Polypyrrole: effect on hydrogen loading and *pH* sensing

The hydrogen loading of the polypyrrole coated and unmodified H₁-e Pd film ($Q_{\text{dep}} = 2500 \mu\text{C}$) deposited onto a 250 μm diameter Pt disc electrodes were compared. **Figure 5.11** shows the differences between the hydrogen loading chronoamperograms into a H₁-e Pd film before and after the modification in aerated aCSF (*pH* 7).

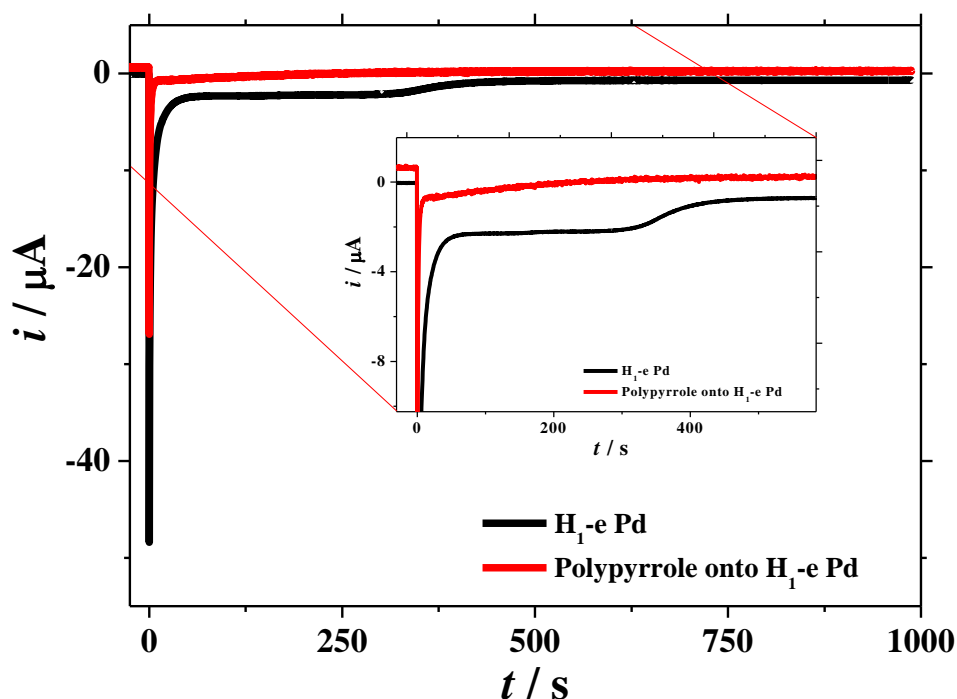


Figure 5.11: Hydrogen loading chronoamperograms into H₁-e Pd film ($Q_{\text{dep}} = 2500 \mu\text{C}$), deposited onto a 250 μm diameter Pt disc electrode, before (black) and after (red) polypyrrole coating in aerated aCSF (*pH* 7), the potential was stepped at $t = 0$ s from the starting potential $E_{\text{strip}} = -0.486$ V to the loading potential $E_{\text{load}} = -1.300$ V vs. SMSE.

The bare H₁-e Pd film needs $t_{\text{load}} = 475$ s to complete the hydrogen loading with a charge $Q_{\text{load}} = -777.06 \mu\text{C}$. This Q_{load} can be converted to the amount of absorbed hydrogen using equation 4.7, giving 8.05×10^{-9} mole of loaded hydrogen.

The polypyrrole coated H_1 -e Pd film does not complete the loading of hydrogen even though the loading time is extended to $t_{load} = 1000$ s, for this duration $Q_{load} = -216.08$ μ C, which corresponds to 2.2×10^{-9} mole of loaded hydrogen. This demonstrates that the polypyrrole with 315 nm thickness does not prevent the absorption of hydrogen absorption into the H_1 -e Pd film but extends the t_{load} , therefore suggesting that the film significantly block the diffusion of hydrogen towards the H_1 -e Pd surface. In 1000 s the polypyrrole coating only allowed 27% of the hydrogen amount that could be absorbed in to the nanostructured Pd.

Figure 5.12 shows the open circuit potential measurement to estimate the pH of aCSF brain fluid (pH 7) using the H_1 -e Pd pH sensor with and without a polypyrrole coating.

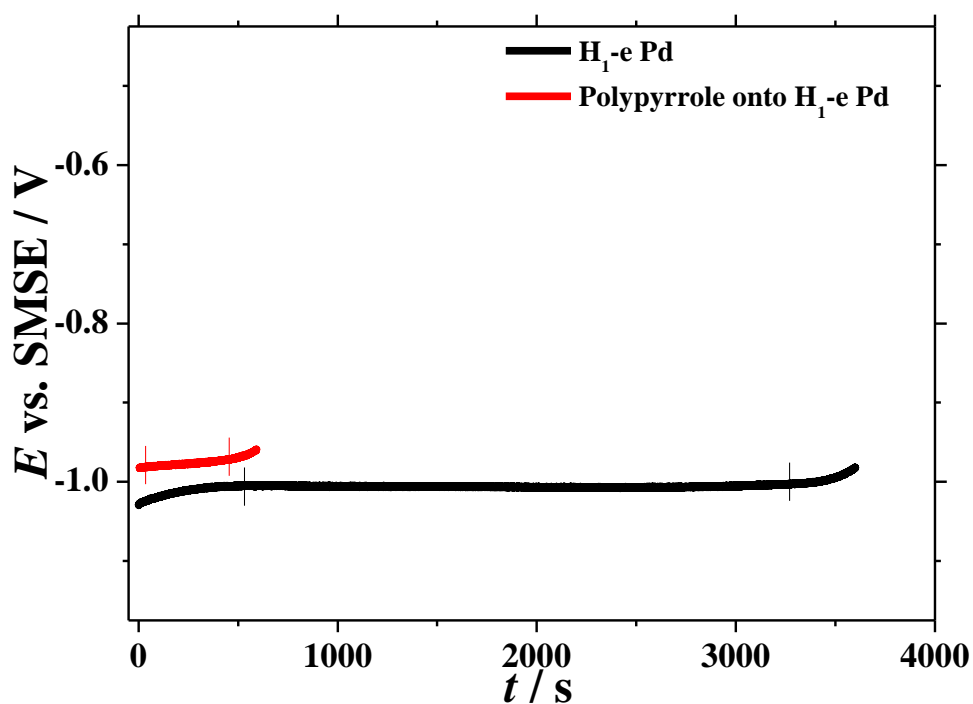


Figure 5.12: Potentiometric measurement of a H_1 -e Pd film ($Q_{dep} = 2500$ μ C) deposited onto a 250 μ m diameter Pt disc electrode, before (black) and after applying the polypyrrole coating (red) in an aerated solution of aCSF brain fluid (pH 7) at 25° C, immediately after hydrogen was loaded into the Pd nanostructure.

It can be inferred from the potentiometric measurement that the polypyrrole coating blocked the majority of the hydrogen from loading into the nanostructure. The evidence for this is the lifetime of $\alpha+\beta$ transition, which has decreased from 2450 s in the unmodified H₁-e Pd sensor to only 420 s in the coated H₁-e Pd sensor. This assumption is in line with the hydrogen loading charge Q_{load} , which is less for the coated electrode than for the uncoated electrode, showing that little hydrogen has been loaded into the palladium lattice. This contrasts with what was observed in section 5.1.4, when the lifetime of the $\alpha+\beta$ transition was extended after the H₁-e Pd electrode was covered with Nafion.

Moreover, the $\alpha+\beta$ transition of the unmodified H₁-e Pd shows a reasonable plateau with an average potential $E_{\text{Pd-H}}$ of -1.004 ± 0.001 V vs. SMSE corresponding to pH 6.99 ± 0.02 . The $\alpha+\beta$ transition of the polypyrrole modified H₁-e Pd electrode does not show a plateau but a slope which gives a large error. The $E_{\text{Pd-H}}$ at the $\alpha+\beta$ transition period has been calculated to be -0.976 ± 0.004 V vs. SMSE corresponding to pH 6.52 ± 0.07 .

5.3. Polyaniline (PANI)

5.3.1. Polyaniline electrodeposition

The H₁-e Pd film was coated with aniline using a three electrodes system: a H₁-e Pd film ($Q_{\text{dep}} = 2500 \mu\text{C}$) deposited onto a 250 μm diameter Pt disc electrode as the working electrode, SCE as the reference electrode and a Pt mesh as the counter electrode. The deposition of conducting polyaniline (PANI) was carried out electrochemically using cyclic voltammetry for twenty scans between -0.25 and +1.2 V vs. SCE at 50 mV s^{-1} in 0.2 M pure aniline + 1 M H₂SO₄ at room temperature [120]. **Figure 5.13** shows the current growing with the number of voltammetric cycles thus indicating the successful formation of new polyaniline layer over the previous layer.

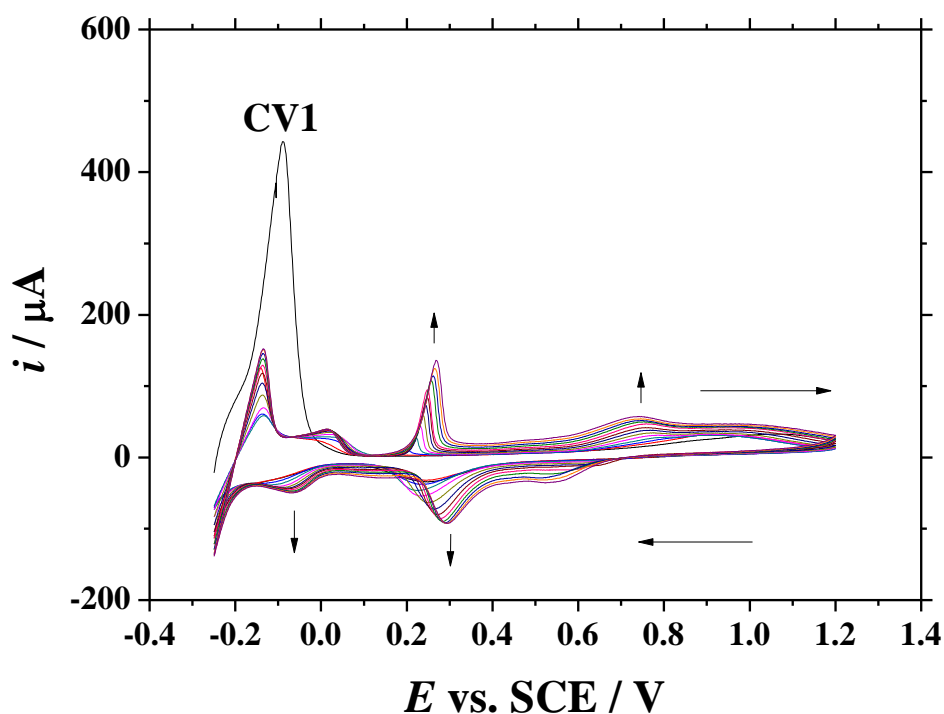


Figure 5.13: Cyclic voltammograms for the deposition of polyaniline at room temperature onto a H₁-e Pd film ($Q_{\text{dep}} = 2500 \mu\text{C}$) itself deposited onto a 250 μm diameter Pt disc electrode, in 0.2 M pure aniline + 1 M H₂SO₄ at 50 mV s^{-1} .

The peaks located between 0.2 and 0.3 V vs. SCE consistent with the redox chemistry of polyaniline and confirm the coating of the H₁-e Pd film with polyaniline.

5.3.2. Polyaniline: SEM imaging

The nanostructured Pd was compared with and without the polyaniline coating using SEM images. In **Figure 5.14** it can be seen that the scanning electron microscopy images confirm that the H₁-e Pd film is not damaged by the polyaniline coating and is still visible under the coating, even though the electrodeposition process involves the oxidation of the nanostructured Pd. Furthermore, it can be noted that the coating has not just covered the electrode surface but has also covered the glass around the H₁-e Pd film. This makes it difficult to calculate the coating thickness for the charge passed. The polyaniline coating appears to be thinner than the H₁-e Pd film (2.2 μm), as the H₁-e Pd film can be observed underneath the polyaniline coating in Figure 5.14.

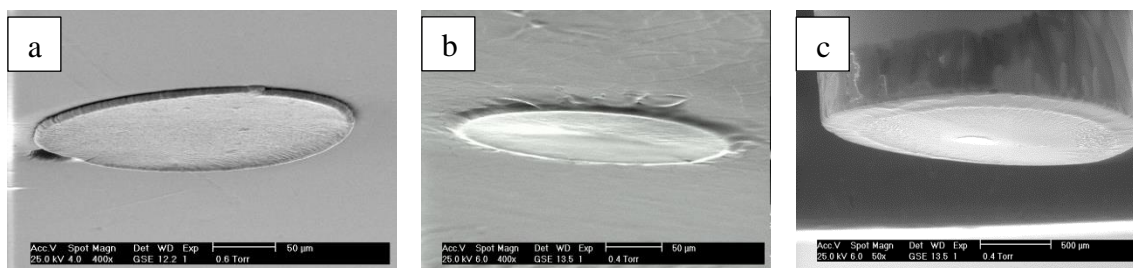


Figure 5.14: Scanning electron microscopy images with different magnifications (a, b equals 50 μm and c equals 500 μm) at tilt angle 70° of a H₁-e Pd film ($Q_{\text{dep}} = 2500 \mu\text{C}$) deposited onto a 250 μm diameter Pt disc electrode before (left), and after the electrodeposition via 20 cycles of polyaniline (middle and right).

5.3.3. Polypolyaniline: oxygen blocking

The ability of the polyaniline coating to obstruct oxygen diffusion towards the H₁-e Pd surface was investigated via cyclic voltammetry. **Figure 5.15** shows the cyclic voltammograms in aerated and deaerated solutions of 0.5 M KCl before and after the depositing polyaniline onto the H₁-e Pd pH sensor.

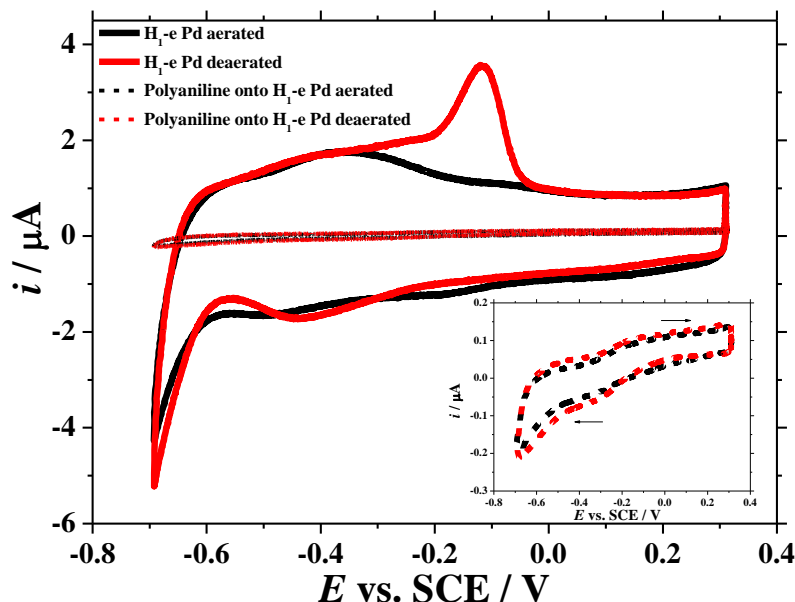


Figure 5.15: The cyclic voltammograms of a H₁-e Pd film ($Q_{\text{dep}} = 2500 \mu\text{C}$) deposited onto a 250 μm diameter Pt disc electrode recorded at 20 mV s^{-1} in 20 ml 0.5 M KCl at 25° C. CVs recorded in aerated solution (black) and in Ar purged (20 min) solution (red), solid lines for uncoated films, dotted lines for films coated with polyaniline.

It can be seen from the voltammograms that the modification has significantly blocked the electrode surface as the double layer charging current is greatly decreased. Moreover, the peaks typical of Pd hydrogen region do not appear on the coated electrode voltammograms. This therefore suggests that the polyaniline layer blocked the diffusion of hydrogen towards the H₁-e Pd film surface. Also, the voltammograms show the massive ability of the coating to block O₂ from reaching the H₁-e Pd pH sensor surface, as the current is nearly equal in aerated or deaerated solutions. This is in contrast with the other modifications performed in this study, which showed a large increase in current in presence of oxygen.

5.3.4. Polyaniline: prevention vs. interfering species

Figure 5.16 shows the cyclic voltammograms for $\text{Ru}(\text{NH}_3)_6^{3+}$ that was used as interfering molecules to assess the blocking ability of the polyaniline coating.

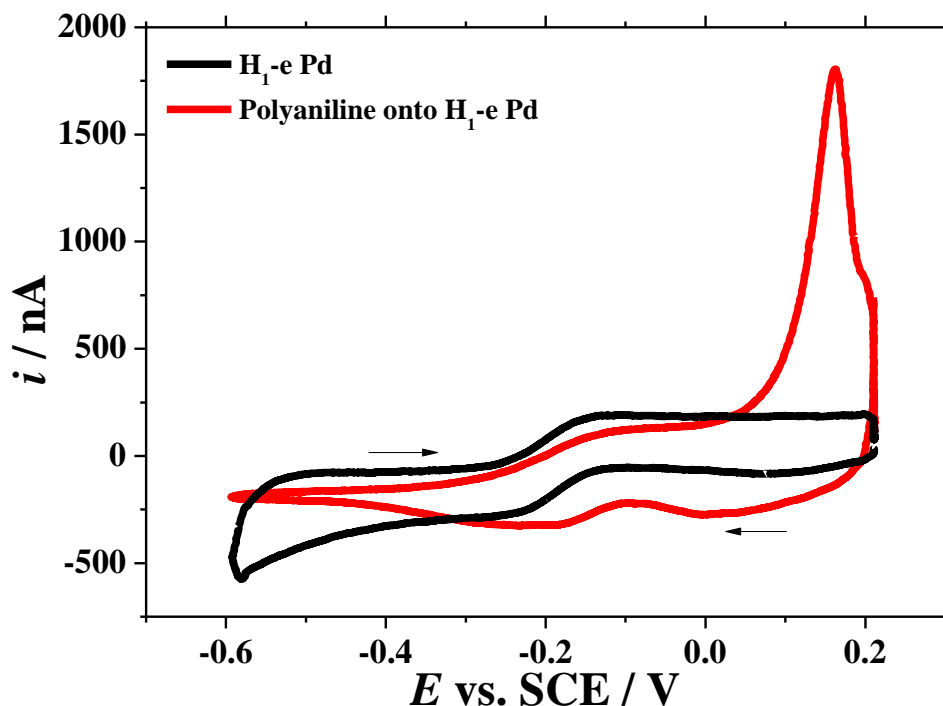


Figure 5.16: Cyclic voltammograms recorded in 5 mM $\text{Ru}(\text{NH}_3)_6^{3+}$ + 0.5 M KCl at 25°C at 2 mV s^{-1} for a $\text{H}_1\text{-e Pd}$ film ($Q_{\text{dep}} = 2500 \mu\text{C}$) deposited onto a 250 μm diameter Pt disc electrode. CVs recorded without (black) and with a polyaniline layer (red) onto $\text{H}_1\text{-e Pd}$ film.

The distinguished shape of the ruthenium cyclic voltammogram has been lost with appearance of a large peak of PANI oxidation approximately at 0.16 V vs. SCE after the modification. The current of the modified electrode has increased slightly around -0.3 V vs. SCE but is clearly much smaller between -0.6 and -0.3 V. This electrochemical behaviour is similar to the cyclic voltammogram of polyaniline [168]. This means that

the polyaniline has the ability to work as an insulator against the interfering species and possibly can prevent them from reaching the surface of the Pd nanostructure.

5.3.5. Polyaniline: effect on hydrogen loading and pH sensing

The loading of hydrogen into H_1 -e Pd films with and without the polyaniline modification was performed in aerated aCSF (pH 7). **Figure 5.17** shows the differences between the hydrogen loading chronoamperograms with and without the polyaniline coating.

The chronoamperograms show that the polyaniline coated H_1 -e Pd film does not reach complete hydrogen loading even though the loading time is extended to $t_{load} = 1000$ s; in comparison the bare H_1 -e Pd film only needs 475 s to complete hydrogen loading. The loading charges Q_{load} of the polyaniline coated H_1 -e Pd film and of the bare H_1 -e Pd film equal -669.83 and -777.06 μC respectively. The hydrogen amounts loaded into modified and uncoated H_1 -e Pd films were calculated using equation 4.7 as 6.94×10^{-9} and 8.05×10^{-9} mole respectively. This indicates that the polyaniline is slowing hydrogen diffusion down to the H_1 -e Pd surface (or blocking absorption sites), as the coating only allows 86% of the hydrogen amount that can be absorbed into the Pd nanostructure in over 1000 s. That is consistent with the reduced currents for the hydrogen region peaks seen in **Figure 5.15**. So, the $\alpha+\beta$ transition lifetime of the coated electrode is expected to be shorter than that of the bare H_1 -e Pd film.

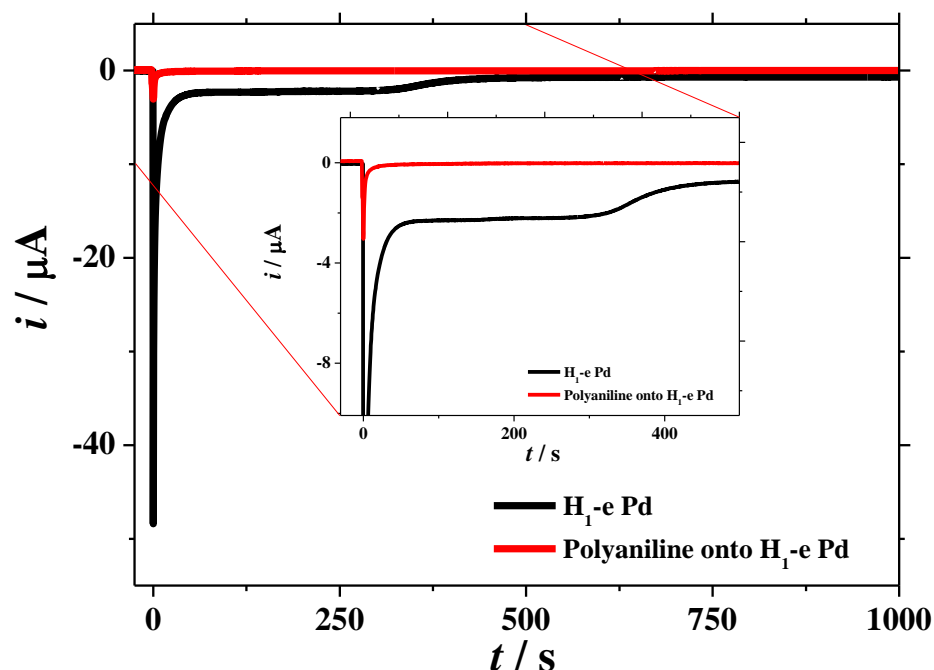


Figure 5.17: Hydrogen loading chronoamperograms into H_1 -e Pd film ($Q_{\text{dep}} = 2500 \mu\text{C}$), deposited onto a $250 \mu\text{m}$ diameter Pt disc electrode, without (black) and with (red) polyaniline coating in aerated aCSF ($pH 7$). The potential was stepped at $t = 0$ s from the starting potential $E_{\text{strip}} = -0.486$ V to the loading potential $E_{\text{load}} = -1.300$ V vs. SMSE.

Figure 5.18 shows the open circuit potential measurement to estimate the pH of aCSF brain fluid ($pH 7$) using the H_1 -e Pd pH sensor with and without polyaniline coating.

The potentiometric measurement indicates that the polyaniline coating shortens the useful life of the H_1 -e Pd pH sensor. The $\alpha+\beta$ transition lifetime is found to decrease from 2740 s in the unmodified H_1 -e Pd sensor to only 310 s in the coated H_1 -e Pd sensor. This observation is in line with the result shown in **Figure 5.17**, as the hydrogen loading charge Q_{load} of the coated electrode is smaller than that of the uncoated electrode. This means that the efficiency of hydrogen loading into the Pd nanostructure is less with the coated electrode. This may be attributed to the multi oxidation and protonation states of polyaniline [168], with hydrogen reacting with polyaniline instead of diffusing through to reach the H_1 -e Pd film. This reduces the amount of hydrogen loaded into the palladium lattice and leads to a shorter $\alpha+\beta$ transition lifetime.

Moreover, the open circuit potential of the coated electrode shows a poor accuracy with large error compared to the unmodified electrode. The average potential $E_{\text{Pd-H}}$ of the modified pH sensor equals -0.736 ± 0.008 V vs. SMSE corresponding to $pH 2.46 \pm 0.14$. That is far off the expected response of the unmodified H_1 -e Pd film, that shows reasonable plateau with average potentials $E_{\text{Pd-H}} = -1.004 \pm 0.001$ V vs. SMSE corresponding to $pH 6.99 \pm 0.02$. The large error in $E_{\text{Pd-H}}$ of the coated sensor could be attributable to the redox reactions of the coating that include protonation of the polyaniline layer [169]. This will decrease the local pH surrounding the H_1 -e Pd pH sensor and cause a large error in potential.

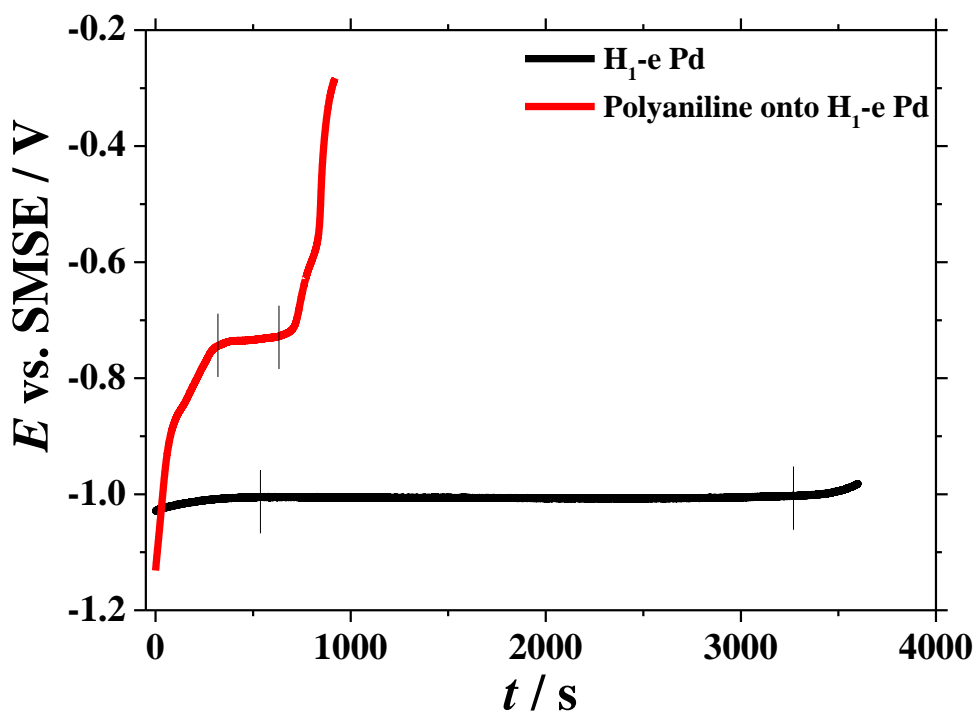


Figure 5.18: Potentiometric measurement of a H_1 -e Pd film ($Q_{\text{dep}} = 2500 \mu\text{C}$) deposited onto a $250 \mu\text{m}$ diameter Pt disc electrode, without (black) and with (red) polyaniline coating in an aerated solution of aCSF brain fluid ($pH 7$) at 25°C , immediately after hydrogen was loaded into the Pd nanostructure.

5.4. Diazonium salt (Boc)

5.4.1. Diazonium salt (Boc): electrografting

The Pd nanostructured film was coated with diazonium salt (Boc) using a three electrode system: a H₁-e Pd film ($Q_{\text{dep}} = 2500 \mu\text{C}$) deposited onto a 250 μm diameter Pt disc electrode as the working electrode, Ag/AgCl as the reference electrode, and a Pt mesh as the counter electrode.

Figure 5.19 shows the cyclic voltammetry of the nanostructured Pd being coated with the diazonium salt (Boc) by cycling the potential. The literature states that a broad reduction peak appears in the coating voltammogram, reducing in current with progressive cycles, since the surface electrode is passivated by an organic layer of diazonium salt (Boc) [129, 170, 171].

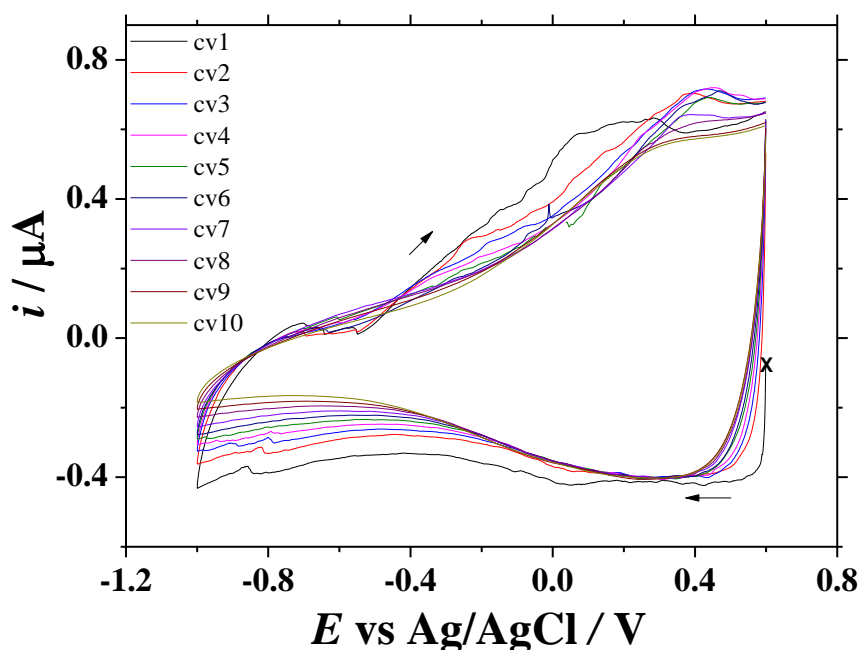


Figure 5.19: Cyclic voltammograms for the electrodeposition of diazonium salt (Boc) at room temperature onto a H₁-e Pd film ($Q_{\text{dep}} = 2500 \mu\text{C}$) deposited onto a 250 μm diameter Pt disc electrode, in 5 mM 4-(N-Boc-aminomethyl) benzene diazonium tetrafluoroborate salt in 5 mM CH₃CN containing 250 mM TBATFB at 50 mV s⁻¹. CVs reflect the cycle order.

A reduction peak can be seen in **Figure 5.19** about 0.4 V vs. Ag/AgCl, which is consistent with the electrochemical formation of a diazonium layer on the electrode. However, the reduction peak current remains stable throughout ten cycles. This suggests that the H₁-e Pd surface is not completely blocked as the coating process continues.

The diazonium salt (Boc) coating is a monolayer that connects to the H₁-e Pd film surface by a covalent bond. Therefore, it was unnecessary to calculate the thickness for this coating. To our knowledge, no one has reported the electrografting of diazonium salt (Boc) on the nanostructured Pd. According to the literature it has only been attached to glassy carbon and gold electrodes [129, 170, 171].

5.4.2. Diazonium salt (Boc): SEM imaging

The nanostructured Pd was compared before and after the coating with diazonium salt (Boc) using SEM images. In **Figure 5.20**, it can be seen that the scanning electron microscopy images confirm that the H₁-e Pd film is still visible under the coating. However, it can be noted that there is some cracking and peeling in the H₁-e Pd film after the modification. The electrodeposition involves the oxidation of Pd leading to damage of the *pH* sensor. This could explain the reason of the unblocking of the H₁-e Pd film during the coating process, as the Pd will be oxidised as the potential sweeping toward more positive leaving behind an uncoated Pd surface, which will be coated with the next cycle toward negative scan, leads to continuous the coating process.

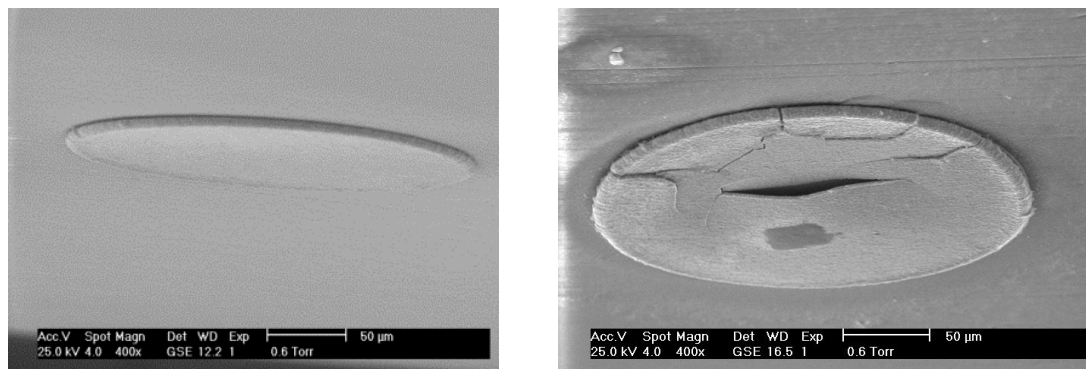


Figure 5.20: Scanning electron microscopy images (tilt angle 70°) with scale bar equals 50 μm of a H₁-e Pd film ($Q_{\text{dep}} = 2500 \mu\text{C}$) deposited onto a 250 μm diameter Pt disc electrode before (left) and after the electrodeposition of a diazonium salt (Boc) monolayer (right).

5.4.3. Diazonium salt (Boc): oxygen blocking

Cyclic voltammetry was used to investigate the viability of the diazonium salt (Boc) coating in obstructing oxygen to reach the H₁-e Pd electrode surface. **Figure 5.21** shows the cyclic voltammograms in aerated and deaerated solution of 0.5 M KCl before and after the coating process with the organic monolayer of diazonium salt (Boc).

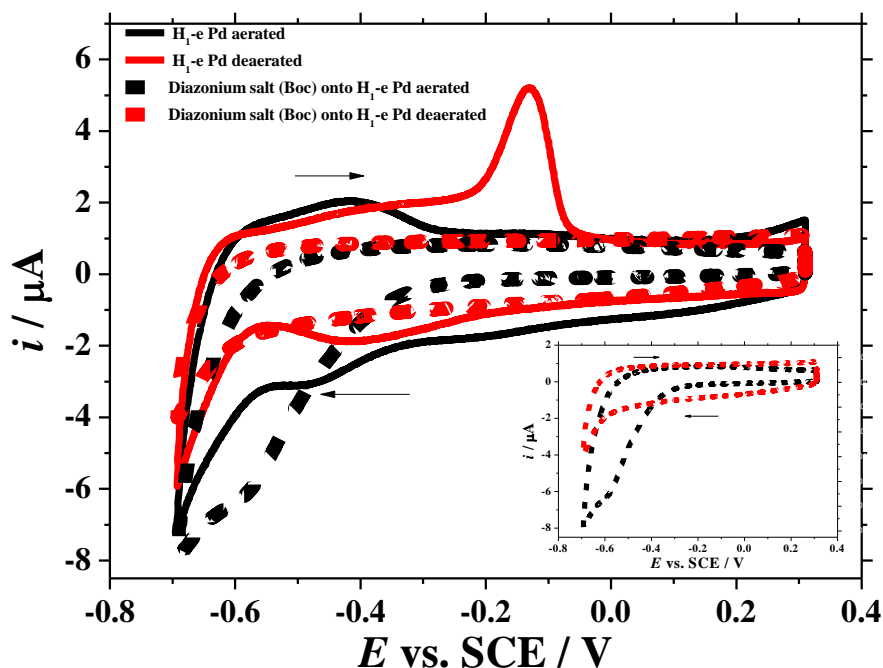


Figure 5.21: The cyclic voltammograms of a H_{1-e} Pd film ($Q_{\text{dep}} = 2500 \mu\text{C}$) deposited onto a $250 \mu\text{m}$ diameter Pt disc electrode recorded at 20 mV s^{-1} in $20 \text{ ml } 0.5 \text{ M KCl}$ at 25°C . CVs recorded in aerated solution (black), and in Ar purged (20 min) solution (red), solid lines for uncoated films, dotted lines for film coated with the diazonium salt (Boc) coating.

The voltammograms confirm that the diazonium salt has successfully modified the surface of the Pd nanostructure, as the electrochemical features of the H_{1-e} Pd film surface change after the modification under the same experimental conditions. The oxygen reduction reaction current was compared using the same electrode before and after the coating at -0.70 V vs. SCE in the aerated solution to assess the effect of the diazonium salt (Boc) on the oxygen reduction reaction. It was found that the current increased from $-7.2 \mu\text{A}$, to $-8.1 \mu\text{A}$ after the modification. This indicates the inability of the diazonium salt (Boc) coating to block the sites where oxygen can be reduced on the H_{1-e} Pd *pH* sensor surface, but it actually activates oxygen reduction reaction.

Moreover, the hydrogen desorption peak located at about -0.3 V vs. SCE is disappearing in deaerated solutions after the modification, therefore suggesting the blocking of

hydrogen adsorption sites by the diazonium salt (Boc) coating. Furthermore, the capacitive current at 0.1 V decreases from 1.26 μA to 0.44 μA after the coating, confirming that the coating process has decreased the electrochemical active surface area of the $\text{H}_1\text{-e Pd}$ electrode.

5.4.4. Diazonium salt (Boc): prevention against interfering species

The prevention of interfering species was studied by the cyclic voltammetry of $\text{Ru}(\text{NH}_3)_6^{3+/2+}$, used as a test interfering molecule to assess the ability of the diazonium salt (Boc) monolayer to block redox processes.

Figure 5.22 shows the effects in the electrochemical active surface area of the modified $\text{H}_1\text{-e Pd}$ electrode after the coating process. The double layer charging current of the $\text{H}_1\text{-e Pd}$ electrode decreased 22% from 121 nA to 94 nA at -0.3 V vs. SCE. Even though, the capacitance has decreased after the coating, it is still closer to the $\text{H}_1\text{-e Pd}$ film than to the substrate Pt electrode capacitance; this indicates that the monolayer of diazonium salt only partially blocks the electroactive area. This will be discussed in the next section. Moreover, the slope of the wave is less, which means that the electron transfer is slower after modification with diazonium salt (Boc).

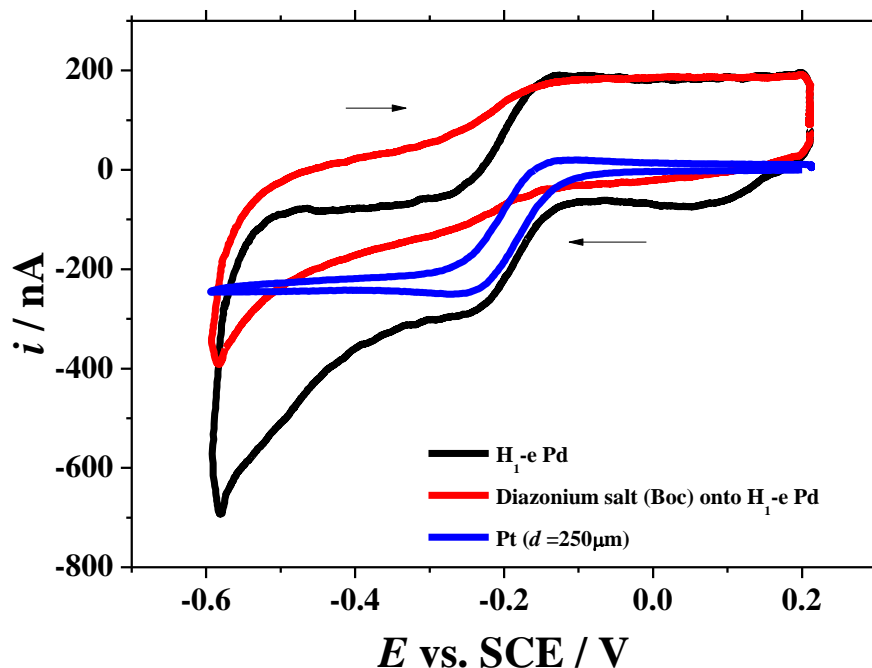


Figure 5.22: Cyclic voltammograms recorded in 5 mM $\text{Ru}(\text{NH}_3)_6^{3+}$ + 0.5 M KCl at 25° C at 2 mV s^{-1} for a $\text{H}_1\text{-e Pd}$ film ($Q_{\text{dep}} = 2500 \mu\text{C}$) deposited onto a 250 μm diameter Pt disc electrode. CVs recorded before (black) and after the modification with the diazonium salt (Boc) coating (red) onto $\text{H}_1\text{-e Pd}$ film. The blue CV was recorded in the base Pt substrate electrode.

5.4.5. Diazonium salt (Boc), effect on hydrogen loading and *pH* sensing

The effect of the diazonium salt (Boc) coating on the hydrogen loading process was monitored using an aerated aCSF (*pH* 7). **Figure 5.23** shows the comparison of hydrogen loading into $\text{H}_1\text{-e Pd}$ films with and without the modification. The chronoamperograms show that the coated $\text{H}_1\text{-e Pd}$ film needs about 625 s to reach a complete hydrogen loading, compared to the bare $\text{H}_1\text{-e Pd}$ film which needs only 475 s,

suggesting that the loading rate was decreased by the modification. The loading charges Q_{load} of the coated diazonium salt (Boc) and the bare H_1 -e Pd film were found to be $-742.18 \mu C$ and $-777.09 \mu C$ respectively. The amount of hydrogen loaded into the modified and unmodified H_1 -e Pd films was calculated using equation 4.7 yielding 7.69×10^{-9} and 8.05×10^{-9} mole respectively. This indicates that the diazonium salt (Boc) allows about 91% of the H loading in 130% of the loading time period t_{load} compared to the unmodified electrode.

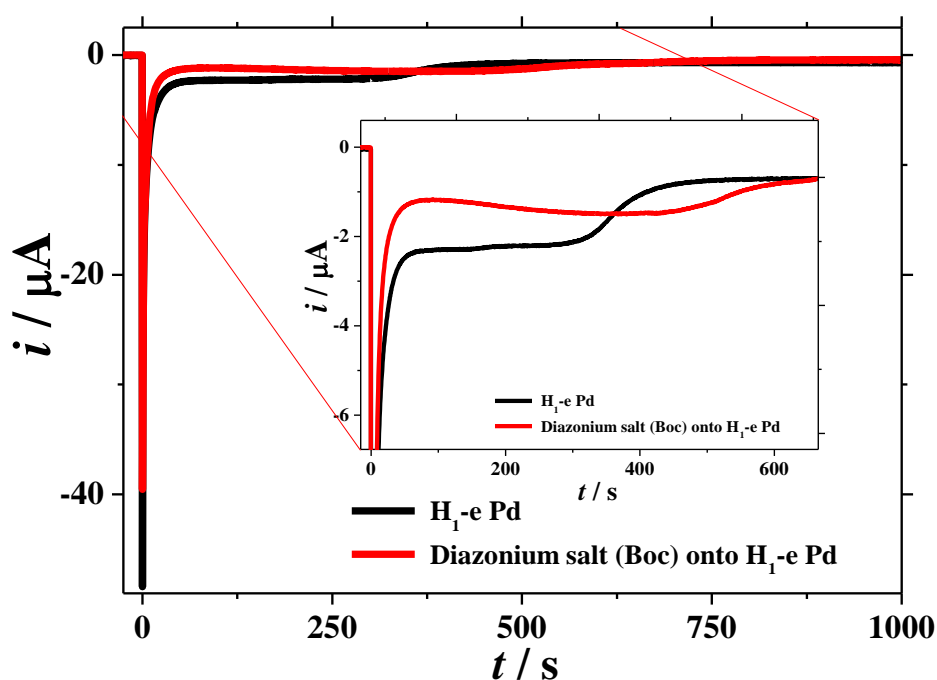


Figure 5.23: Hydrogen loading chronoamperograms into H_1 -e Pd film ($Q_{dep} = 2500 \mu C$), deposited onto a $250 \mu m$ diameter Pt disc electrode, without (black) and with (red). The modification of diazonium salt (Boc) coating in aerated aCSF ($pH 7$), the potential was stepped at $t = 0$ s from the starting potential $E_{strip} = -0.486$ V to the loading potential $E_{load} = -1.300$ V vs. SMSE.

The open circuit potential measurement was carried out to estimate the pH with and without the modification. **Figure 5.24** shows the potentiometric experiment in aCSF brain fluid ($pH 7$) using the H_1 -e Pd pH sensor with and without diazonium salt (Boc)

coating. The potentiometric measurement indicates that the modification has improved the performance of the H_1 -e Pd pH sensor by increasing the $\alpha+\beta$ transition lifetime - as it increased from 2450 s with bare H_1 -e Pd film to 4270 s after the coating.

This can be attributed to the coating's ability to slow down the rate of the oxygen reduction reaction, but this observation is not consistent with the increased oxygen reduction reaction current seen in presence of diazonium salt (Boc) coat, **Figure 5.21**.

However, the potentiometric measurement of the coating electrode shows poor accuracy with a large error in comparison to the unmodified electrode, as the average potential E_{Pd-H} of the modified pH sensor equals -0.867 ± 0.081 V vs. SMSE, corresponding to pH 4.67 ± 1.36 . That is not close to the response of the unmodified H_1 -e Pd film which shows a reasonable plateau with an average potential $E_{Pd-H} = -1.004 \pm 0.001$ V vs. SMSE corresponding to pH 6.99 ± 0.02 .

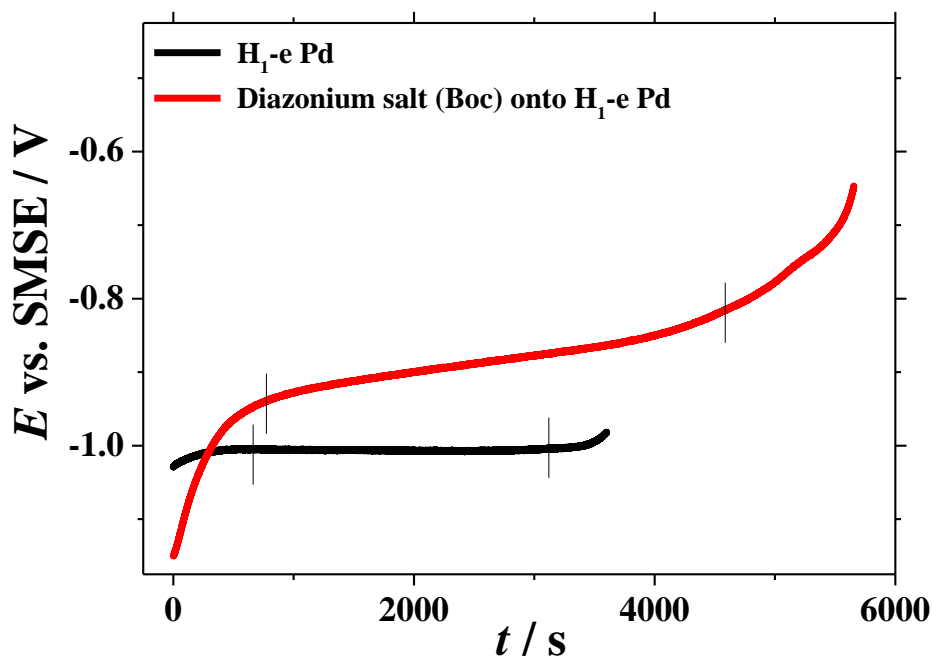


Figure 5.24: Potentiometric measurement of a H_1 -e Pd film ($Q_{dep} = 2500 \mu C$) deposited onto a $250 \mu m$ diameter Pt disc electrode, without (black) and with (red) diazonium salt (Boc) coating in an aerated solution of aCSF brain fluid (pH 7) at $25^\circ C$, immediately after hydrogen was loaded into the Pd nanostructure.

5.5. 1,2-diaminobenzene in H₂SO₄ (OPD)

5.5.1. 1,2-diaminobenzene in H₂SO₄: electrodeposition

The Pd nanostructured film was coated with 1,2-diaminobenzene (i.e. o-1,2-phenylenediamine OPD) in a three electrode system: a H₁-e Pd film ($Q_{\text{dep}} = 2500 \mu\text{C}$) deposited onto a 250 μm diameter Pt disc was the working electrode. SCE was the reference electrode and a Pt mesh the counter electrode. The reported coating procedure involves oxidation of the monomer which could lead to damage of the nanostructured Pd [172]. Thus, the potential range and the number of cycles required were adjusted to prevent extended oxidation of the H₁-e Pd film. So, the potential was scanned from -0.2 to +1.1 V in the first cycle to initiate the oxidation of the monomer and then from -0.2 to + 0.6 V vs. SCE in the second cycle, instead of cycling 25 times between -0.2 to + 1.1 V vs. SCE. **Figure 5.25** shows the voltammetry for coating 1,2-diaminobenzene onto the H₁-e Pd film. The film does not appear to have blocked the electrode as there is a clear hydrogen region and the oxide formation is not affected, even during the second cycle.

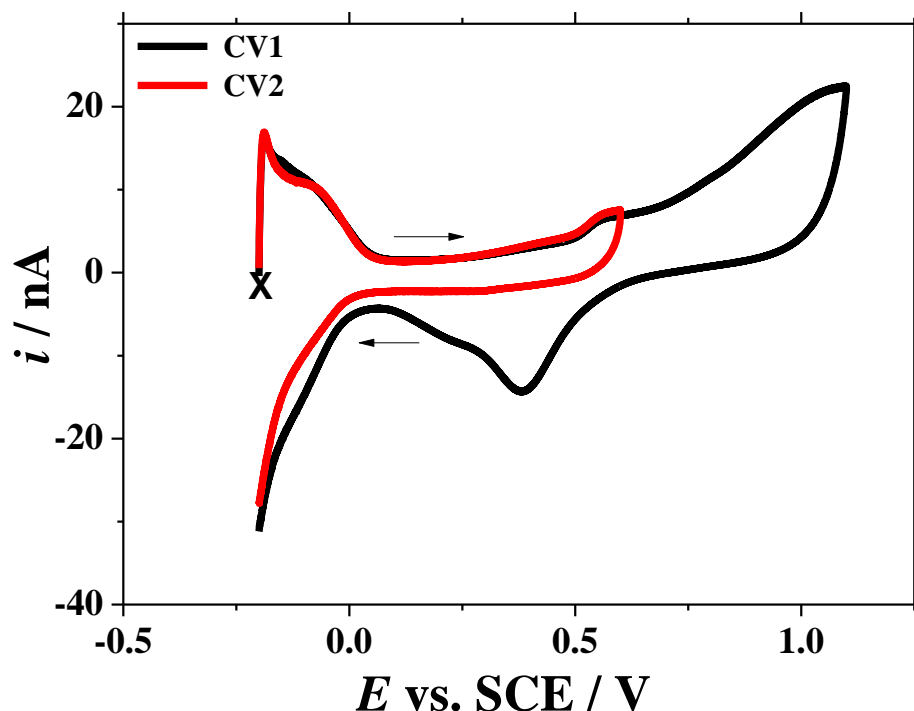


Figure 5.25: Voltammograms recorded while electrodepositing 1,2-diaminobenzene onto a H₁-e Pd film ($Q_{\text{dep}} = 2500 \mu\text{C}$) deposited onto a 250 μm diameter Pt disc electrode, in 10 mM 1,2-diaminobenzene in 0.5 M H₂SO₄, at 50 mV s⁻¹ at room temperature. CV1 and CV2 reflect the first and the second cycles.

5.5.2. 1,2-diaminobenzene in H₂SO₄: SEM imaging

The nanostructured Pd was compared before and after the modification process to monitor any variations onto the surface of the H₁-e Pd film. **Figure 5.26** shows the SEM images before and after the 1,2-diaminobenzene coating. The scanning electron microscopy images confirm that the H₁-e Pd film is not damaged by the coating and is still visible after the modification, even though the electrodeposition process involves oxidising the nanostructured Pd. This is likely to be due to the adjustment of the potential range and scanning times during the coating procedure. The coating cannot be seen in the micro scale of the SEM images in **Figure 5.26**, it appears to be thinner than the H₁-e Pd film (2.2 μm), as the H₁-e Pd film can be observed underneath the coating as expected for a thin coating.

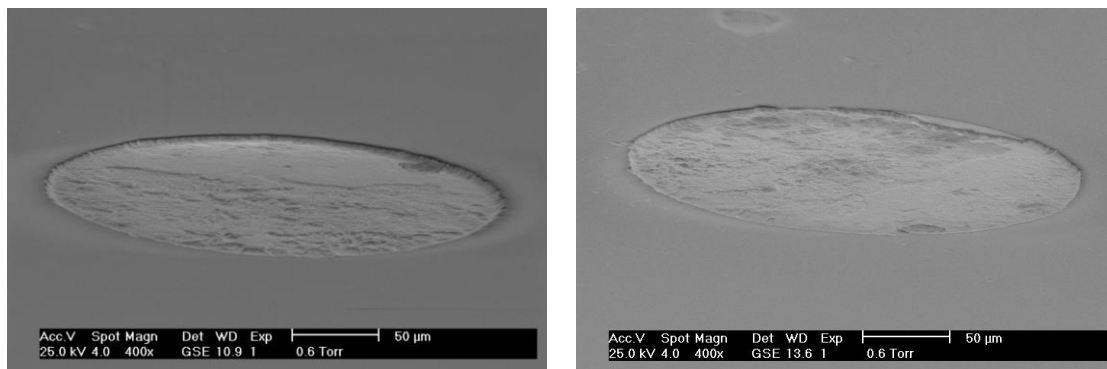


Figure 5.26: Scanning electron microscopy images (tilt angle 70°) with scale bar equals $50\ \mu\text{m}$ of a $\text{H}_1\text{-e Pd}$ film ($Q_{\text{dep}} = 2500\ \mu\text{C}$) deposited onto a $250\ \mu\text{m}$ diameter Pt disc electrode before (left), and after the electrodeposition of 1,2-diaminobenzene (right).

5.5.3. 1,2-diaminobenzene in H_2SO_4 : oxygen blocking

The obstruction of oxygen from reaching the $\text{H}_1\text{-e Pd}$ surface was investigated in phosphate buffer pH 7. **Figure 5.27** shows the cyclic voltammetry of aerated and deaerated test solutions before and after applying the 1,2-diaminobenzene coating onto the nanostructured Pd. The voltammetric features of the $\text{H}_1\text{-e Pd}$ film have changed after the coating process, indicating the coating formation. The capacitance at 0.1 V was slightly reduced after the modification. Also, it can be seen from the voltammograms that the modification is showing moderate oxygen blocking, as the current of the modified electrode in O_2 presence is $-1.438\ \mu\text{A}$ at $-0.7\ \text{V}$ vs. SCE. That is similar to the $-2.166\ \mu\text{A}$ recorded for the unmodified electrode in absence of O_2 . This means that the coating did not completely prevent oxygen from reacting with the surface.

Moreover, the double layer charging current is almost symmetric before and after the coating, therefore it is expected that the modification did not affect the number of hydrogen adsorption sites.

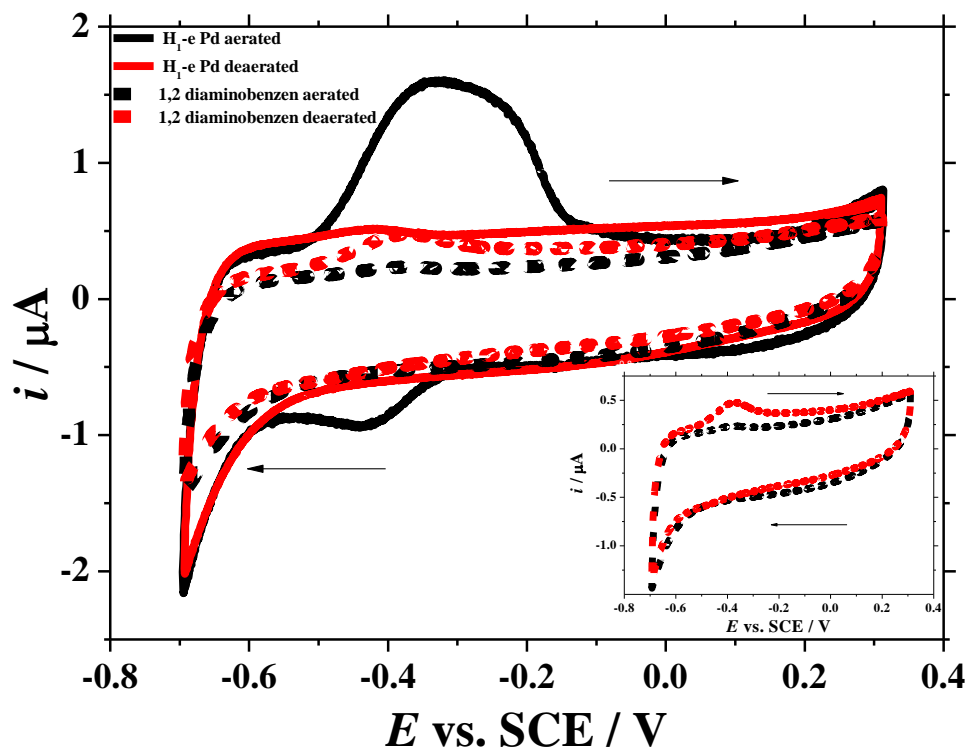


Figure 5.27: The cyclic voltammograms of a H_1-e Pd film ($Q_{\text{dep}} = 2500 \mu\text{C}$) deposited onto a $250 \mu\text{m}$ diameter Pt disc electrode recorded at 20 mV s^{-1} in 20 phosphate buffer pH 7 at 25°C in aerated solution (black), and in Ar purged (20 min) solution (red); solid lines for uncoated film, dotted lines for film covered with the 1,2-diaminobenzene coating.

5.5.4. 1,2-diaminobenzene in H_2SO_4 : prevention vs. interfering species

The prevention of interfering species to reach the H_1-e Pd pH sensor surface was studied by the cyclic voltammetry of $\text{Ru}(\text{NH}_3)_6^{3+/2+}$, used as interfering molecules to verify if 1,2-diaminobenzene coating onto H_1-e Pd provides a barrier to potentially contaminating species. **Figure 5.34** shows that similar between the voltammetry of $\text{Ru}(\text{NH}_3)_6^{3+/2+}$ is barely affected by the process of the coating. The wave is at the same

potential, the limiting current appears similar and the double layer charging current is also similar. Also the reversibility of the process is unaffected.

The coating process therefore did not seem to affect the electrochemical active surface area of the H₁-e Pd electrode. This indicates that the 1,2-diaminobenzene coating does not block the electroactive area of the H₁-e Pd electrode.

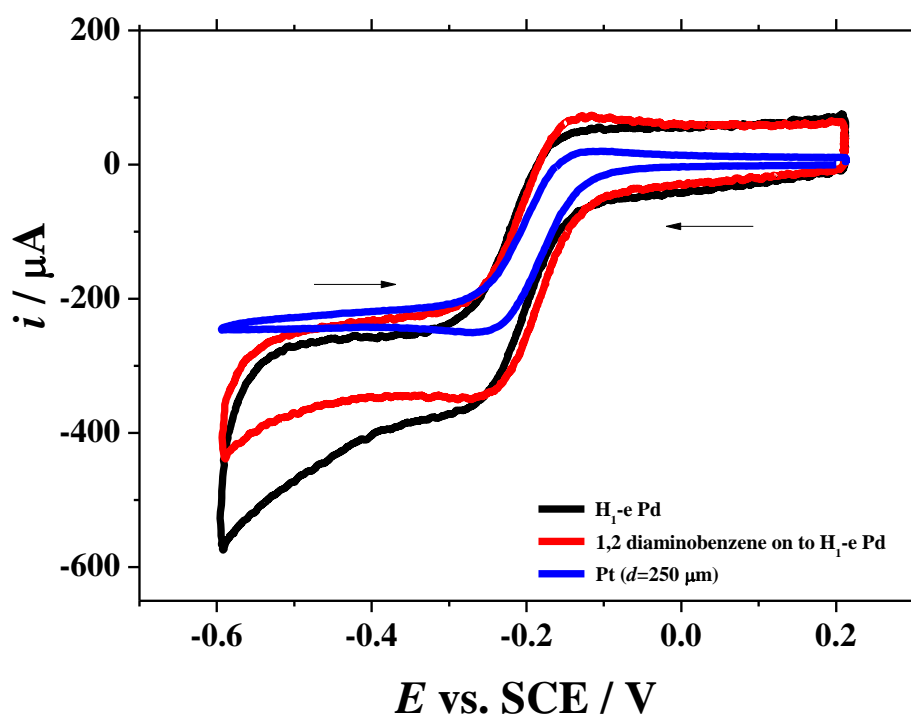


Figure 5.28: Cyclic voltammograms recorded in 5 mM Ru(NH₃)₆³⁺ + 0.5 M KCl at 25° C at 2 mV s⁻¹ for a H₁-e Pd film ($Q_{\text{dep}} = 2500 \mu\text{C}$) deposited onto a 250 μm diameter Pt disc electrode. CVs recorded without (black) and with 1,2-diaminobenzene coating (red) onto H₁-e Pd film, comparing to a 250 μm diameter Pt disc electrode (blue).

5.5.5. 1,2-diaminobenzene in H₂SO₄: hydrogen loading and *pH* sensing

Figure 5.29 shows the hydrogen loading into the unmodified and modified H₁-e Pd electrode in aerated aCSF solution (*pH* 7). This comparison can be used to monitor the effect of the 1,2-diaminobenzene coating on the hydrogen loading.

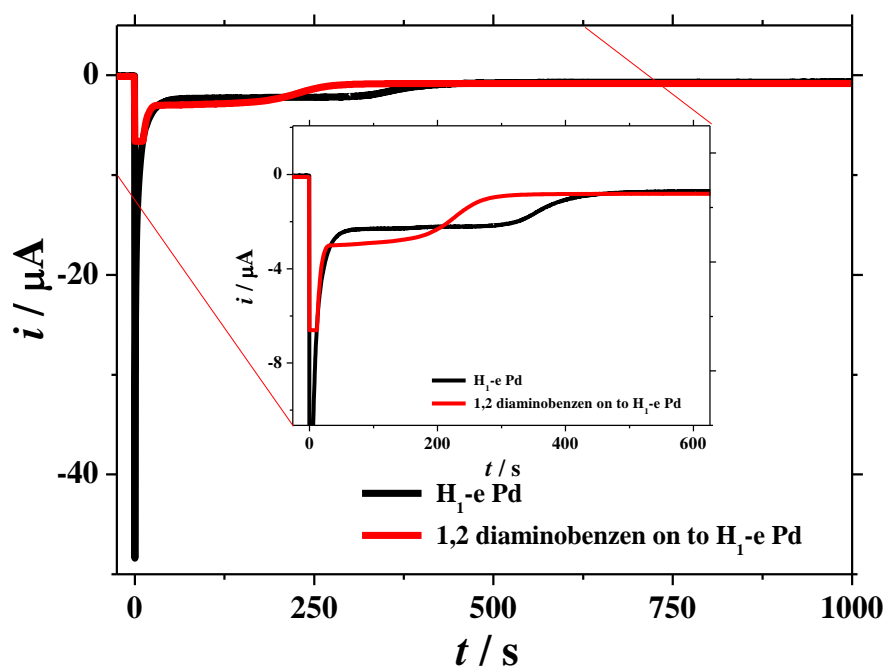


Figure 5.29: Hydrogen loading chronoamperograms into H₁-e Pd film ($Q_{\text{dep}} = 2500 \mu\text{C}$), deposited onto a 250 μm diameter Pt disc electrode, without (black) and with (red) the modification of 1,2-diaminobenzene in aerated aCSF (*pH* 7). The potential was stepped at $t = 0$ s from the starting potential $E_{\text{strip}} = -0.486$ V to the loading potential $E_{\text{load}} = -1.300$ V vs. SMSE.

The full hydrogen loading into a bare electrode requires 475 s with loading charge $Q_{\text{load}} = -777.06 \mu\text{C}$ – equivalent to 8.05×10^{-9} mole of hydrogen loaded. However, the complete loading of hydrogen into the coated electrode was 310 s with loading charge $Q_{\text{load}} = -527 \mu\text{C}$ – equivalent to 5.46×10^{-9} mole of hydrogen loaded.

The *pH* estimation of aerated aCSF solution (*pH* 7) was compared using the open circuit potential conditions with and without the 1,2-diaminobenzene coating onto the

palladium nanostructure. **Figure 5.30** shows open circuit potential before and after the modification.

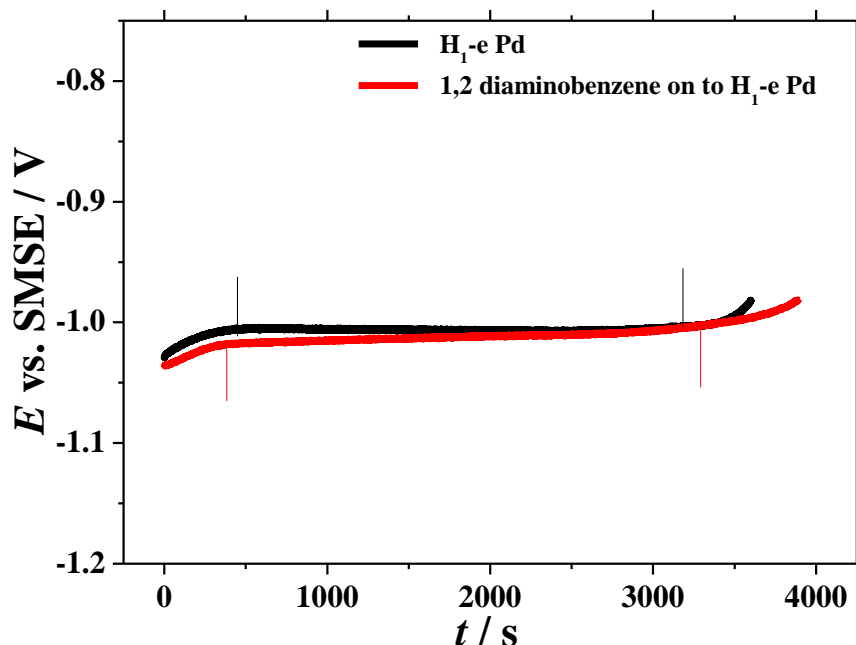


Figure 5.30: Potentiometric measurement of a H_1 -e Pd film ($Q_{\text{dep}} = 2500 \mu\text{C}$) deposited onto a $250 \mu\text{m}$ diameter Pt disc electrode, without (black) and with (red) 1,2-diaminobenzene coating in an aerated solution of aCSF brain fluid ($pH 7$) at 25°C , immediately after hydrogen was loaded into the Pd nanostructure.

The potentiometric measurements confirm the coat formation, as the lifetime of the $\alpha+\beta$ transition increased from 2470 to 2910 s after the coating. Furthermore, the coated H_1 -e Pd film has maintained the plateau that was lost when modifying with Nafion, polypyrrole and diazonium salt (Boc). As the average potential $E_{\text{Pd-H}}$ of the coated sensor equals $-1.011 \pm 0.008 \text{ V vs. SMSE}$ that corresponds to $pH 7.10 \pm 0.13$. On the other hand, the $\alpha+\beta$ transition of the bare H_1 -e Pd shows a plateau with minimal error, as the average potentials $E_{\text{Pd-H}}$ equals $-1.004 \pm 0.001 \text{ V vs. SMSE}$, which corresponds to $pH 6.99 \pm 0.02$.

5.6. Poly (phenylene oxide)

5.6.1. Poly (phenylene oxide): electrodeposition

The Pd nanostructure film was coated with poly (phenylene oxide) by a three electrode system: a H₁-e Pd film ($Q_{\text{dep}} = 2500 \mu\text{C}$) deposited onto a 250 μm diameter Pt disc electrode as the working electrode, SCE as the reference electrode, and a Pt mesh as the counter electrode. The electrochemical coating process was carried out by scanning the potential through two cycles. **Figure 5.31** shows the cyclic voltammetry of the nanostructured Pd coating with the poly (phenylene oxide).

The peak that appears about 0.4 V vs. SCE corresponds to the nanostructure Pd oxidation, which requires reducing the scanning cycle as much as possible. While the peak about 0.65 V during the coating process corresponds to the phenol oxidation – that will be suppressed in the next cycle [122]. This indicates the successful formation of an insulating film of poly (phenylene oxide) onto the nanostructured Pd surface. This suggests that poly (phenylene oxide) layer has covered the electrode surface. Assuming that the current only comes from the coating deposition, the deposition charge of the first cycle is equal to 3.9×10^{-7} C, this corresponds to a (phenylene oxide) coat thickness of 6.8 nm, using equation 3.4.

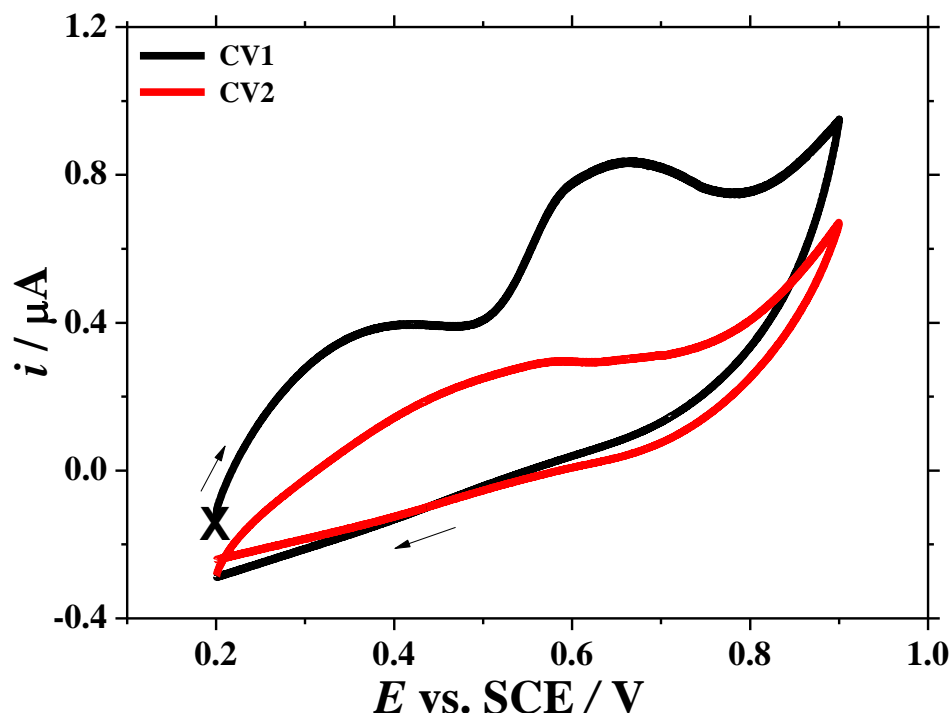


Figure 5.31: The electrodepositing cyclic voltammetry of poly(phenylene oxide) at room temperature onto a $\text{H}_1\text{-e}$ Pd film ($Q_{\text{dep}} = 2500 \mu\text{C}$) deposited onto a $250 \mu\text{m}$ diameter Pt disc electrode at room temperature in 50 mM phenol, 150 mM disodium hydrogen orthophosphate pH 7 buffer, at 50 mV s^{-1} . CV1 and CV2 reflect the first and second cycles.

5.6.2. Poly (phenylene oxide): SEM imaging

The nanostructured Pd was compared before and after the modification with poly (phenylene oxide) to monitor any variations onto the surface of the $\text{H}_1\text{-e}$ Pd film. Figure 5.32 shows the SEM images, which confirm that the $\text{H}_1\text{-e}$ Pd film is not damaged by the poly (phenylene oxide) coating and is still visible after the modification, even though the electrodeposition process involves the oxidation of Pd film. Furthermore, the coating cannot be seen on the scale of the SEM images, demonstrating that the poly (phenylene oxide) is a very thin coating.

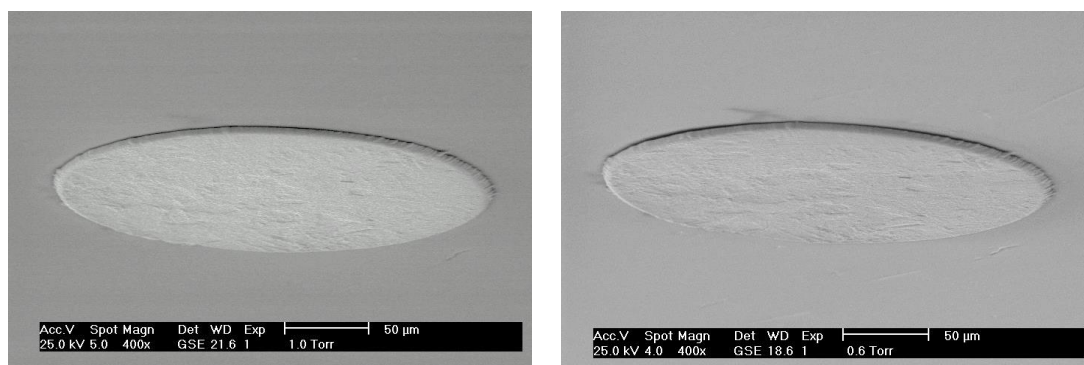


Figure 5.32: Scanning electron microscopy images (tilt angle 70°) with scale bar equals 50 μm of a $\text{H}_1\text{-e Pd}$ film ($Q_{\text{dep}} = 2500 \mu\text{C}$) deposited onto a 250 μm diameter Pt disc electrode before (left), and after the electrodeposition process to cover the electrode surface with poly (phenylene oxide) (right).

5.6.3. Poly (phenylene oxide): oxygen blocking

Cyclic voltammetry was used to investigate the viability of the poly (phenylene oxide) layer in blocking oxygen from reaching the $\text{H}_1\text{-e Pd}$ pH sensor surface. **Figure 5.33** shows cyclic voltammograms in aerated and deaerated solutions of phosphate pH 7 buffer with and without the modification of poly (phenylene oxide).

The oxygen reduction reaction current was compared with and without the poly (phenylene oxide) coat at -0.3 V vs. SCE to display the variance in the current. The current in aerated solution is almost identical to that in the deaerated solution $-0.85 \mu\text{A}$ without the modification and $-0.84 \mu\text{A}$ with the coated electrode. This indicates that the poly (phenylene oxide) coating did not prevent the O_2 reaching the $\text{H}_1\text{-e Pd}$ pH sensor surface.

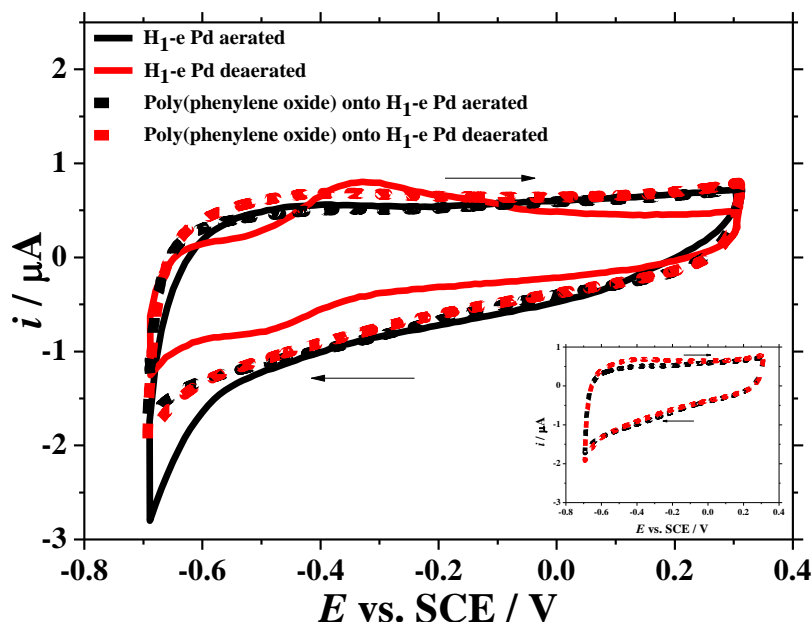


Figure 5.33: The cyclic voltammograms of a H₁-e Pd film ($Q_{\text{dep}} = 2500 \mu\text{C}$) deposited onto a 250 μm diameter Pt disc electrode recorded at 20 mV s^{-1} in 20 ml phosphate pH 7 buffer at 25°C . CVs recorded in aerated solution (black), and in Ar purged (20 min) solution (red). Solid lines for uncoated films, dotted lines for film coated with poly(phenylene oxide).

5.6.4. Poly (phenylene oxide): prevention vs. interfering species

The prevention of interfering species to reach the H₁-e Pd pH sensor surface was studied by the cyclic voltammetry of $\text{Ru}(\text{NH}_3)_6^{3+/2+}$, that was used as interfering molecules to verify if poly(phenylene oxide) coating provides a barrier to potentially contaminating species. **Figure 5.34** shows the similarity between the double layer capacitances before and after the modification. Thus, the coating process does not affect in the electrochemical active surface area of the modified H₁-e Pd electrode. This means that the layer of poly(phenylene oxide) does not block the nanostructured Pd pores and might improve the sensor features. This needs to be confirmed by comparing the hydrogen loading before and after the coating process and will be presented in the next section.

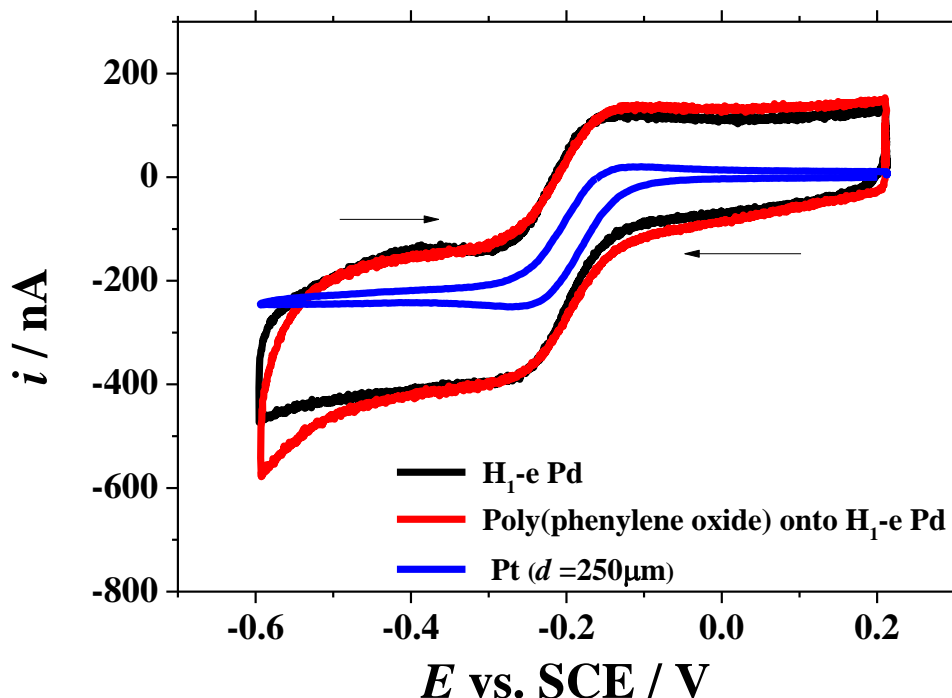


Figure 5.34: Cyclic voltammograms recorded in 5 mM $\text{Ru}(\text{NH}_3)_6^{3+}$ + 0.5 M KCl at 25° C at 2 mV s⁻¹ for a H₁-e Pd film ($Q_{\text{dep}} = 2500 \mu\text{C}$) deposited onto a 250 μm diameter Pt disc electrode. CVs recorded before (black) and after the modification with the poly (phenylene oxide) (red) onto H₁-e Pd film.

5.6.5. Poly (phenylene oxide): H loading and *pH* sensing

The hydrogen was loaded into bare and coated H₁-e Pd films to observe the impact of the poly (phenylene oxide) coating on the loading process. **Figure 5.35** shows the chronoamperograms of hydrogen loading into nanostructured Pd with and without the modification in aerated aCSF solution (*pH* 7).

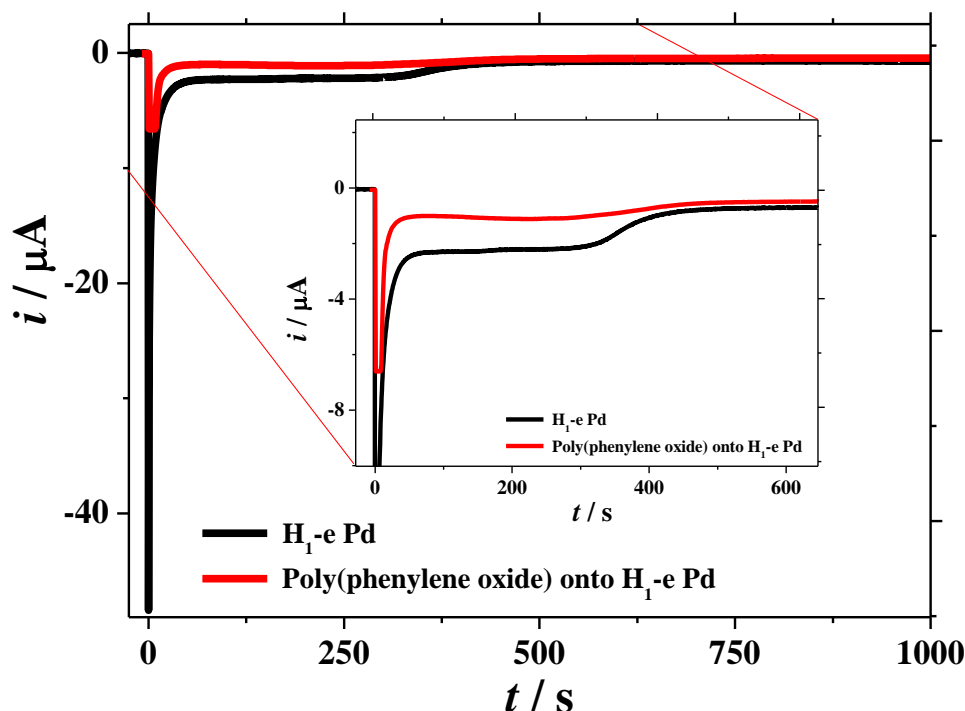


Figure 5.35: Hydrogen loading chronoamperograms into H₁-e Pd film ($Q_{\text{dep}} = 2500 \mu\text{C}$), deposited onto a 250 μm diameter Pt disc electrode. The uncoated H₁-e Pd film (black) and the poly (phenylene oxide) modified electrode (red) were loaded with H in aerated aCSF ($pH 7$); the potential was stepped at $t = 0$ s from the starting potential $E_{\text{strip}} = -0.486$ V to the loading potential $E_{\text{load}} = -1.300$ V vs. SMSE.

The loading charges (Q_{load}) were 302 and 777.06 μC with and without the modification respectively. While the loading time (t_L) was 520 and 475 s to complete hydrogen loading. The amount of loaded hydrogen for the modified and uncoated H₁-e Pd film were calculated using equation 4.7 yielding 3.13×10^{-9} and 8.05×10^{-9} mole respectively. The coating only allows 36.3% of the hydrogen amount that can be absorbed in to the Pd nanostructure. This means that the efficiency of hydrogen loading into the Pd nanostructure is less with the coated electrode. This is reflected in the decrease of the $\alpha + \beta$ transition lifetime for the coated electrode in comparison to the unmodified H₁-e Pd film. **Figure 5.36** shows the open circuit potential measurement to estimate the pH of aCSF brain fluid ($pH 7$) using the H₁-e Pd pH sensor with and without the coating.

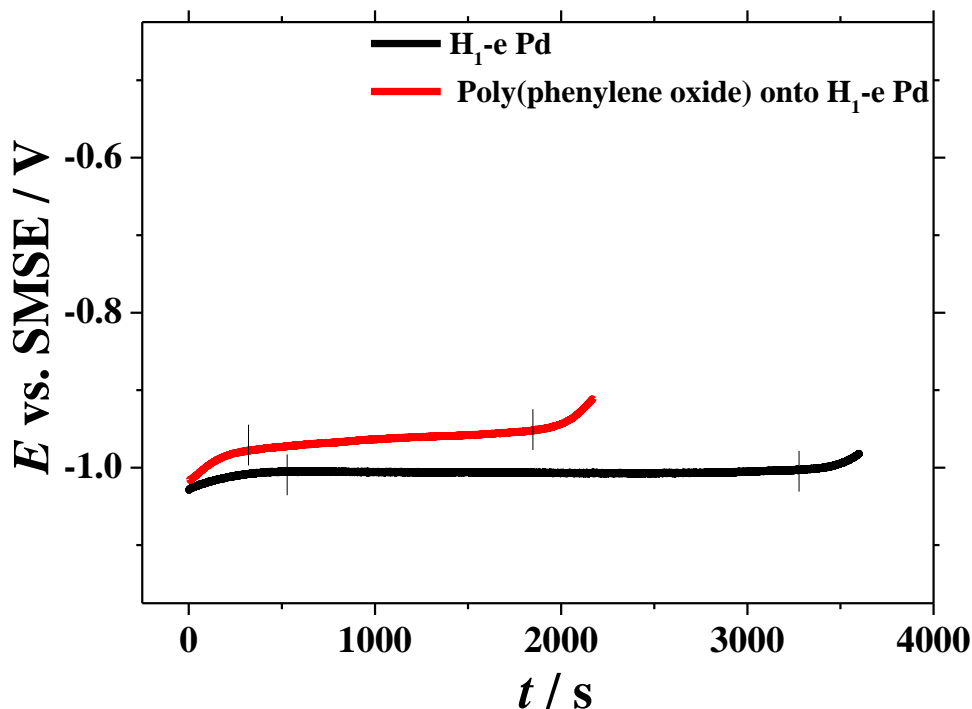


Figure 5.36: Potentiometric measurement of a H_1 -e Pd film ($Q_{\text{dep}} = 2500 \mu\text{C}$) deposited onto a $250 \mu\text{m}$ diameter Pt disc electrode, without (black) and with (red) poly(phenylene oxide) coating in an aerated solution of aCSF brain fluid ($pH 7$) at 25°C , immediately after hydrogen was loaded into the Pd nanostructure.

The potentiometric measurement indicates that covering the electrode with poly(phenylene oxide) will shorten the period H_1 -e Pd can be used as a pH sensor, as the $\alpha+\beta$ transition lifetime decreased from 2740 s with the unmodified H_1 -e Pd sensor to 1515 s with the coated H_1 -e Pd sensor. This is in agreement with what was stated in **Figure 5.35** as the Q_{load} for the coated electrode is less compared to uncoated electrode. Also, the coating shows a weak blocking of O_2 , that will consume hydrogen in the palladium lattice leading to a shorter $\alpha+\beta$ transition lifetime.

Moreover, the open circuit potential of the coated electrode shows a decrease in the accuracy compared to the unmodified H_1 -e Pd film. As the average potential $E_{\text{Pd-H}}$ of the modified pH sensor equals $-0.965 \pm 0.013 \text{ V vs. SMSE}$ correspond to $pH 6.33 \pm 0.22$. This does not match the expected response of the unmodified H_1 -e Pd film, that shows $E_{\text{Pd-H}} = -1.004 \pm 0.001 \text{ V vs. SMSE}$ correspond to $pH 6.99 \pm 0.02$.

5.7. Summary

The previous coatings were chosen as they have been successfully used to modify other electrodes. These coatings can be compared by their differing influence on the $\alpha+\beta$ transition lifetime and the accuracy of the pH measurement. This comparison will show the contribution of the coatings to improving or deteriorating the performance of H₁-e Pd pH sensor.

Table 5.2 shows the electrode performance before and after the modifications.

Table 5.2: The influence of several coatings in the $\alpha+\beta$ transition lifetime and the accuracy of the pH estimation.

Electrode	Coating thickness	$Q_{load} / \mu C$	$\alpha+\beta$ lifetime / s	pH
H ₁ -e Pd film	N/A	-777.1	2450	6.99 ± 0.02
Nafion	30 μm	-309.3	17000	8.18 ± 0.62
Polypyrrole	315 nm	-216.1	420	6.52 ± 0.07
Polyaniline	< 2.2 μm	-669.8	310	2.46 ± 0.14
Diazonium salt (Boc)	Monolayer	-742.2	4270	4.67 ± 1.36
1,2-diaminobenzene	< 2.2 μm	-527.0	2910	7.10 ± 0.13
Poly (phenylene oxide)	6.8 nm	-302.0	1515	6.33 ± 0.22

The comparison between the coatings can be summarized in more details as follows: Nafion has a high ability to block the oxygen and slow the interfering species diffusion, noticeably extending the lifetime of the $\alpha+\beta$ transition, leading to an improvement in the performance of the H₁-e Pd pH sensor. However, Nafion has some disadvantages such as: it cannot be electrodeposited and hence the coating thickness cannot be controlled, it will slow the rate of hydrogen absorption into the nanostructured Pd with longer t_{load} , and it will decrease the accuracy of the sensor, which is an important factor in the biomedical applications. This requires using other more accurate and controllable coatings.

Polypyrrole can be considered as an effective coat for blocking species to the H_1 -e Pd electrode surface, however this includes hydrogen. Therefore, the coating will slow hydrogen diffusion and severely limit absorption into the Pd nanostructure. Hence, polypyrrole is not a suitable coating for the H_1 -e Pd electrode that will be used for brain fluid pH estimation, as the coating inhibits the hydrogen loading into the palladium lattice that is a prerequisite for it to act as a pH sensor.

Polyaniline has some chemical characteristics that can affect the PdH system, as the coating inhibits the hydrogen loading into the palladium lattice and shifts up the average potentials E_{Pd-H} of the $\alpha+\beta$ transition. Therefore, the polyaniline is also not a suitable coating for the H_1 -e Pd electrode that will be used for brain fluid pH estimation.

The diazonium salt coating semi-protects the electrode surface from interfering species. In addition, the coating improved the performance of the H_1 -e Pd pH sensor by increasing the $\alpha+\beta$ transition lifetime. The potentiometric measurement of modified electrode with diazonium salt coating shows a slope in the $\alpha+\beta$ transition such as Nafion, that will lead to errors in the pH estimation.

The 1,2-diaminobenzene is another coating that can be used to improve the H_1 -e Pd sensor. The formation procedure of this coating has been adjusted to avoid the H_1 -e Pd film oxidation by modifying the potential range and the number of the cycles. The calculation of the coating thickness indicates a thick coating (11.4 μm). Although, this coating cannot be seen in SEM image, this means that a part of the charge passed could not reflect the formation of the film but the H_1 -e Pd film oxidation. However, the voltammetry features of H_1 -e Pd surface have changed after the coating process indicating the coating formation. 1,2-diaminobenzene coating has a moderate ability to block oxygen to reach the surface of the pH sensor. The modification improves the sensor features to block the electroactive species as it allows positively charged molecules to interact at the coating reaching to H_1 -e Pd electrode with the rejection of the negatively charged species. The coating reduced the amount of the loading hydrogen into the palladium nanostructured. However, the lifetime of the $\alpha+\beta$ transition was

increased by reducing the hydrogen diffusion rate through the coating. The coated H₁-e Pd film has maintained the plateau that was lost in the other modifications with little error in the *pH* of aerated aCSF.

The poly (phenylene oxide) coating cannot successfully block the oxygen or protect the electrode surface from interfering species, also it allows smaller amounts of hydrogen to absorb into the H₁-e Pd film. Therefore the coating decreased the performance of the H₁-e Pd *pH* sensor by shorting the $\alpha+\beta$ transition lifetime.

Table 5.2 shows a comparison between uncoated H₁-e Pd film that has lifetime equals 2450 s with an error equals ± 0.02 and all the previous coatings. The H₁-e Pd film that coated with Nafion has longest lifetime but with largest error. On the contrary, H₁-e Pd film that was coated with polypyrrole has a reasonable error with short lifetime. Polyaniline coating makes the H₁-e Pd film behaviour worse, since it has a short lifetime and a large error. Diazonium salt (Boc) coating gives the H₁-e Pd film a long lifetime but with a large error. 1,2-diaminobenzene coating onto the H₁-e Pd film makes the lifetime acceptable but with large error. Finally, the poly (phenylene oxide) will be shorted the lifetime and increased the error. To sum up, none of the previous coatings is good to use.

The *pH* of the coated electrodes were calculated using the calibration curve of the uncoated H₁-e Pd electrode. It would be worth recording calibration curves for the coated electrodes, as it may be that this response is accurate after recalibration. So the important parameters are the life time and stability of the plateau potentials, not so much the *pH* values derived from the potentials.

Page intentionally left blank

Chapter 6. Conclusion and further work

pH measurements have an important place in neurobiological studies, especially in the fluid surrounding the brain, which affects the *pH* of other body fluids. The significance of the brain fluid *pH* emphasizes the need for an accurate, practical and reliable *pH* sensor that avoids the disadvantage of the current *pH* sensors such as: need for refreshing the electrode surface (hydrogen electrode), necessity for regular calibration (glass electrode) and poor accuracy and reproducibility (metal oxide electrodes). Moreover, measuring the *pH* sensor of the brain fluid necessarily requires a small size sensor due to the limited space to measure the *pH* in vivo, and the limited sample quantities (typically a few microliters) available for lab work in vitro.

A palladium hydride electrode can overcome the limitations of other *pH* sensors with a rapid, stable and reproducible response. It also does not need to be calibrated before and after each experiment. This is because the obtained potential is independent of composition within the $\alpha+\beta$ transition at H/Pd ratios between 0.02 and 0.6. The PdH electrode shows a Nernstian agreement with a linear potential-*pH* calibration curve, and the practical potentiometric response is in agreement with theoretical response. However, the limited surface area of the Pd microdisc electrode makes hydrogen loading slow and the potential becomes unstable as hydrogen continues to diffuse into the Pd wire. Therefore, the true liquid crystal templating technique was used to create a nanostructured Pd *pH* probe with a high surface area whilst maintaining the geometric surface area of the electrode. The structure accelerates the rate of hydrogen loading and provides a highly stable potential despite the micrometer size of the electrode.

A range of H_{1-e} Pd films were deposited onto Pt disc electrodes ($d = 25, 50$ and $250 \mu\text{m}$) by applying deposition charges Q_{dep} of 25, 100 and 2500 μC respectively, to maintain a uniform deposition charge density j of 5.09 C cm^{-2} and yield a uniform thickness of the H_{1-e} Pd film. The deposition was controlled by recording the chronoamperograms and monitoring the charge passed. Moreover, the geometric surface features of the Pd nanostructured films were compared with those of the substrate electrode, of a similar diameter polished Pd and of a plain Pd film electrode

deposited with a comparable charge using SEM images and cyclic voltammetry. The comparison clearly displays the enhancement in electroactive area that was achieved using the H₁-e Pd nanostructured film, even though other electrodes have the same or larger geometric area. This is because of the contribution from the internal area due to the large numbers of nanostructured pores. The nanostructured palladium works as a solid state reservoir of hydrogen, so a H₁-e Pd film ($Q_{\text{dep}} = 2500 \mu\text{C}$) deposited onto a 250 μm diameter Pt disc electrode was chosen as the working electrode during the potentiometric measurements. Hydrogen loading was carried out into the Pd nanostructure whether by the potentiostatic or by the galvanostatic techniques. The galvanostatic loading of hydrogen is preferred because the loading charge Q_{load} which reflects the quantity of hydrogen loaded into the H₁-e Pd film can be directly obtained from the applied current and loading time. In addition, the galvanostatic hydrogen loading can be done in a shorter period than by the potentiostatic technique simply by applying a large loading current.

The H₁-e Pd electrode can work as a *pH* sensor since the $\alpha+\beta$ transition potential of the Pd hydride is stable and reproducible. There is a constant potential during the $\alpha+\beta$ transition between $0.02 \leq \text{H/Pd} \leq 0.6$, since the $E_{\text{Pd-H}}$ is independent of the electrode composition which depends only on the *pH* of the solution. The *pH* of the solution was estimated via conversion of the measured potential by the Nernst equation or via calibration curves. The $\alpha+\beta$ transition potential was followed by chronopotentiometric measurement, which was done immediately after the hydrogen loading. Chronoamperometric comparison was done with various loading potentials to choose the most appropriate E_{load} : an extreme positive potential would make the hydrogen loading period t_{load} too long to reach full hydrogen loading at $\text{H/Pd} = 0.6$, and an extreme negative E_{load} would cause H₂ gas to evolve on the electrode surface potentially damaging from H₁-e Pd film. Stripping voltammetry was used to studies the H stripping charge verses the H loading charge and to identify the potentials where H desorbed from the Pd lattice and Pd surface.

The calibration curve of $E_{\text{Pd-H}}$ vs. *pH* was created at the human body temperature of 37° C through various *pH* solutions, and it was found that $E_{\text{Pd-H}}$ is in a linear relationship

with pH . Then, the calibration curve of artificial cerebral spinal fluid (aCSF) at human body temperature was performed by titration. It was found that the E_{Pd-H} was quite stable in the $\alpha+\beta$ transition potential, with a reasonable response time (within 5 s) during the titration, and that the calibration curve of E_{Pd-H} was in a linear relationship with pH in the aCSF solution.

The sensing of the pH of a limited quantity of real brain fluid was done in vitro at room temperature, since the sample would evaporate during the measurement, thus changing the concentrations of analytes. The calibration curve at 22° C shows that the slope and the intercept agreed with those of the theoretical calculations, and the sensitivity of the H_{1-e} Pd pH sensor ($\pm pH$) equals ± 0.03 which corresponds to $E_{Pd-H} \pm 0.002$ V.

The presence of oxygen in the measured solution accelerates the hydrogen consuming process of palladium hydride, and decreases the sensor performance period (i.e. lifetime of the $\alpha+\beta$ transition), so the hydrogen reservoir of H_{1-e} Pd film needs regular hydrogen reloading. The degassing with Ar was impractical to clear O_2 from the brain fluid, which initially contains O_2 . Therefore, some attempts were made to cover the surface of the H_{1-e} Pd pH sensor with different types of coatings to stop O_2 from reacting with the H_{1-e} Pd surface. The H_{1-e} Pd films were covered by: ionomers (Nafion), polymer (polypyrrole, polyaniline, poly (phenylene oxide)) and covalent monolayer (diazonium salt (Boc), 1,2-diaminobenzene)). These coatings have the ability to allow hydrogen infiltration through the coat, and stop or at least slow the redox O_2 and interfering species diffusion to the H_{1-e} Pd surface and remain stable with long term usage. These coatings were compared by their influence on the $\alpha+\beta$ transition lifetime and the accuracy of the pH measurements. The comparison between the coats shows that:

Nafion has a high ability to block the oxygen, by slowing down its diffusion, and similarly to slow down the diffusion of interfering species, noticeably extending the lifetime of the $\alpha+\beta$ transition, and leading to an improvement in the performance of the H_{1-e} Pd pH sensor. However, the Nafion has some disadvantages such as that it cannot be electrodeposited and hence the coating thickness cannot be controlled, it also slows the rate of hydrogen absorption into the nanostructured Pd, and it decreases the accuracy of the sensor.

Polypyrrole can be considered as an effective coating for blocking species to the H₁-e Pd electrode surface. However, this includes hydrogen as the coating inhibits the hydrogen loading into the palladium lattice that is a prerequisite for it to act as a *pH* sensor. Polyaniline has some chemical characteristics that can affect the PdH system, as the coating inhibits the hydrogen loading into the palladium lattice and shifts up the average potential $E_{\text{Pd-H}}$ of the $\alpha+\beta$ transition. Therefore, the polyaniline is also not a suitable coating for the H₁-e Pd electrode.

The diazonium salt coating successfully blocks the oxygen, and semi-protects the electrode surface from interfering species. In addition, the coating has improved the performance of the H₁-e Pd *pH* sensor by increasing the $\alpha+\beta$ transition lifetime. The potentiometric measurement of the modified electrode with diazonium salt coating shows a slope in the $\alpha+\beta$ transition leading to an error in the *pH* estimation.

The poly (phenylene oxide) coating cannot block the oxygen or protect the electrode surface from interfering species. In addition, it allows smaller amounts of hydrogen to absorb into the H₁-e Pd film. Therefore, the coating decreased the performance of the H₁-e Pd *pH* sensor by shortening the $\alpha+\beta$ transition lifetime.

The 1,2-diaminobenzene coating has a moderate ability to block oxygen to reach the surface of the *pH* sensor. This coating improves the sensor features to block the electroactive species. The coating reduced the amount of the hydrogen loaded into the palladium nanostructure. However, the lifetime of the $\alpha+\beta$ transition was increased by reducing the hydrogen diffusion rate through the coating. The coated H₁-e Pd film maintained the plateau that was lost in the other modifications with little error in the *pH* of aerated aCSF.

The aim of the project was to create a microelectrode *pH* sensor to measure the *pH* of brain fluids, because neurobiological *pH* measurements require a small sensor, as a result of the limited biological sample quantities available. This was achieved with a H₁-e Pd film which chosen as the required *pH* sensor, on the grounds that it has a high surface due to the contribution of the internal area of the large numbers of nanostructured pores. The project was done using a H₁-e Pd electrode to estimate the *pH* of 240 μl of real brain fluid. The results obtained demonstrate the applicability of such

electrodes to function as *pH* sensors in brain fluid. However, these measurements have been done in vitro at room temperature. So, the future work can be done in vivo or in a catheter at body temperature. The sensor stability as long as possible is an important issue in *pH* measurements of brain fluid, which can be achieved by enlargement the Pd amount of the sensor taking into consideration the sensor size for the application and the packaging.

In addition, the biomedical applications require a sensor that should not be affected by the biological samples contaminations or by oxygen presence. Attempts have been made to improve the nanostructured Pd electrodes performance by covering their surface with coatings to stop the biological impurities and hinder O₂, but this part of the research needs to continue until an ideal coating is formed. Further work can be done by concentrating on this objective.

Page intentionally left blank

References

1. Mexal, S. et al., Brain pH has a significant impact on human postmortem hippocampal gene expression profiles. *Brain Research* 2006, **1106**, 1-11.
2. Vorstrup, S. et al., Neuronal pH regulation: constant normal intracellular pH is maintained in brain during low extracellular pH induced by acetazolamide-³¹P NMR study. *Journal of Cerebral Blood Flow & Metabolism* 1989, **9**(3), 417-421.
3. Hardy, J.A.; Wester, P.; Winblad, B.; Gezelius, C.; Bring, G.; Eriksson, A., The patients dying after long terminal phase have acidotic brains; Implications for biochemical measurements on autopsy tissue. *J. Neural Transmission* 1985, **61**, 253-264.
4. Mutch, W.; Hansen, A.J.; Extracellular pH changes during spreading depression and cerebral ischemia: mechanisms of brain pH regulation. *Journal of the International Society of Cerebral Blood Flow and Metabolism* 1984, **4**(1), 17.
5. Kaila, K.; Ransom, B.R.R., *pH and Brain Function*. 1998, p. 688, John Wiley, New York.
6. Levine, S.H.; Helpern, J.A.; Welch K.M.; Vande Linde A.M.; Sawaya, K.L.; Brown, E.E.; Ramadan, N.M.; Deveshwar, R.K.; Ordidge, R.J., Human focal cerebral ischemia: evaluation of brain pH and energy metabolism with P-31 NMR spectroscopy. *Radiology* 1992, **185**(2), 537.
7. Monoranu, C.M.; Apfelbacher, M.; Grünblatt, E.; Puppe, B.; Alafuzoff, I.; Ferrer, I.; Al-Saraj, S.; Keyvani, K.; Schmitt, A.; Falkai, P.; Schittenhelm, J.; Halliday, G.; Kril, J.; Harper, C.; McLean, C.; Riederer, P.; Roggendorf, W., pH measurement as quality control on human post mortem brain tissue: a study of the BrainNet Europe consortium. *Neuropathology and Applied Neurobiology* 2009, **35**(3), 329-337.
8. Imokawa, T., *Fabrication and characterisation of nanostructured palladium hydride microelectrode pH sensors*, Department of Chemistry 2003. University of Southampton.
9. Williams, K.-J., *Development of nanostructured palladium microelectrode for pH monitoring in scanning electrochemical microscopy* 2008.
10. Imokawa, Toru; Williams, K.-J.; Denuault, G., Fabrication and characterization of nanostructured Pd hydride pH microelectrodes. *Analytical Chemistry* 2006, **78**(1), 265-271.
11. Calle-Vallejo, F.; Koper, M.T.M., First-principles computational electrochemistry: Achievements and challenges. *Electrochimica Acta*. Online at <http://www.sciencedirect.com/science/article/pii/S0013468612006184>
12. Ives, D.J.G.; Janz, G.J., Reference electrodes: theory and practice. *Journal of the Electrochemical Society* 1961, **108**, 246C.
13. Compton, R.G.; Giles, H.J., *Electrode Potentials*. 1996, Oxford University Press.
14. McLauchlan, G. et al., Electrodes for 24 hours pH monitoring—a comparative study. *Gut* 1987, **28**(8), 935-939.

15. Rajendraprasad, N. et al., Titrimetric assay of hydroxyzine dihydrochloride in pharmaceuticals and formulations in non-aqueous medium. *Intl. J. ChemTech Res* 2013, **5**(1), 105-111.
16. Ansari, R.; Khanesar, P.H., Application of spent tea leaves as an efficient low cost biosorbent for removal of anionic surfactants from aqueous solutions. *European Chemical Bulletin* 2013, **2**(5).
17. Ives, G.J.; Janz, D.J.G., *Reference Electrodes, Theory and Practice*, 1961, New York, Academic Press.
18. Bard, A.; Faulkner, L. *Electrochemical Methods: Fundamentals and applications*. 2nd edn, 1980. New York, Wiley.
19. Alberty, R.A.; Sibey, R.J, *Physical Chemistry*, 1992. New York, Wiley.
20. Bates, R.G., *Determination of pH; Theory and practice*. 1973. New York, Wiley.
21. Teixeira, M.F.S. et al., A solid Fe₂O₃ based carbon-epoxy electrode for potentiometric measurements of pH. *Journal of Analytical Chemistry* 2002, **57**(9), 826-831.
22. O'Hare, D.; Parker, K.H.; Winlove, C.P. *Metal-metal oxide pH sensors for physiological application. Medical Engineering & Physics* 2006, **28**(10), 982-988.
23. Wipf, D.O.; Fuyun, G.; Spaine; Thomas W.; Baur, John E., Microscopic measurement of pH with iridium oxide microelectrodes. *Analytical Chemistry* 2000, **72**(20), 4921-4927.
24. Yang Ha; Wang, M., Capillary melt method for micro antimony oxide pH electrode. *Electroanalysis* 2006, **18**(11), 1121-1125. NB AUTHORS IN CITATION.
25. Koncki, R.; Mascini, M. Screen-printed ruthenium dioxide electrodes for pH measurements. *Analytica Chimica Acta* 1997, **351**(1-3), 143-149.
26. Yamamoto, K. et al., Solid-state pH ultramicrosensor based on a tungstic oxide film fabricated on a tungsten nanoelectrode and its application to the study of endothelial cells. *Analytica Chimica Acta* 2003, **480**(1), 109-117.
27. Kreider, K.G.; Tarlov, M.J.; Cline, J.P., Sputtered thin-film pH electrodes of platinum, palladium, ruthenium, and iridium oxides. *Sensors and Actuators B: Chemical* 1995, **28**(3), 167-172.
28. Prats-Alfonso, E. et al., Iridium oxide pH sensor for biomedical applications. Case urea-urease in real urine samples. *Biosensors and Bioelectronics* 2013, **39**(1), 163-169.
29. Kinoshita, E. et al., Polycrystalline and monocrystalline antimony, iridium and palladium as electrode material for pH-sensing electrodes. *Talanta* 1986, **33**(2), 125-134.
30. Fog, A.; Buck, R.P., Electronic semiconducting oxides as pH sensors. *Sensors and Actuators* 1984, **5**(2), 137-146.
31. Huang, W.-D. et al., A flexible pH sensor based on the iridium oxide sensing film. *Sensors and Actuators A: Physical* 2011, **169**(1), 1-11.
32. Wang, M., Yao, S.; Madou, M., A long-term stable iridium oxide pH electrode. *Sensors and Actuators B: Chemical* 2002, **81**(2-3), 313-315.

33. Pan, Y. et al. *Optimization of Sputtering Condition of IrOx Thin Film Stimulation Electrode for Retinal Prosthesis Application*, 2012. IOP Publishing.
34. Li, J.; Du, Y.; Fang, C., Developing an iridium oxide film modified microelectrode for microscale measurement of pH *electroanalysis* 2007, **19**(5), 608-611.
35. Bezbaruah, A.N.; Zhang, T.C., Fabrication of anodically electrodeposited iridium oxide film pH microelectrodes for microenvironmental studies. *Analytical Chemistry* 2002, **74**(22), 5726-5733.
36. VanHoudt, P.; Lewandowski, Z.; Little, B., Iridium oxide pH microelectrode. *Biotechnology and Bioengineering* 1992, **40**(5), 601-608.
37. Rosenfeldt, F.L. et al., Evaluation of a miniature antimony electrode for measurement of myocardial pH. *Journal of Medical Engineering & Technology* 1999, **23**(4), 119-126.
38. Horrocks, B.R. et al., Scanning electrochemical microscopy. 19. Ion-selective potentiometric microscopy. *Analytical Chemistry* 1993, **65**(9), 1213-1224.
39. Mihell, J.A.; Atkinson, J.K., Planar thick-film pH electrodes based on ruthenium dioxide hydrate. *Sensors and Actuators B: Chemical* 1998, **48**(1-3), 505-511.
40. McMurray, H.N.; Douglas, P.; Abbot, D., Novel thick-film pH sensors based on ruthenium dioxide-glass composites. *Sensors and Actuators B: Chemical* 1995, **28**(1), 9-15.
41. Dimitrakopoulos, L.D.; Alexander, T.; Logic, P.W.; Hibbert, D., A tungsten oxide coated wire electrode used as a pH sensor in flow injection potentiometry. *Analytical Communications* 1998, **35**(12), 395-398.
42. Liu, C. et al., A palladium-palladium oxide miniature pH electrode. *Science* 1980, **207**(4427), 188-189.
43. Kim, J.Y.; Lee, Y.H., Pd-PdO pH microprobe for local pH measurement. *Biotechnology and Bioengineering* 1989, **34**(1), 131-136.
44. Graham, T., *Philos. Trans. R. Soc.*, 1866, **156**, 415.
45. Ksar, F. et al., Palladium urchin-like nanostructures and their H₂ sorption properties. *Nanotechnology* 2011, **22**(30), 305-609.
46. Calles, J.A.; Sanz, R.; Alique, D., Influence of the type of siliceous material used as intermediate layer in the preparation of hydrogen selective palladium composite membranes over a porous stainless steel support. *International Journal of Hydrogen Energy* 2012, **37**(7), 6030-6042.
47. Korin, E. et al., Preparation of a novel Pd hydride electrode based on polymer embedded nanosized Pd incorporated in porous carbon substrate. *Electrochemical and Solid-state Letters* 2004, **7**, A484.
48. Fernández, M.B. et al., Hydrogenation of edibleoil over Pd catalysts: A combined theoretical and experimental study. *Journal of Molecular Catalysis A: Chemical* 2005, **237**(1-2), 67-79.
49. Klotz, E.; Mattson, B., Hydrogen and palladium foil: Two classroom demonstrations. *Journal of Chemical Education* 2009, **86**(4), 465.

50. Lewis, F., The palladium-hydrogen system: A survey of hydride formation and the effects of hydrogen contained within the metal lattices. *Platinum Metals Rev.* 1982, **26**(1), 20-27.
51. Wolf, R.J. et al., Pressure-composition isotherms for palladium hydride. *Physical Review B* 1993, **48**(17), 12415-12418.
52. Nace, D.M.; Aston, J.G., Palladium hydride. I. The thermodynamic properties of Pd₂H between 273 and 345°K.1. *Journal of the American Chemical Society* 1957, **79**(14), 3619-3623.
53. Tripodi, P., Di Gioacchino, D.; Vinko, J.D., Superconductivity in PdH: phenomenological explanation. *Physica C: Superconductivity* 2004, **408-410**, 350-352.
54. Wei, I.-Y.; Brewer, J., Desorption of Hydrogen from Palladium Plating. *AMP Journal of Technology* 1996, **5**, 49-53. Online at http://www.te.com/documentation/whitepapers/pdf/5jot_7.pdf
55. McLennan, K.G., Structural studies of the palladium-hydrogen system, in *School of Science* 2006, Griffith University, Australia.
56. Wheeler, J.M.; Clyne, T.W., Nanoindentation of palladium-hydrogen. *International Journal of Hydrogen Energy* 2006, **31**, 223-229.
57. Adams, B.D.; Ostrom, C.K.; Chen, A., Hydrogen electrosorption into Pd-Cd nanostructures, *Langmuir* 2010, **26** (10), 7632-7637.
58. Hoare, J.P.; Schuldiner, S., Effects of hydrogen content on the resistance and the potential in the palladium-hydrogen-acid system. *Journal of Physical Chemistry* 1957, **61**(4), 399-402.
59. Aben, P.C.; Burgers, W.G., Surface structure and electrochemical potential of palladium while absorbing hydrogen in aqueous solution. *Transactions of the Faraday Society* 1962, **58**, 1989-1992.
60. Flanagan, T.B.; Lewis, F.A., Electrode potentials of the palladium + hydrogen system. *Transactions of the Faraday Society* 1959, **55**, 1409-1420.
61. Vasile, M.J.; Enke, C.G., The preparation and thermodynamic properties of a palladium-hydrogen electrode. *Journal of the Electrochemical Society* 1965. **112**(8), 865-870.
62. Bartlett, P.N.; Marwan, J., The effect of surface species on the rate of H sorption into nanostructured Pd. *Physical Chemistry Chemical Physics* 2004, **6**(11), 2895-2898.
63. Digby, D.; Macdonald, P.R.W.; Scott, Arthur C., *The measurement of pH in aqueous systems at elevated temperatures using palladium hydride electrodes.* *J. Electrochem. Soc.* 1980, **127**(8), 1745-1751.
64. Tsuruta, T.; Macdonald, D.D., *Measurement of pH and redox potential in boric acid/lithium hydroxide buffer solutions at elevated temperatures.* *Journal of the Electrochemical Society* 1981, **128**(6), 1199-1203.
65. Jasinski, R., A palladium hydride pH electrode for use in buffered fluoride etch solutions. *Journal of the Electrochemical Society* 1974, **121**(12), 1579-1584.
66. Wolfe, R.C. et al., Measurement of pH gradients in the crevice corrosion of iron using a palladium hydride microelectrode. *Journal of The Electrochemical Society* 2005, **152**(2), B82-B88.

67. Gabrielli, C. et al., Study of the hydrogen/palladium system by fast quartz microbalance techniques. *Electrochimica Acta* 2002, **47**(13-14), 2199-2207.
68. Zhang, W.-S.; Zhang, X.W.; Li, H.-Q., The maximum hydrogen (deuterium) loading ratio in the Pd|H₂O (D₂O) electrochemical system. *Journal of Electroanalytical Chemistry* 1997, **434**(1-2), 31-36.
69. Mengoli, G. et al., The insertion/extraction of deuterium (hydrogen) at Pd sheet electrodes in D₂O(H₂O) + LiOD(LiOH) electrolyte. *Journal of Electroanalytical Chemistry* 1996, **403**(1-2), 143-151.
70. Lim, C.; Pyun, S.-I., Impedance analysis of hydrogen absorption reaction on Pd membrane electrode in 0.1 M LiOH solution under permeable boundary conditions. *Electrochimica Acta* 1994, **39**(3), 363-373.
71. Vigier, F.; Jurczakowski, R.; Lasia, A., Determination of hydrogen absorption isotherm and diffusion coefficient in Pd₈₁Pt₁₉ alloy. *Journal of Electroanalytical Chemistry* 2006, **588**(1), 32-43.
72. Szpak, S. et al., *Absorption of deuterium in palladium rods: model vs. experiment.* *Journal of Electroanalytical Chemistry* 1994. **365**(1-2), 275-281.
73. Czerwiński, A., Kiersztyn, I.; Grdeń, M., Temperature influence on hydrogen sorption in palladium limited-volume electrodes (Pd-LVE). *Journal of Solid State Electrochemistry* 2003. **7**(6), 321-326.
74. Conway, B.E.; Jerkiewicz, G., Thermodynamic and electrode kinetic factors in cathodic hydrogen sorption into metals and its relationship to hydrogen adsorption and poisoning. *Journal of Electroanalytical Chemistry* 1993, **357**(1-2), 47-66.
75. Łukaszewski, M., Grden, M.; Czerwinski, A., Comparative study on hydrogen electrosorption in palladium and palladium-noble metal alloys. *Journal of New Materials for Electrochemical Systems* 2006, **9**: 409-417.
76. Hofman, M. et al., Cyclovoltammetric studies of carbon materials-supported palladium. *Reaction Kinetics, Mechanisms and Catalysis* 2012, 106:203-216.
77. Czerwiński, A. et al., The study of hydrogen sorption in palladium limited volume electrodes (Pd-LVE): Part I. Acidic solutions. *Journal of Electroanalytical Chemistry* 1999, **471**(2) 190-195.
78. Czerwiński, A.; Kiersztyn, I.; Grdeń, M., The study of hydrogen sorption in palladium limited volume electrodes (Pd-LVE): Part II. Basic solutions. *Journal of Electroanalytical Chemistry* 2000, **492**(2), 128-136.
79. Laughlin, R.G., *The Aqueous Phase Behavior of Surfactants.* 1994, Cambridge University Press.
80. Bartlett, P. N.; Guerin, S.; Marwan, J., The preparation and characterisation of H₁-e palladium films with a regular hexagonal nanostructure formed by electrochemical deposition from lyotropic liquid crystalline phases. *Phys. Chem. Chem. Phys.* 2002, **4**: 3835–3842.
81. Mitchell, D. et al. Phase behaviour of polyoxyethylene surfactants with water. *J. Chem. Soc.* 1983, **79**, 975–1000.
82. Cook, D.A., An investigation the electrochemical properties of nanostructured metals and their application as amperometric biosensors 2005, University of Southampton.

83. Attard, G.S.; Glyde; J.C.; Goltner, C.G., Liquid-crystalline phases as templates for the synthesis of mesoporous silica. *Nature* 1995, **378**(6555), 366-368.
84. Attard, G.S. et al., Mesoporous platinum films from lyotropic liquid crystalline phases. *Science* 1997, **278**: 838 -840.
85. Guerin, S., An application of electrodeposited mesoporous palladium films for the detection of combustible gases in Department of Chemistry 1999, University of Southampton.
86. Bartlett, P.N.; Marwan, J., Electrochemical deposition of nanostructured (H1-e) layers of two metals in which pores within the two layers interconnect. *Chemistry of Materials* 2003, **15**(15), 2962-2968.
87. Pletcher, D.; Greef, R.; Peat, R.; Peter, L.M.; Robinson, J., *Instrumental Methods in Electrochemistry*, 2006 edn, 1985, Chichester, East Sussex, Ellis Horwood.
88. El-Hallag, I.S., Electrochemical and SEM properties of Co²⁺ ion in hexagonal mesophase of pluronic lyotropic liquid crystal template. *Indian Academy of Sciences* 2009, **32**(5), 555-560.
89. Wen-Jia Zhou, M.-W.X., Zhao, D.-D.; Xu; C.-L.; Li, H.-L., Electrodeposition and characterization of ordered mesoporous cobalt hydroxide films on different substrates for supercapacitors. *Microporous and Mesoporous Materials* 2009, **117**: 55–60.
90. Al-Bishri, H.M.; El-Hallag, I.S.; El-Mossalamy, E.S.H., Preparation and characterization of ordered nanostructured cobalt films via lyotropic liquid crystal templated electrodeposition method. *Bulletin of the Korean Chemical Society* 2010, **31**(12), 3730-3734.
91. Nelson, P.A.; Elliot, J.M.; Attard, G.S.; Owen, J.R., Mesoporous nickel/nickel oxide—a nanoarchitected electrode. *Chem. Mater.* 2002, **14**: 524-529.
92. Bartlett, P.N.; Marwan, J., Preparation and characterization of H1-e rhodium films. *Microporous and Mesoporous Materials* 2003, **62**(1-2), 73-79.
93. Dellinger, T.M.; Braun, P.V., Lyotropic liquid crystals as nanoreactors for nanoparticle synthesis. *Chemistry of Materials* 2004, **16**(11), 2201-2207.
94. Ding, J.H.; Gin, D.L., Catalytic Pd nanoparticles synthesized using a lyotropic liquid crystal polymer template. *Chem. Mater.* 2000, **12**, 22-24.
95. Zhao, D.-D. et al., Preparation of ordered mesoporous nickel oxide film electrodes via lyotropic liquid crystal templated electrodeposition route. *Electrochimica Acta* 2008, **53**(6), 2699-2705.
96. Liu, L.H. et al., Fabrication and characteristics of TiO₂ nanomaterials templated by lyotropic liquid crystal. *Advanced Materials Research* 2012, **399**, 532-537.
97. Mubeen, S. et al., Palladium nanoparticles decorated single-walled carbon nanotube hydrogen sensor. *Journal of Physical Chemistry C* 2007, **111**(17), 6321-6327.
98. Shuji Harada, Tanaka, H.; Araki, H.; Kubota, M., Effect of oxygen on hydrogen outgassing process from palladium hydride. *Materials Transactions* 2008, **49**(12), 2895-2898.

99. Christen, T. et al., Measuring brain oxygenation in humans using a multiparametric quantitative blood oxygenation level dependent MRI approach. *Magnetic Resonance in Medicine* 2012, **68**(3), 905-911.
100. Kinlen, P.J., Heider, J.E.; Hubbard, D.E., A solid-state pH sensor based on a Nafion-coated iridium oxide indicator electrode and a polymer-based silver chloride reference electrode. *Sensors and Actuators B: Chemical* 1994, **22**(1), 13-25.
101. Bertonecello, P.; Peruffo, M.; Unwin, P.R.; Formation and evaluation of electrochemically-active ultra-thin palladium-Nafion nanocomposite films. *ChemComm* 2007, 1597-1599.
102. Choi, P.; Jalani, N.H.; Datta, R., Thermodynamics and proton transport in nafion. *Journal of the Electrochemical Society* 2005, **152**(3), E123-E130.
103. Hickner, M.A. et al., Alternative polymer systems for proton exchange membranes (PEMs). *Chemical Reviews* 2004, **104**(10), 4587-4612.
104. Kreuer, K.-D. et al., Transport in proton conductors for fuel-cell applications: simulations, elementary reactions, and phenomenology. *Chemical Review* 2004, **104**(10), 4637-4678.
105. Zimmerman, J.B.; Wightman, R.M., Simultaneous electrochemical measurements of oxygen and dopamine in vivo. *Analytical Chemistry* 1991, **63**(1), 24-28.
106. Elliott, J.M.; Cabuché, L.M.; Bartlett, P.N., *Electrochemical characterization of a templated insulating polymer-modified electrode. Analytical Chemistry* 2001, **73**(13), 2855-2861.
107. Kanazawa, K.K. et al., 'Organic metals': Polypyrrole, a stable synthetic 'metallic' polymer. *Journal of the Chemical Society, Chemical Communications* 1979, 19, 854-855.
108. Tietje-Girault, J.; Ponce de León, C.; Walsh, F.C., Electrochemically deposited polypyrrole films and their characterization. *Surface and Coatings Technology* 2007, **201**(12), 6025-6034.
109. Sadki, S. et al., The mechanisms of pyrrole electropolymerization. *Chemical Society Reviews* 2000, **29**(5), 283-293.
110. Malinauskas, A., Chemical deposition of conducting polymers. *Polymer* 2001, **42**(9), 3957-3972.
111. Alemán, C. et al., Cross-linking in polypyrrole and poly(N-methylpyrrole), Comparative experimental and theoretical studies. *Polymer* 2008, **49**(4), 1066-1075.
112. Freund, M.; Bodalbhai, L.; Brajter-Toth, A., Anion-excluding polypyrrole films. *Talanta* 1991, **38**(1), 95-99.
113. Hsueh, C.; Brajter-Toth, A., Electrochemical preparation and analytical applications of ultrathin overoxidized polypyrrole films. *Analytical Chemistry* 1994, **66**(15), 2458-2464.
114. Debiemme-Chouvy, C.; Gallois, M., Characterization of a very thin overoxidized polypyrrole membrane: application to H₂O₂ determination. *Surface and Interface Analysis* 2010, **42**(6-7), 1144-1147.

115. Arrigan, D.W.M, Permselective behaviour at overoxidised Poly[1-(2-carboxyethyl)pyrrole] films: Dopamine versus ascorbate. *Analytical Communications* 1997, **34**(9), 241-244.
116. Ghita, M.; Arrigan, D.W.M., *Electrochemical overoxidation of polyindole and its cation-permselective behavior. Electroanalysis* 2004, **16**(12), 979-987.
117. Choi, K.M.; Kim, C.Y.; Kim, K.H., *Polymerization mechanism and physicochemical properties of electrochemically prepared polyindole tetrafluoroborate. Journal of Physical Chemistry* 1992, **96**(9), 3782-3788.
118. Wu, Z.-Y. et al., Nanofracture on fused silica microchannel for Donnan exclusion based electrokinetic stacking of biomolecules. *Lab on a Chip* 2012, **12**(18), 3408-3412.
119. Sayyah, S.M. et al., Electropolymerization of o-phenylenediamine on Pt-electrode from aqueous acidic solution: Kinetic, mechanism, electrochemical studies and characterization of the polymer obtained. *Journal of Applied Polymer Science* 2009, **112**(6), 3695-3706.
120. Dinh, H.N.; Birss, V.I., Effect of substrate on polyaniline film properties a cyclic voltammetry and impedance study. *Journal of the Electrochemical Society* 2000, **147**(10), 3775-3784.
121. Bleda-Martínez, M.J.; Morallón, E.; Cazorla-Amorós, D., Polyaniline/porous carbon electrodes by chemical polymerisation: Effect of carbon surface chemistry. *Electrochimica Acta* 2007, **52**(15), 4962-4968.
122. Bartlett, P.N.; Tebbutt, P.; Tyrrell, C.H., Electrochemical immobilization of enzymes. 3. Immobilization of glucose oxidase in thin films of electrochemically polymerized phenols. *Analytical Chemistry* 1992, **64**(2), 138-142.
123. Bartlett, P.N.; Caruana, D.J., Electrochemical immobilization of enzymes. Part V. Microelectrodes for the detection of glucose based on glucose oxidase immobilized in a poly(phenol) film. *Analyst* 1992, **117**(8), 1287-1292.
124. Wang, J.; Jiang, M.; Lu, F., *Electrochemical quartz crystal microbalance investigation of surface fouling due to phenol oxidation. Journal of Electroanalytical Chemistry* 1998, **444**(1), 127-132.
125. Yuqing, M.; Jianrong, C.; Xiaohua, W., Using electropolymerized non-conducting polymers to develop enzyme amperometric biosensors. *Trends in Biotechnology* 2004, **22**(5), 227-231.
126. Barbier, B. et al., Electrochemical bonding of amines to carbon fiber surfaces toward improved carbon-epoxy composites. *Journal of The Electrochemical Society* 1990, **137**(6), 1757-1764.
127. Stewart, M.P. et al., Direct covalent grafting of conjugated molecules onto Si, GaAs, and Pd surfaces from aryldiazonium salts. *Journal of the American Chemical Society* 2003, **126**(1), 370-378.
128. Chrétien, J.-M. et al., Covalent tethering of organic functionality to the surface of glassy carbon electrodes by using electrochemical and solid-phase synthesis methodologies. *Chemistry—A European Journal* 2008, **14**(8), 2548-2556.
129. Ghanem, M.A. et al., Covalent modification of glassy carbon surface with organic redox probes through diamine linkers using electrochemical and solid-

- phase synthesis methodologies. *Journal of Materials Chemistry* 2008, **18**(41), 4917-4927.
130. Ghanem, M.A. et al., *Electrochemical and solid-phase synthetic modification of glassy carbon electrodes with dihydroxybenzene compounds and the electrocatalytic oxidation of NADH*. *Bioelectrochemistry* 2009, **76**(1-2), 115-125.
131. Cai, J.Y. et al., An improved method for functionalisation of carbon nanotube spun yarns with aryldiazonium compounds. *Carbon* 2012, **50**(12), 4655-4662.
132. Bartlett, P.N., In *Biosensors: A Practical Approach*. 1990, Oxford University Press.
133. Compton, R.G.; Banks, C.E., *Understanding Voltammetry*. 2011, Imperial College Pr.
134. Seiler, H., Secondary electron emission in the scanning electron microscope. *Journal of Applied Physics* 1983, **54**(11), R1-R18.
135. Pletcher, D., *A First Course in Electrode Processes*, 2nd edn. 2009, p. 136. Romsey, Electrochemical Consultancy.
136. Dickinson, E.J.F. et al., How much supporting electrolyte is required to make a cyclic voltammetry experiment quantitatively 'diffusional'? A theoretical and experimental investigation. *Journal of Physical Chemistry C* 2009, **113**(25), 11157-11171.
137. Zoski, Cynthia G., Ultramicroelectrodes: Design, fabrication, and characterization. *Electroanalysis* 2002, **14**(15-16), 1041-1051.
138. Trasatti, S.; Petrii, O.A., Real surface area measurements in electrochemistry. *Journal of Electroanalytical Chemistry* 1992, **327**(1-2), 353-376.
139. Pyo, M.; Bard, J.A., *Scanning electrochemical microscopy. 35. Determination of diffusion coefficients and concentrations of Ru(NH₃)₆³⁺ and methylene blue in polyacrylamide films by chronoamperometry at ultramicrodisk electrodes*. *Electrochimica Acta* 1997, **42**(20-22), 3077-3083.
140. Pyo, M.; Bard, J.A. Scanning electrochemical microscopy. 35. Determination of diffusion coefficients and concentrations of Ru(NH₃)₆³⁺ and methylene blue in polyacrylamide films by chronoamperometry at ultramicrodisk electrodes. *Electrochimica Acta* 1997. **42**(20-22), 3077-3083.
141. Banks, C.E., Reeves, N.V.; Compton, R.G., Sonoelectrochemistry in acoustically emulsified media. *Journal of Electroanalytical Chemistry* 2002, **535**: 41-47.
142. Sterzik, K.; Rosenbuch, B.; Sasse, V.; Wolf, A.; Beier, H.M.; Lauritzen, C., A new variation of in-vitro fertilization: Intravaginal culture of human oocytes and cleavage stages. *Human Reproduction* 1989, **4**, 83-86.
143. Compton, R.G. et al., Room temperature ionic liquid carbon nanotube paste electrodes: Overcoming large capacitive currents using rotating disk electrodes. *Electroanalysis* 2007, **19**(14), 1483-1489.
144. Lu, P.W.T.; Ammon, R.L., An investigation of electrode materials for the anodic oxidation of sulfur dioxide in concentrated sulfuric acid. *Journal of the Electrochemical Society* 1980, **127**(12), 2610-2616.

145. Rand, D.A.J.; Woods, R., A study of the dissolution of platinum, palladium, rhodium and gold electrodes 1 M sulphuric acid by cyclic voltammetry. *J. Electroanal. Chem.* 1972, **35**: 209-218.
146. Mallia, J.S.; Straub, Stephen V.; McBride, John R., An electrochemical puzzle: The catalyzed anodic dissolution of i-coated palladium in halide-free acid solutions. *The Chemical Educator* 1998. **3**(5), 1-16.
147. Denuault, G., *Electrochemical techniques and sensors for ocean research.* Ocean Sci. 2009. **5**: 697-710.
148. Juodkazis, K.; Šebeka, B.; Stalnionis, G.; Lukinskas, A., Anodic dissolution of palladium in sulfuric acid: An electrochemical quartz crystal microbalance study. *Russian Journal of Electrochemistry* 2003, 954-959.
149. Burke, L.; Casey, J., *An examination of the electrochemical behavior of palladium electrodes in acid.* *Journal of the Electrochemical Society* 1993, **140**(5), 1284-1291.
150. Rodríguez, D. et al., Determination of the real surface area of Pt electrodes by hydrogen adsorption using cyclic voltammetry. *Journal of Chemical Education* 2000, **77**: 1195.
151. Wang, M., et al., Solid-state dye-sensitized solar cells using ordered TiO₂ nanorods on transparent conductive oxide as photoanodes. *Journal of Physical Chemistry C* 2012.
152. Wenzel, R.N., Surface roughness and contact angle. *Journal of Physical and Colloid Chemistry* 1949, **53**(9), 1466-1467.
153. Elliott, J.M. et al., Nanostructured platinum (HI-ePt) films: Effects of electrodeposition conditions on film properties. *Chemistry of Materials* 1999. **11**(12), 3602-3609.
154. Nowakowski, R.; Grzeszczak, P.; Dus, R., Hydrogen-induced stress relaxation in thin Pd films: Influence of carbon implementation. *Langmuir* 2007, **23**(4), 1752-1758.
155. Bonnefont, A. et al., Hydrogen electrooxidation on PdAu supported nanoparticles: An experimental RDE and kinetic modeling study. *Catalysis Today* 2013, **202**(15) 70-78.
156. Shrestha, B.R.; Nishikata, A.; Tsuru, T., Channel flow double electrode study on palladium dissolution during potential cycling in sulfuric acid solution. *Electrochimica Acta* 2012, **70**, 42-49.
157. Pourbaix, M., *Atlas of Electrochemical Equilibria in Aqueous Solutions.* M. Pourbaix, 1974, p. 644, NACE.
158. Kelly, J.; Goffe, J.; Tseung, R., Internally charged palladium hydride reference electrode: II Automatically controlled palladium hydride electrode. *Medical and Biological Engineering and Computing* 1981, **19**(3), 333-339.
159. White, M. et al., Human body temperature and new approaches to constructing temperature-sensitive bacterial vaccines. *Cellular and Molecular Life Sciences* 2011, 1-13.
160. McNay, E.C.; Sherwin, R.S., From artificial cerebro-spinal fluid (aCSF) to artificial extracellular fluid (aECF), microdialysis perfusate composition effects

- on in vivo brain ECF glucose measurements. *Journal of Neuroscience Methods* 2004, **132**(1), 35-43.
161. Bolduc, O.R.; Masson, J.-F.O., Monolayers of 3-mercaptopropyl-amino acid to reduce the nonspecific adsorption of serum proteins on the surface of biosensors. *Langmuir* 2008, **24**(20), 12085-12091.
162. Mathur, A. et al., Development of a biosensor for detection of pleural mesothelioma cancer biomarker using surface imprinting. *PLOS ONE* 2013, **8**(3), e57681. DOI: 10.1371/journal.pone.0057681
163. Zhang, Y. et al., *Estrogen facilitates spinal cord synaptic transmission via membrane-bound estrogen receptors: Implications for pain hypersensitivity.* *J Biol Chem* 2012, **287**(40), 33268-81.
164. Estey, T. et al., BSA degradation under acidic conditions: A model for protein instability during release from PLGA delivery systems. *Journal of Pharmaceutical Sciences* 2006, **95**(7), 1626-1639.
165. Shao, L.-Y. et al., Fiber optic pH sensor with self-assembled polymer multilayer nanocoatings. *Sensors* 2013, **13**(2), 1425-1434.
166. Feuerstein, D. et al., Dynamic metabolic response to multiple spreading depolarizations in patients with acute brain injury: An online microdialysis study. *Journal of Cerebral Blood Flow & Metabolism* 2010, **30**(7), 1343-1355.
167. Li, S. et al., Molecular sieving in a nanoporous b-oriented pure-silica-zeolite MFI monocystal film. *Journal of the American Chemical Society* 2004, **126**(13), 4122-4123.
168. Denuault, G.; Frank, M.H. Troise; Peter, L.M., Scanning electrochemical microscopy: Potentiometric probing of ion fluxes. *Faraday Discussions* 1992, **94**, 23-35.
169. Dhaoui, W. et al., Redox behaviour of polyaniline–palladium catalytic system in the presence of formic acid. *Synthetic Metals* 2010, **160**(23-24), 2546-2551.
170. Sosna, M. et al., Monolayer anthracene and anthraquinone modified electrodes as platforms for *Trametes hirsuta* laccase immobilisation. *Physical Chemistry Chemical Physics* 2010, **12**(34), 10018-10026.
171. Griveau, S. et al., Electrochemical grafting by reduction of 4-aminoethylbenzenediazonium salt: Application to the immobilization of (bio)molecules. *Electrochemistry Communications* 2007, **9**(12), 2768-2773.
172. Selvaraju, T.; Ramaraj, R., Simultaneous determination of dopamine and serotonin in the presence of ascorbic acid and uric acid at poly(o-phenylenediamine) modified electrode. *Journal of Applied Electrochemistry* 2003, **33**(8), 759-762.

Page intentionally left blank